Modeling the Development of Joint Faulting for Bonded Concrete Overlays of Asphalt Pavements (BCOA)

by

John William DeSantis

B.S. Civil Engineering, University of Pittsburgh, 2014

B.S. Mathematics, Saint Vincent College, 2013

Submitted to the Graduate Faculty of the

Swanson School of Engineering in partial fulfillment

of the requirements for the degree of

Doctor of Philosophy

University of Pittsburgh

2020

UNIVERSITY OF PITTSBURGH

SWANSON SCHOOL OF ENGINEERING

This dissertation was presented

by

John William DeSantis

It was defended on

December 6, 2019

and approved by

John Harvey, Ph.D, Professor, Department of Civil and Environmental Engineering, University of California - Davis

Vikas Khanna, Ph.D, Associate Professor, Department of Civil and Environmental Engineering

Lev Khazanovich, Ph.D, Professor, Department of Civil and Environmental Engineering

Dissertation Director: Julie Vandenbossche, Ph.D, Professor, Department of Civil and Environmental Engineering

Modeling the Development of Joint Faulting for Bonded Concrete Overlays of Asphalt Pavements (BCOA)

John William DeSantis, PhD

University of Pittsburgh, 2020

Bonded concrete overlays of asphalt pavements (BCOAs), also known as whitetopping, consist of a thin concrete overlay on distressed asphalt or composite pavements. They typically have smaller panel sizes than traditional jointed plain concrete pavements (JPCP) in order to reduce stress levels. A distress that can occur in BCOAs is transverse joint faulting, but to date there is no predictive faulting model available for these structures. To be able to develop a faulting prediction model, a better understanding of the joint performance and the pumping mechanism that leads to this distress is necessary. It was determined that pumping in BCOAs is dictated by the depth of joint activation and can develop either at the bottom of the overlay slab within the asphalt layer or at the bottom of the asphalt layer in the granular layer. To account for the conditions unique to BCOA, a computational model was developed to predict the response of these structures. The model was validated using falling weight deflectometer (FWD) data from existing field sections at the Minnesota Road Research Facility (MnROAD) as well as at the University of California Pavement Research Center (UCPRC). A fractional factorial analysis was performed using the field validated computational models to develop predictive models, in the form of artificial neural networks (ANNs). The ANNs are able to rapidly estimate the structural response at the joint in BCOAs to environmental and traffic loads. The structural response is then related to damage using the differential energy (DE) concept. The DE concept is commonly used in faulting prediction models in order to relate damage to faulting. The final steps include conducting

a calibration as well as a sensitivity analysis on the prediction capabilities of the model. The overall framework for predicting faulting for BCOAs is presented and is based on the model in the Pavement Mechanistic-Empirical (ME) design software. Improvements were made to the previous framework to be able to better characterize BCOAs so the accuracy of the predicted faulting could be improved. Future work includes implementation of the BCOA faulting prediction model into the BCOA-ME design guide developed at the University of Pittsburgh.

Table of Contents

List of Tables

List of Figures

Preface

First, I would like to thank my advisor, Professor Julie M. Vandenbossche for her educational and financial support and mentorship throughout my PhD study. I would have never been able to accomplish this without her continuous support. I would also like to give thanks to the other faculty members on my committee: Professors Lev Khazanovich, Vikas Khanna, and John Harvey. In addition, I would also like to extend my appreciation to my fellow graduate and undergraduate students who have helped with my research, i.e. Dr. Kevin Alland, Dr. Steven Sachs, Dr. Zichang Li, Ms. Nicole Duffala, Mr. Alex Voutto, Mr. Nathan Bech, Mr. Andrew Rogers, Mr. Aldo Ferreira Montenegro, Ms. Katherine Chmay, Ms. Nicole Souder, Ms. Marci Carter, Ms. Jamie Cooper, Ms. Gemma Wilson, Mr. Dustin Chickis, Mr. Charles Donnelly, Mr. James Bumstead, and Mr. Nathan Buettner. I would also like to thank Mr. Charles C. Hager for his assistance and friendship.

I would also like to acknowledge the assistance provided by Angel Mateos of the University of California – Berkeley, Andrew Bennett and Benjamin Krom of the Michigan Department of Transportation, Thomas Burnham and Dave Van Deusen at the MnROAD Research Facility of the Minnesota Department of Transportation, Stacy Lloyd of the Pennsylvania Department of Transportation, Tyson Rupnow and Xingwei Chen of the Louisiana Department of Transportation, Randall Riley formerly of the American Concrete Pavement Association, Bruce Bird, Amy Kohnert, and Ryan Peterson of the Illinois Department of Transportation, John Donahue of the Missouri Department of Transportation, and Todd LaTorrella of the Missouri/Kansas Chapter American Concrete Pavement Association.

To my parents, I would have never been able to accomplish my goals without you. You have been pushing me along my journey from start to finish, and even more so in the end when I was struggling to see the light. To my sisters, thanks for always being there when times were tough and for staying close although physically, we are not. Finally, I would like to thank my entire family for their continuous love and support. Not only having a large Italian/Irish family but an extremely close family has helped form me into the man I am today. I am forever grateful.

1.0 Introduction

A bonded concrete overlay of asphalt pavement (BCOA), also known as thin or ultra-thin whitetopping, consist of a new Portland cement concrete (PCC) overlay placed on an existing distressed asphalt or composite pavement. This rehabilitation technique is intended as a cost-effective solution for marginally distressed asphalt pavements. The existing asphalt is often milled prior to overlay construction to remove any surface distress and to increase the surface area, which may promote greater bond between the PCC and asphalt. These structures typically have smaller panel sizes than traditional jointed plain concrete pavements (JPCP) to reduce curling and warping stresses and bending stresses produced by applied loads (Mack et al. 1993; Mack et al. 1998; Wu et al. 1998). In BCOA, the existing asphalt layer assists in carrying a portion of the load because these overlays are typically thin in comparison to JPCP. There are three main categories for the different thicknesses of the PCC overlay. The three categories can be seen in Table 1-1.

Table 1-1 Whitetopping categories (Barman et al. 2011).

Category	PCC thickness (in)
Conventional Whitetopping	≥ 6
Thin Whitetopping (TWT)	4 – 6
Ultra-Thin Whitetopping (UTW)	2 – 4

1.1 Background and Problem Statement

Faulting, the difference in elevation between adjacent slabs across a transverse joint, is a distress in jointed concrete pavements that is a primary design consideration. It affects both the structural integrity and roughness of the road. Faulting develops as a result of pumping. Pumping is the ejection of fines under the approach slab and out of the joints from beneath the leave slab. This results in a void under the leave slab and an uplift of the approach slab from the ejected fines. Pumping occurs as a result of the repeated application of heavy vehicle loads, the presence of moisture beneath the slab, an erodible underlying layer, and large differential deflections between the loaded and unloaded slabs on adjacent sides of the transverse joint.

In earlier versions of the AASHTO Pavement Design Guide (AASHTO 1993), faulting was addressed indirectly. Faulting and cracking were coupled and accounted for by maintaining a serviceability above a defined threshold. In the 1990's, an effort was made to decouple these two distresses and to predict faulting independently as a function of the pavement design, traffic, climatic conditions (Simpson et al. 1994) and a mechanistic response of the pavement structure, such as deflection (Yu et al. 1997, 1998, Owusu-Antwi et al. 1997, Titus-Glover et al. 1999, Hoerner et al. 1999, and Byrum et al. 1997). The first model to account for a mechanistic response of the pavement in the development of faulting was provided by the Portland Cement Association (PCA) in 1977 (Packard 1977). Unlike the PCA model, the faulting models developed in the later part of the 1990's also began to account for the erodibility of the base material. The faulting models have continued to evolve (Bakhsh and Zollinger 2014 and Jung and Zollinger 2012) with Khazanovich (et al. 2004) and culminated into the faulting model currently adopted into the AASHTOWare Pavement ME Design Software.

The faulting model currently adopted in the Pavement ME design procedure accounts for the pavement response, climatic conditions, traffic, and erodibility of the base (ARA 2004). The same faulting model is applied to all jointed concrete pavements regardless of the pavement structure (conventional concrete pavement, unbonded concrete overlay, bonded concrete overlay, etc.). This implies the pumping mechanism is the same for all pavement structures. It also assumes that the rate of the development of faulting and the maximum faulting that will occur is the same regardless of the pavement structure.

The development of faulting in BCOAs is currently not considered in the design process. It is possible to use the Pavement ME to assess faulting for a BCOA by using a newly constructed JPCP on an asphalt stabilized base (ASB) using conventional joint spacings. However, there are a number of limitations when utilizing this procedure to assess faulting for BCOAs. First, the structural response model employs equivalency concepts and combines the base and overlay into one effective slab. This can be seen in Figure 1-1a. This proposes an issue when estimating the response of BCOAs because joints in BCOAs can activate through the PCC overlay or can activate through both the PCC and the asphalt (Figure 1-1b and Figure 1-1c). The model may provide the correct structural response when a joint activates through the PCC and asphalt, however it cannot when a joint only activates through the PCC layer.

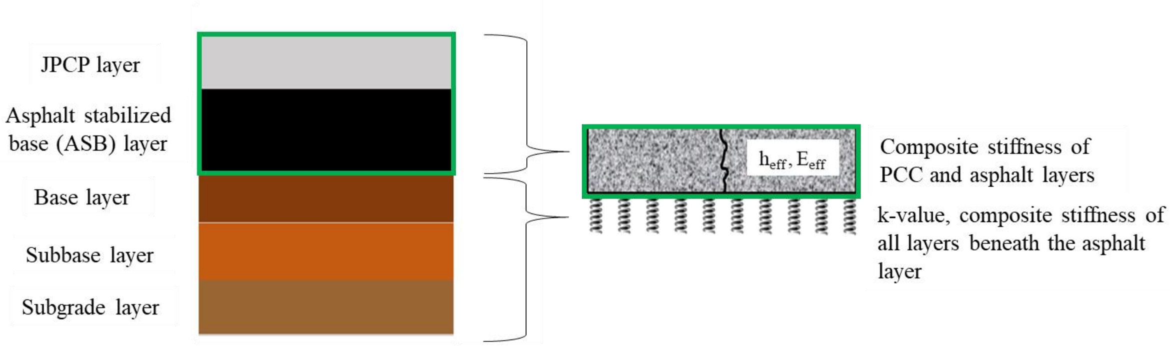

a) Pavement ME equivalency concept

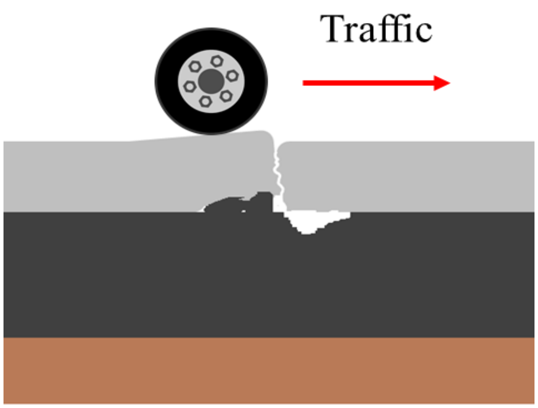

b) Joint activation through PCC only

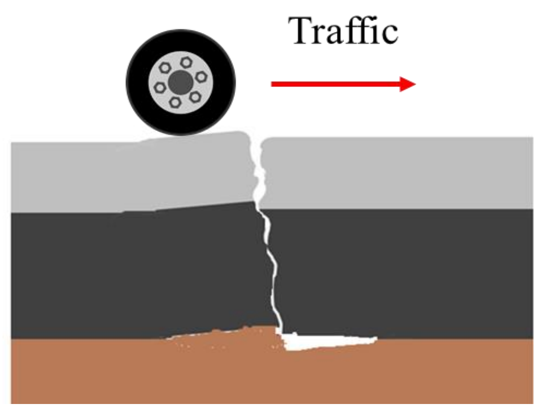

c) Joint activation through PCC and asphalt

Figure 1-1 Limitations of the Pavement ME structural model (ARA 2004).

In addition, the different depths of joint activation in BCOAs can lead to different layers undergoing the pumping mechanism. The classification of the erodibility of the base layer in the current framework within the Pavement ME faulting prediction model needs further enhancement in order to accurately predict faulting in BCOAs. Currently the erodibility index is used to establish the erosion potential of the base material using a numeric value between 1 (extremely erosion resistant) and 5 (extremely erodible). There are two limitations of this approach when analyzing BCOAs. First, as previously mentioned, two different depths of joint activation can occur, which result in a different layer of material to undergo pumping. This is important to consider because it is possible for joints within a given section to have joints activate only through the PCC layer, activate through the PCC and asphalt layers, and lead to joints that do not activate at all. It is important to differentiate between the different types of materials undergoing pumping because each type of material can result in different rates in the development of faulting. Second, if the joint only activates through the PCC layer, the Pavement ME classifies the erodibility of the asphalt layer as 1 (extremely erosion resistant). However, this does not take into consideration different asphalt mixtures can develop faulting. Therefore, it is important to be able to differentiate between the performance of different asphalt mixtures.

Another limitation of the current procedure is that the length of the joint spacing is limited to longer slabs more suitable for a conventional JPCP. A shorter joint spacing that includes slab widths that are less than a full lane width are commonly used in BCOAs to reduce the stress in these thin overlays. The Pavement ME module only considers full lane width panels and a minimum transverse joint spacing of 10 ft. Therefore, any joint configuration with partial lane width panels and a joint spacing less than 10 ft cannot be considered.

1.2 Research Objective and Outline

The overall objective of this research is to develop a mechanistic-empirical (ME) predictive faulting model for BCOAs. The intention is also to implement this predictive model into the BCOA-ME, the current design procedure for BCOAs developed at the University of Pittsburgh. In order to reach the overall objective, the following steps need to be taken. First, an in-depth investigation of in-service concrete pavements and overlays is necessary to understand how faulting is occurring in these pavements and assess the suitability of applying one model for different concrete pavement structures (Chapters 2 and 3). Second, a structural response model needs to be developed to be able to accurately predict the response of in-service BCOAs (Chapter 4). The next step is to develop artificial neural networks (ANNs) to rapidly predict the structural response of BCOAs without the need of the structural response model (Chapter 4). The fourth step is to calibrate the faulting prediction model using measured faulting data from in-service BCOAs. This includes validating the prediction model and conducting a sensitivity analysis of the different parameters considered (Chapter 5). The final step is to be able to implement the field calibrated predictive faulting model into the BCOA-ME design procedure. In order for implementation, the model needs to account for a number of variables relating to climatic features. Regression models need to be developed so the design process can be decoupled form the software used for climatic modeling (Chapter 6). Figure 1-2 presents the outline of the process followed in the development of a series of models that can be used together for predicting the development of faulting in BCOAs.

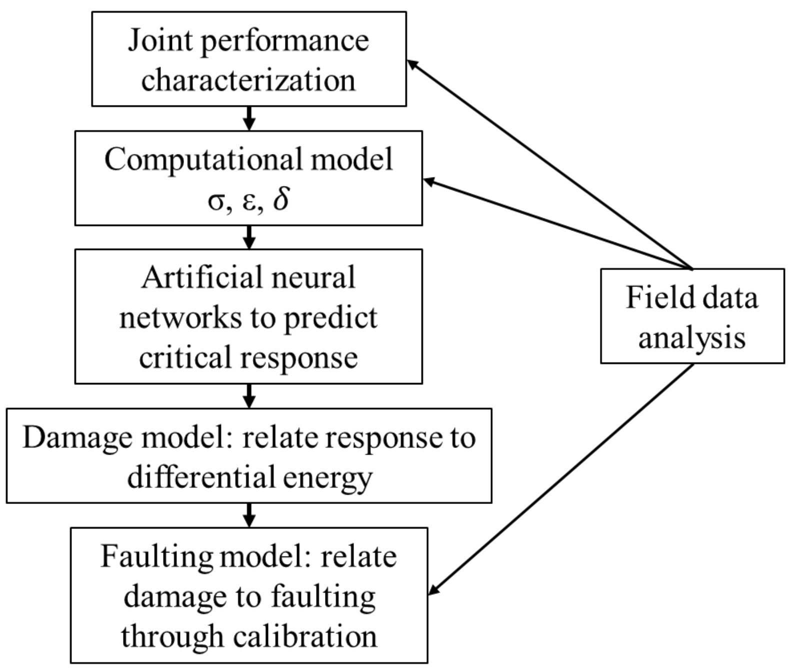

Figure 1-2 BCOA faulting model flow diagram.

2.0 Depth of Joint Activation at Transverse Joints in Bonded Concrete Overlays of Asphalt Pavements

2.1 Introduction

Before faulting can be incorporated into the design process for BCOAs, a better understanding of where it initiates and how it develops must be achieved. Pumping in BCOA can develop at either the bottom of the overlay slab within the asphalt layer or below the asphalt in the granular layer. If the transverse joint in the overlay does not activate through the asphalt layer then pumping of the asphalt material occurs at the top of the asphalt layer, as shown in Figure 2-1a. If the transverse joint activates through the asphalt layer, then the PCC and asphalt act as a monolithic structure and faulting develops due to pumping of the granular material below the asphalt, as shown in Figure 2-1b. Voids beneath the slab can also develop due to break down of the asphalt layer, as shown in Figure 2-1c (Rasmussen et al. 2002). However, while these voids will likely result in the development of longitudinal cracks in the wheelpath, or diagonal cracks originating at the intersection of the wheelpath and transverse joint at the bottom of the slab, it is unclear on the contribution to faulting. It is possible faulting can initiate from this mechanism due to a breakdown of the asphalt matrix. This can create a larger void or more space for entrapped water and can result in a build-up of water pressure when a wheel load is introduced. Further examination of this mechanism is presented in Chapter 3.

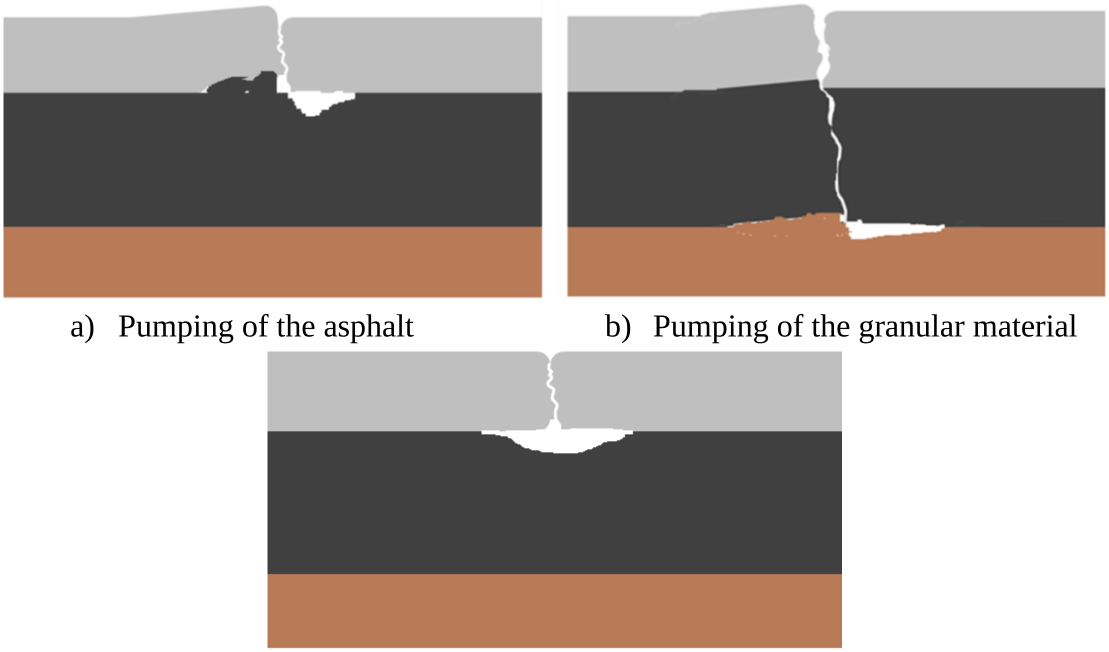

a) Pumping of the asphalt b) Pumping of the granular material

c) Deterioration of the asphalt

Figure 2-1 Joint activation depth in BCOAs (DeSantis et al. 2016).

2.2 Scope of Work

There are three main objectives in this section. The first objective is to use the extensive falling weight deflectometer (FWD) data and distress data available at the Minnesota Road Research Facility (MnROAD) to identify which joints in BCOAs at the test facility activate and activate through the asphalt. The testing facility has a wide range of BCOAs with different structural designs and joint spacings. The deflection load transfer efficiency (LTE) of a joint can be used to identify if a crack has fully activated through the asphalt layer (Roesler et al. 2008). The measured LTE at a fully activated joint will be lower than at a joint that has not activated through the asphalt. Differential deflections as well as the maximum deflections also provide useful information in interpreting the depth of crack activation. Cores at the joint are taken to validate the methods of classifying joint activation using the FWD data.

The second objective is to determine if the depth of joint activation can be established based on critical design features without the availability of extensive FWD data. Once the depth of activation is established using FWD data under the first objective, the combination of the critical design features contributing to joint activation through the asphalt layer can be identified.

The third objective is to investigate the influence of the different depths of joint activation in respect to the development of faulting over time in BCOA. Specifically, it is important to determine 1. if and when faulting occurs, 2. if the shape of the faulting development curve is similar regardless if pumping is occurring at the PCC/asphalt interface or at the top of the granular layer directly below the asphalt, and 3. the influence of design features on the development of faulting.

2.3 Depth of Joint Activation

FWD data was examined for all the BCOAs constructed at MnROAD to identify the depth of joint activation. The 21 sections examined as part of this study are part of the mainline test section that is loaded with live interstate traffic diverted from I-94. The design features for each test section are provided in Table 2-1. All of the test sections were placed on an existing hot mix asphalt pavement that was constructed in 1993 on a silty-clay subgrade. The existing pavement was milled to the thicknesses shown in Table 2-1 prior to construction of the overlay. This removed any surface distresses and increased the surface area for bonding between the overlay and asphalt layer. None of these sections have edge drains. The mainline is subjected to approximately 1 million 18-kip equivalent single axle loads (ESALs) per year. Cells 60 through 63 were subjected to 6.74 million ESALs over 6.6 years (Li and Vandenbossche 2013).

Table 2-1 BCOA cells at MnROAD (DeSantis et al. 2016).

Cell	Panel size, LxW (ft)	Dowels (in)	Transverse jt. sealant	PCC thickness (in)	Asphalt thickness (in)	Year constructed	Year removed	Shoulder	Fibers	Cell length (ft)
60	5x6	No	Yes	5	7	2004	2013	Asphalt	None	225
61	5x6	No	No	5	7	2004	2013	Asphalt	None	225
62	5x6	No	Yes	4	8	2004	2013	Asphalt	None	225
63 [1]	5x6	No	No	4	8	2004	2013	Asphalt	None	225
92	10x12	1	Yes	6	7	1997	2010	Asphalt	Polypropylene	180
93	4x4	No	Yes	4	9	1997	2004	Asphalt	Polypropylene	300
94	4x4	No	Yes	3	10	1997	2004	Asphalt	Polypropylene	300
95	5x6	No	Yes	3	10	1997	2004	Asphalt	Polyolefin	300
96 [1]	5x6	No	Yes	6	7	1997	-	Asphalt	Polypropylene	180
97	10x12	No	Yes	6	7	1997	2010	Asphalt	Polypropylene	160
114	6x6	1	Yes	6	5	2008	-	Asphalt	None	99
214	6x6	No	Yes	6	5	2008	-	Asphalt	None	24
314	6x6	1	Yes	6	6	2008	-	Asphalt	None	138
414	6x6	No	No	6	6	2008	-	Asphalt	None	30
514	6x6	1	No	6	7	2008	-	Asphalt	None	36
614	12x6	Flat Plate	No	6	7	2008	-	Asphalt	None	108
714	6x6	1	No	6	7.5	2008	-	Asphalt	None	18
814	6x6	No	No	6	8	2008	-	Asphalt	None	24
914	6x6	1	No	6	8	2008	-	Asphalt	None	78
160	6x6	No	Yes	5	6	2013	-	Asphalt	Fiber-mesh 650	444
162	6x6	No	Yes	4	7	2013	-	Asphalt	Fiber-mesh 651	462

[1] 0.25 in of diamond grinding was performed on September 8, 2011 (http://dotapp7.dot.state.mn.us/research/dataproduct/Data%20Release/)

The FWD data collected in the outer wheelpath of the driving lane was used to determine the LTE, differential deflection between the loaded and unloaded side of the joint, and the maximum measured deflection at the center of the load plate. First, the LTE was used to determine if the transverse joints had fully activated through the PCC and asphalt layers, as shown in Figure 2-1b. In BCOA, when the asphalt is continuous and uncracked it will contribute significantly more to LTE than if a crack is present. The LTE was measured on both the approach and leave side of the joint and was defined using the following equation:

$$LTE = \frac{\Delta_{UL}}{\Delta_L} * 100 \tag{2-1}$$

Where:

Δ_{UL} is the deflection of the unloaded slab (mils), and

Δ_L is the deflection of the loaded slab (mils).

The minimum LTE between the approach and leave LTE was used. FWD testing was conducted at four joints in each of Cells 60, 61, 62, and 63 throughout their service lives and half of the total joints were tested before being taken out of service. Testing was conducted at the four joints per cell at a minimum of twice a year. Cells 93, 94, and 95 were tested at two joints, each at a minimum of twice a year. Cells 92, 96 and 97 were tested at two joints, each over the first four years. After this, testing was increased to approximately 10 joints per cell. One to three joints per cell were tested in Cells 114 through 914 (these cells were primarily used for verification of the findings from the test sections tested more frequently). If the LTE of a joint was very low (below 50%) or much lower (more than 20% lower) than the LTE of a typical joint in the cell, then the joint was considered to activate through the asphalt.

Two joints in Cell 96 (6-in thick) that exhibited transverse joint faulting were examined to validate the method for determining the depth of activation at the joint based on LTE. It is believed based on the LTE data, that faulting at these joints was occurring due to pumping at different depths within the BCOA. The LTE at Joint B (Joint 2241) is also about 20 percent less than at Joint A (Joint 2236), which is a good indication that this joint has cracked through the asphalt. Faulting and LTE data can be seen in Figure 2-2. Faulting measurements six years after construction indicate Joints A and B had similar magnitudes of faulting, as shown in Figure 2-2. This cell was diamond ground to restore ride after 14 years in-service. When a pavement is diamond ground, only the surface distress is removed. Therefore, it is expected that faulting trends would continue after grinding. However, comparing these two joints four years after grinding, the fault depth at Joint B is 0.08 in greater than Joint A. This could be attributed to the fact that the pumping mechanism continues to transfer the base material and the fault depth continued to increase at Joint B. However, it is difficult to establish the faulting that developed at these joints due to the lack of measurements between 2003 and 2014. Cores were taken recently at these joints to validate the findings. As predicted, Joint B exhibited a crack through the asphalt, similar to the joint shown in Figure 2-1b, whereas Joint A did not. Joint A is more representative of the joint shown in Figure 2-1a. These cores can be seen in Figure 2-3. Note the condition of the asphalt directly below the concrete.

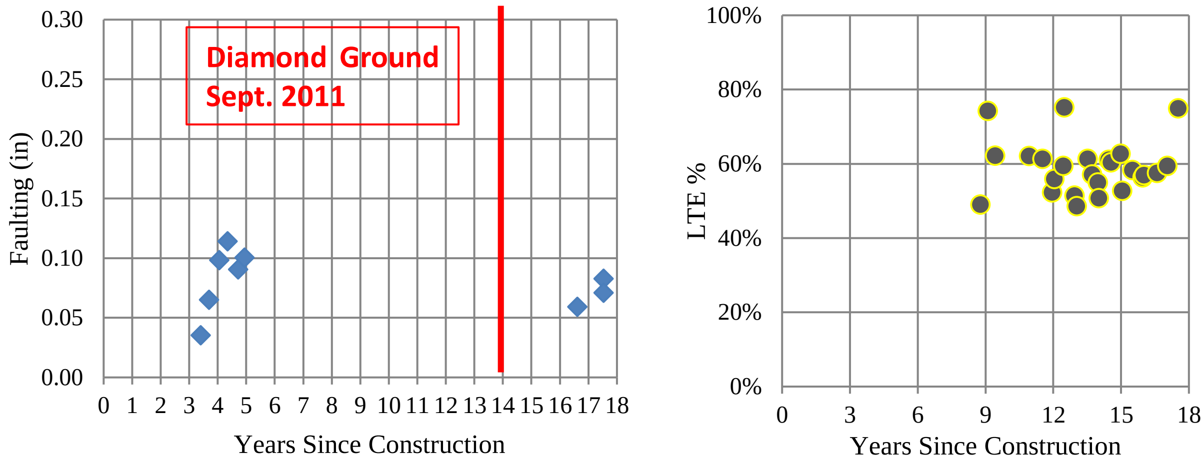

a) Joint A: Crack through PCC only

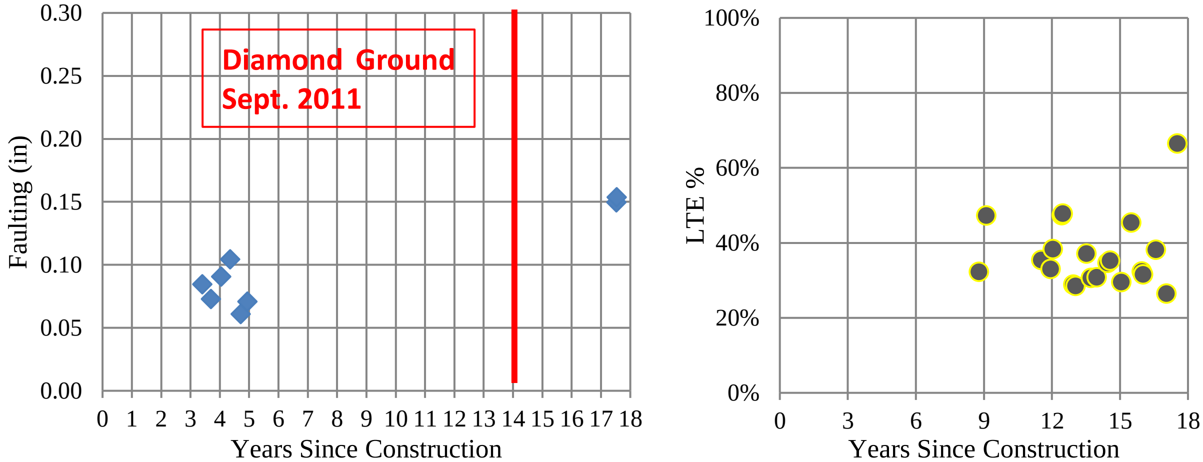

b) Joint B: Crack through PCC and asphalt

Figure 2-2 Faulting and LTE for joints in Cell 96 (DeSantis et al. 2016).

a) Joint A

b) Joint B

Figure 2-3 Cell 96 field cores (DeSantis et al. 2016).

Table 2-2 presents whether full-depth activation through the asphalt is expected out of the total number of joints tested for each MnROAD cell for different criteria. Based on the LTE from this analysis, it appears that joints activated through the asphalt for all of the joints in the large undoweled panels of Cell 97. Joints activated through the asphalt for at least some of the joints in Cells 60, 61, and 96, but did not appear to activate through the asphalt for Cells 62, 63, 93, 94, and 95. Cell 92 was inconclusive based upon LTE because the joints contained dowel bars and maintained a high LTE of 70 percent at all of the joints.

Table 2-2 Full-depth activation (DeSantis et al. 2016).

	Full-depth activation based on:		
Cell	**LTE**	**Differential deflections**	**Maximum deflections**
60	1/4	1/4	1/4
61	1/4	1/4	2/4
62	0/4	0/4	0/4
63	0/4	0/4	0/4
92	Inconclusive		
93	0/2	0/2	0/2
94	0/2	0/2	0/2
95	0/2	0/2	0/2
96	4/9	3/9	3/9
97	10/10	10/10	10/10

Another parameter examined was the deflections in the outer wheelpath under the 9-kip FWD load. Large differential deflections between the adjacent slabs are required for pumping to occur in PCC pavements. The same deflections used to calculate the LTE were used to determine the differential deflection across the joint. The following equation was used:

$$Differential\ Deflection = \Delta_L - \Delta_{UL} \qquad \textbf{(2-2)}$$

Where:

Δ_L is the maximum deflection of the loaded slab (mils), and

Δ_{UL} is the maximum deflection of the unloaded slab (mils).

The maximum differential deflection between testing on the approach and leave slab was used in the analysis. Figure 2-4a shows the differential deflections for Joint A (discussed previously), and Figure 2-4b shows the differential deflections for Joint B. It can be seen that the differential deflections and the maximum deflections are both higher and more scattered when the joint activates through the asphalt.

For Cells 93, 94, 95 and 97, the initial differential deflections over the first few years in-service remained between 0 and 0.001 in for a 9-kip load. The differential deflections were between 0 and 0.002 in for Cells 60 through 63 and 96 over the first few years in-service. If the joint exhibited an increase in differential deflections that was greater than 0.006 in and exhibited some variability, similar to Figure 2-4b, it indicates the joint most likely activated through the asphalt. This variability, or scatter, is similar to what is seen in traditional JPCP and may be due to the discontinuity in the asphalt allowing the adjacent slabs to curl freely with changing temperature gradients. When minimal or no differential deflections are present, then it is likely that the joint did not activate through the asphalt. The cells in which at least some of the joints activated can be seen in Table 2-2. The results of the determination of the joints with full-depth activation based upon differential deflections is identical to what was found by evaluating LTE.

The maximum deflection measured at the center of the load plate was also examined as a potential indicator of the depth at which the joint activated, as can be seen in Figure 2-4. When this deflection was greater than 0.012 in for a 9-kip load, it appears the joints cracked through the asphalt. It should be remembered that this criterion, as well as the criteria above, was established based on the subgrades and materials used at MnROAD and might not be representative of other BCOA. From Table 2-2, the results of the determination of full-depth activation based upon maximum deflection are identical to the determination from LTE.

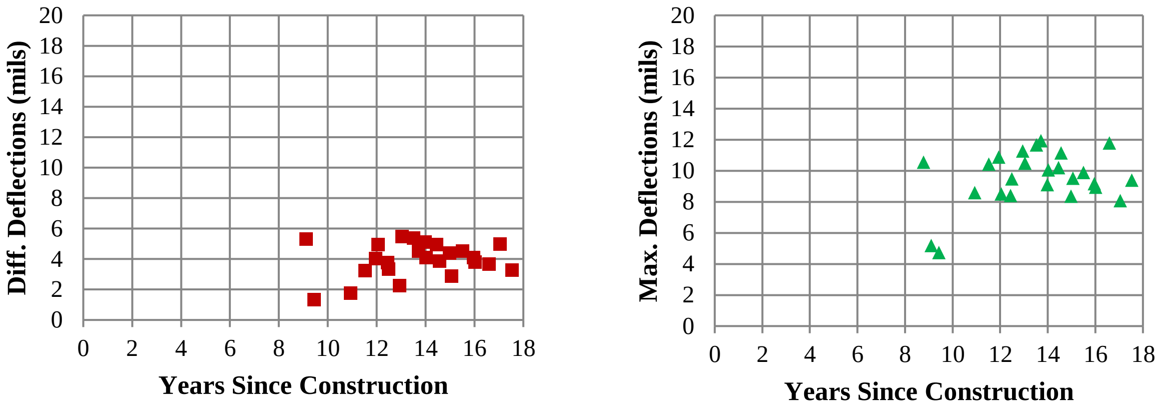

a) Joint A: Joint activates through PCC only

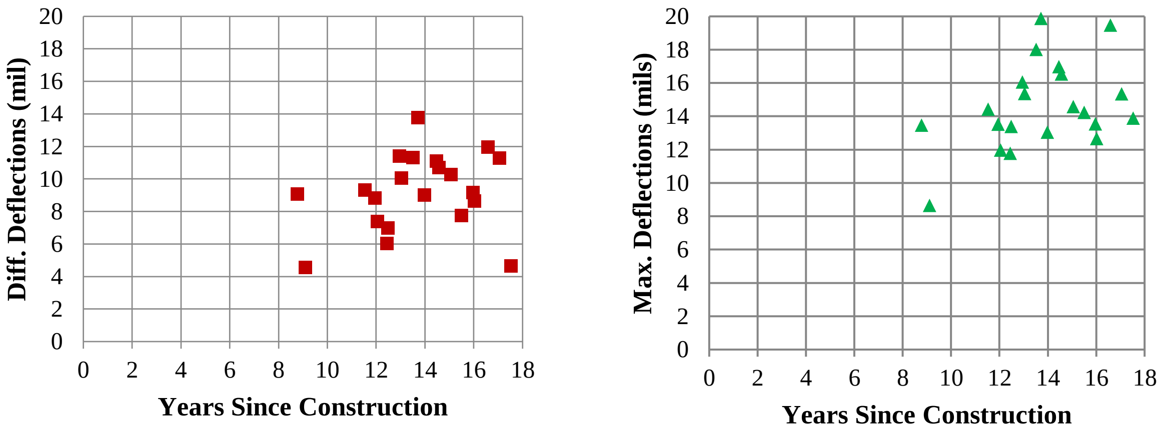

b) Joint B: Joint activates through PCC and asphalt

Figure 2-4 Deflections under 9-kip load (DeSantis et al. 2016).

2.4 Factors Affecting Depth of Joint Activation

Joint activation in BCOA is a complicated process involving the coupling of the structural properties, material properties, and environmental conditions experienced by the BCOA. Critical stresses in the asphalt layer at the joint are likely a combination of Mode I (direct tension) and Mode II (shear) failures. When the overlay experiences a uniform volume reduction due to a temperature decrease or drying shrinkage, the continuous asphalt layer restrains the shrinkage. If the viscoelastic and fracture properties of the asphalt do not allow for the layer to absorb the strain without fracturing, the asphalt will fail in a Mode I fracture activating the joint through the asphalt. This stress is critical in the winter when the stiffness of the asphalt is highest, the maximum allowable strain in the asphalt is lowest, and the contraction of the concrete overlay is the highest. The asphalt also exhibits shear stress along the joint due to wheel loads. These stresses would be critical in the summer months when the asphalt stiffness is at a minimum. This critical stress, however, occurs when LTE due to aggregate interlock would be highest. Therefore, the joint activation mechanism is most likely dominated by Mode I fracture (Knott 1973).

The mechanism of joint activation is similar in many ways to the activation of reflective thermal cracks into the PCC overlay from the existing asphalt layer. This cracking was previously studied at MnROAD using the same BCOA sections previously described. It was determined that the most influential variable in predicting if reflective cracking would activate up from the asphalt into the overlay was the flexural stiffness ratio (FSR) between the PCC and asphalt layers. The flexural stiffness of each layer can be calculated using Equation (2-3). It was shown that thermal cracks in the asphalt would reflect up into the overlay if the FSR was less than 1 (Vandenbossche and Fagerness 2002).

$$Flexural\ Stiffness = D_i = \frac{E_i h_i^3}{12(1-\mu_i^2\ )} \tag{2-3}$$

$$FSR = \frac{D_{PCC}}{D_{Asphalt}} \tag{2-4}$$

Where:

D is the flexural stiffness of layer i (lb-in),

E is the elastic modulus of layer i (psi), h is the thickness of layer i (in), and

μ is the Poisson's ratio of layer i.

This was found to also be a critical value for determining whether joints activate through both the overlay and the asphalt layer.

Based on the joint activation mechanisms previously described, panel size is also likely to influence the depth of joint activation. Smaller panels result in less accumulated strain occurring at each joint, reducing the total stress in the asphalt at the joints. Material properties such as the difference in the coefficient of thermal expansion (CTE) between that of the PCC and asphalt, ultimate drying shrinkage of the PCC, creep compliance of the asphalt, and fracture properties of the PCC and asphalt also can influence whether cracks activate through the asphalt.

The effect of panel size on the depth of joint activation is coupled with the environmental conditions. Environmental strains in the overlay can develop relatively rapidly, such as through a daily temperature cycle. The magnitude of the strain in the asphalt is then a function of the magnitude of the daily temperature swings and the panel size. Environmental strains can also develop more slowly, due to seasonal temperature changes or long-term drying shrinkage. While these can be larger in magnitude, as compared to the daily cycles in temperature, the slower development time provides a greater opportunity for the strains in the asphalt to dissipate through creep. Of course, the magnitude of these strains are a function of both the yearly climatic conditions as well as the panel size.

Based on the discussion presented above, the design features of the cells at MnROAD were evaluated to determine if the depth of crack activation could be established based on several critical design features. To begin, the FSR for the cells at MnROAD representing conditions during the summer and winter months were calculated and are provided in Table 2-3. The stiffness of the asphalt was obtained based on a relationship established between the resilient modulus measured from cores taken from these cells and temperature (Vandenbossche and Fagerness 2002). The asphalt stiffness in the summer is based on an asphalt temperature of 100℉ and a temperature of -4℉ in the winter. These values were established based on temperatures measured in the asphalt layer using thermocouples. The material properties of the PCC for Cells 60 through 63 were provided by Burnham (Burnham 2006). The material properties of the PCC for Cells 93 through 97 and further information about these cells has been summarized as well elsewhere (Vandenbossche and Rettner 1999; Vandenbossche and Fagerness 2002; Burnham 2005). Using this information and the analysis performed under objective 1, the BCOAs that exhibited an average FSR less than or equal to 0.4 in the winter months were determined to be unlikely to develop a crack through the asphalt layer. A BCOA with a ratio greater than or equal to 0.9 in the winter months are likely to develop a crack through the asphalt layer. No conclusions can be made at this time for structures with ratios in between this range. Unfortunately, at MnROAD the panel size is confounded with FSR, so it is difficult to determine whether panel size influenced the activation of joints through the asphalt. Additionally, all of the materials used in the BCOA cells at MnROAD have similar material properties and are exposed to the same environmental conditions making it difficult to quantify the effect of these factors on joint activation.

It is interesting to note that in Cells 62, 63, 93, 94, and 95 the joints did not activate through the asphalt but thermal cracks did reflect up into the PCC overlay (Vandenbossche and Barman 2010). It can also be noted that Cells 60, 92, 96, and 97 showed that the joints activated through the asphalt but these cells did not exhibit reflective thermal cracking (Vandenbossche and Barman 2010). Cell 61, which is the same design as Cell 60 but with unsealed joints, exhibited joint activation through the asphalt and also was identified as having thermal cracks reflect up into the PCC overlay.

Table 2-3 Pavement design features influencing full-depth joint activation (DeSantis et al. 2016).

Cell	Panel size, LxW (ft)	PCC elastic modulus (ksi)	Asphalt elastic modulus		PCC Poisson's ratio	Asphalt Poisson's ratio	FSR (summer)	FSR (winter)	Full-depth jt. activation (FSR/FWD)
			Summer (ksi)	Winter (ksi)					
60	5x6	4600	170	1600	0.18	0.35	9.0	1.0	(Yes/Some)
61	5x6	4400	170	1600	0.18[1]	0.35	8.7	0.9	(Yes/Some)
62	5x6	4900	170	1600	0.18[1]	0.35	3.3	0.4	(No/None)
63	5x6	5000	170	1600	0.18[1]	0.35	3.4	0.4	(No/None)
92	10x12	4800	170	1600	0.2	0.35	16.4	1.8	(Yes/Unknown)
93	4x4	4800	170	1600	0.19	0.35	2.3	0.2	(No/None)
94	4x4	4800	170	1600	0.18	0.35	0.7	0.1	(No/None)
95	5x6	4400	170	1600	0.19	0.35	0.6	0.1	(No/None)
96	5x6	4800	170	1600	0.2	0.35	16.4	1.8	(Yes/Some)
97	10x12	4800	170	1600	0.2	0.35	16.4	1.8	(Yes/All)

[1]Poisson's ratio reported for these cells are unreasonably low, typical values were assumed.

2.5 Trends in Development of Faulting

2.5.1 Evidence of pumping

Pumping and faulting occurs whether or not the joint activates all the way through the asphalt layer. Staining along the shoulder, typically seen as an indicator of pumping, occurs at MnROAD in locations where the joint activates through the asphalt, as well as in joints that just activate through the concrete layer. Figure 2-5 shows the shoulders at a joint in Cell 61, which likely activated through the asphalt, and a joint in Cell 63, which likely did not activate through the asphalt. In both cases the shoulders show evidence of pumping. It is also important to note that the shoulders at MnROAD are not full-depth. The observed signs of pumping may be due to lane shoulder pumping.

a) Cell 61: FSR_{Winter}=0.9, PCC = 5 in, Asphalt = 7 in

b) Cell 63: FSR_{Winter}=0.4, PCC = 4 in, Asphalt = 8 in

Figure 2-5 Evidence of pumping at MnROAD (DeSantis et al. 2016).

2.5.2 Influence of joint activation depth on faulting

The rate of faulting and the shape of the faulting development curve vary based on several factors, including whether the joint activates through the asphalt, panel size, and the presence of joint sealant. Transverse joint faulting measurements were taken, on average, twice per year at approximately half of the joints in Cells 60 through 63 and at every joint in Cells 92 through 97, 114 through 914, 160, and 162. Although measurements were taken in both wheelpaths and in the driving and passing lanes, this study focuses on the faulting measurements taken in the outside wheelpath of the driving lane.

When the FSR_{winter} of the section was low (below 0.4), very little faulting occurred in the first few years, followed by a rapid increase in the magnitude of the faulting. An example of this faulting development can be seen in Figure 2-6a. When a BCOA has a low FSR, the pumping mechanism occurs at the interface between the PCC and asphalt layers. Early in the life of the pavement, the bond between the PCC and asphalt is intact. This prevents water from penetrating the PCC/asphalt interface, thereby minimizing the pumping mechanism during the first few years. When this bond deteriorates, water can penetrate this interface. Since the asphalt layer has very little permeability, this water can be effectively trapped and lead to the rapid development of stripping and faulting at the PCC/asphalt interface.

When the FSR_{winter} of the section is high (above 0.9), little faulting is observed in the first few years, followed by a gradual development of faulting, with the rate of the development of faulting decreasing with time. Examples of this faulting pattern can be seen in Figure 2-6b and Figure 2-6c. The initial low rate of faulting is likely caused by two factors. First, it may take time for the crack at the joint to activate completely through the asphalt layer. Therefore, asphalt continuity may be conserved for the first few years of the service life, limiting differential deflections. Also, the sections are primarily undoweled. Load transfer through aggregate interlock is higher early in the service life. Therefore, differential deflections will be lower in this period.

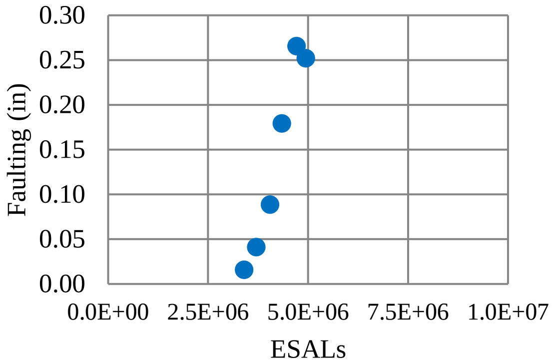

a) Cell 93, FSR= 0.2, 4 ft by 4 ft

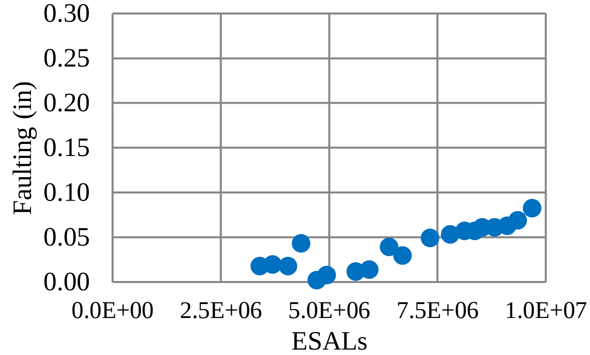

b) Cell 96, FSR = 1.8, 5 ft by 6 ft

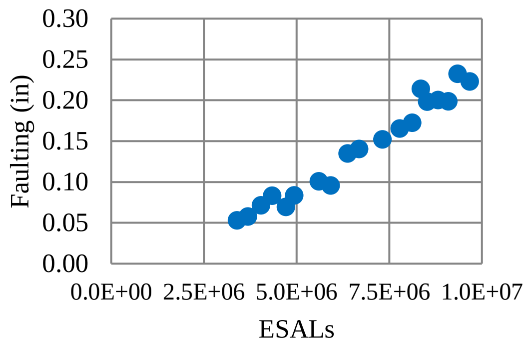

c) Cell 97, FSR = 1.8, 10 ft by 12 ft

Figure 2-6 Faulting development of MnROAD BCOA based on panel sizes (DeSantis et al. 2016).

2.5.3 Influence of design features on fault development

An important design feature influential to fault development in BCOA and all JPCP pavements is the usage of joint sealant. In particular for BCOAs, when the joint does not activate through the asphalt, sealing of the joints can have a significant influence on the development of faulting. Water is required for the pumping mechanism to occur. If the joint does not activate through the asphalt, the only way for water to enter the joint is through the pavement surface. The asphalt layer has very low permeability, so once water enters the joint, it can become trapped. As significant traffic levels accumulate, this trapped water can lead to debonding at the interface between the PCC overlays and asphalt layer and eventually causes a rapid development of faulting. This makes sealing the joints more critical for BCOA with a low FSR than for other BCOA pavement structures. The influence of joint sealant might not be as critical for thicker overlays or medium to high FSR. The structure of Cells 62 and 63 are identical, however, Cell 62 has sealed joints and Cell 63 does not. Cell 63 developed significantly more faulting than Cell 62. The faulting depths of the joints along the two cells can be seen in Figure 2-7. Also note, these measurements were taken right before these sections were taken out of service and Cell 63 was diamond ground two years prior to these measurements. The influence of joint sealant on joint LTE for Cells 62 and 63 can be seen in Figure 2-8. The LTE is presented for a representative number of joints within each section. These measurements were taken prior to these sections being taken out of service, as were the faulting measurements.

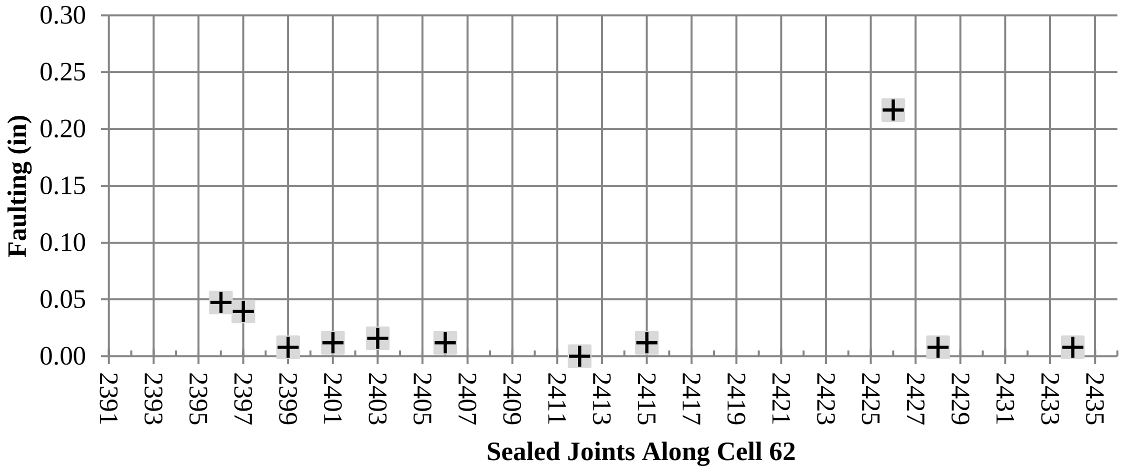

a) Cell 62, FSR = 0.4, 5 ft by 6 ft

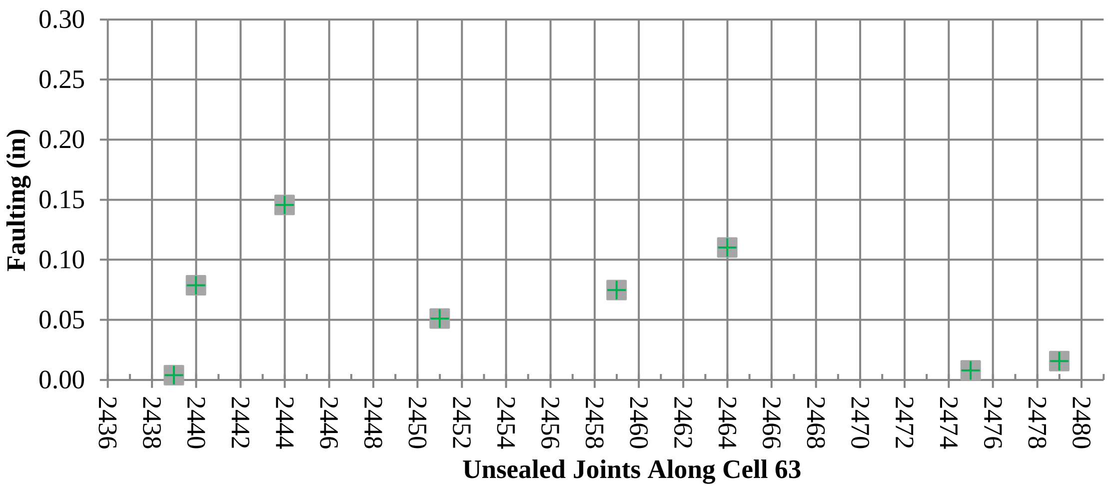

b) Cell 63, FSR = 0.4, 5 ft by 6 ft

Figure 2-7 Influence of joint sealant on faulting development in BCOAs (DeSantis et al. 2016).

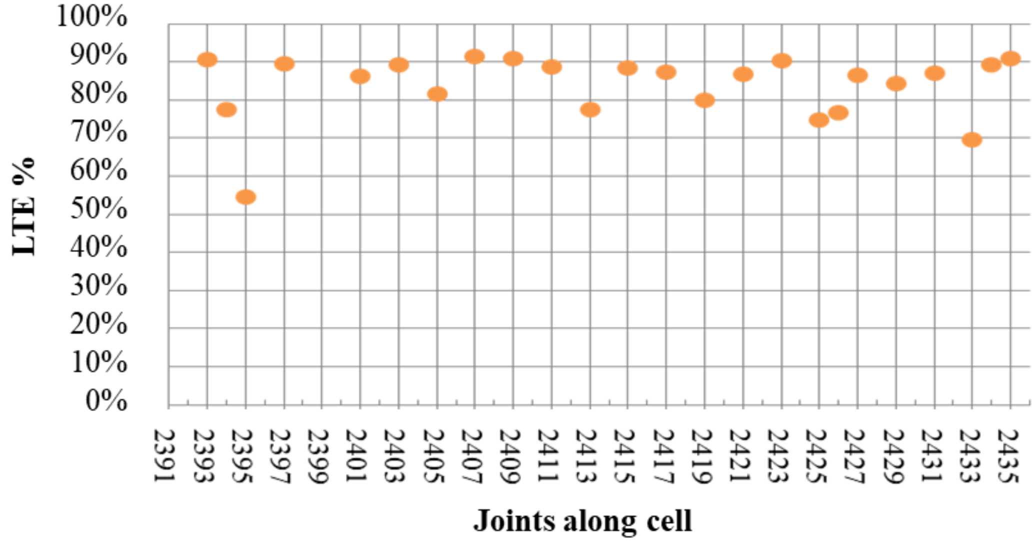

a) Cell 62, FSR = 0.4, 5 ft by 6 ft (sealed jts.)

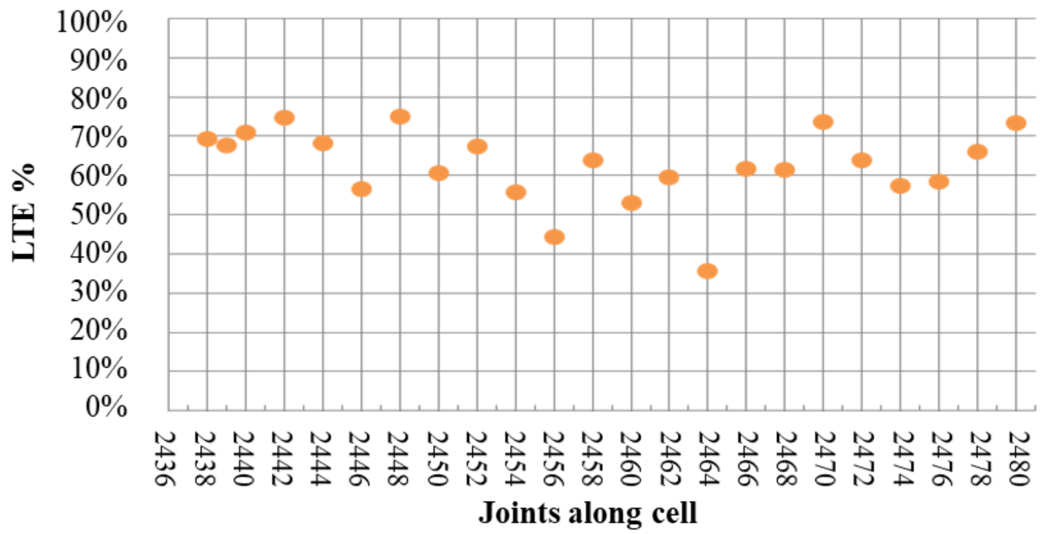

b) Cell 63, FSR = 0.4, 5 ft by 6 ft (unsealed jts.)

Figure 2-8 Influence of joint sealant on LTE in BCOAs.

Panel size may also influence fault development. Larger panel sizes, greater than or equal to 10 ft will have wider joints than smaller panel sizes, which will reduce the effectiveness of aggregate interlock load transfer. This likely accelerates the development of faulting in BCOA sections with larger panel sizes. Cell 96 and 97, which are shown in Figure 2-6b and Figure 2-6c, have similar designs. Only the panel size varies with Cell 96 has 5 ft by 6 ft panels and Cell 97 has 10 ft by 12 ft panels. The joints shown in the figures likely both activated through the asphalt layer, however Cell 97 experienced significantly more faulting. This provides evidence of the influence of a larger joint spacing on the magnitude and development of faulting in BCOAs.

The effect of the magnitude of faulting for these different panel sizes has a major influence on pavement roughness. Smaller panel sizes may result in lower magnitudes of faulting compared to large panels. However, due to the increased number of transverse joints, pavement roughness can be amplified on pavements with smaller panel sizes. With the same magnitude of faulting, a pavement with a longer joint spacing could have a lower International Roughness Index (IRI) than a pavement with a short joint spacing. As previously noted, the designs for Cells 96 and 97 are identical except the panel size. The joint spacing for Cell 96 is 5 ft while the spacing is 10 ft for Cell 97. The IRI for the cells were similar, as can be seen in Figure 2-9a. However, as can be seen in Figure 2-9b, the magnitude of faulting for the joints in Cell 97 is higher than the magnitude of the faulting in Cell 96. Therefore, the closer joint spacing produced a similar ride to the longer joint spacing despite having significantly lower faulting. It should be noted that Cell 96 has not exhibited any cracking and Cell 97 only exhibited mid-slab longitudinal cracking so the only distress contributing to the decrease in IRI for both is faulting. The interesting aspect is that if just the average faulting along the section was evaluated then the performance of Cell 96 and 97 would appear to be different. However, if the two sections were evaluated based upon IRI (purely a function of faulting in this scenario), the performance appears to be the same, as shown in Figure 2-10. The contribution of the faulting to the increase in IRI can only be found by evaluating the faulting of individual joints. The increase in roughness caused by the additional joints for the shorter slabs when compared to the same magnitude of faulting for longer slabs must be accounted for when establishing faulting failure criteria for BCOAs with short slabs.

a) IRI for MnROAD Cells 96 and 97

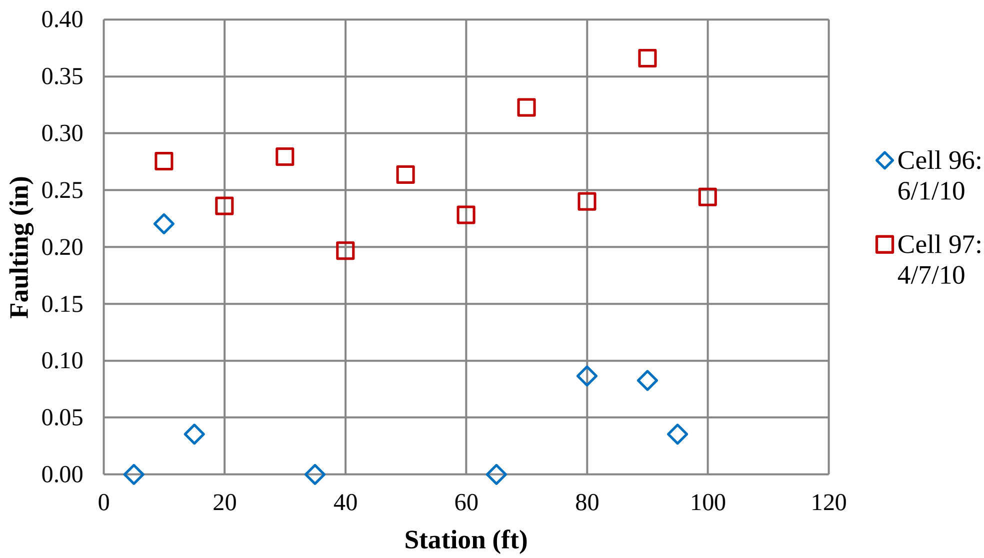

b) Faulting for MnROAD Cells 96 and 97

Figure 2-9 IRI and faulting for MnROAD Cells 96 and 97 (DeSantis et al. 2016).

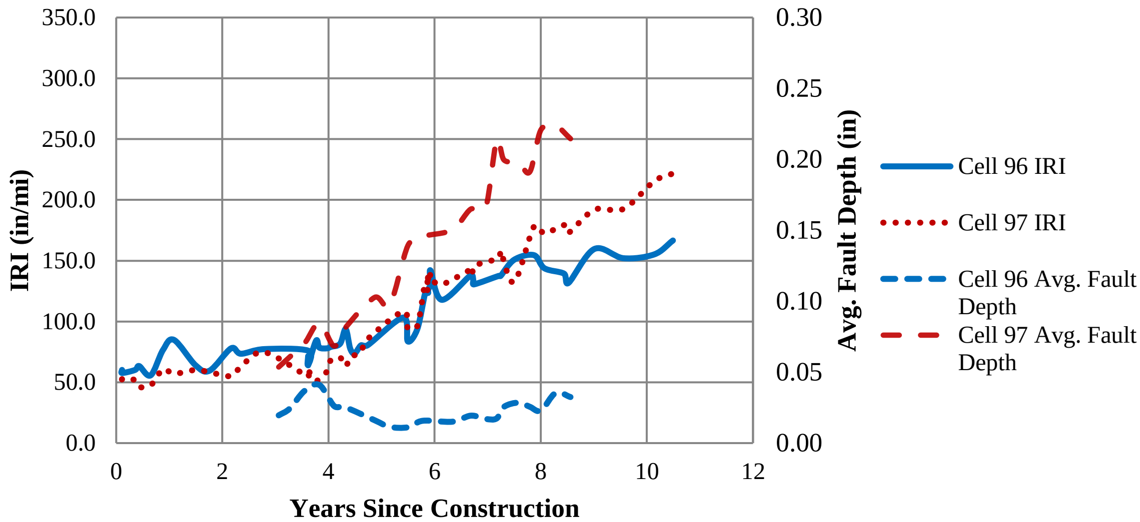

Figure 2-10 IRI and average faulting for MnROAD Cells 96 and 97 (DeSantis et al. 2016).

2.6 Joint Activation Depth Criteria for BCOA

From this analysis, it is important to derive a general criterion for the depth of joint activation. In order to develop such criterion, an extensive analysis was performed, in conjunction with the work presented in this chapter, examining faulting and FWD data. From this study, it has been shown that the mechanism for the development of faulting is different depending on if the activated joint activates full-depth. Previous work has shown that the depth the joint activates is a function of the following factors: FSR between the PCC and asphalt layers, panel size and, climate (DeSantis et. al 2016, Vandenbossche and Barman 2010). Unlike conventional JPCPs, the thickness of a BCOA is typically 3 to 6 in with the asphalt layer beneath the thinner overlays commonly being 1.5 to 2 times as thick as the PCC overlay. Therefore, the joint does not always activate through the asphalt. As previously mentioned, BCOAs also typically have a short joint spacing with 6 ft by 6 ft being a panel size that is currently commonly used. However, not all of the joints for these smaller panel sizes will necessarily activate and those that do activate might not all activate to the same depth. Structural fibers are sometimes used in thin concrete overlays and the type and quantity of the fiber used will also affect the spacing between joints that activate. Both the frequency of joint activation as well as the depth of activation will dictate the rate of the development of faulting. Performance data for the BCOA sections at MnROAD is used to further investigate the frequency of joint activation and the depth of activation as a function of the structural design features of BCOA.

At MnROAD, Cells 95 and 96 had 5- by 6-ft slabs. Cell 95 had a 3-in overlay with structural fibers on 10 in of asphalt and Cell 96 was a 6-in overlay on 7 in of asphalt. Cell 96 was originally not supposed to have structural fibers but it appears that some of the fibers from Cell 95 migrated into Cell 96 during the construction process. FWD deflection data and the rate of the development of faulting indicates that the activated joints only activated through the PCC in Cell 95, so faulting will develop from pumping of the asphalt layer (DeSantis et al. 2016). Figure 2-11 shows faulting for each of the joints within Cells 95, 96, and 97 at MnROAD. As can be seen in Figure 2-11a, faulting occurred in Cell 95 at only every sixth to eighth joint. For Cell 96, some of the joints only activated through the PCC layer, while others activated down through both the PCC and asphalt layers. This was established using FWD and faulting data, and also validated through coring (Figure 2-3). The larger flexural stiffness of the concrete layer with respect to the asphalt layer resulted in some of the joints propagating through the asphalt layer. While pumping occurred in the granular layer beneath the asphalt at some joints in Cell 96, pumping also occurred in the asphalt layer directly beneath the slab at some of the other joints. Figure 2-11b shows faulting developed more frequently along the section for this thicker overlay, as compared to Cell 95, with every third joint exhibiting faulting.

Cell 97 was the same design as Cell 96 but the joint spacing was increased to 10 ft and a nonstructural fiber was used. All joints activated through both the concrete and asphalt layers and all joints exhibited faulting, as can be seen in Figure 2-11c. This most likely can be attributed to the fact that the joint movement was larger since the joint spacing was twice as long (10 ft vs 5 ft). An assumption made in current design procedures for conventional pavements is that all joints within the pavement section fault at the same rate. While this might be a reasonable assumption for conventional pavements, it is evident from these results that this is not true for BCOA.

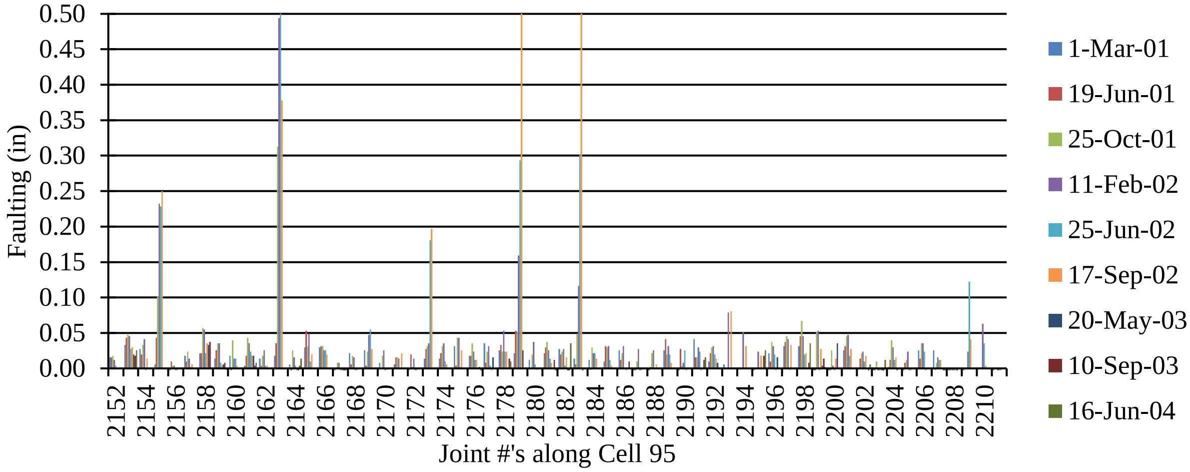

a) Cell 95, FSR = 0.1, 5 ft by 6 ft (Jt. activation = PCC only)

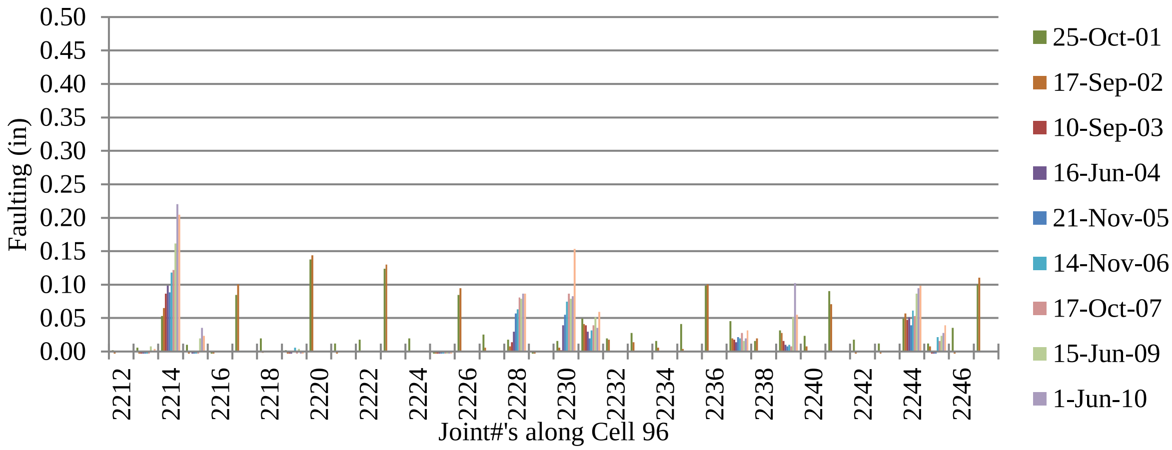

b) Cell 96, FSR = 1.8, 5 ft by 6 ft (Jt. activation depth varies)

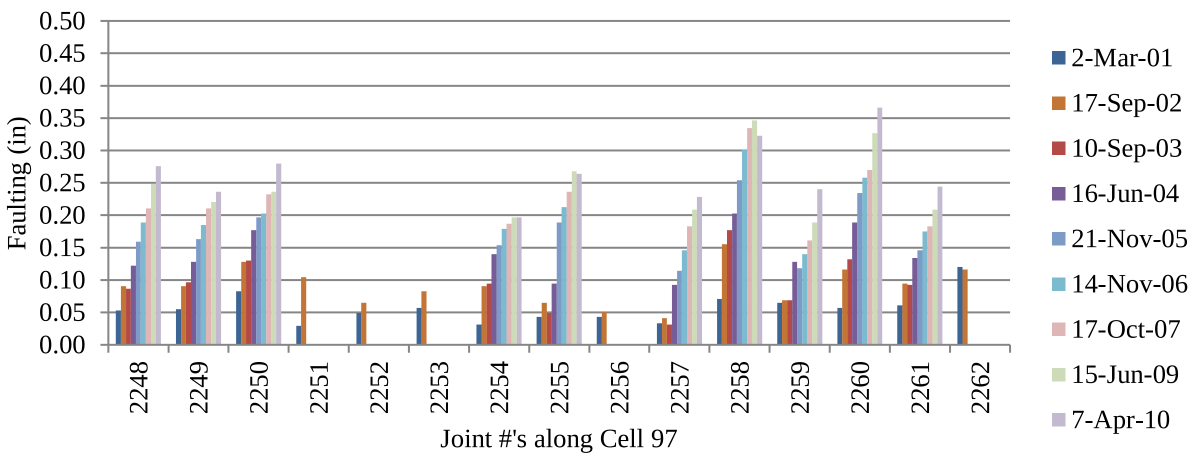

c) Cell 97, FSR = 1.8, 10 ft by 12 ft (Jt. activation = PCC and asphalt)

Figure 2-11 Joint faulting for each joint along MnROAD cells (DeSantis et al. 2019).

In addition to faulting for consecutive joints, the LTE for consecutive joints was also examined. It is important to be able to develop a criterion for the frequency of the anticipated activated joint depth. This is possible by analyzing faulting and LTE for consecutive joints for a number of BCOA sections. At MnROAD, Cells 60 and 61 both had a 5-in overlay on 7 in of asphalt. Both sections were believed to have both depths of joint activation based on FWD testing and the FSR. By examining the LTE for consecutive joints, it is clear that some joints are performing better than others. This is a good indication that some of the joints activated only through the PCC and others activated through the PCC and asphalt layers. This can be seen for both Cell 60 and Cell 61 in Figure 2-12. From this analysis and with the analysis of the faulting data, on average, every 6th joint appears to activate through the PCC and asphalt layer for partial lane width panels.

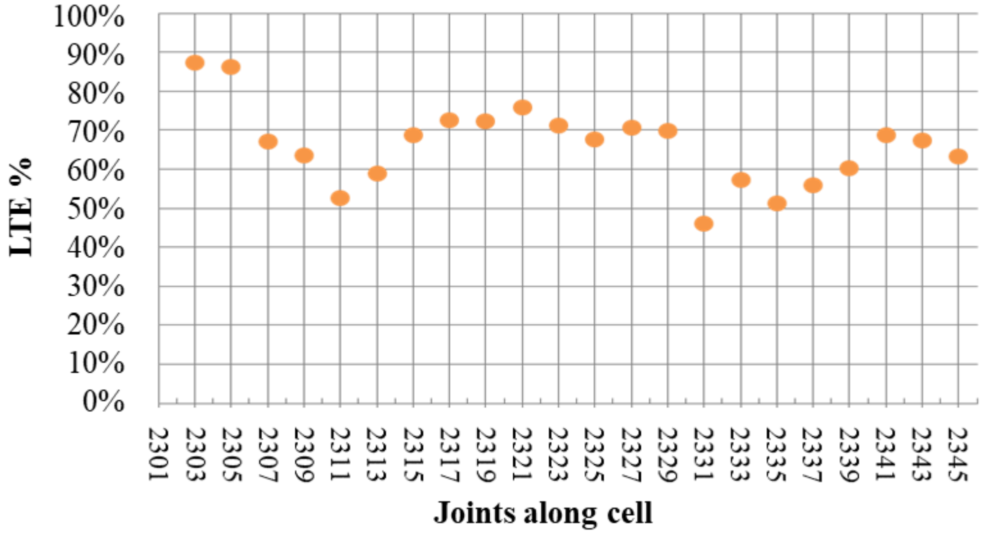

a) Cell 60, FSR = 1.0, 5 ft by 6 ft (Jt. activation depth varies)

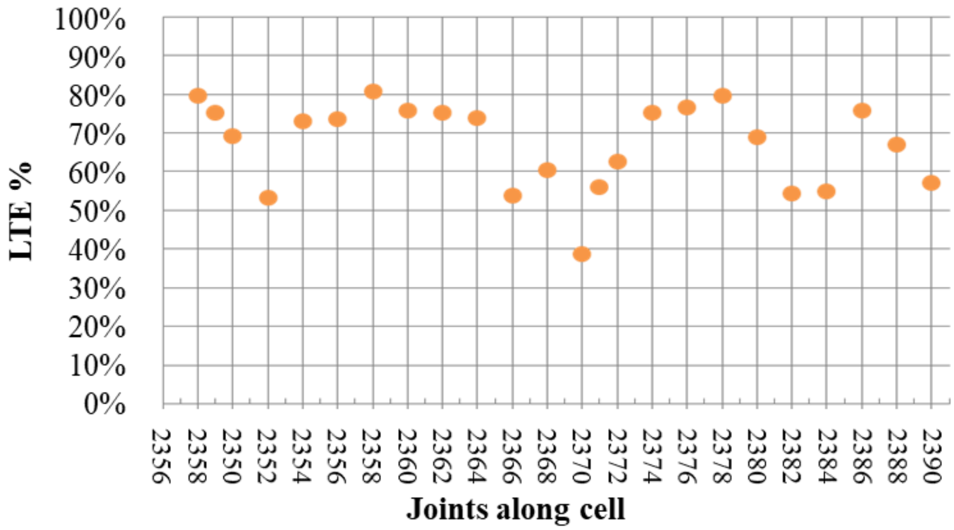

b) Cell 61, FSR = 0.9, 5 ft by 6 ft (Jt. activation depth varies)

Figure 2-12 Joint LTE for consecutive joints for MnROAD Cells 60 and 61.

Table 2-4 presents the overall criteria for different joint activation depths and frequency of the anticipated joint depth based upon structural design features, primarily the FSR and panel size. This work will be incorporated into the development of the computational model for predicting the response of BCOA structures (presented in Chapter 4) and the fault prediction model (presented in Chapter 5).

Table 2-4 Joint activation depth criteria.

	FSR_{winter}		
Panel Size	**$\leq$ 0.4**	**0.4 < FSR_{winter} < 0.9**	**$\geq$ 0.9**
Partial lane width panels (ex. 6x6 ft)	PCC depth only	PCC depth only w/ Every 6th jt. = PCC and asphalt	PCC depth only w/ Every 6th jt. = PCC and asphalt
Full lane width panels (ex. 12x12 ft)	n/a	PCC and asphalt	PCC and asphalt

2.7 Conclusions and Recommendations

Faulting in BCOA can develop from pumping that occurs either at the top of the asphalt or in the granular material beneath the asphalt. The layer where pumping will occur is dictated based on the depth of joint activation. The joint can activate either down through only the PCC layer, down through both the PCC and asphalt layers, or not active at all. When the joint does not activate through the asphalt, pumping will occur on the top of the asphalt layer. However, when a joint activates through both the PCC and the asphalt layers, pumping will occur in the granular layer below the asphalt. The depth at which the joint has activated for an in-service BCOA can be determined using FWD data. The measured LTE at a fully activated joint will be lower than at a joint that has not activated through the asphalt. Field coring provided verification that the FWD data could be used to reliably provide an accurate estimate of the depth the joint had activated.

Several factors will dictate if the joint will activate through the asphalt. One of the primary factors is the FSR between the PCC layer and the asphalt layer. A BCOA with a FSR_{winter} less than or equal to 0.4 is likely to have joints that activate only through the PCC layer, resulting in pumping of the asphalt material. A BCOA with a FSR_{winter} greater than or equal to 0.9 is likely to have joints that activate through the asphalt layer, resulting in pumping of the granular material. BCOA sections with a FSR_{winter} between 0.4 and 0.9 will likely result in some joints activating only through the PCC and other joints activating through the PCC and asphalt layer. In addition, the panel size also likely has an effect on the depth of joint activation. However, panel size is confounded by the FSR at MnROAD, making it difficult to isolate the effect of panel size on joint activation depth. Finally, material properties such as the CTE of the materials, drying shrinkage of the PCC, creep of the asphalt, and fracture properties of the materials will also influence joint activation depth.

Evidence of stained shoulders provides verification that pumping is occurring in these structures whether or not the joint activates through the asphalt. The shape of the faulting development curve depends on whether the joint activates through the asphalt. If the joint activates through the asphalt minimal to no faulting will develop in the first few years, followed by a gradual increase in the development of faulting. If the joint does not activate through the asphalt there is a similar dormant period, followed by a rapid development of faulting. Joint sealant was also found to be important to the performance of BCOA when the crack does not activate through the asphalt. Water, which enters joints that have not activated through the asphalt, can become trapped and lead to debonding at the interface between the PCC overlay and asphalt layer. This debonded region develops gradually and delays the onset of faulting. However, after this delayed period the development of faulting increases at a rapid rate. In addition, panel size can influence the crack width at the joint and therefore the rate at which faulting develops. Joints in BCOAs with larger panels will have a wider crack opening during the colder temperatures and will develop faulting more rapidly than BCOAs with smaller panels. The magnitude of faulting may be lower for the slabs with a shorter joint spacing as compared to slabs with larger joint spacings, but, due to the frequency of the joints, the IRI is very similar. This is an indication that the failure criteria of 0.12 in of average faulting may not be appropriate when short joint spacings are used.

From this analysis, a general criterion was established for the depth of joint activation and the anticipated depth of activation for consecutive joints. For partial lane width panels, it was determined when the FSR_{winter} is less than or equal to 0.4, joints will only activate through the PCC layer. For partial lane width panels with a FSR_{winter} greater than 0.4, every 6^{th} joint is likely to activate through the asphalt layer while the intermittent joints will only activate through the PCC overlay. In addition, full lane width panels (greater than or equal to 10 ft) with transverse joint spacing greater than or equal to 10 ft will result in all joints activating down through the asphalt layer.

3.0 Mechanisms Contributing to the Development of Faulting

3.1 Introduction

The objective of this chapter is to assemble a calibration database that can be used for the development of models for the prediction of faulting in BCOAs. The first step is to examine the mechanisms behind the development of faulting in these structures and determine if there are commonalities between that of BCOAs and other structures, specifically JPCPs and UBOLs. The next step is to determine if there are similarities between the rate of the development of faulting in BCOA and that of the other structures. The suitability of applying one faulting model to all pavement structures, as is currently done in Pavement ME, can then be established. If this is found to not be a valid approach, finding similarities between the trends in the development of faulting for specific structures is still useful. The performance data for these structures can then be used to supplement the calibration database.

3.2 Pavement Structures Investigated

The pavement structures investigated include: BCOA, UBOL, JPCP on granular bases (GB), JPCP on a cement stabilized base (CSB), and JPCP on an asphalt stabilized base (ASB). The primary difference between concrete overlays and conventional JPCP is that the joint spacing is traditionally reduced for overlays. Also, the overlay may be on either a new asphalt layer or aged asphalt that was existing prior to the placement of the overlay. For BCOA or a JPCP with an

ASB, the asphalt is typically 3 in or more (ERES 1999). For UBOL and JPCP with an ASB, the underlying asphalt can be either a permeable open graded layer or a dense graded asphalt. The interlayer for an UBOL is typically relatively thin, ranging from 1 – 3 in.

3.3 Pumping and Erosion Mechanisms

The depth to which the joint activates will vary based on the pavement design features. The layer from which the fines are being pumped will then be a function of the depth to which the joint activated. While the source of fines being pumped for some pavements is directly below the surface layer, for others it is directly below the base. For BCOAs, both locations must be considered, as is described in detail in Chapter 2 (see Figure 3-1a and Figure 3-1b).

Voids beneath the slab can develop due to breakdown (or erosion) of the asphalt layer, as shown in Figure 3-1c and Figure 3-1e. These voids develop in the wheelpath adjacent to the transverse joint. They will likely result in the development of faulting, longitudinal cracks in the wheelpath, diagonal cracks originating at the intersection of the wheelpath and a transverse joint at the bottom of the slab (Alland et al. 2016). Joints will activate through the surface layer and therefore fines will be pumped from the layer directly below the surface layer for all UBOL and some JPCPs and BCOAs (see Figure 3-1a and Figure 3-1d, respectively). For JPCP, this will occur for granular bases and a low strength CSB that consists of cement mixed in-situ with the granular material (see Figure 3-1f). For UBOL, the joint activates through the overlay, and most likely the asphalt interlayer, but the presence of the concrete layer beneath the asphalt interlayer will not allow pumping to occur beneath the asphalt. Therefore, faulting will always occur within the asphalt interlayer (see Figure 3-1d). When the joint activates through the lean concrete or asphalt stabilized layers, then faulting will develop due to pumping of the granular material below this layer. This occurs in BCOAs and JPCPs on an ASB or a CSB consisting of a lean concrete mixture (see Figure 3-1b).

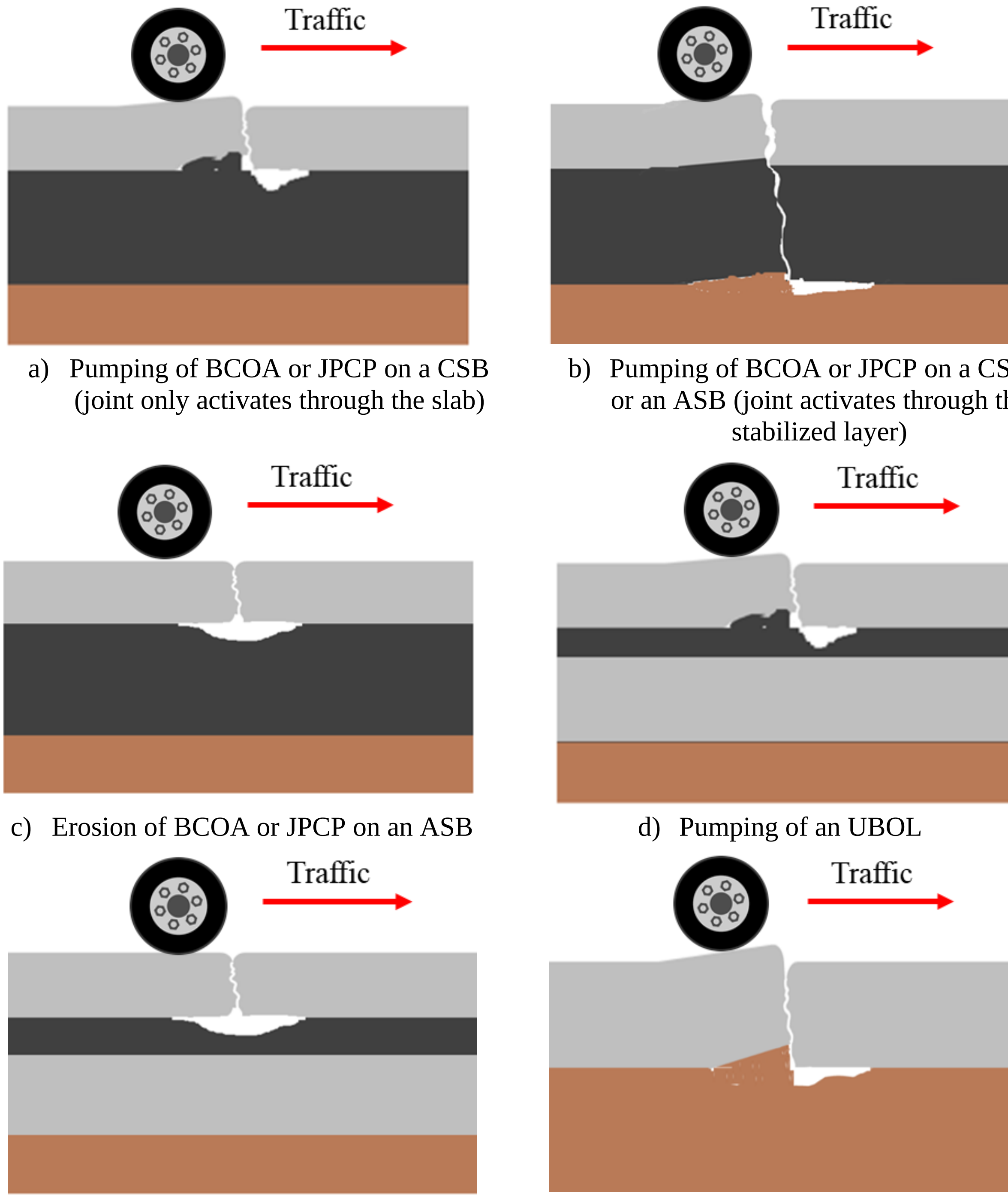

a) Pumping of BCOA or JPCP on a CSB (joint only activates through the slab)

b) Pumping of BCOA or JPCP on a CSB or an ASB (joint activates through the stabilized layer)

c) Erosion of BCOA or JPCP on an ASB

d) Pumping of an UBOL

e) Erosion of an UBOL

f) Pumping of a JPCP on a granular base

Figure 3-1 Source of fines being pumped and location of erosion (DeSantis et al. 2019).

Voids can also develop at the top of a new asphalt layer for an UBOL, if additional consolidation of the layer occurs after the overlay is placed. This could be the result of insufficient compaction during the construction process, an asphalt mixture with a high air void content, or insufficient stability (Sachs et al. 2016). However, this mechanism is unlikely to occur in BCOAs because it is unlikely to place a new asphalt layer on the existing asphalt prior to the PCC overlay. This would result in increased time and cost for construction completion.

3.4 Data Sources

Faulting data for a broad range of pavement structures is needed to characterize how faulting develops in general for these structures. The primary sources of data available include the Long-Term Pavement Performance (LTPP) sections, MnROAD sections, and miscellaneous sections from department of transportations (DOTs) across the country. The conventional JPCPs from the LTPP database used in this study were limited to the sections included in the last calibration of the AASHTO Pavement ME Software (Sachs et al. 2015). A brief summary of the data included in this study is summarized in Table 3-1.

Table 3-1 Summary of test sections available for different pavement structures (DeSantis et al. 2019).

Source	BCOA	UBOL	JPCP on GB	JPCP on CSB	JPCP on ASB
LTPP	n/a	14	71	65	61
MnROAD	21	6	5	0	4
DOTs	20 from MN	8 from MI	0	0	0

MI-Michigan; MN-Minnesota

3.5 General Observations

A summary of the faulting data for the LTPP sections is provided in Table 3-2 (downloaded in September 2016). Unfortunately, there are no BCOA sections in the LTPP database (as of 2016). There are a large number of JPCP sections, that can be compared to BCOA sections from MnROAD and the Minnesota DOT. It can be seen in Table 3-2 that of the 150 JPCPs with dowels, negligible faulting was observed. Eight of the 150 sections exhibited faulting greater than 0.1 in, five on granular bases, two on CSB, and one on an ASB. The traffic ranged from 7,600,000 to 62,500,000 ESALs. Of the undoweled sections, 22 of the 45 sections exhibited faulting. A similar trend was observed for the UBOLs with all six of the doweled sections not exhibiting any faulting and three of the seven undoweled sections exhibiting faulting. All of the UBOLs investigated had an asphalt interlayer. The traffic on these sections ranged from 23,500 to 34,000,000 ESALs. Plots depicting comparable sections with one section being doweled and the companion section undoweled are shown in Figure 3-2. The corresponding structural design features for each of these pavement sections is provided in Table 3-3. It is interesting to note that faulting developed in both wet and dry climates for undoweled JPCP and UBOLs regardless of the base type. This shows stabilizing the base might delay but is unlikely to prevent faulting without reducing the magnitude of the differential deflections with dowel bars.

Table 3-2 Ratios of LTPP sections with faulting > 0.1 in over the total number of sections (DeSantis et al. 2019).

Structure	Climate							
	WF		WNF		DNF		DF	
	Restraint							
	D	U	D	U	D	U	D	U
BCOA	n/a	n/a	n/a	n/a	n/a	n/a	n/a	n/a
UBOL	0/11	1/3	0/2	1/3	0/2	0/0	0/0	1/1
JPCP on GB	3/37	9/16	0/2	0/0	1/5	1/2	1/4	2/5
JPCP on CSB	0/37	3/3	1/2	1/3	0/4	1/4	1/6	3/6
JPCP on ASB	1/40	2/5	0/3	0/0	0/4	0/2	0/6	0/1

WF-Wet Freeze; WNF-Wet no-freeze; DF-Dry Freeze; DNF-Dry no-freeze
D-Doweled; U-Undoweled

Table 3-3 Description of the doweled and undoweled pavement sections (DeSantis et al. 2019).

BCOA	**MnROAD Cell 97 (undoweled)**	**MnROAD Cell 92 (1.0 in dowels)**
PCC thickness (in)	6.0	6.0
Joint spacing (ft)	10	10
Climatic region	WF	WF
Base	7.0 in dense graded asphalt	7.0 in dense graded asphalt
UBOL	**18_9020 (undoweled)**	**28-7012 (1.0 in dowels)**
PCC thickness (in)	10.2	10.5
Joint spacing (ft)	15.0	15.0
Climatic region	WF	WNF
Interlayer	5.0 in dense graded asphalt interlayer	5.3 in dense graded asphalt interlayer
Existing PCC thickness (in)	10.2	8.3
JPCP on GB	**19_3055 (undoweled)**	**23_3013 (1.125 in dowels)**
PCC thickness (in)	10.0	10.5
Joint spacing (ft)	20.0	20.0
Climatic region	WF	WF
Base	3.2 in A-1-b (28 ksi)	4.4 in A-1-a (28 ksi)
JPCP on CSB	**32_3010 (undoweled)**	**4_7614 (1.25 in dowels)**
PCC thickness (in)	9.5	9.5
Joint spacing (ft)	17.0 random	17.0 random
Climatic region	DF	DNF
Base	5.6 in (400 ksi)	5.2 in (400 ksi)
JPCP on ASB	**40_3018 (undoweled)**	**23_3013 (1.25 in dowels)**
PCC thickness (in)	9.0	9.0
Joint spacing (ft)	15.0	15.0
Climatic region	WF	WF
Base	3.6 in dense graded asphalt	5.0 in dense graded asphalt

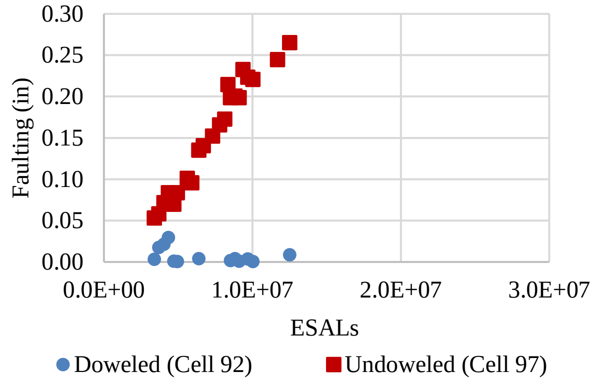

a. BCOA (MnROAD sections)

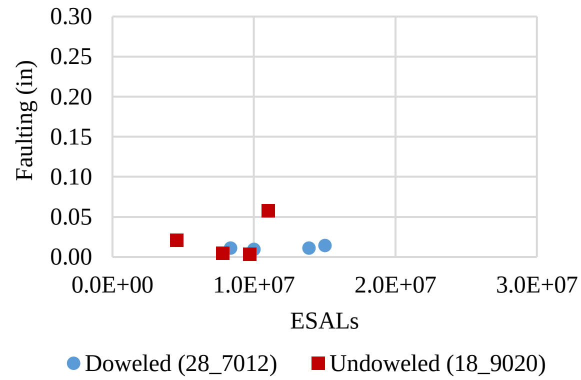

b. UBOL with asphalt interlayer

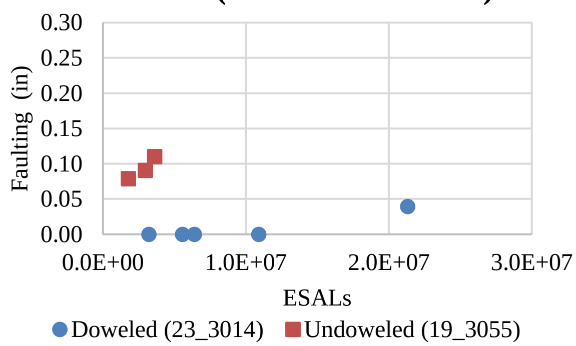

c. JPCP on granular base

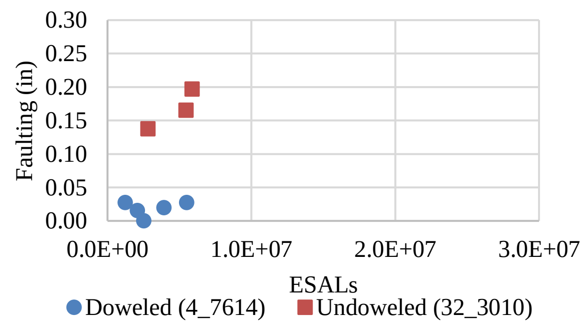

d. JPCP on CSB

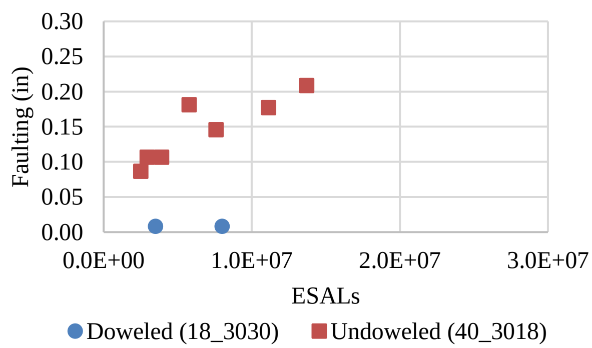

e. JPCP on ASB

Figure 3-2 Comparison of the faulting that develops for doweled and undoweled pavements (DeSantis et al. 2019).

3.6 Concrete Overlays

Overlay design features can differ from conventional JPCP designs in a couple of ways. The joint spacing is commonly reduced for jointed concrete pavement overlays. This reduces the high curling/warping stresses that are generated due to the stiff support conditions as a result of the existing asphalt or concrete pavement beneath the overlay (Mack et al. 1993, 1998, and Wu et al. 1998). The overlays are typically thinner than conventional JPCP and are commonly undoweled. The short joint space will result in a reduced joint opening, thereby limiting moisture infiltration and increasing aggregate interlock. Both of these are beneficial in decreasing the development of faulting.

3.6.1 BCOA

It is important to determine if the development of faulting in BCOA is similar to that for conventional JPCP so the applicability of current faulting models to these structures can be assessed. It is also important to determine if any of the JPCP structures develop faulting in a manner similar to that of BCOAs because the performance data for JPCPs could then be used to supplement a BCOA calibration database. As explained in great detail in the previous chapter, the rate of faulting and the shape of the fault development curve can vary based on the activation depth of a joint. In BCOA, the joint can activate through just the PCC overlay or both the PCC and asphalt layers, as shown in Figure 3-1a and Figure 3-1b (Roesler et al. 2008). The criteria established in the previous chapter can be used to establish the different depths of joint activation (DeSantis et al. 2016).

Voids that develop beneath the slab due to breakdown of the asphalt layer, as shown above in Figure 3-1c, will affect the fatigue life of the overlay. These voids will contribute to the development of longitudinal cracks in the wheelpath, or diagonal cracks originating at the intersection of the wheelpath and transverse joint at the bottom of the slab (Li and Vandenbossche 2013 and Rasmussen et al. 2002). This gap will result in increased deflections that cause erosion, pumping of the asphalt, and eventually faulting. Evidence of this phenomena can be seen through the data collected for the BCOA sections at MnROAD. In Cell 63 (4-in PCC, 8-in asphalt, 5 ft by 6 ft panels), a longitudinal crack developed in the wheelpath between joint numbers 2439 and 2440 after about 5 years. The performance of these joints can be seen in Figure 3-3a and Figure 3-3b.

These plots depict faulting and deflections measured at a joint throughout the life of the pavement. The deflection was recorded directly under the load plate for a 9-kip load applied with an FWD when testing in the wheelpath, adjacent to the transverse joint. The data shows an increase in the deflections prior to the development of the crack. This could be indicative of a loss of support from the breakdown of the asphalt beneath the joint that resulted in the longitudinal crack along the wheelpath at Joint 2440. This was followed by pumping of the asphalt material and the development of faulting. It is believed that the increase in deflection is a result of a void that developed in the top of the asphalt layer because the stress level is not sufficiently high under a fully supported condition for a crack to initiate. The brittle nature of the concrete results in a very short period of time between crack initiation and the time the crack activates fully through the slab. Therefore, this gradual increase in deflection can be attributed to a void developing and not a reduction in the stiffness of the concrete due to crack development and activation. Another example of longitudinal cracking in the wheelpath developing before an increase in faulting is observed can be seen in Figure 3-3c for Cell 60 (5-in PCC, 7-in asphalt, 5 ft by 6 ft panels).

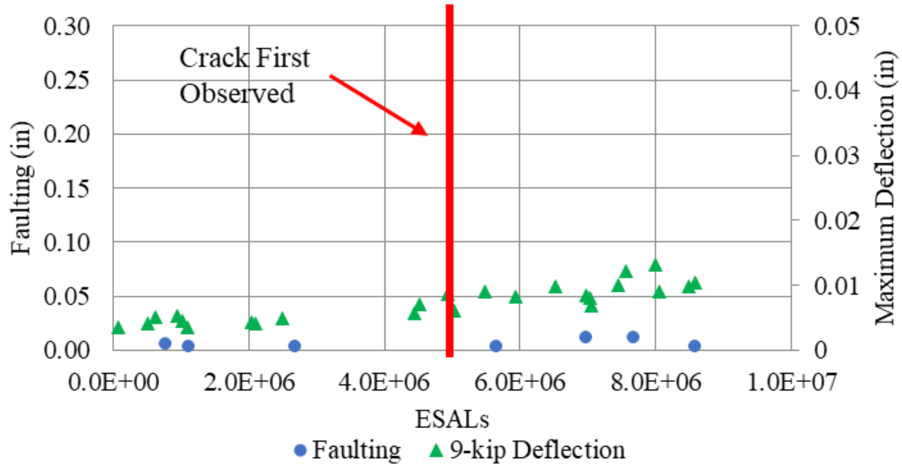

a) Cell 63: Joint 2439 – long. cracking occurs after 5 years

b) Cell 63: Joint 2440 – long. cracking occurs after 5 years

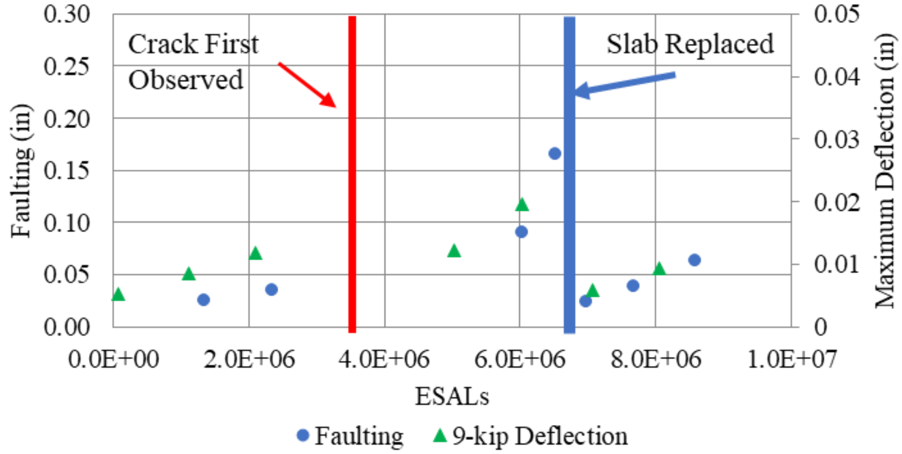

c) Cell 60: Joint 2331 – long. cracking occurs after 4 years and slab is replaced after 7 years

Figure 3-3 Faulting and 9-kip FWD deflection for BCOA at MnROAD (DeSantis et al. 2019).

Another trend observed in the development of faulting, is faulting in the passing lane was the same as that in the driving lane for a couple of BCOA sections even though the amount of traffic was lower. This can be seen in Cell 96 at MnROAD. The development of faulting appears to be identical between the driving and passing lanes for the joints activating through both the concrete and asphalt layers. However, the passing lane was subjected to significantly less traffic than the driving lane (approximately 12.5 million ESALs vs 3.0 million ESALs after 12 years of being in-service). This phenomenon also occurred in Cell 97 at MnROAD, where all of the joints activated through both the concrete and asphalt layers. This can be seen in Figure 3-4. The faulting appears to stabilize for both passing lanes around 0.15 in. Along with being influential on the maintenance, this will also have an impact on faulting prediction. Lower traffic levels in the passing lane will result in less damage to the BCOA and lead to a lower prediction of faulting in comparison to higher traffic levels observed in the driving lane. Due to this phenomenon, it is important to eliminate the passing lane for sections (Cells 96 and 97) with activated joints through the asphalt layer from the calibration database. The faulting data for these passing lanes should not be included in the calibration database due to the large dependency it has on the magnitude of the faulting in the driving lane.

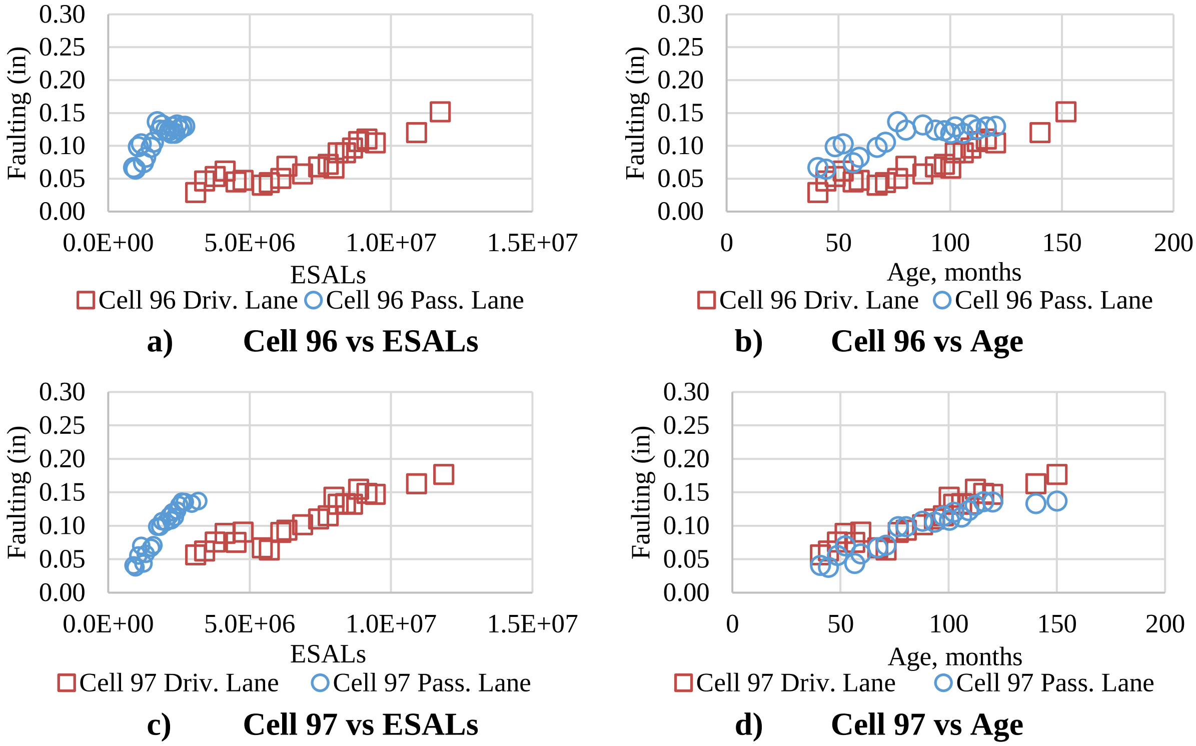

Figure 3-4 Average joint faulting for activation through the asphalt layer with respect to traffic and age (DeSantis et al. 2019).

3.6.2 UBOL

Faulting develops in UBOLs as a result of pumping in the asphalt interlayer (the layer placed between the existing distressed pavement and the overlay to prevent distress from reflecting up into the overlay), as shown in Figure 3-1d. It is important to determine if the development of faulting in UBOL is similar to that of BCOAs (when the joint only activates through the PCC) to determine if these structures can be used to supplement the BCOA calibration. To do this, the performance of several UBOLs are investigated, including the UBOL LTPP sections that are a part of the General Pavement Study (GPS)-9 (Unbonded PCC Overlays on PCC Pavements). Nine of the LTPP sections investigated had a dense graded asphalt interlayer ranging from 1 to 4-in thick and four sections had a chip seal interlayer. MnROAD constructed six UBOLs as part of the mainline test study that were also considered. These overlays are thinner than any other sections available and are also undoweled. These interlayers consist of either an open graded asphalt or nonwoven geotextile fabric. Finally, a large number of UBOLs that have been constructed in the state of Michigan were included. These UBOLs have a 1-in asphalt interlayer that were either dense or open graded. The open graded asphalt interlayer was significantly different from that used in Minnesota since it was not nearly as open graded, had a higher asphalt cement content and had a lower percent of fines.

The first observation for the UBOLs was that, similar to the other pavement structures, UBOLs did not exhibit faulting when adequately doweled. This was based on UBOLs in the LTPP database that were a minimum of 14 years old with approximately 500,000 ESALs and UBOLs in Michigan that were a minimum of 12 years old. Two undoweled LTPP sections with asphalt interlayers did exhibit faulting: (Section 06_9107: 9-in PCC, 1-in dense graded asphalt, 7.5-in existing PCC) (18_9020: 10-in PCC, 5-in dense graded asphalt, 10.2-in existing PCC). Section 18_9020 had a 15.5-ft joint spacing and Section 06_9107 has a 12-, 15-, 13-, 14-ft random joint spacing. In Section 06_9107, the average faulting in the outer wheelpath was 0.12 in, with 13 of the 32 joints measured exhibiting fault depths greater than 0.16 in after 14 years and 5 million ESALs. The average faulting was 0.06 in for Section 18_9020 after 17 years and 11 million ESALs, with 2 joints greater than or equal to 0.15 in. The faulting measured for these sections can be seen in Figure 3-5.

Sections that had interlayers that were chip seals experienced fault depths, which were, on average, half of the thickness of the chip seal layer with 104 of the 132 measured joints in these sections having a fault depth of 0.08 in or greater. This shows that the chip seal interlayers are not durable and are susceptible to pumping and erosion.

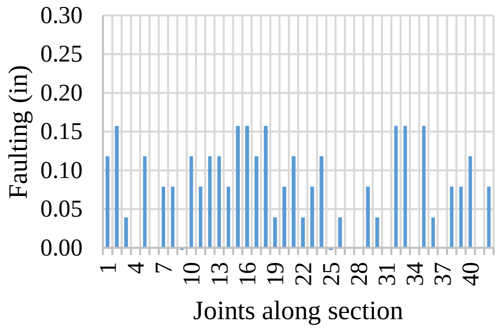

a) 06_9107 Faulting along section @ 14 years, 5 million ESALs

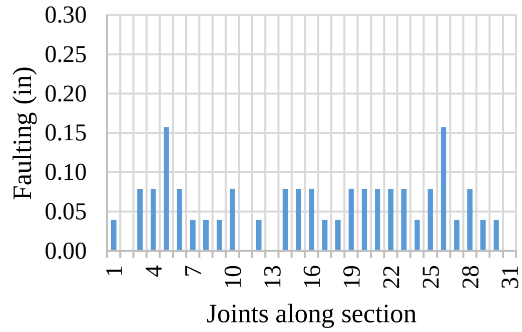

b) 18_9020 Faulting along section @ 17 years, 11 million ESALs

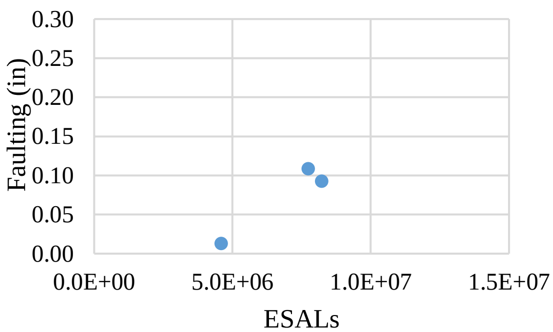

c) 06_9107 Average section faulting

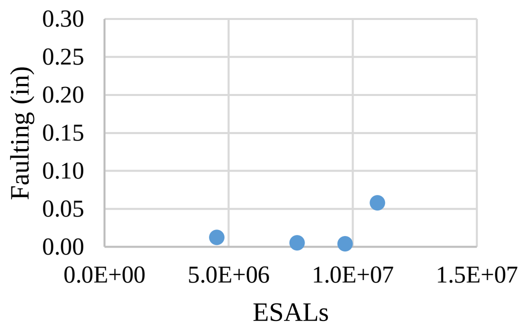

d) 18_9020 Average section faulting

Figure 3-5 LTPP UBOL undoweled sections (DeSantis et al. 2019).

Non-woven geotextile fabrics and open graded asphalts provide increased drainability over dense graded asphalt. Drainage through the interlayer prevents water pressure build-up. At the same time, sufficient resistance to stripping has to be provided so that binder is not stripped away as water flows through the open graded asphalt interlayer. An advantage to the fabric is that good drainability can be achieved without stripping concerns. The disadvantage is that the better the drainage characteristics, the less stiff the interlayer tends to be, which could have an adverse effect on the fatigue life of the overlay.

Recently, non-woven geotextile fabrics have become a popular alternative as an interlayer in these structures. The use of fabrics is an adaptation of the German application of using fabrics to separate newly constructed PCC pavements from cement stabilized bases (Rasmussen and Garber 2009). UBOL with a geotextile interlayer are not expected to fault because there is no material available between the two layers of concrete pavement that can be pumped. This is supported with field data as MnROAD Cells 505 and 605 have negligible faulting over the first 4 years of being in service. Therefore, sections with a fabric interlayer were not considered in an attempt to supplement the calibration database for BCOAs.

MnROAD had four UBOLs with an open graded asphalt interlayer. These sections had an open graded 1-in permeable asphalt stabilized stress relieving course (PASSRC) interlayer and were undoweled. Cells 105 and 205 had 4-in overlays, while Cells 305 and 405 have 5-in overlays, and all four sections had a 15-ft joint spacing with undoweled joints. Cells 105 and 205 were taken out of service after 3 years in order to construct Cells 505 and 605 with a geotextile fabric interlayer. The two cells taken out of service were developing up to 0.1 in of faulting in the outer wheelpath with an average joint faulting of 0.055 in. If these cells were not taken out of service, it is believed that the fault depths would continue to increase. This was the case for Cells 305 and 405 in Figure 3-6, which remained in-service and show faulting for each joint along the section as well as average faulting for each section. The average faulting for these sections after 6.5 million ESALs is 0.09 in. It has been observed that the PASSRC interlayer material can be stripped away and broken down under loading. This material is then susceptible to pumping, which can lead to the observed faulting for these cells. This further illustrates the importance of a durable non-erodible interlayer material. The sections in Michigan with an asphalt interlayer are doweled and have negligible faulting (<0.03 in) after being in-service between 6 to 13 years, depending on the section.

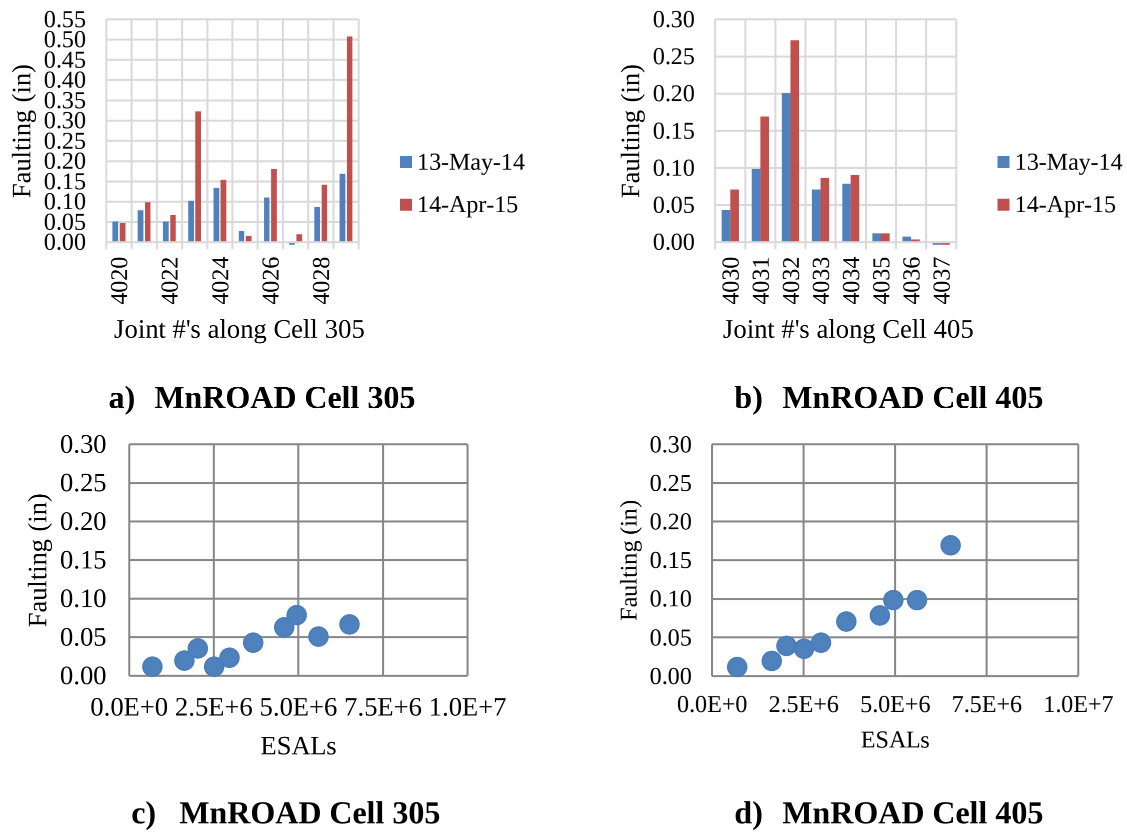

Figure 3-6 Comparison between faulting trends in UBOL (DeSantis et al. 2019).

Figure 3-5 and Figure 3-6 depict the development of faulting in UBOLs with asphalt interlayers. This is similar to the trend observed in the development of faulting for BCOA. There is a dormant period in the beginning when the asphalt begins to break down. After a period of time, pumping begins within the deteriorated asphalt layer and this eventually leads to the development of faulting. The development of faulting within the section appears to be relatively uniform between joints. This could be attributed to the fact that the minimum joint spacing was 10 ft long and therefore each joint activates, as did the BCOAs with a 10-ft joint spacing. An example of this can be found in Figure 3-5. However, Joints 5 and 26 in 18_9020 from Figure 3-5b and Joints 4023 and 4029 of Cell 305 from Figure 3-6a have wider than average joints. This may indicate that averaging the faulting over the section is not, by itself, sufficient to characterize faulting for a section.

Voids beneath the slab that develop due to breakdown of the asphalt layer can develop in UBOL as well as BCOA. These voids will contribute to the development of longitudinal cracks in the wheelpath, or diagonal cracks originating at the intersection of the wheelpath (Alland et al. 2016). This gap will result in increased deflections that cause erosion, pumping of the asphalt, and eventually faulting. Cracks in the wheelpath believed to be from erosion, were observed in UBOLs at both MnROAD as well as within the LTPP database. However, there was insufficient performance data to observe the subsequent development of faulting and increased FWD deflections at the joint, as was seen with the BCOA.

3.7 JPCP

Figure 3-7 shows the development of faulting for the undoweled JPCPs with different base types in the LTPP database. A description of the base and subgrades for each section is provided in Table 3-4. The faulting development trends for each base type is described below.

3.7.1 Granular Base

Faulting data for the JPCP sections with a granular base can be seen in Figure 3-7a. Faulting in these undoweled sections appears to initiate almost immediately (after between 0 to 500,000 ESALs). There was a rapid increase in the development of faulting up to around 0.12 in after 2,000,000 ESALs. The magnitude of faulting begins to stabilize at approximately 0.12 in. The only exception to this is Section 01_ 3028 where the faulting continues well beyond 0.12 in. As can be seen in Table 3-4, this section has a very poor subgrade (AASHTO A-6) with 45% fines. Additionally, the mean annual precipitation at Section 01_3028 is 52 in, which is much greater than the average precipitation of 27 in for the other sections.

3.7.2 Cement Stabilized Base

The JPCPs with a CSB in the LTPP database can be seen in Figure 3-7b. The performance of these undoweled sections varied greatly. Two different trends were observed and are differentiated by symbols. One trend observed was that some of the sections exhibited faulting similar to that observed for the JPCP with granular bases with faulting initiating almost immediately and developing rather quickly until it stabilizes at a maximum of 0.12 in after 2,000,000 ESALs. The other trend observed was that the onset of the development of faulting is delayed, as compared to the JPCP with a granular base. In this case, faulting initiates after between 500,000 and 1,000,000 ESALs. These sections are represented by circular data markers in Figure 3-7b.

Both a lean concrete base and cement stabilized base are categorized as CSB in the LTPP database. The LTPP sections with a CSB that exhibited the largest amount of faulting (star markers in Figure 3-7b), had a lower resilient modulus for the base material, indicating that these bases were stabilized bases and not lean concrete. This can be seen in Table 3-4. Since the CSB sections that faulted have good subgrades with a low fines content, it appears that the cement stabilized base material is being pumped. All of the CSB sections that stabilized at a lower maximum faulting have a resilient modulus that is greater than 1000 ksi for the base material, indicating that these are more likely to be lean concrete bases. It is noticed that the faulting for the pavements with lean concrete bases appear to level off at a lower level of faulting as the number of fines in the subgrade decreases. This would indicate that the transverse joint tends to activate through the lean concrete base and the material being pumped is the subgrade below the base.

3.7.3 Asphalt Stabilized Base

The LTPP JPCP sections with an ASB consisted of both open and dense graded asphalt. Faulting data for these sections is shown in Figure 3-7c. The performance of these sections varied greatly, similar to the JPCP sections with the CSB, resulting in two different faulting trends. One trend was similar to that exhibited for JPCPs with a granular base. In this case, faulting initiates almost immediately and the rate at which the faulting develops is high. These sections are represented by star shaped data markers in Figure 3-7c. Section 40_3018 did continue to increase higher than 0.1 in but the rate of increase appears to diminish after 0.12 in. The asphalt layer for both sections is characterized as a sand asphalt. The granular layer beneath the asphalt base was an AASHTO A-7-6 material with greater than 35 percent fines for the two sections exhibiting this trend (Sections 40_3018 and 40_4160), as shown in Table 3-4. In the second trend, faulting developed more slowly with respect to the JPCP on a granular base. This trend can be observed for Sections 40_4157, 40_4162, and 32_7084. These sections are represented by circular data markers in Figure 3-7c. The asphalt layer for these sections is characterized as a dense graded asphalt.

In summary, the development of faulting is similar for JPCPs for both granular and stabilized bases when there are a large amount of fines in the granular layer beneath the stabilized base or the cement stabilized base is weakly stabilized. Faulting begins to develop almost immediately with a rapid increase in the development of faulting up to 0.12 in and then the faulting begins to stabilize. Faulting took significantly longer to develop in the other JPCPs with stabilized bases.

Table 3-4 Description of undoweled JPCP LTPP pavement sections considered (DeSantis et al. 2019).

Granular base

Section ID	PCC (in)	Base (in)	Base type	Resilient mod. base (ksi)	Jt. space (ft)	Subgrade	Resilient mod. subgrade (ksi)	% Fines of subgrade	MAT [1] (ºF)	Precip. (in)
01_3028	***10.2***	***7.0***	***A-1-a***	***40.0***	***20***	***A-6***	***40.0***	***45***	***62.1***	***52.0***
19_3055	10.0	3.2	A-1-b	28.0	20	A-4	13.1	50	46.9	26.0
46_3013	9.4	3.5	A-1-b	38.0	17	A-6	19.0	75	46.9	15.0
46_3053	8.2	1.3	A-1-b	38.0	17	A-4	36.0	65	41.0	17.0
53_3011	9.6	14.0	A-1-b	39.0	15	A-2-4	10.0	25	50.0	38.0
53_3013	8.2	3.0	A-1-a	40.0	18	A-4	7.0	37	48.0	18.0
53_3014	10.4	5.4	A-1-a	40.0	13	A-2-4	4.1	19	55.0	8.0
53_3813	8.0	1.5	A-1-a	40.0	17	A-2-4	4.1	27	53.1	40.0
83_3802	9.8	10.8	A-1-a	29.0	17	A-7-5	9.0	92	41.0	22.0
89_3002	9.2	8.3	A-1-a	40.0	15	A-1-b	4.1	14	46.0	33.0

Cement stabilized base

Section ID	PCC (in)	Base (in)	Resilient mod. base (ksi)	Jt. space (ft)	Subgrade	Resilient mod. subgrade (ksi)	% Fines of subgrade
6_3021	***8.1***	***5.4***	***400.0***	***15***	***A-1-b***	***13.6***	***14.4***
12_4138	***8.0***	***4.9***	***400.0***	***22***	***A-2-4***	***18.6***	***14.7***
32_3010	***9.7***	***5.6***	***400.0***	***17***	***A-1-b***	***40.0***	***19.4***
6_3017	8.1	3.3	1000.0	15	A-1-b	7.0	13.8
6_7456	11.7	4.8	2444.4	15	A-6	7.5	47.8
8_3032	8.6	4.5	2099.5	17	A-1-a	13.1	7.4
13_3017	9.9	6.1	1000.0	22	A-2-4	8.6	35.3
13_3018	9.9	5.8	1000.0	21	A-4	23.9	43.2
31_3028	8.4	2.4	1000.0	17	A-7-6	10.4	97.8
49_3011	10.2	4.0	2567.4	15	A-4	14.9	35.75
49_7082	9.8	4.2	2820.5	12	A-1-b	28.0	18
49_7086	10.1	5.4	3107.9	12	A-6	3.5	38.4
55_6353	10.5	3.2	3275.0	17	A-1-a	18.0	8.7
89_3001	9.0	6.5	1000.0	17	A-2-4	7.0	13.9

Asphalt stabilized base

Section ID	PCC (in)	Base (in)	Binder type	Jt. space (ft)	Subgrade	Resilient mod. subgrade (ksi)	% Fines of subgrade
40_3018	***8.9***	***3.6***	***PG 85-100***	***15***	***A-7-6***	***17.0***	***88.4***
40_4160	***9.2***	***3.0***	***PG 85-100***	***15***	***A-7-6***	***11.0***	***80.2***
40_4157	9.1	3.8	AC – 20	17	A-2-4	14.9	17.8
40_4162	9.0	3.0	PG 85-100	17	A-4	10.4	41.5
32_7084	11.0	5.0	AC – 20	15	A-2-4	23.9	60.6

[1]MAT - mean annual temperature, [2]Sections in bold and italics have star data markers in Figure 3-7.

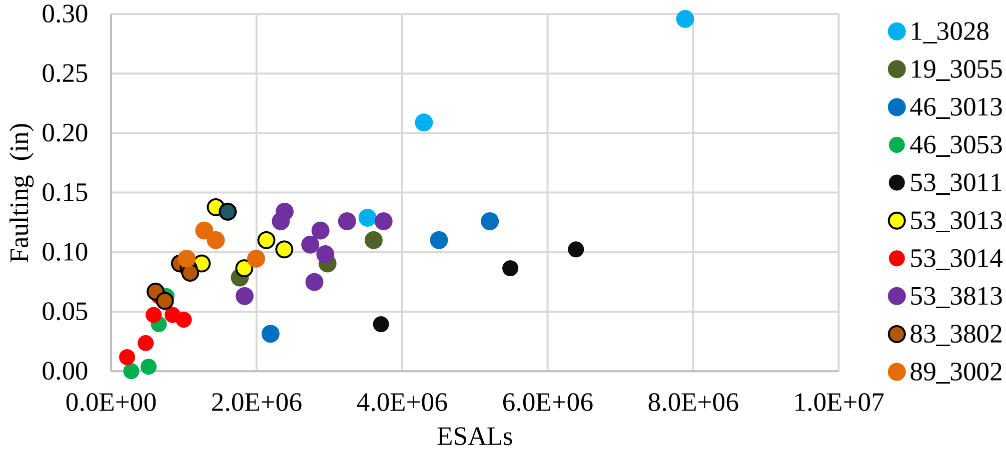

a) Granular base

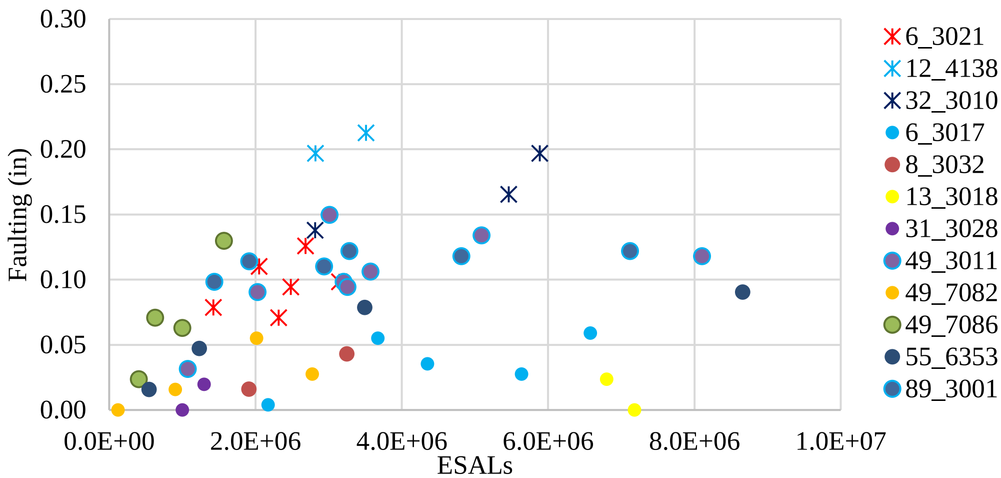

b) CSB

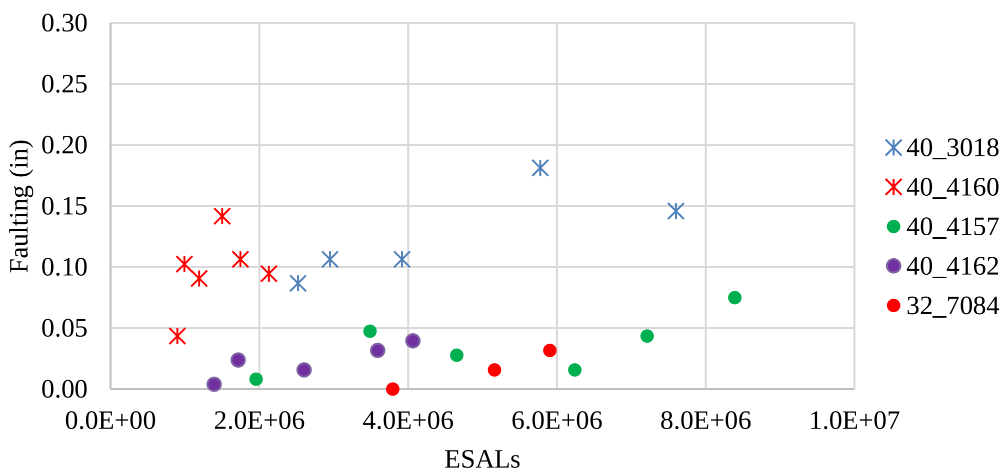

c) ASB

Figure 3-7 Faulting for undoweled JPCP LTPP sections with different base types (DeSantis et al. 2019).

3.8 Pavement ME Evaluation

In order to assess the applicability of a single prediction model in Pavement ME for all concrete pavement types, a sensitivity analysis was performed. The LTPP sections presented above for the different structures were all analyzed using Pavement ME. Figure 3-8 presents the comparisons between the observed and predicted faulting for corresponding traffic levels. A line of best fit is plotted on each graph for comparison. A y-intercept of 0.0, a slope of 1.0, and a high R^2 is desired.

Faulting predictions for JPCPs on a granular base can be seen in Figure 3-8a. The overall predictability for this base type is the best out of the different structures, returning an R^2 of 0.66 with a line of best fit close to y=x. One section that is being underpredicted is LTPP Section 83_3802. This may be attributed to the very poor subgrade (A-7-5) with 92% fines and very cold temperatures (mean annual temperature equal to 41 ^{o}F).

Figure 3-8b presents the faulting comparisons for JPCPs on a CSB. The faulting predictions for this base type returned an R^2 of 0.29 and strayed from the desired line of best fit. It appears that Pavement ME underpredicts faulting for LTPP Sections 6_3021 and 12_4138 (indicated by stars). This can be attributed to the stiffness of the base layer, which dictates the depth of joint activation and the material that undergoes pumping. It is also possible that this mechanism is occurring for LTPP Section 89_3001, as the base has a resilient modulus of 1000 ksi. The over prediction for Section 12_4138 may be attributed to the joint activation. Based on the model, the joint likely activated through the base layer and the subgrade is undergoing pumping. The subgrade for this section is an A-2-4.

The effects for an ASB can be seen in Figure 3-8c. Figure 3-8c also includes two BCOA cells from MnROAD. To be able to model Cell 97 and Cell 92 in Pavement ME, they are both modeled as a JPCP on an ASB to analyze faulting. Cell 97 is indicated by stars because the level of stiffness of the asphalt layer is similar to the other sections designated by a star. Cell 92 is the same design as Cell 97 with the addition of 1-in diameter dowels and is indicated using squares. A limitation of Pavement ME is the slab length must be greater than or equal to 10 ft. It appears from this plot, that there is a need to develop a separate faulting model that can better predict the performance of BCOAs.

Figure 3-8d presents the comparison for UBOLs. It is very clear from this plot, that there is a need to develop a separate faulting model to better predict the performance of UBOLs, as well. Note, the range of values on the y-axis is much larger than the other plots to be able to show the large predictions from Pavement ME.

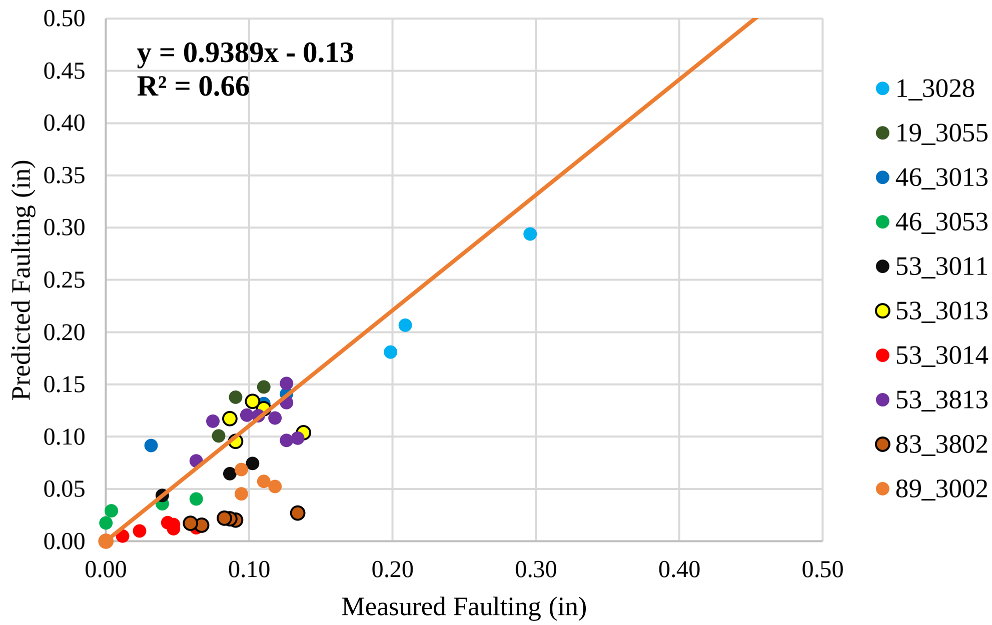

a) Granular base

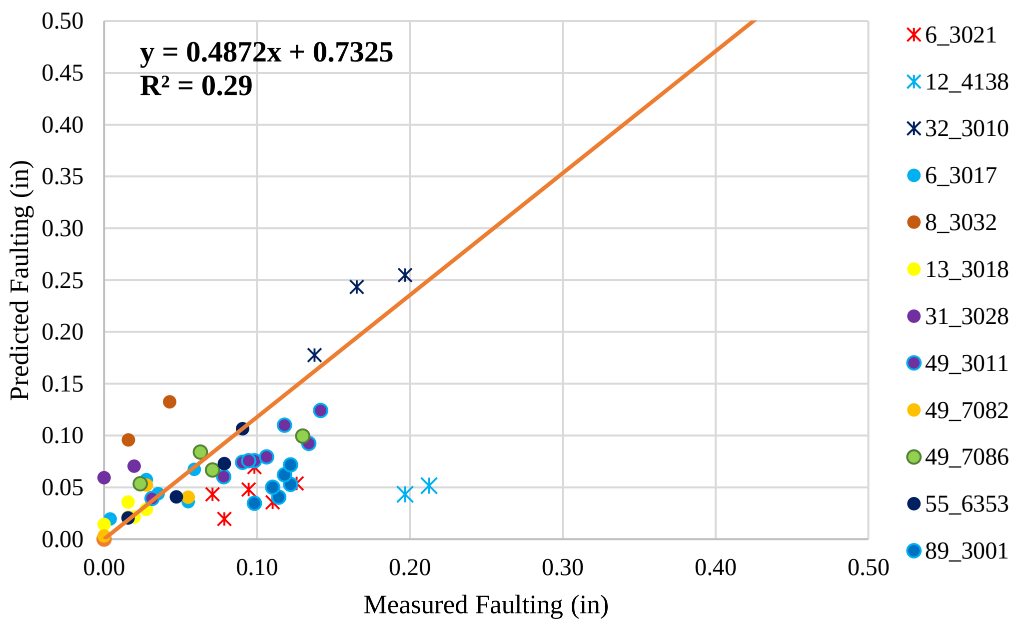

b) CSB

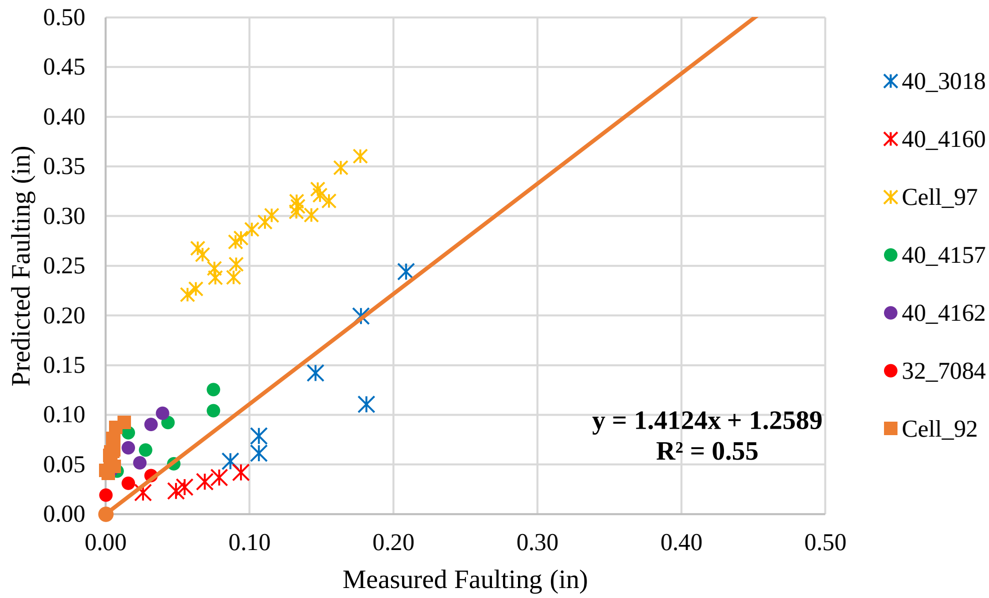

c) ASB

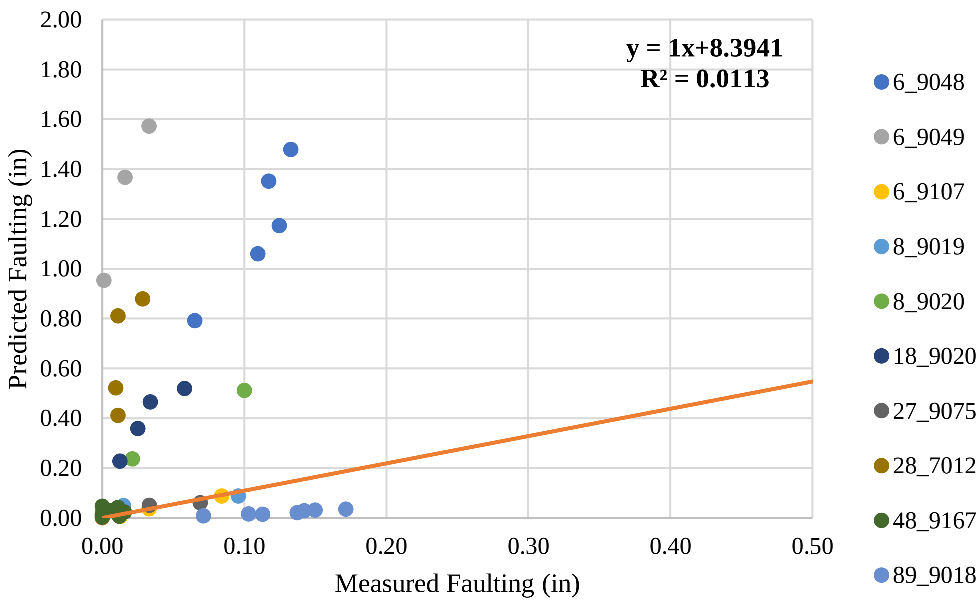

d) UBOL

Figure 3-8 Faulting for undoweled JPCP LTPP sections with different base types vs. Pavement ME predictions (DeSantis et al. 2019).

Along with examining the predicted vs observed relationship, it is also important to examine the difference between the observed and predicted faulting trends over time. Figure 3-9 presents the observed and predicted faulting with respect to traffic for the different base types and structures. The predicted faulting for each section is presented as a line with triangular markers using the corresponding color and circular markers for the measured faulting. Similarly to Figure 3-8, the sections with measured faulting indicated by stars can be attributed to the different levels of stiffness of the base layer, which dictates the depth of joint activation and the material that undergoes pumping (these sections are italicized in Table 3-4).

In Pavement ME, an interaction is present between the top of the base layer and the bottom of the concrete layer. This interaction is either modeled as full friction or no friction, depending on the base type. Loss of full friction may occur over time and is a direct input into the software. The number of months it takes until full bond is lost was used for calibration purposes in the cracking model. However, this causes the faulting prediction to rapidly increase once the full bond is lost and faulting does not appear to ever stabilize. The default value is 240 months (20 years). The influence of debonding can be seen for Sections 12_4138 (CSB) and 40_3018 (ASB) in Figure 3-9b and Figure 3-9c, respectively. UBOL are also modeled with a stabilized asphalt interlayer and develop faulting at a rapid rate, similarly to the stabilized bases once full bond is lost. This can be seen in Figure 3-9d.

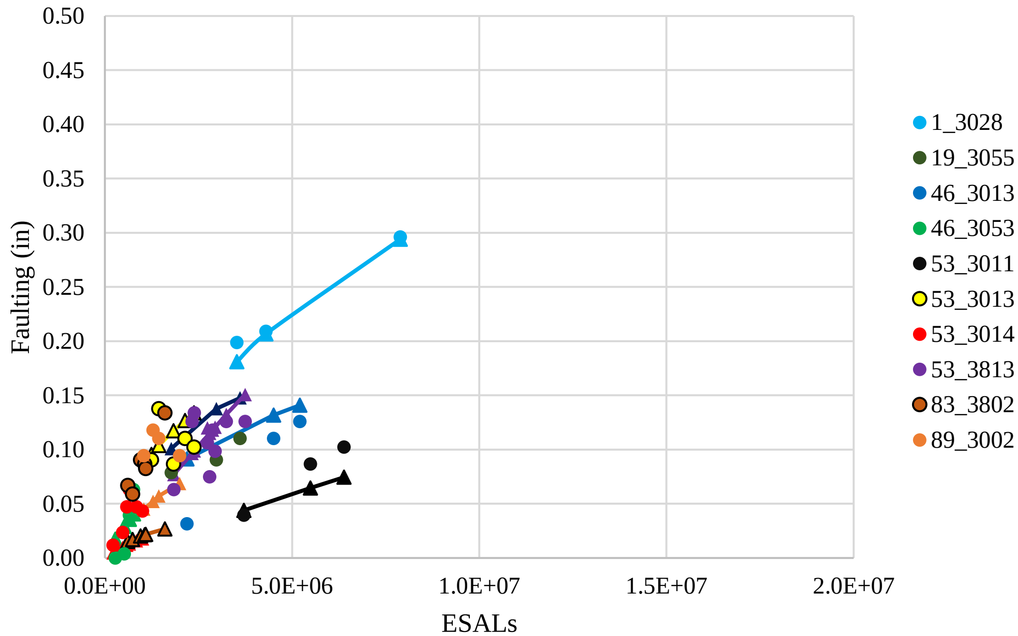

a) Granular base

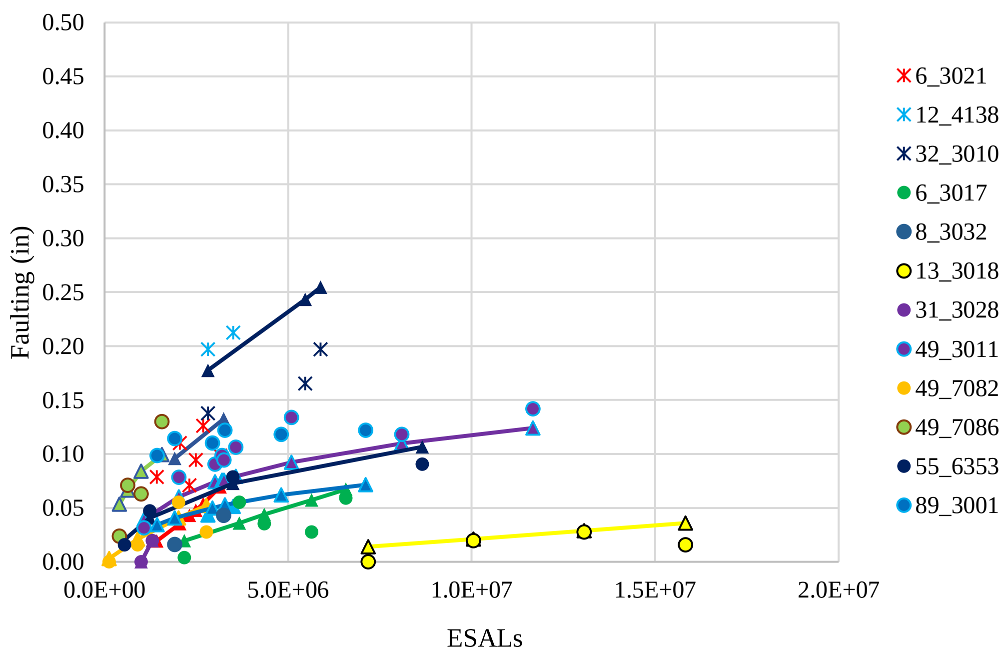

b) CSB

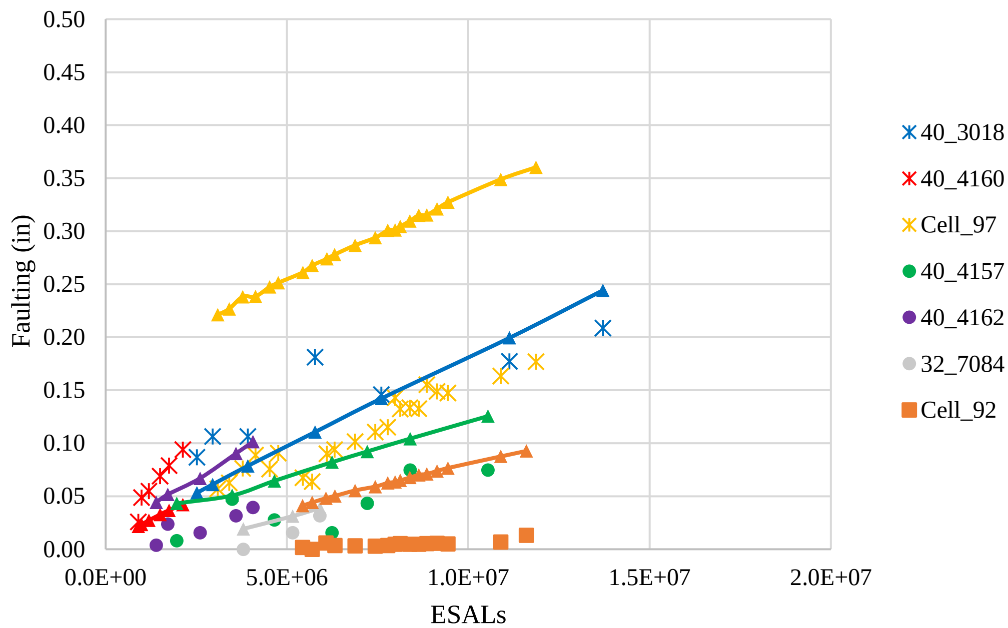

c) ASB

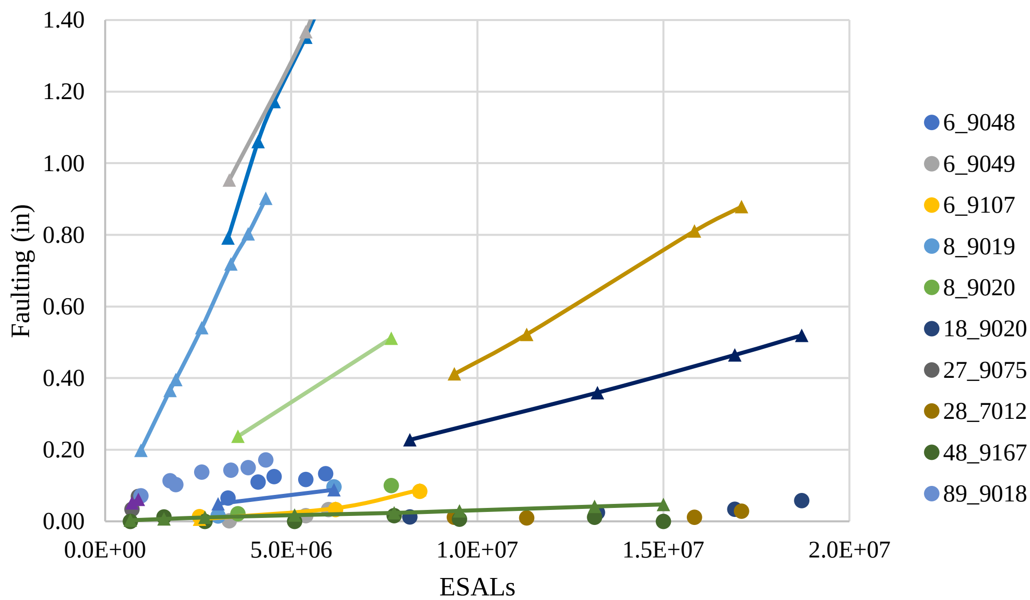

d) UBOL

Figure 3-9 Observed and predicted faulting for undoweled JPCP LTPP sections (triangles indicate predicted faulting for corresponding color of circles and stars that indicate measured faulting for each LTPP section) (DeSantis et al. 2019).

3.9 Conclusions

The mechanisms contributing to the development of voids beneath the slabs and faulting for a range of pavement structures was investigated to be able to potentially supplement a BCOA calibration database with faulting data for other pavement structures. The suitability of applying one faulting model to all pavement structures (conventional JPCPs and unbonded concrete overlays) was also assessed. The following conclusions were made:

- Dowels significantly reduce the potential for the development of faulting for each structure examined.
- Pumping will occur in BCOA either directly below the slab in the asphalt layer (if the joint only activates through the slab) or in the granular layer below the asphalt (if the joint activates through both the slab and the asphalt). Voids are sometimes created below the PCC overlay (erosion/deterioration of the asphalt layer) at the transverse joint in the wheelpath, when the joint does not activate full-depth prior to the development of faulting. This needs to be accounted for because this gap will result in increased deflections that cause erosion, pumping of the asphalt, and eventually faulting. It will also contribute to the development of longitudinal cracking.
- The initiation of the development of the faulting is delayed significantly in BCOA and UBOL as compared to JPCP with a granular base. The rate at which faulting developed was also more gradual and was less likely to stabilize at a peak of 0.12 in, as was the case for the JPCP with a granular or a weakly cement stabilized base. In addition, it is also possible the faulting stabilized at a peak of 0.12 in for the mentioned JPCP sections as a function of diamond grinding because the failure criteria for faulting is 0.12 in.

- The assumption that all joints within the pavement section fault at the same rate, and therefore can be represented by an average of the faulting for all joints throughout the section, is not necessarily applicable to BCOA and UBOL with shorter joint spacings. The development of faulting for these sections is not uniform throughout the section since not all of the joints activate and those that do might not all activate to the same depth for BCOA. Therefore, the average faulting for these structures may not be as informative as it would be for sections where faulting develops at the same rate for the majority of the joints.
- Two different trends in the development of faulting can be seen for JPCPs with CSBs and ASBs. The first trend is similar to the trends observed for JPCP with granular bases. When there are a large amount of fines in the granular layer beneath the stabilized base or the CSB is weakly stabilized, faulting begins to develop almost immediately with a rapid increase in the development of faulting up to 0.12 in after 2,000,000 ESALs. The magnitude of faulting then begins to stabilize. The second trend is similar to the development of faulting in BCOA or UBOL. These sections experience a dormant period prior to the initiation of pumping and faulting and develop faulting at a slower rate of increase in comparison to the JPCP with a granular base.
- In general, if the Pavement ME model is modified to account for the time it takes for a joint to activate through the asphalt and use the erodibility index of the base layer instead of the asphalt layer, it may be useful in predicting the development of faulting in BCOAs when the joints activate through the asphalt. However, it might be more of a challenge for the Pavement ME model to be used when predicting faulting in joints that do not activate

through the asphalt. Faulting development in these joints could be artificially controlled by the rate of bond deterioration between the PCC and asphalt layers.

Based on these conclusions, the current model used for the prediction of faulting in the Pavement ME design software is not able to accurately account for the trends in fault development in a BCOA or an UBOL, when pumping occurs at the top of the asphalt layer.

4.0 Structural Response Model

4.1 Introduction

The development of pumping, and therefore faulting, is directly related to the structural response of the pavement to applied loads. Therefore, it is necessary to estimate the response of the pavement to environmental and traffic loadings to predict faulting.

In order to estimate the response of BCOAs to these loading conditions, computational models are developed. The accuracy of these models are validated using FWD data collected for in-service BCOA structures. The incorporation of these computational models into a design procedure that performs incremental analyses is not feasible, as the analysis time would be unreasonable long. To address this, the BCOA response obtained from the computational models is used to populate a database for the development of ANNs. The ANNs can accurately reproduce the responses obtained from the computational models, given a certain set of required inputs. These ANNs can then be used to estimate the response of the BCOA for use in a faulting prediction model, similar to what is done within Pavement ME for JPCPs (ARA 2004, Khazanovich et. al 2004).

The objective of this chapter is to develop ANNs to be used to in conjunction with performance data to produce a mechanistic empirical faulting model for BCOA. First, field validated computational models are developed. Second, a fractional factorial analysis is performed for a range of parameters to generate a database to train the ANNs. Third, ANNs are trained using the generated database to predict the critical response of the BCOA, deflection basins and corner deflections. Finally, the ANNs are validated and a sensitivity analysis is conducted to assess the predictability of the ANNs.

4.2 Effect of Depth of Joint Activation on Deflections

A better understanding of joint behavior for BCOAs is necessary to accurately model the response of these structures. Joints can activate through just the PCC layer, both the overlay and the underlying asphalt layer, or can have both depths of activation along the same overlay, as described in Chapter 2.

The depth at which the joint activates plays an important role in the magnitude of the corner deflections due to curling and vehicle loads. A fully bonded BCOA with a continuous asphalt layer will decrease the curling deflections due to moment transfer, as compared to that when a joint activates the full-depth of the BCOA. A continuous asphalt layer results in lower differential deflections and therefore a reduced potential for pumping, as compared to an activated joint through the asphalt layer. Therefore, it is important to be able to accurately capture the effect of the depth of joint activation in the computational model so the impact it has on the development of faulting can be quantified. The estimated depth of joint activation with respect to the FSR is defined in Table 2-4 of Chapter 2 and will be incorporated into this analysis.

4.2.1 FEM Software Selection

The development of the deterministic portion of the computational model required a finite element modeling (FEM) software, which is able to account for both depths of joint activation.

Two different software programs were investigated, ABAQUS and ISLAB (ABAQUS 2004, Khazanovich et al. 2000). ABAQUS is a 3-D general purpose FEM software. ISLAB is a "2.5-D" Pavement Specific FEM software based on plate theory.

The first software examined, ABAQUS, has the capability to account for both depths of joint activation through modeling a continuous asphalt layer as well as a joint that activates through both the overlay and the asphalt layer. ABAQUS also has the capability to model the interface between the PCC and asphalt as fully bonded, unbonded, or partially bonded. This can be achieved through tied constraints, hard contact properties which allow separation between layers, and by using translational springs with a lower finite stiffness, respectively. Shear stresses and strains in the asphalt layer at the joint can also be accounted for. Figure 4-1 presents the different options available for modeling BCOA using ABAQUS.

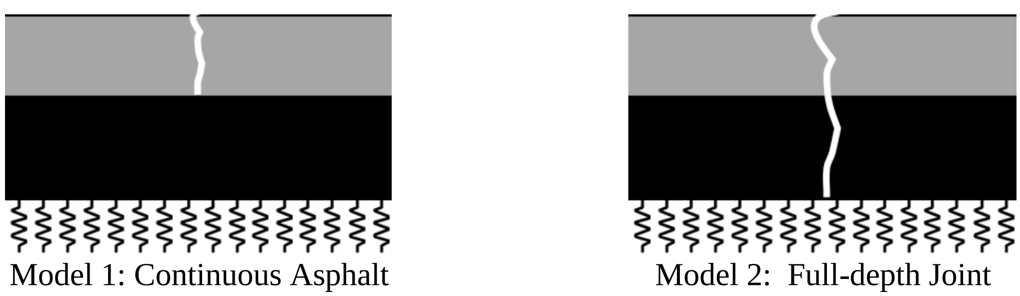

Figure 4-1 FEM modeling options in Abaqus.

The second FEM software examined, ISLAB, combines the flexural stiffness of the concrete and the asphalt into a single composite later. This makes it difficult to model joint activation only through the overlay (Khazanovich et al. 2000). Three options were examined to be able to account for the different depths of joint activation in ISLAB. Option 1 in ISLAB is for a bonded interface where the top plate is the PCC and the bottom plate is the asphalt, ignoring the continuity of the asphalt through the joint. Continuity of the asphalt through the joint can be considered using a Totsky model. The Totsky model consists of two plate elements that model bending, separated by springs that account for the direct compression that can occur (ARA Inc. 2004). A Totsky model is able to be employed when two layers are either fully bonded or fully unbonded. Option 2 is a Totsky Model which consists of an unbonded interface where the top plate is the PCC and the bottom plate is the asphalt. Between these two plates are springs which account for the direct compression between the two layers, however there is no shear transfer between the two plates. Option 3 is a Totsky model consisting of a bonded interface modeled between the top PCC layer and the top few inches of asphalt. The remaining asphalt is included in the lower plate beneath the Totsky interface and allows moment transfer through the joint. A schematic of the 3 options can be seen in Figure 4-2.

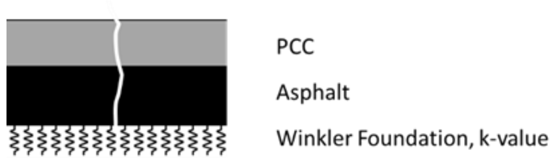

a) ISLAB Option 1

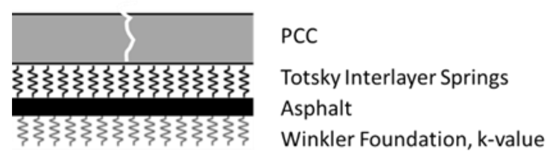

b) ISLAB Option 2 – Totsky Model

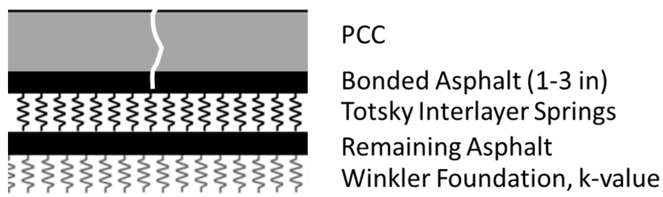

c) ISLAB Option 3 – Modified Totsky Model

Figure 4-2 FEM modeling options in ISLAB.

Option 1 (bonded case) automatically generates a joint through the entire structure (PCC and asphalt) and does not allow the asphalt to be modeled as a continuous layer. Option 1 is also able to converge when a temperature gradient is introduced. However, the LTE of the asphalt is automatically set equal to the LTE of the PCC overlay. This may be of some concern because it is believed that the interface of the asphalt at a joint will wear away instead of providing any load transfer through aggregate interlock. Therefore, the use of Option 1 is a possibility only when the joint activates fully through the PCC and asphalt layer and not when the joint activates only through the PCC.

There are two issues with Options 2 and 3. First, these models tend to suffer from instability issues, and often do not converge when a temperature gradient is considered. In addition, it is difficult to define the stiffness of the springs. In the initial comparison testing between ISLAB and ABAQUS, bonded and unbonded plate theory was used to determine the stiffness of the springs (Ioannides et al. 1992). There are no known studies that employed this method. Therefore, more work would need to be performed to determine the validity. Another variable to examine when using ISLAB is the bonded behavior at the interface between the PCC and asphalt layers. If a Totsky model is used, the shear stress will not be modeled accurately.

ABAQUS was selected as the FEM program because it is able to more accurately represent the response of a BCOA, specifically in the vicinity of the joint where the depth to which the joint will activate can vary. ABAQUS can model both a continuous asphalt layer as well as a discontinuous layer when the joint activates full-depth. In addition, a temperature gradient can be applied to quantify the effects of curling by applying a temperature difference to the top and bottom of the PCC layer, and achieving convergence is not problematic.

4.3 Description of Computational Models

The computational models consist of at least one full lane width; an 8-slab system was used for partial lane width panels (6 ft by 6 ft and 8 ft by 8 ft), and a 4-slab system was used for full lane width panels (12 ft by 12 ft). The 8-slab system consists of two adjacent panels in the transverse direction and 4 panels in the longitudinal direction. The 4-slab system consists of four full lane width panels in the longitudinal direction. The effects from the adjacent lane were negligible for the full lane width panels, due to the critical response location being the interior corner. Therefore, a single lane was used. Both slab systems include a shoulder that is 6 ft wide and is either tied PCC or asphalt. Figure 4-3 presents the 3-D FEM model.

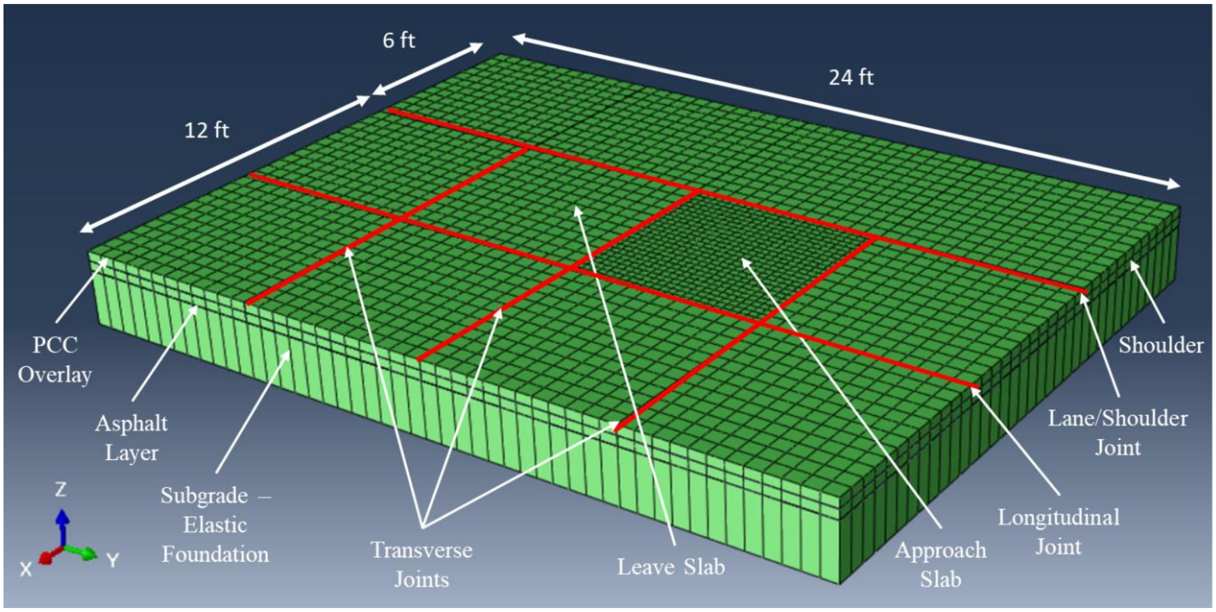

a) 8-slab system: 6 by 6 ft panels

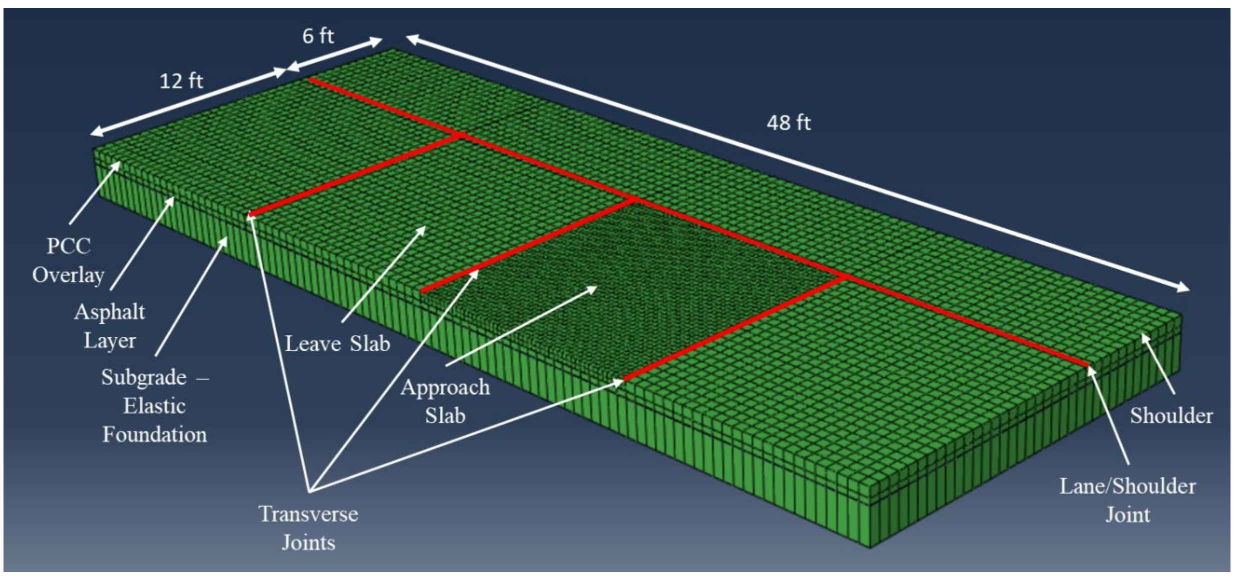

b) 4-slab system: 12 by 12 ft panels

Figure 4-3 Model configuration.

4.3.1 Interface Between Layers

The interface between the PCC (elastic solid) and the asphalt (elastic solid) layer was fully bonded. Composite action is essential for the performance of BCOA. This was achieved by using a “Tie” constraint, which treats adjacent nodes as rigidly connected to one another at the interface between the PCC and asphalt layers (ABAQUS 2004). However, when a joint only activates through the PCC layer and the asphalt layer remains continuous beneath the joint, differential deflections between the approach and leave slabs are negligible. Therefore, the response of in-service BCOAs could be more accurately modeled by creating a debonded region near the joint when a joint only activates through the PCC layer. This debonded region facilitates the development of the differential deflections necessary for pumping, thus allowing faulting to develop. A 6-in region around the edges of both the approach and leave slab was modeled as unbonded, while the interior portion of the slabs maintained a full bond. The unbonded region was modeled using a tangential behavior interaction. This interaction uses a “Penalty – Friction” assignment and is defined such that no shear forces develop and the contact surfaces are free to slide (ABAQUS 2004). The debonded region can be seen in Figure 4-4. A dense liquid foundation beneath the asphalt was simulated using a “Linear” interface interaction with a rigid fully constrained body (ABAQUS 2004). This allows the asphalt to become unsupported unlike the “Foundation” support interaction in ABAQUS (ABAQUS 2004). The stiffness of the interaction is defined by a modulus of subgrade reaction, k-value (psi/in).

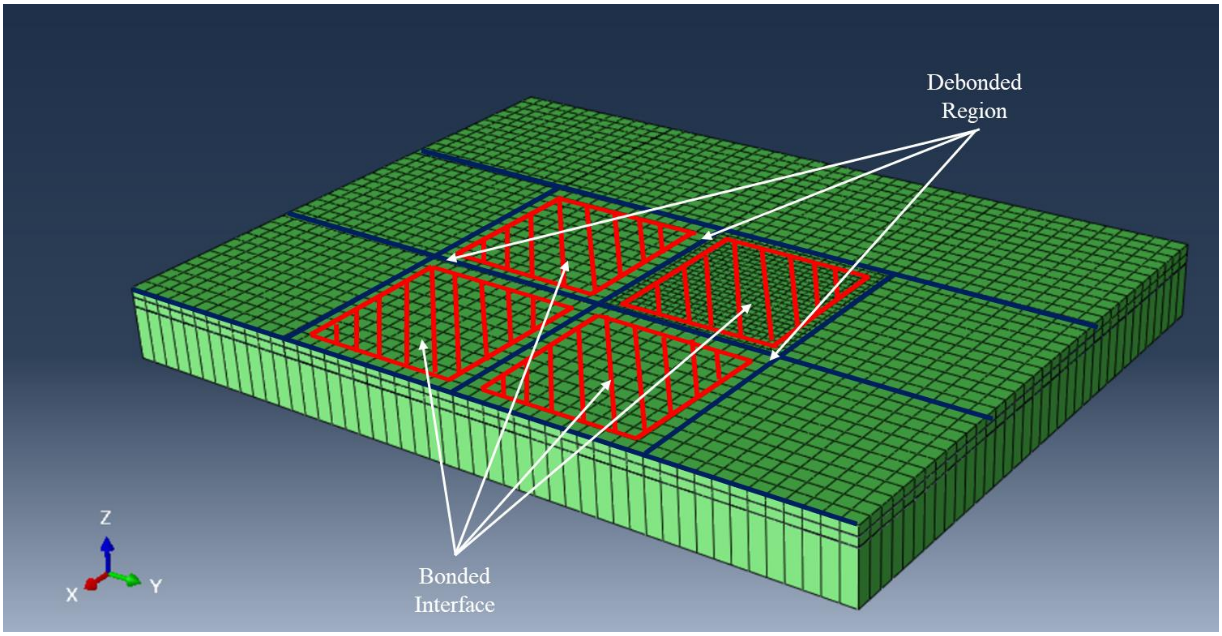

Figure 4-4 Debonded region at the interface for the 8-slab system (PCC depth only).

4.3.2 Joints

The joints are another important feature in the BCOA that must be accurately captured in the computational model. When joint activation through the asphalt is expected, the asphalt layer is discontinuous at the transverse joint and no interaction is assumed within the asphalt layer across adjacent slabs. When the joint activates only through the PCC layer for the 8-slab system, the asphalt is modeled as a continuous layer beneath all transverse joints. When the 8-slab system is used to model a full-depth joint, the central transverse joint is modeled to go through both the PCC and the asphalt layers but all other transverse joints are assumed to only activate through the PCC layer. For the 4-slab system, all transverse joints were modeled as full-depth joints. These joints are likely to activate full-depth because the 4-slab system is used for modeling BCOAs with longer panels that have larger joint width movement and thicker overlays with a high FSR. These assumptions on joint activation were based on an extensive study that was performed to better understand joint performance in BCOAs (DeSantis et al. 2019) that is presented in Chapter 2. The asphalt remains continuous for both joint depths for all longitudinal joints within the driving lane. However, the asphalt layer is not continuous across the lane/shoulder joint.

Aggregate interlock across the PCC joints is addressed by using shear springs. The spring stiffness per unit area is calculated for a given LTE based on the following equation developed by Crovetti (Crovetti 1994).

$$AGG^* = \left(\frac{\frac{1}{LTE} - 0.01}{0.012} \right)^{-1/0.849} \tag{4-1}$$

Where:

AGG* is the non-dimensional joint stiffness of the transverse joint, and

LTE is the corresponding LTE to the assigned joint stiffness.

The stiffness of the individual springs is calculated based on the tributary area. The longitudinal joints in the driving lane are modeled with the same LTE as the defined LTE for the transverse joints. The lane/shoulder joint is defined as 90% LTE when it is a tied PCC shoulder, and 0% when it is an asphalt shoulder. For both shoulder conditions, the asphalt layer is not continuous across the lane/shoulder joint and is assumed to provide no support. The full-depth asphalt shoulder is also assumed to provide no support. A “Hard” contact surface interaction is also applied to all joint faces to allow compression at the joint faces if they come into contact with each other.

4.3.3 Wheel and Thermal Loads

Loading is performed in two steps: thermal loading and traffic loading. The first step, an equivalent linear temperature gradient (ELTG) is applied, which accounts for curling due to temperature gradients, drying shrinkage, and built in curl. The ELTG is applied by defining nodal temperatures at each of the five layers of nodes in the PCC slab. The temperature at the bottom of the PCC is set to 0°F. The ELTG varies linearly from the bottom to the top of the PCC. All nodes in the asphalt layer are set to 0°F. Traffic is applied as a uniform pressure evenly distributed over the tire footprint. Single and tandem axle loads were considered. The dual tire footprint can be seen in Figure 4-5.

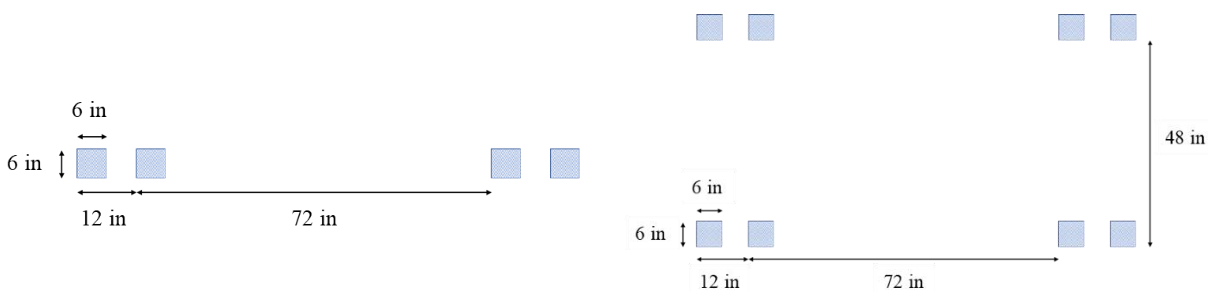

a) Single axle configuration   b) Tandem axle configuration

Figure 4-5 Axle configuration.

4.3.4 Finite Element Mesh

An accurate prediction of structural response is dependent on using an appropriate FEM mesh in the computational models. Quadratic brick elements have been shown to be able to predict pavement behavior well (Guo et al. 2007). Twenty node quadratic brick elements (C3D20) were used in ABAQUS. These elements are similar to elements used in pavement specific FEM, such as EverFE (Davids et al. 1998). This node configuration has been shown to be able to provide a high level of accuracy, along with an acceptable computational time demand (Kuo 1994).

The mesh size was selected based on the results of a mesh convergence study. Both depths of joint activation were examined with different mesh fineness. Two structures were examined for both the 6-ft panel size and 12-ft panel size models. Table 4-1 presents the different structures examined in the convergence study. Mesh convergence was achieved using 3 in by 3 in by half of the layer thickness for the loaded slab, and 6 in by 6 in by the layer thickness for the remainder of the models. Because second-order elements are used, one element along the thickness for each layer is sufficient for modeling flexure (Kuo 1994).

Table 4-1 Mesh convergence study parameters.

Joint depth	Panel size, L x W ft	PCC thickness, in	Asphalt thickness, in	Modulus of subgrade reaction, psi/in
PCC only	6 x 6	3	7	100
PCC only	6 x 6	3	7	315
PCC only	6 x 6	5	7	100
PCC only	6 x 6	5	7	315
PCC only	12 x 12	3	7	100
PCC only	12 x 12	3	7	315
Full-depth	12 x 12	6	7	100
Full-depth	12 x 12	6	7	315

4.4 Model Validation

It is essential that the computational model accurately predicts the pavement response. To validate the FEM model, five test sections from two testing facilities were used. Three BCOA sections from MnROAD, Cells 60, 96, and 97, and two sections from the University of California Pavement Research Center (UCPRC) Heavy vehicle simulator (HVS) test sections, Sections B and F, were used. The parameters used for the validation sections can be seen in Table 4-2. The parameters for the MnROAD sections were obtained from construction reports and research summary publications (Vandenbossche et al. 2016, Burnham 2006, Vandenbossche and Fagerness 2002, Barman et al. 2011, Mu and Vandenbossche 2011, Li et al. 2017). The asphalt stiffness at the time of the FWD testing was established using a mastercurve derived using laboratory data and temperatures measured from thermocouples embedded at mid-depth in the asphalt layer. FWD testing at mid-slab was used to backcalculate the k-value of the subgrade. The parameters corresponded well with previous research conducted on the BCOA sections at MnROAD (Burnham 2006, Vandenbossche and Fagerness 2002, Barman et al. 2011, Mu and Vandenbossche 2011, Li et al. 2017). The asphalt stiffness for the UCPRC sections was estimated using FWD and laboratory test data to develop mastercurves at a frequency of 20 Hz, based on the loading rate of the HVS.

Table 4-2 Pavement parameters for validation sections.

Parameter	Cell 60	Cell 96	Cell 97	Section B	Section F[1]
PCC thickness, in	5	6	6	4.5	4.5
Asphalt thickness, in	7	7	7	4.5	1 (RHMA) 3.5 (HMA)
PCC modulus of elasticity, 10^6 psi	4.6	4.7	4.7	7.54	7.54
Modulus of subgrade reaction, k-value psi/in	315	315	315	720	720
Asphalt modulus of elasticity, 10^6 psi	0.35	0.90	0.35	0.475	0.95 (RHMA) 0.55 (HMA)
Asphalt testing temperature, ^{o}F	90	68	90	95	85
Asphalt testing load frequency, Hz	25	25	25	20	20
Panel size, L x W ft	5 x 6	5 x 6	10 x 12	6 x 6	6 x 6

[1]Section F consisted of a 1-in newly placed rubberized hot-mixed asphalt (RHMA) layer on top of an older 3.5-in HMA layer.

Figure 4-6 presents the deflections measured with the FWD and predicted from the computational model as a 9-kip load is applied in the outer wheelpath adjacent to the transverse joint. Section B at UCPRC was tested using a 13.5-kip FWD load. The temperatures at the time of loading was considered in the analysis with respect to the asphalt stiffness and temperature gradients within the PCC overlay. For Cell 60, the asphalt layer was expected to not be continuous through the joint. For Cell 96, the asphalt layer was expected to be continuous underneath the joint in the overlay. For Cell 97, both depths of joint activation are expected. Early in the service life, the asphalt layer is likely still continuous and later in the service life the asphalt layer was not. The presumed depth of joint activation for the MnROAD cells were based on measured deflections from FWD testing. For Sections B and F, the asphalt is likely continuous during the time of testing based on measured deflections and visual inspection.

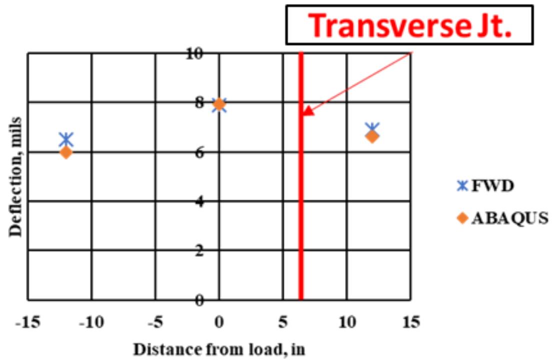

a) Cell 60: Not-continuous asphalt (9-kip load)

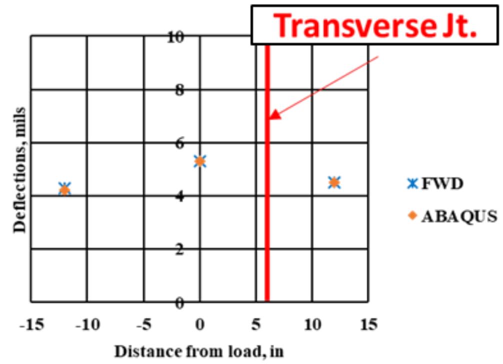

b) Cell 96: Continuous asphalt (9-kip load)

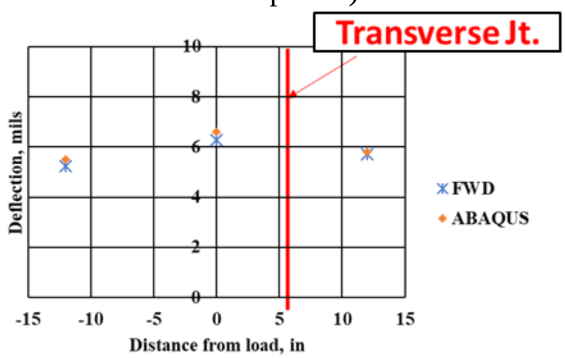

c) Cell 97: Continuous asphalt (9-kip load)

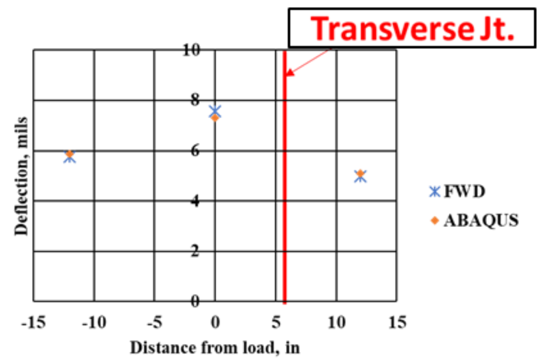

d) Cell 97: Not-continuous asphalt (9-kip load)

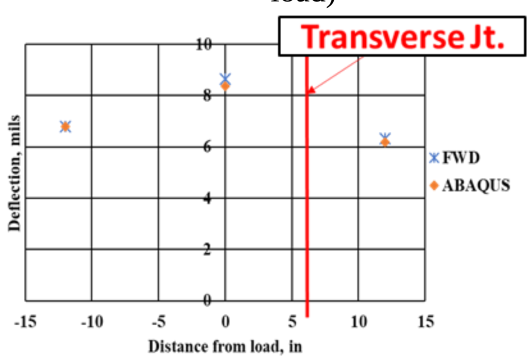

e) Section B: Continuous asphalt (13.5-kip load)

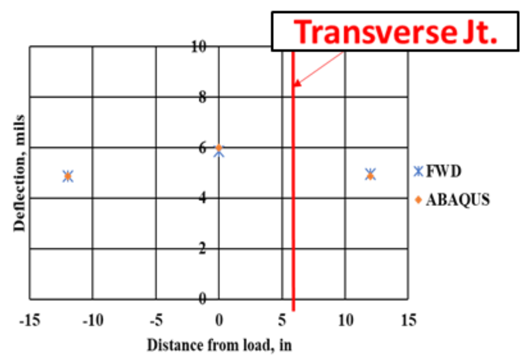

f) Section F: Continuous asphalt (9-kip load)

Figure 4-6 Model validation.

From these plots, it is evident that the computational models can accurately predict the response of the in-service BCOA structures to applied loads.

4.5 Artificial Neural Network Response Prediction Models

Performing a computational analysis of all combinations of loading configurations and environmental conditions throughout the analysis periods for faulting is computationally prohibitive. Therefore, the use of ANNs is beneficial to produce responses rapidly, similar to the methodology employed in Pavement ME and the linear regression stress prediction models in the BCOA-ME (ARA 2004, Vandenbossche et al. 2016, Li and Vandenbossche 2013, Li et al. 2013).

4.5.1 Critical Response Parameters

The critical responses from the structural model are to be used to calculate the differential energy of subgrade deformation, shown in Equation (4-2). The critical response to be obtained from the computational model is the deflection basin on the approach and leave slab after the environmental loading step and the traffic loading step. The deflection basin is defined as 2 ft long by 6 ft wide on both sides of the transverse joint, adjacent to the lane/shoulder joint. The volume of the deflection basin is calculated as the sum of the nodal deflections in the basin multiplied by the tributary area corresponding to the nodes. The same number of nodal deflections are used for the approach and leave slab basins. The deflection basin can be seen in Figure 4-7. When the joint depth is through the PCC only, the response is recorded at the bottom of the PCC layer. When the joint is full-depth, the response is recorded at the bottom of the asphalt layer. In Pavement ME, the critical responses to determine differential energy for concrete pavement design are the deflections at the corners on both the loaded (approach slab) and unloaded (leave slab) sides of the joint (ARA 2004). In this study, corner deflections, full lane width deflection basins, triangular deflection basins and 2 ft by 6 ft deflection basins were all considered. The deflection basin was used instead of deflections at the corner, because the maximum deflection is not always at the corner of the slab for BCOAs. This is especially true when the wheelpath occurs at mid-slab. Selection of the 2 ft by 6 ft basin allowed for consideration of the basin in the area most heavily influenced by the load. The selection of this basin area also provided an improved accuracy between predicted and measured performance during the calibration process.

$$DE = \frac{1}{2}k(B_L^2 - B_{UL}^2) \tag{4-2}$$

Where:

> DE is the differential energy of subgrade deformation (lb-in),
>
> k is the modulus of subgrade interaction (psi/in),
>
> B_L is the deflection basin on the loaded slab (in^2), and
>
> B_{UL} is the deflection basin on the unloaded slab (in^2).

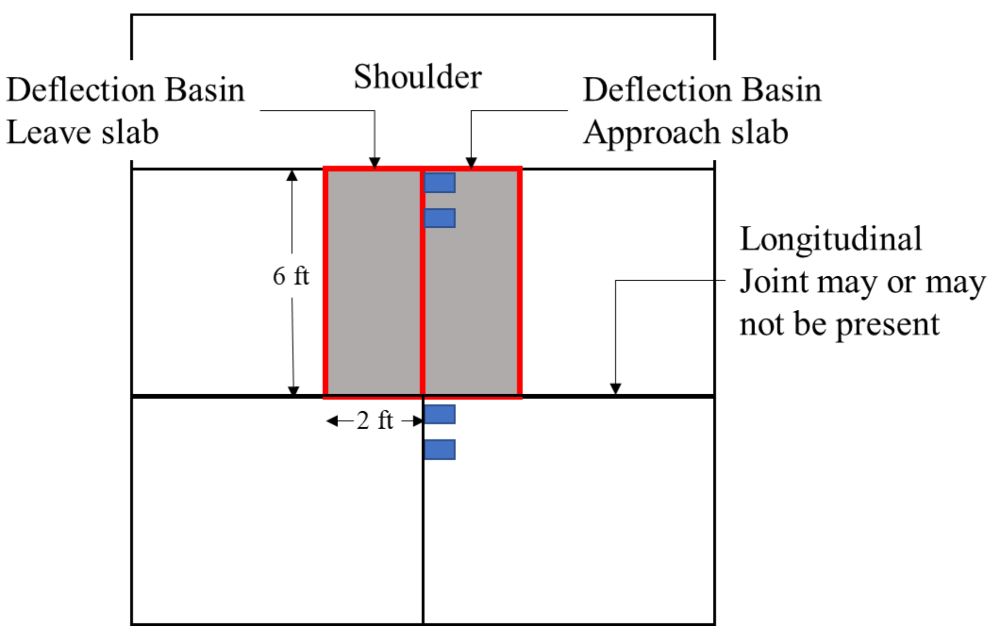

Figure 4-7 Deflection basin definition.

An accurate predictive model requires the computational model be analyzed over an inference space with 10 parameters. A database to be used in developing the ANNs is populated by using the computational models to evaluate these 10 parameters for a large range of values. All parameters considered, along with their corresponding values, can be seen in Table 4-3. A full factorial would result in a total of approximately 105,000 FEM analyses. In order to account for the different joint depths, there are 18 possible combinations examining joint depth, PCC thickness, and asphalt thickness. However, only 12 of these combinations are feasible based on the FSR established by DeSantis et al. (2016). Three structures are analyzed with a joint that activated through the PCC, three structures are analyzed with a full-depth joint, and three structures are analyzed considering both joint activation depths separately, resulting in 12 combinations. This reduces the total number of analyses to 23,328 per joint spacing for the partial lane width panels and 11,664 for the large panels because only full-depth joint activation is considered for the large panels. To further reduce the number of analyses required, a fractional factorial is used (Montgomery 2013). Additional analyses were not performed to account for the three level of asphalt stiffness. Instead, each level of asphalt stiffness (low, medium, or high) is assigned to one third of the analyses in a full factorial of the other parameters. This reduces the required number of analyses by two thirds. The total amount of FEM analyses conducted in ABAQUS is 19,440 (7,776 analyses for each of the partial lane width panels, and 3,888 analyses for the full lane width panels) using the fractional factorial design.

Table 4-3 Overall design matrix.

Joint activation depth	PCC only	PCC & Asphalt (0% LTE through Asphalt)	
PCC thickness (in)	3.5	5.5	8
PCC modulus of elasticity (psi)	4.0E+06		
PCC Poisson's ratio	0.18		
PCC CTE (in/in/^{o}F)	5.5E-06		
PCC joint spacing (ft)	6	8	12
PCC temp. difference (^{o}F)	-12	0	24
Asphalt thickness (in)	3.5	5.5	7.5
Asphalt modulus of elasticity (psi)	1.0E+05	8.0E+05	3.0E+06
Asphalt Poisson's ratio	0.35		
Modulus of subgrade reaction, k-value (psi/in)	100	250	400
Shoulder width (ft)	6		
Lane shoulder LTE (%)	0 (Asphalt)	90 (Tied PCC)	
Transverse joint LTE (%)	50	70	95
Wheel wander (in)	0	6	18
Single axle (kip)	18	30	
Tandem axle (kip)	36	60	

4.5.2 Development of Artificial Neural Networks

The ANNs are developed to predict the deflection basins for both the loaded and unloaded side of the joint. To train and test the ANNs using the factorial of analyses, the neural network toolbox in MATLAB® was used (MATLAB 2013). A total of 15 ANNs were trained, 10 ANNs for the medium size panels, and 5 for the large size panels. These networks are separated into loaded or unloaded slab, axle type, joint activation depth, and temperature. Due to symmetry of the temperature loading condition, only one ANN is developed for both the loaded and unloaded sides of the joint (Sachs 2017). Each of the ANNs with each of their predictors are shown in Equations (4-3) through (4-5).

$$NN_{\Sigma B,A,JD}(JTSpace, l_{eff}, q_i^*, k, \frac{AGG}{k * l_{eff}}, LTE_{shoulder}, s, \Phi) \tag{4-3}$$

$$NN_{\Sigma C,A,JD}(JTSpace, l_{eff}, q_i^*, k, \frac{AGG}{k * l_{eff}}, LTE_{shoulder}, s, \Phi) \tag{4-4}$$

$$NN_{\Sigma T,JD}(JTSpace, l_{eff}, q_i^*, k, \frac{AGG}{k * l_{eff}}, LTE_{shoulder}, s, \Phi) \tag{4-5}$$

Where:

$NN_{\Sigma B,A,JD}$ is the neural network for the difference between the squared sum of the 2-ft by 6-ft deflection basin for the loaded slab and the squared sum of the 2-ft by 6-ft deflection basin for the unloaded slab for axle type A (1 for single and 2 for tandem) and joint activation depth JD (0 for PCC only and 1 for full-depth) (in^4).

$NN_{\Sigma C,A,JD}$ is the neural network for the difference between the corner deflection on the loaded slab and the unloaded slab for axle type A (1 for single and 2 for tandem) and joint activation depth JD (0 for PCC only and 1 for full-depth) (in).

$NN_{\Sigma T,JD}$ is the neural network for the corner deflection for the condition when only temperature is present for joint activation depth JD (0 for PCC only and 1 for full-depth) (in).

$JTSpace$ is the joint spacing of the overlay (in).

l_{eff} is the effective radius of relative stiffness of the overlay (in) using bonded plate theory and can be seen in Equation (4-6).

$$l_{eff} = \sqrt[4]{\frac{\text{Plate Stiffness}}{(1 - \mu_{PCC}{}^2)k}} \tag{4-6}$$

Where:

Plate Stiffness is determined using bonded plate theory (psi*in^3) (Khazanovich 1994*)*,

μ_{PCC} is the Poisson's ratio of the PCC, and

k is the modulus of subgrade reaction (psi/in).

q_i^* is the adjusted load/pavement weight ratio and can be seen in Equation (4-7).

$$q_i^* = \frac{P_i}{A * \gamma_{eff} * h_{eff}} \tag{4-7}$$

Where:

P_i is the axle load (lbs.),

A is the parameter for axle type (1 for single and 2 for tandem axles),

γ_{eff} is the effective unit weight (pci), and

h_{eff} is the effective height (in).

$\frac{AGG}{k * l_{eff}}$ is the non-dimensional joint stiffness and can be seen in Equation (4-8).

$$\frac{AGG}{k * l_{eff}} \tag{4-8}$$

Where:

AGG is the joint stiffness representing aggregate interlock and presence of dowels (psi),

k is the modulus of subgrade reaction (psi/in), and

l_{eff} is the effective radius of relative stiffness of the overlay (in).

$LTE_{shoulder}$ is the lane/shoulder LTE (%),

s is wheel wander offset from the lane/shoulder joint (in), and

Φ is Korenev's non-dimensional temperature gradient, which is shown in Equation (4-9).

$$\Phi = \frac{2\alpha_{pcc}(1 + \mu_{pcc})l_{eff}^2}{h_{eff}^2}\frac{k}{\gamma_{eff}} * \Delta T \quad \textbf{(4-9)}$$

Where:

α_{pcc} is the coefficient of thermal expansion for the PCC overlay (in/in/^{o}F) and

ΔT is the temperature difference in the overlay (^{o}F).

The training of ANNs can have a relatively high variability due to the possibility of local minima in the objective function (Ripley 1996). To reduce this variability, 10 ANNs are trained for each predictive model with different semi-random starting conditions. The model prediction is obtained by taking a robust average of the 10 ANNs and discarding the two highest and two lowest estimates. Each ANN was trained using 2 hidden layers of 20 neurons each, which was found to provide enough flexibility for an accurate prediction. Overfitting was prevented by using the Bayesian Regularization training algorithm which includes weight decay. This method was selected over early stopping algorithms, such as Levenberg-Marquardt optimization, since computational time for training was not a concern. To evaluate model performance, 85% of the data was used in the training set and the remaining 15% in the testing set. The performance of the predictive models for each of the test sets can be seen in Table 4-4.

Table 4-4 Predictability of ANNs.

ANNs	Slab Size	ANN	Axle (A)	Joint activation depth (JD)	R^2
$NN_{\Sigma B,A,JD}$	Medium	Basin	Single	PCC only	0.99
$NN_{\Sigma B,A,JD}$	Medium	Basin	Tandem	PCC only	0.99
$NN_{\Sigma C,A,JD}$	Medium	Corner	Single	PCC only	0.99
$NN_{\Sigma C,A,JD}$	Medium	Corner	Tandem	PCC only	0.99
$NN_{\Sigma T,JD}$	Medium	Corner (Temp. only)	-	PCC only	0.99
$NN_{\Sigma B,A,JD}$	Medium	Basin	Single	Full-depth	0.99
$NN_{\Sigma B,A,JD}$	Medium	Basin	Tandem	Full-depth	0.99
$NN_{\Sigma C,A,JD}$	Medium	Corner	Single	Full-depth	0.99
$NN_{\Sigma C,A,JD}$	Medium	Corner	Tandem	Full-depth	0.99
$NN_{\Sigma T,JD}$	Medium	Corner (Temp. only)	-	Full-depth	0.99
$NN_{\Sigma B,A,JD}$	Large	Basin	Single	Full-depth	0.99
$NN_{\Sigma B,A,JD}$	Large	Basin	Tandem	Full-depth	0.99
$NN_{\Sigma C,A,JD}$	Large	Corner	Single	Full-depth	0.99
$NN_{\Sigma C,A,JD}$	Large	Corner	Tandem	Full-depth	0.99
$NN_{\Sigma T,JD}$	Large	Corner (Temp. only)	-	Full-depth	1.0

The performance of the ANNs was assessed using the test sets and the results are summarized in Figure 4-8 through Figure 4-16. Figure 4-8 shows the performance of the ANNs in predicting deflection basins for the medium sized slabs with the joint only activating through the PCC layer and loaded with single and tandem axles. Figure 4-9 shows the performance of the ANNs in predicting corner deflections of medium sized slabs when the joint only activates through the PCC layer and loaded with single and tandem axles. Figure 4-10 shows the performance of the ANNs in predicting corner deflections of medium sized slabs when the joint only activates through the PCC layer and a linear temperature gradient is present.

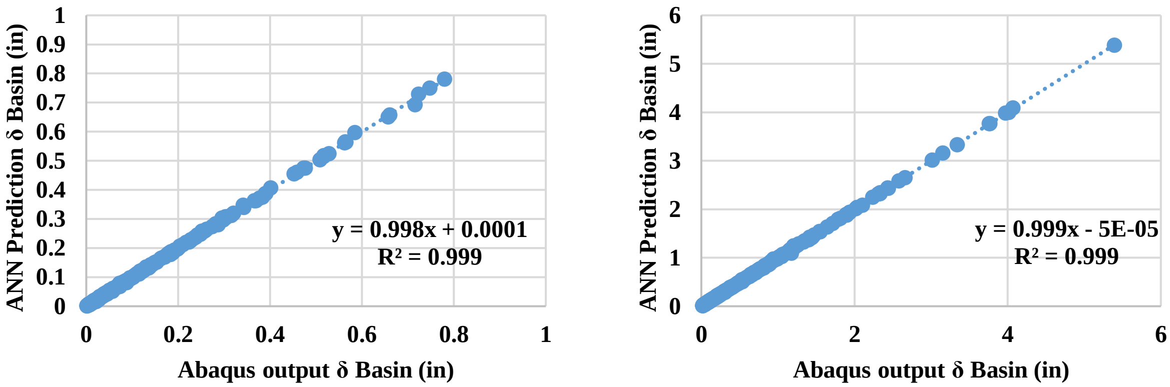

a) Single axle (A=1): PCC depth only

b) Tandem axle (A=2): PCC depth only

Figure 4-8 Basins for 8-slab model (joint activates only through PCC).

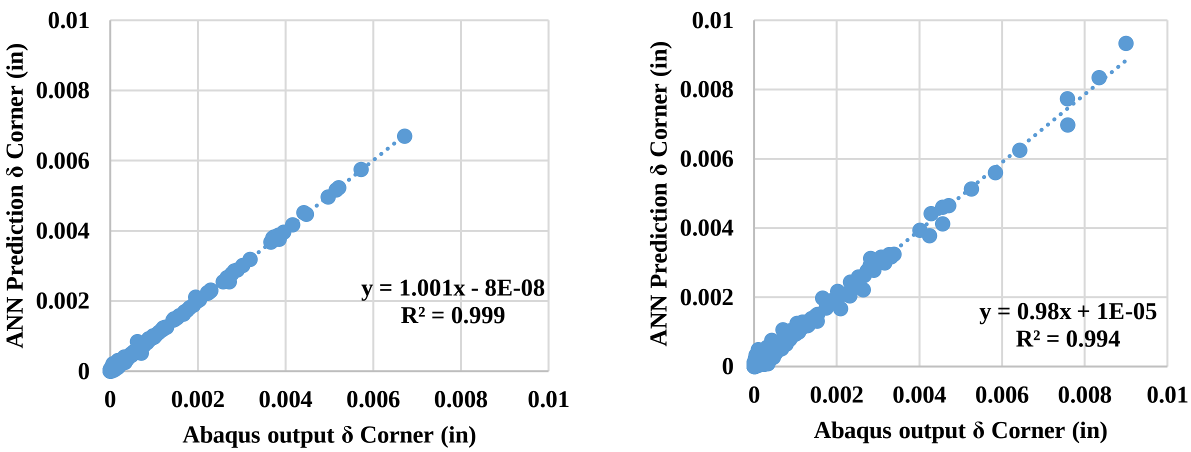

a) Single axle (A=1): PCC depth only

b) Tandem axle (A=2): PCC depth only

Figure 4-9 Corner deflections for 8-slab model (jont activates only through PCC).

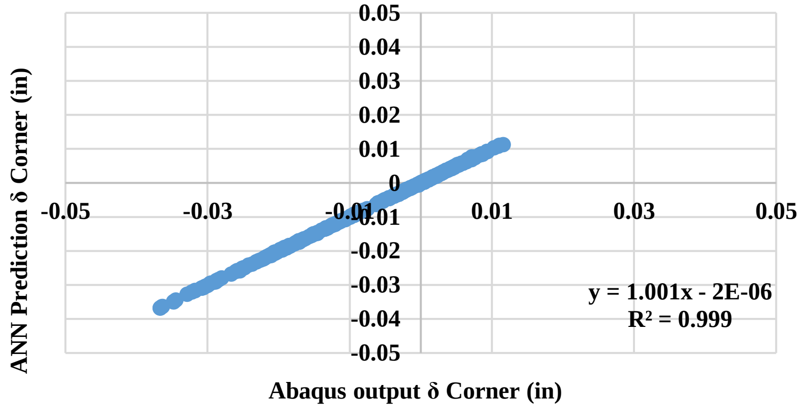

Figure 4-10 Corner deflections due to temperature for 8-slab model (joint activates only through PCC).

Figure 4-11 shows the performance of the ANNs in predicting deflection basins for the medium sized slabs with the joint activating through the PCC and asphalt layer and loaded with single and tandem axles. Figure 4-12 shows the performance of the ANNs in predicting corner deflections for the medium sized slabs with the joint activating through the PCC and asphalt layer and loaded with single and tandem axles. Figure 4-13 shows the performance of the ANN in predicting the corner deflection of medium sized slabs when the joint only activates through both the PCC and asphalt layer and a linear temperature gradient is present.

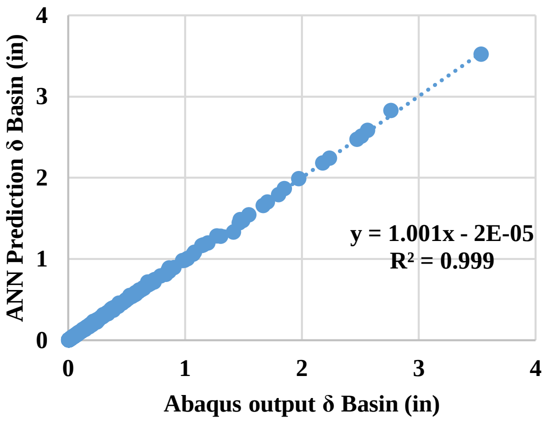

a) Single axle (A=1): Full-depth

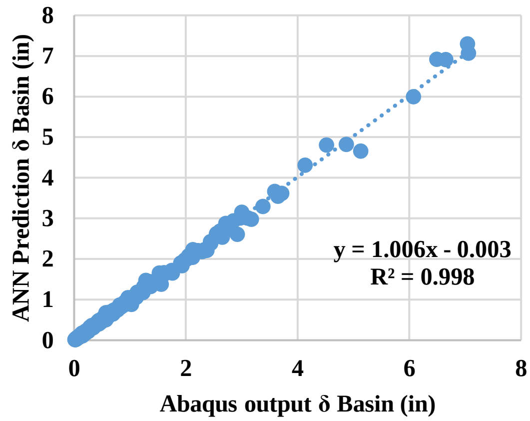

b) Tandem axle (A=2): Full-depth

Figure 4-11 Basins for 8-slab model (joint activation is full-depth).

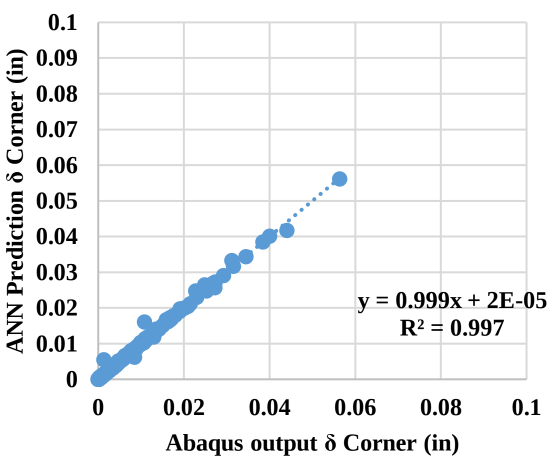

a) Single axle (A=1): Full-depth

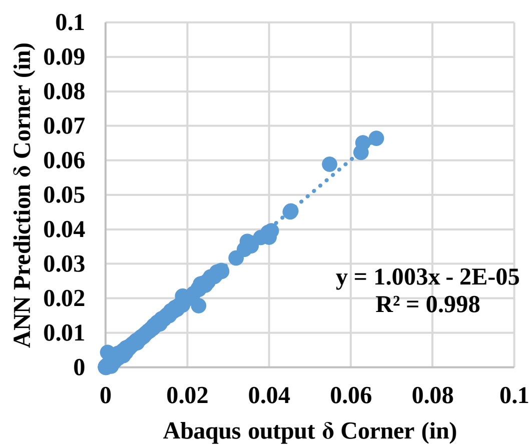

b) Tandem axle (A=2): Full-depth

Figure 4-12 Corner deflections for 8-slab model (joint activation is full-depth).

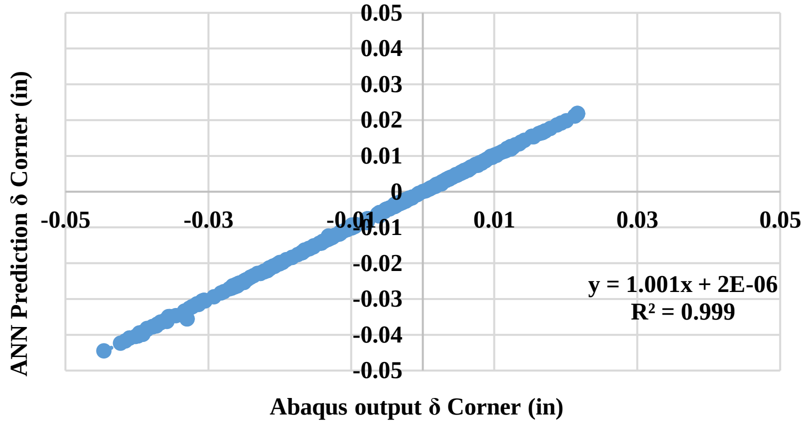

Figure 4-13 Corner deflections due to temperature for 8-slab model (joint activation is full-depth).

Figure 4-14 shows the performance of the ANNs in predicting deflection basins for the large slabs with the joint activating through the PCC and asphalt layer and loaded with single and tandem axles. Figure 4-15 shows the performance of the ANNs in predicting corner deflections for the large slabs with the joint activating through the PCC and asphalt layer and loaded with single and tandem axles. Figure 4-16 shows the performance of the ANN in predicting the corner deflection of large slabs when the joint only activates through both the PCC and asphalt layer and a linear temperature gradient is present.

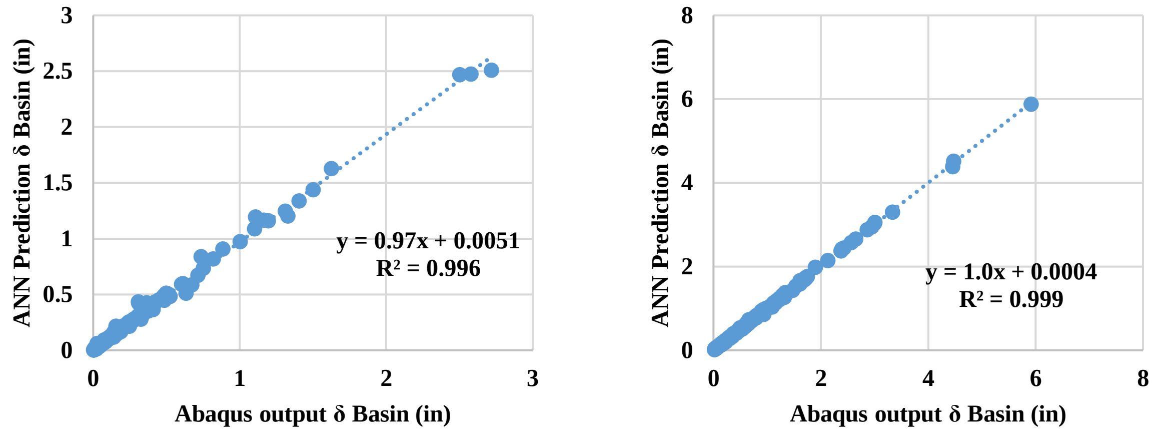

a) Single axle (A=1): Full-depth   b) Tandem axle (A=2): Full-depth

Figure 4-14 Basins for 4-slab model (joint activation is full-depth).

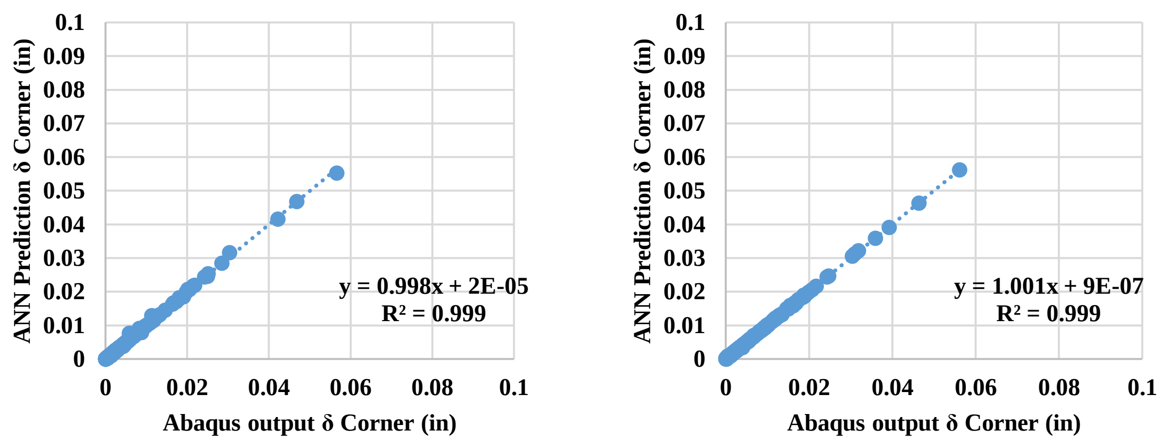

a) Single axle (A=1): Full-depth   b) Tandem axle (A=2): Full-depth

Figure 4-15 Corner deflections for 4-slab model (joint activation is full-depth).

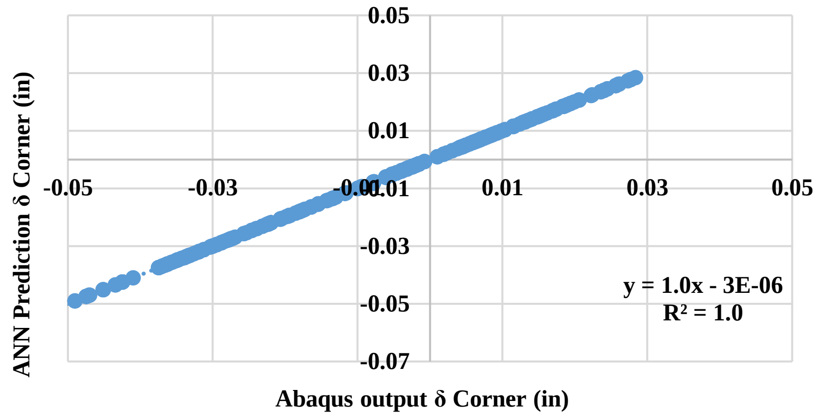

Figure 4-16 Corner deflections due to temperature for 4-slab model (joint activation is full-depth).

A small validation study was conducted to investigate the effects of wheel offset for two separate structures using the ANNs for predicting the response of the medium sized slabs. The joint spacing, PCC stiffness, asphalt stiffness, and k-value for both structures was 6 ft, 4E+06 psi, 8E+05 psi, and 100 psi/in, respectively. Both depths of joint activation were also considered. The comparisons can be seen in Figure 4-17.

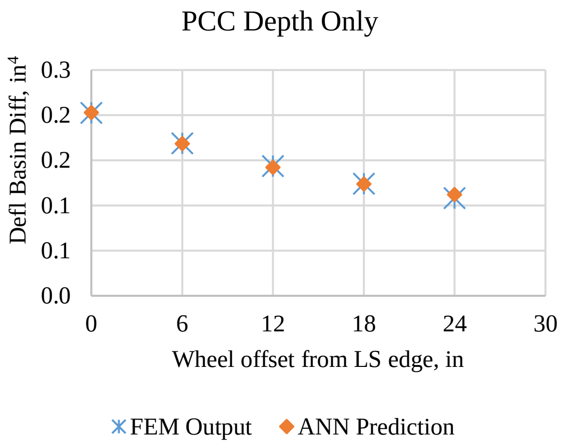

a) Single Axle: PCC = 3.5 in, Asphalt = 3.5 in

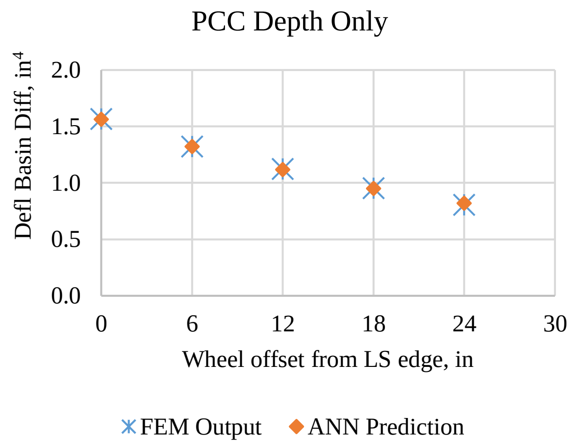

b) Tandem Axle: PCC = 3.5 in, Asphalt = 3.5 in

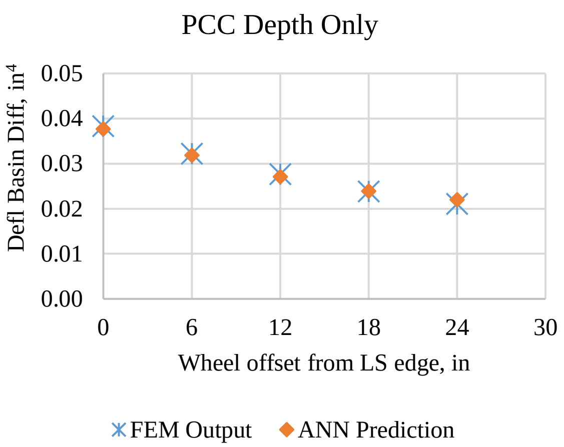

c) Single Axle: PCC = 8 in, Asphalt = 7.5 in

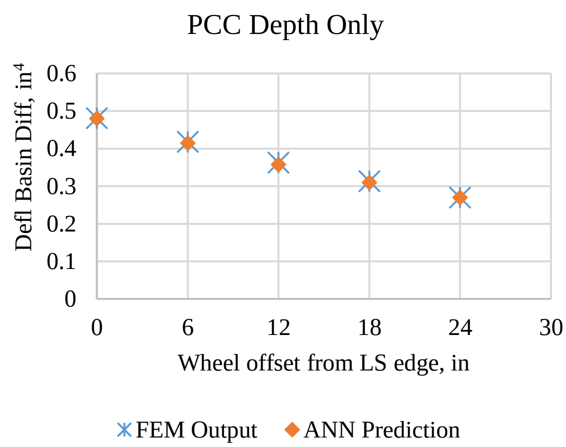

d) Tandem Axle: PCC = 8 in, Asphalt = 7.5 in

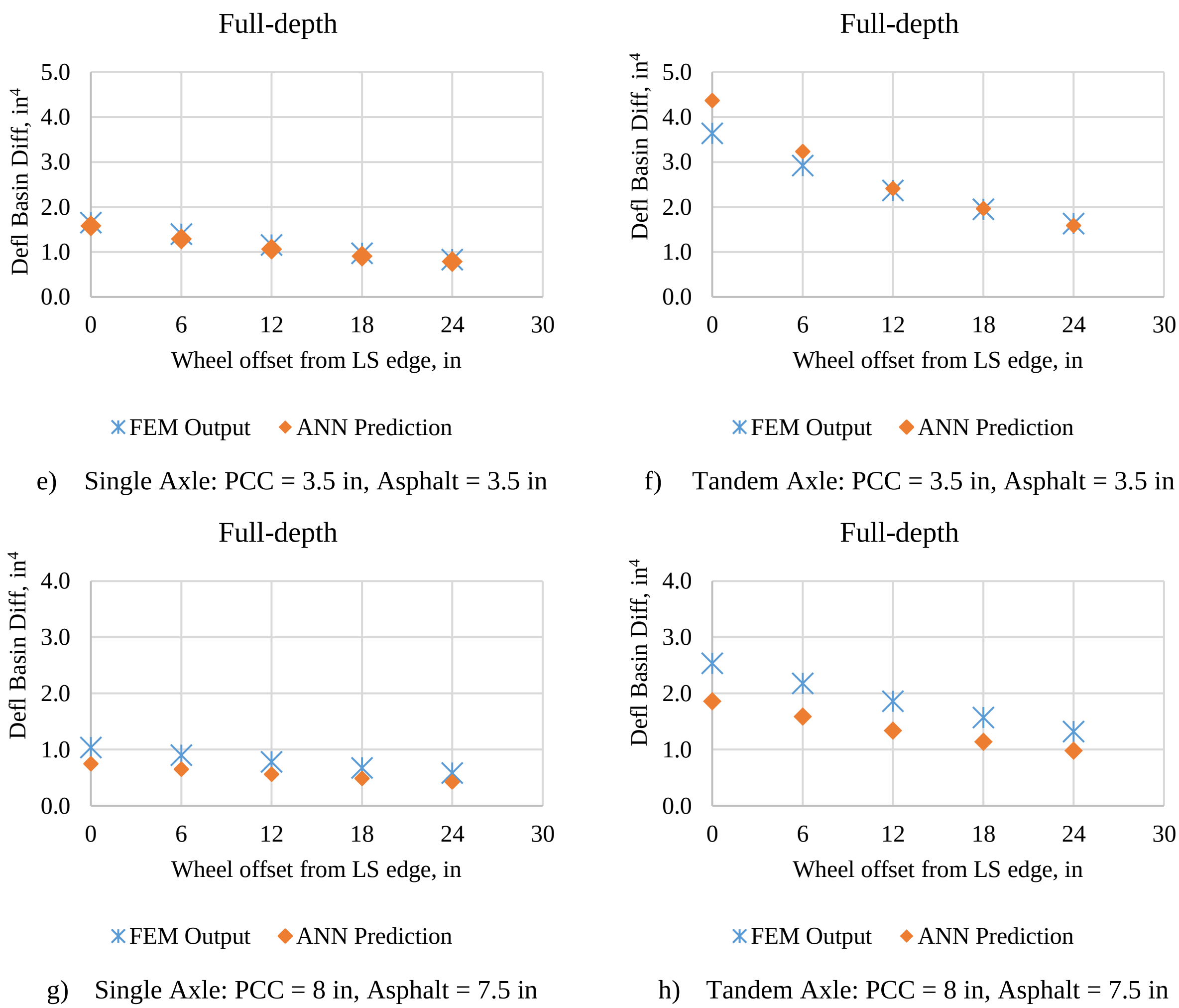

e) Single Axle: PCC = 3.5 in, Asphalt = 3.5 in

f) Tandem Axle: PCC = 3.5 in, Asphalt = 3.5 in

g) Single Axle: PCC = 8 in, Asphalt = 7.5 in

h) Tandem Axle: PCC = 8 in, Asphalt = 7.5 in

Figure 4-17 Validation of ANNs.

In addition to the validation analysis of the ANNs, a sensitivity analysis was also performed to ensure the range of parameters used in training the networks was sufficient. For the different joint spacings presented, different ANNs needed to be used based on the depth of joint activation. Therefore, when a 6x6 ft joint spacing is presented, and the joint only activates through the PCC layer it is denoted as 6x6 PCC only. When a 6x6 ft joint spacing has a joint activation depth that extends through both the PCC and asphalt layer, it is denoted as 6x6 Full-depth. The ANNs for full lane width slabs are used when the joint spacing is greater than or equal to 10 ft. The first comparison evaluates the effect of joint spacing when an 18-kip single axle load is applied. The range of parameters considered are presented in Table 4-5, and the results can be seen in Figure 4-18.

Table 4-5 ANNs sensitivity analysis parameters: single axle – layer thicknesses.

Parameter	
PCC thickness, in	Varies
Asphalt thickness, in	Varies
PCC modulus of elasticity, 10^6 psi	4.0
Modulus of subgrade reaction, k-value psi/in	250
Asphalt modulus of elasticity, 10^6 psi	0.80
Panel size, L x W ft	Varies
Shoulder type	Asphalt
Joint depth	Varies
Axle type	Single
Load, lbs	18,000
Wheel wander, in	6

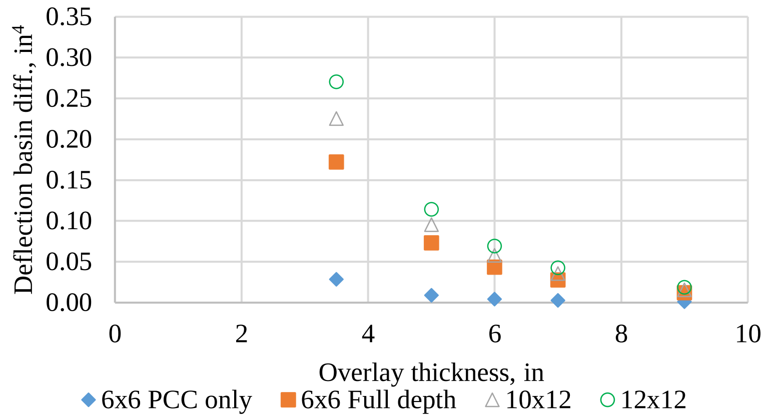

a) Asphalt = 3.5 in

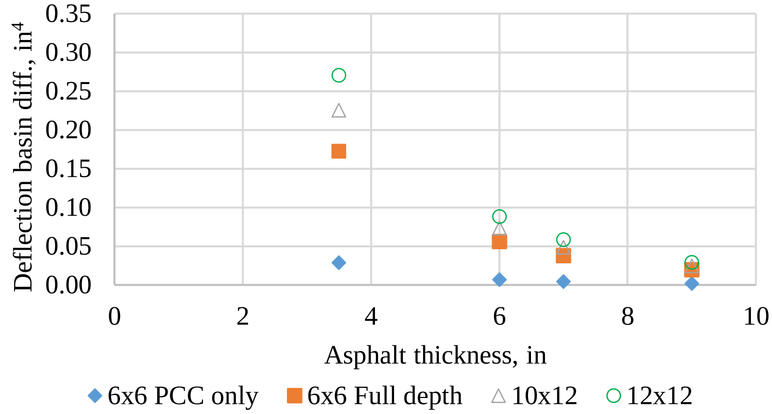

b) PCC = 3.5 in

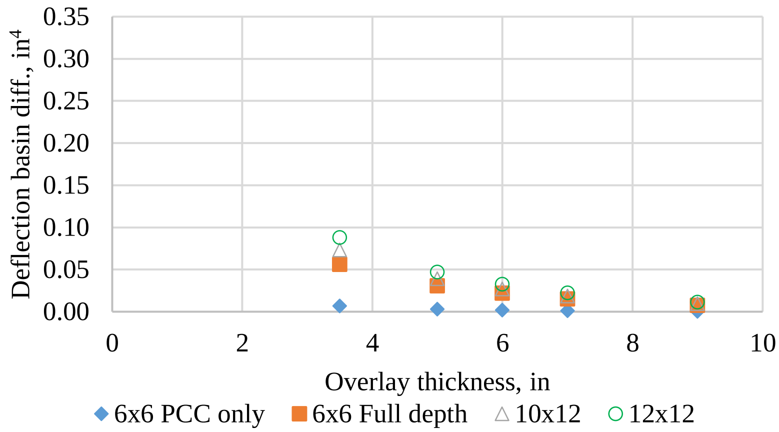

c) Asphalt = 6.0 in

Figure 4-18 ANNs sensitivity analysis: single axle – layer thicknesses.

The second comparison evaluates the effect of joint spacings for a 36-kip tandem axle load. The parameters evaluated can be seen in Table 4-6, and the results can be seen in Figure 4-19.

Table 4-6 ANNs sensitivity analysis parameters: tandem axle – layer thicknesses.

Parameter	
PCC thickness, in	Varies
Asphalt thickness, in	Varies
PCC modulus of elasticity, 10^6 psi	4.0
Modulus of subgrade reaction, k-value psi/in	250
Asphalt modulus of elasticity, 10^6 psi	0.80
Panel size, L x W ft	Varies
Shoulder type	Asphalt
Joint depth	Varies
Axle type	Tandem
Load, lbs	36,000
Wheel wander, in	6

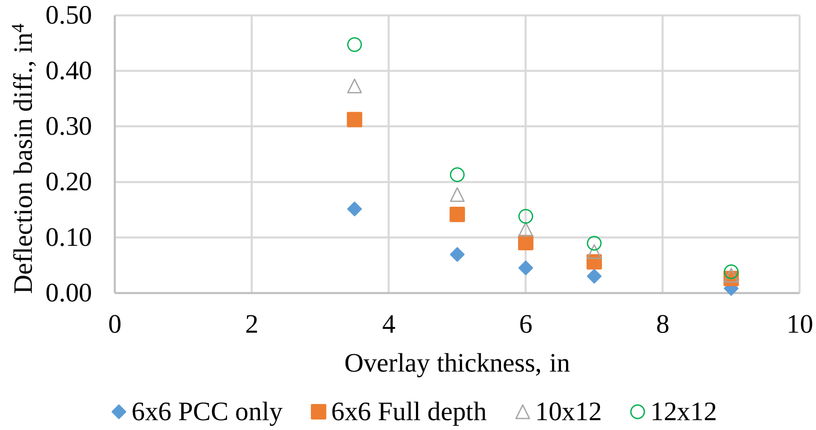

a) Asphalt = 3.5 in

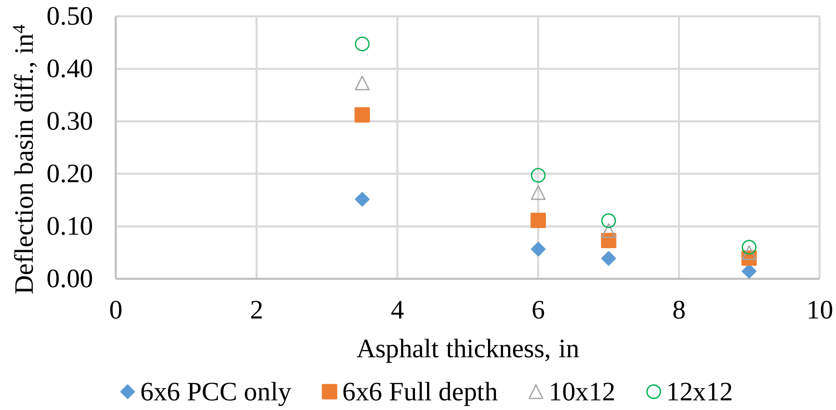

b) PCC = 3.5 in

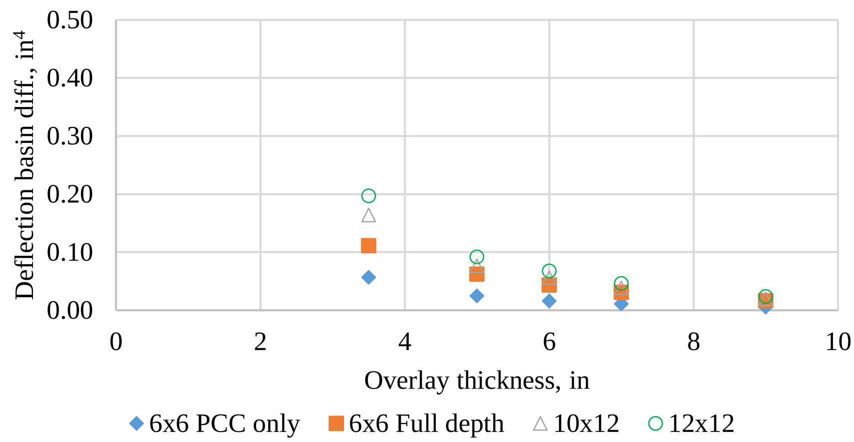

c) Asphalt = 6 in

Figure 4-19 ANNs sensitivity analysis: tandem axle – layer thicknesses.

The third comparison evaluates the effect of the modulus of subgrade reaction, k-value, for the different joint spacings when an 18-kip single axle load is applied. These parameters can be seen in Table 4-7, and the results can be seen in Figure 4-20.

Table 4-7 ANNs sensitivity analysis parameters: modulus of subgrade reaction.

Parameter	
PCC thickness, in	Varies
Asphalt thickness, in	4.0
PCC modulus of elasticity, 10^6 psi	4.0
Modulus of subgrade reaction, k-value psi/in	Varies
Asphalt modulus of elasticity, 10^6 psi	0.80
Panel size, L x W ft	Varies
Shoulder type	Asphalt
Joint depth	Varies
Axle type	Single
Load, lbs	18,000
Wheel wander, in	6

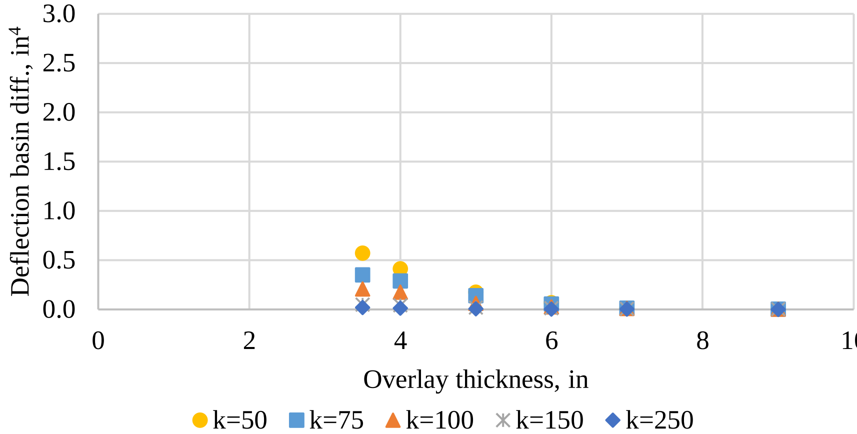

a) 6x6 ft PCC only: Asphalt = 4.0 in

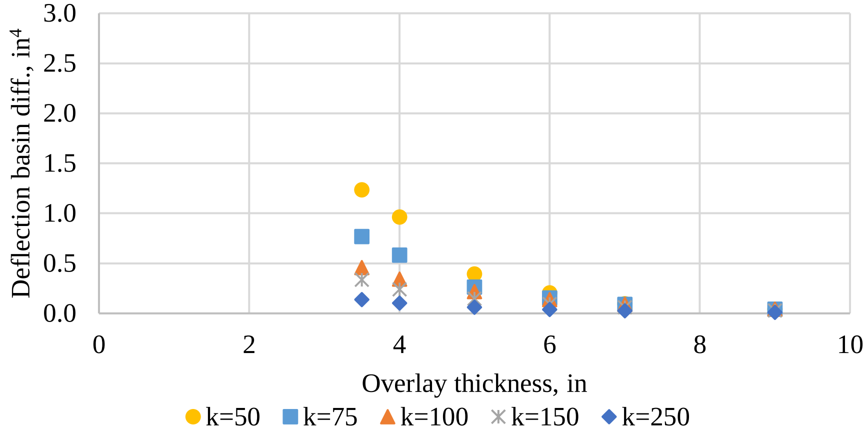

b) 6x6 ft Full-depth: Asphalt = 4.0 in

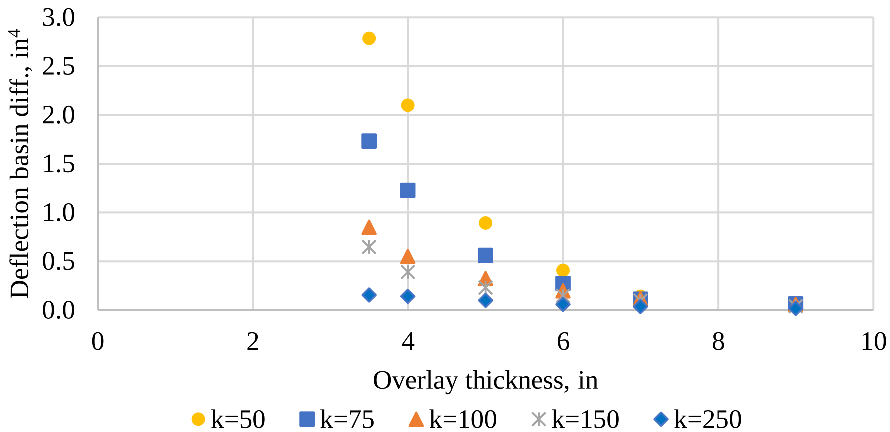

c) 12x12 ft Full-depth: Asphalt = 4.0 in

Figure 4-20 ANNs sensitivity analysis: modulus of subgrade reaction.

The fourth comparison evaluates the effect of joint spacing when dowels are present and an 18-kip single axle load is applied. These parameters can be seen in Table 4-8, and the results can be seen in Figure 4-21.

Table 4-8 ANNs sensitivity analysis parameters: presence of dowels.

Parameter	
PCC thickness, in	3.5 and 6.0
Asphalt thickness, in	3.5
PCC modulus of elasticity, 10^6 psi	4.0
Modulus of subgrade reaction, k-value psi/in	250
Asphalt modulus of elasticity, 10^6 psi	0.80
Panel size, L x W ft	Varies
Shoulder type	Asphalt
Joint depth	Varies
Axle type	Single
Load, lbs	18,000
Wheel wander, in	6

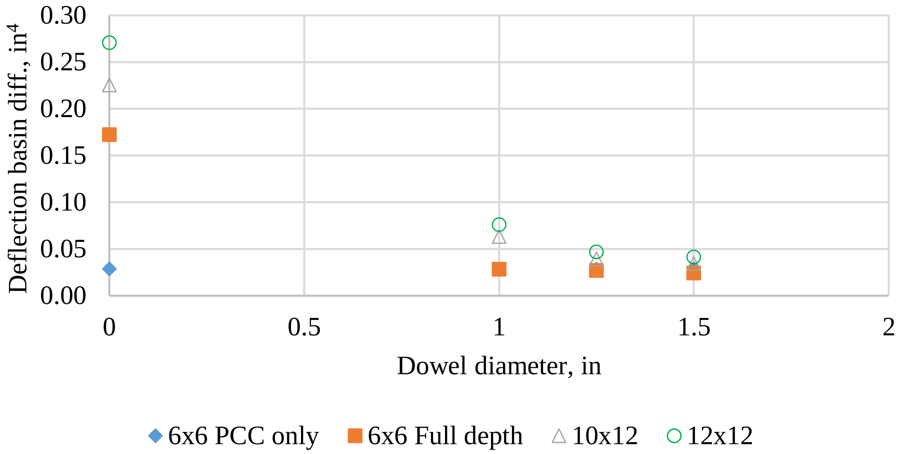

a) PCC = Asphalt = 3.5 in

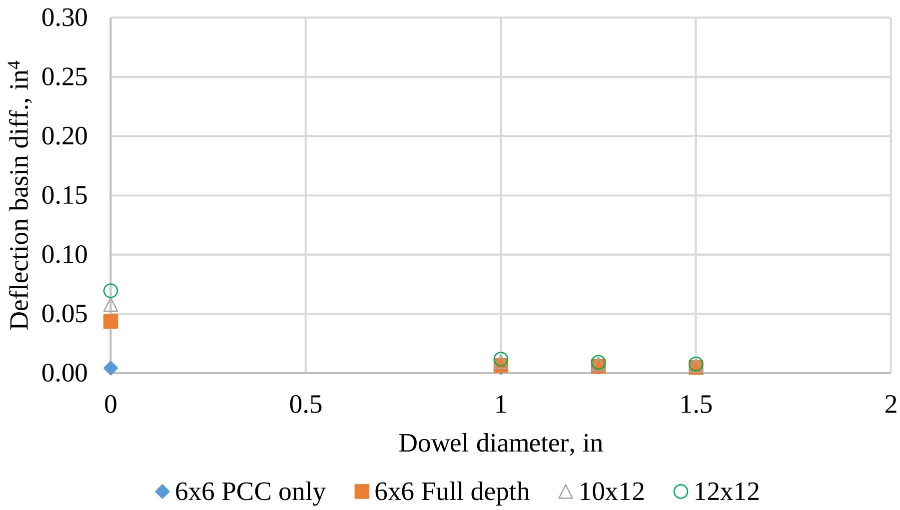

b) PCC = 6 in, Asphalt = 3.5 in

Figure 4-21 ANNs sensitivity analysis: presence of dowels.

The next set of comparisons evaluates the effects of temperature gradients. The first comparison evaluates the effect of the overlay thickness for different joint spacings when an 18-kip single axle load is applied. These parameters can be seen in Table 4-9, and the results can be seen in Figure 4-22.

Table 4-9 ANNs sensitivity analysis parameters: temperature difference – PCC thickness.

Parameter	
PCC thickness, in	Varies
Asphalt thickness, in	3.5
PCC modulus of elasticity, 10^6 psi	4.0
Modulus of subgrade reaction, k-value psi/in	250
Asphalt modulus of elasticity, 10^6 psi	0.80
Panel size, L x W ft	Varies
Shoulder type	Asphalt
Joint depth	Varies
Axle type	Single
Load, lbs	18,000
Wheel wander, in	6

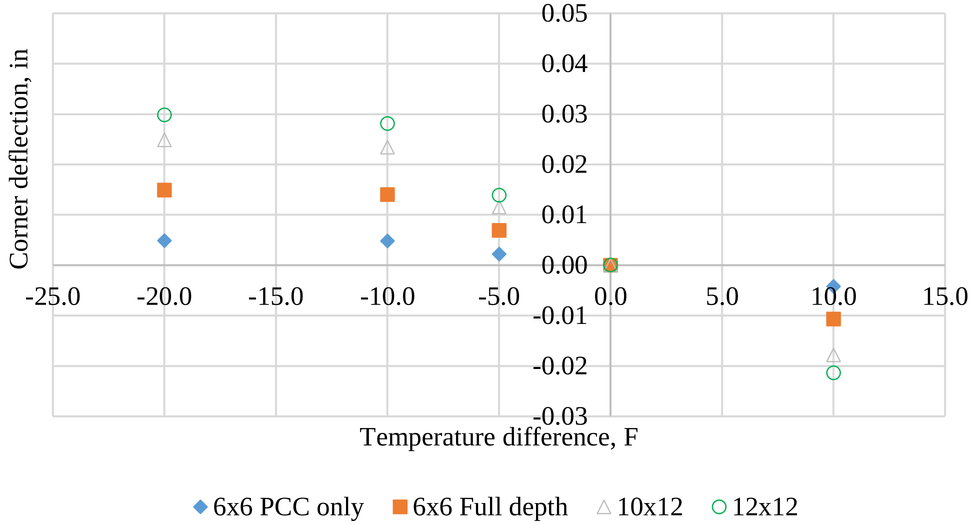

a) PCC=Asphalt=3.5 in (Note: y-axis different from other plots)

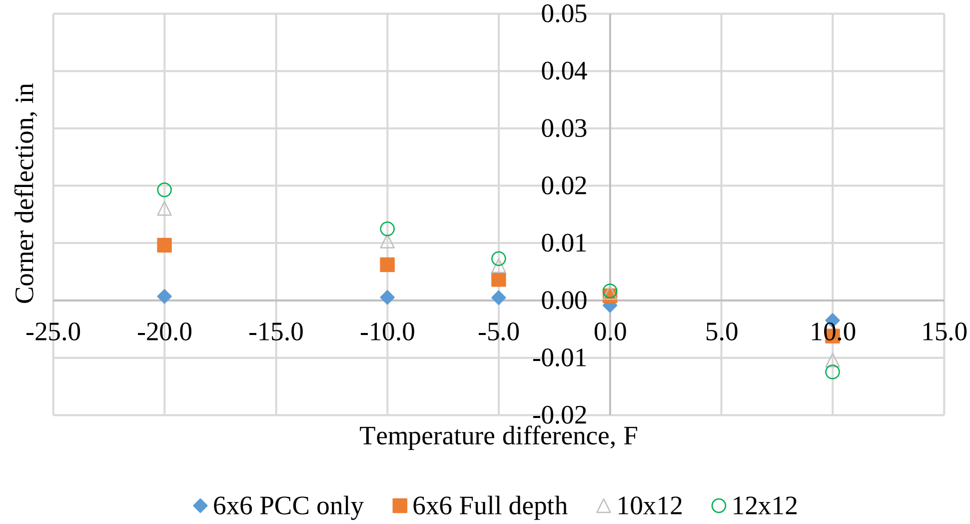

b) PCC=6 in Asphalt=3.5 in

Figure 4-22 ANNs sensitivity analysis: temperature difference – PCC thickness.

The second comparison evaluates the effects of asphalt thickness for different joint spacings when an 18-kip single axle load is applied. These parameters can be seen in Table 4-10, and the results can be seen in Figure 4-23.

Table 4-10 ANNs sensitivity analysis parameters: temperature difference – asphalt thickness.

Parameter	
PCC thickness, in	6.0
Asphalt thickness, in	Varies
PCC modulus of elasticity, 10^6 psi	4.0
Modulus of subgrade reaction, k-value psi/in	250
Asphalt modulus of elasticity, 10^6 psi	0.80
Panel size, L x W ft	Varies
Shoulder type	Asphalt
Joint depth	Varies
Axle type	Single
Load, lbs	18,000
Wheel wander, in	6

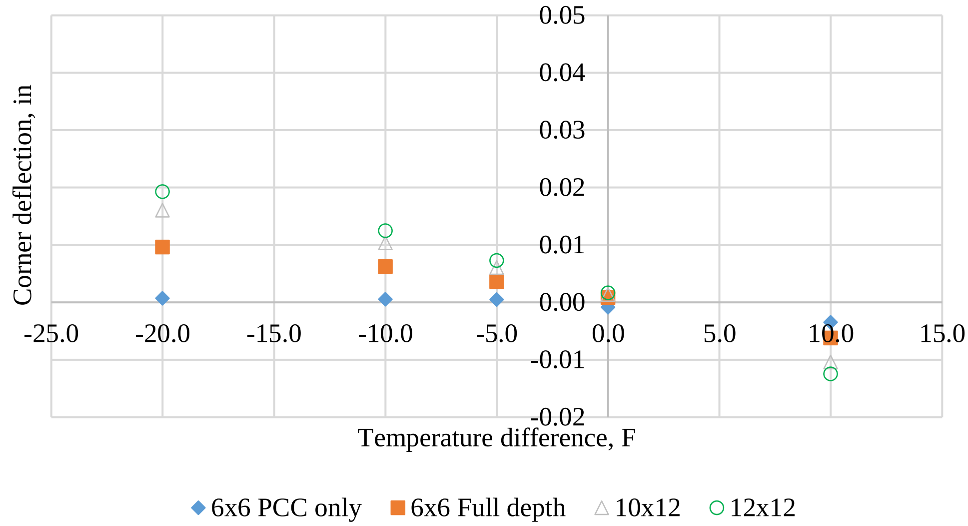

a) PCC=6 in Asphalt=3.5 in

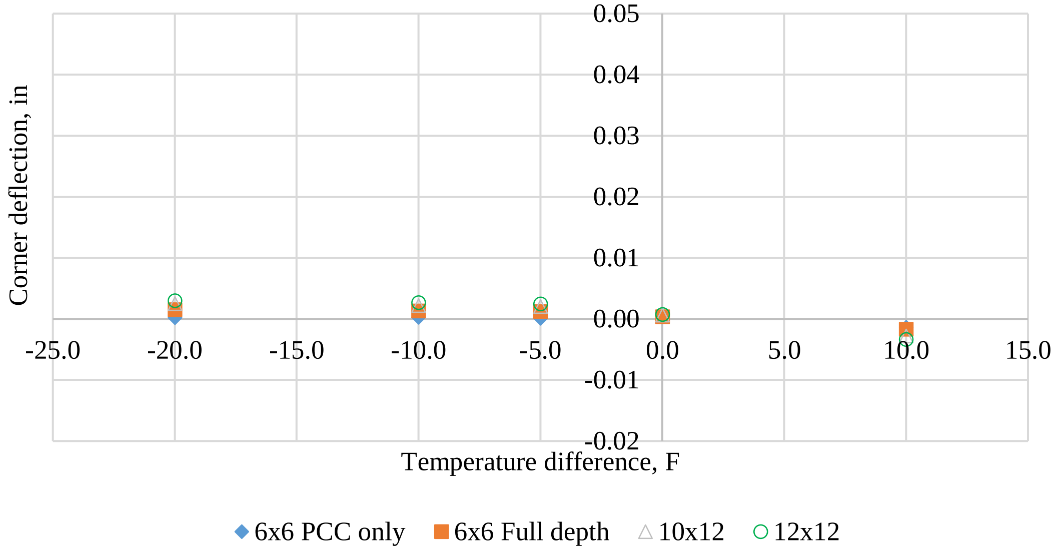

b) PCC=6 in Asphalt=7.0 in

Figure 4-23 ANNs sensitivity analysis: temperature difference – asphalt thickness.

The third and final comparison evaluates the effects of the modulus of subgrade reaction for a range of joint spacings when an 18-kip single axle load is applied. These parameters can be seen in Table 4-11, and the results can be seen in Figure 4-24.

Table 4-11 ANNs sensitivity analysis parameters: temperature difference – modulus of subgrade reaction.

Parameter	
PCC thickness, in	3.5
Asphalt thickness, in	3.5
PCC modulus of elasticity, 10^6 psi	4.0
Modulus of subgrade reaction, k-value psi/in	Varies
Asphalt modulus of elasticity, 10^6 psi	0.80
Panel size, L x W ft	Varies
Shoulder type	Asphalt
Joint depth	Varies
Axle type	Single
Load, lbs	18,000
Wheel wander, in	6

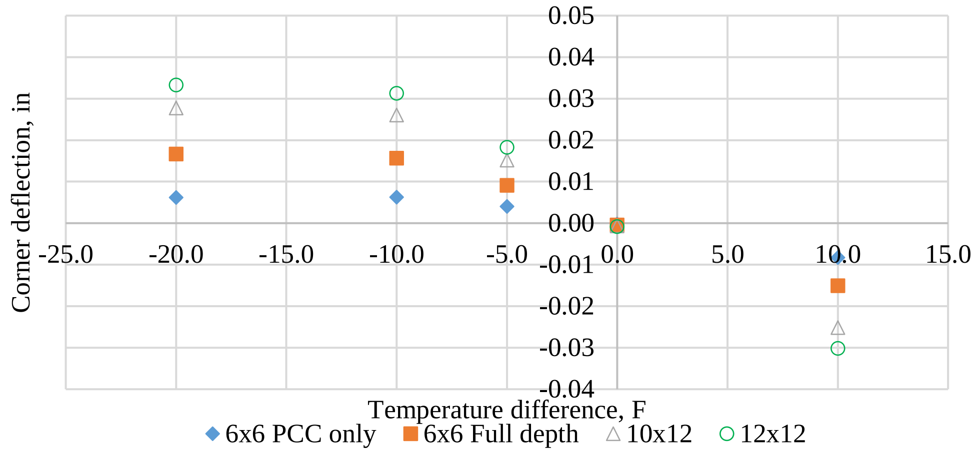

a) k-value = 50 psi/in

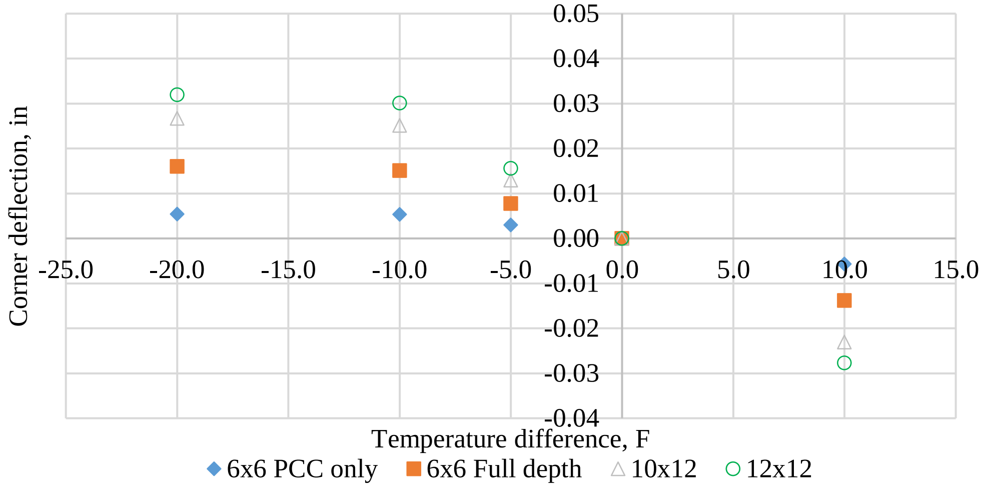

b) k-value = 150 psi/in

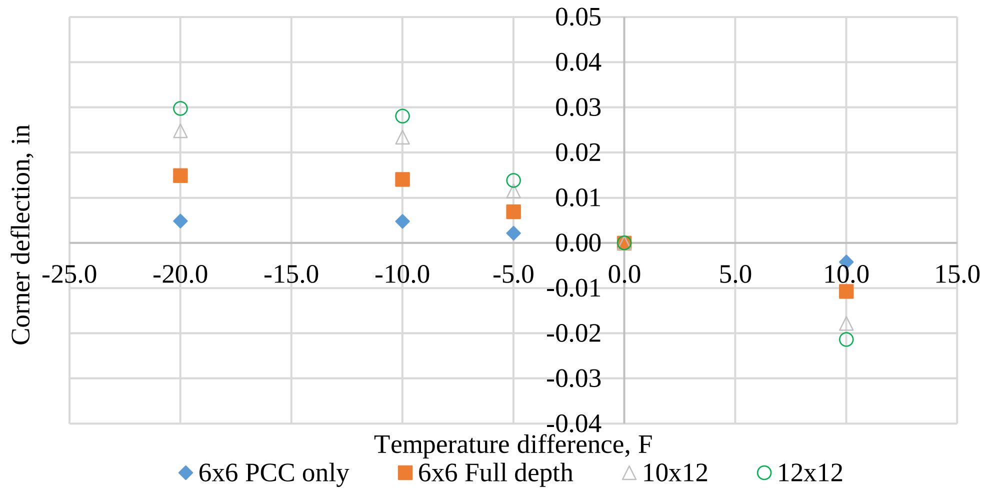

c) k-value = 250 psi/in

Figure 4-24 ANNs sensitivity analysis: temperature difference – modulus of subgrade reaction.

The sensitivity analysis revealed the trends are as expected. The validation and sensitivity analysis provide evidence the ANNs are able to accurately predict the response of the BCOAs. Therefore, the ANNs can now be used within the framework of the predictive faulting model presented in Chapter 5.

4.6 Summary

Models were developed for predicting the response of BCOA to environmental and traffic loading conditions. This eliminates the need to perform an FEM analysis for each loading condition and each different pavement structure when performing the incremental analysis incorporated within the design process. These BCOA response prediction models can now be incorporated into the framework for predicting the development of faulting in BCOA.

To accomplish this, first computational models were developed using a 3-D FEM software, ABAQUS, to accurately predict the behavior of BCOA. These models were validated with sections at MnROAD and the UCPRC testing facility. The computational model included two models. One accounts for a joint that only activates through the PCC and the other when the joint activates through both the PCC and asphalt layers. The critical response for each model is the deflection basin on the approach and leave slabs. When the joint only activates through the PCC, the deflection basin at the bottom of the PCC layer is used. When the joint activates full-depth, the deflection basin at the bottom of the asphalt layer is used. The deflection basins are to be used to more accurately represent the difference in energy density on both sides of the joint in lieu of corner deflections, as has been traditionally used.

Finally, a fractional factorial analysis was performed for a range of parameters, resulting in 19,440 FEM analyses that were used to populate a database for training the ANNs. These ANNs were developed to estimate the mechanistic response of BCOAs using a defined set of inputs. The use of ANNs allow predictions to be made very accurately and quickly. These estimates can be used in conjunction with performance data to produce a mechanistic empirical predictive faulting model for BCOA.

.

5.0 Joint Faulting Model Development

5.1 Introduction

This chapter details the development of the BCOA faulting model. The framework used is first presented. This framework incorporates an incremental analysis so the effects of hourly changes in temperature throughout the pavement structure on damage can be characterized. Detailed information on the climatic as well as the other model inputs is provided. Next, the calibration sections are presented with detailed section information provided in Appendix A. The calibration process is then described and the resulting calibration coefficients are presented. The calibrated model is validated by comparing measured and predicted faulting. A sensitivity analysis is then performed to further evaluate the predictive capabilities of the faulting model. Finally, the standard deviation model, which will be used to quantify reliability, is presented.

5.2 Faulting Model Framework

The framework for the faulting prediction model consists of using the ANNs developed in the previous chapter to determine the differential energy. Once the critical response is related to damage using differential energy, the next step is to relate damage to faulting. Within this framework, an iterative incremental analysis is performed to relate damage to faulting. This is then followed by a discussion on the functional form of the current faulting calculation. The overall framework is presented in Figure 5-1.

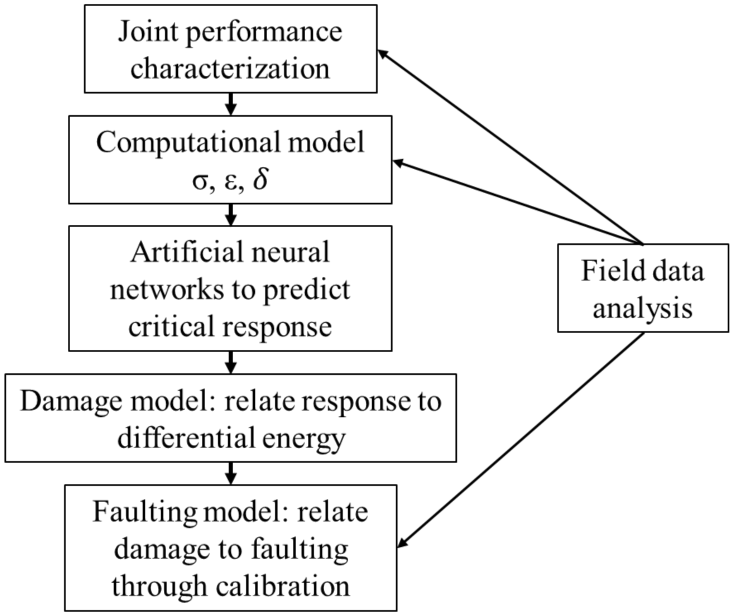

Figure 5-1 Faulting model framework.

Prior to performing the incremental analysis, initial parameters must be defined. These initial parameters include climatic considerations, traffic information, design features, and layer material properties. First, the treatment of climatic features is presented. Secondly, the traffic analysis is conducted using load spectra and is also presented in terms of ESALs for an easier assessment within the sensitivity analysis. This is then followed by the incremental analysis. The overall prediction framework can be seen in Figure 5-2.

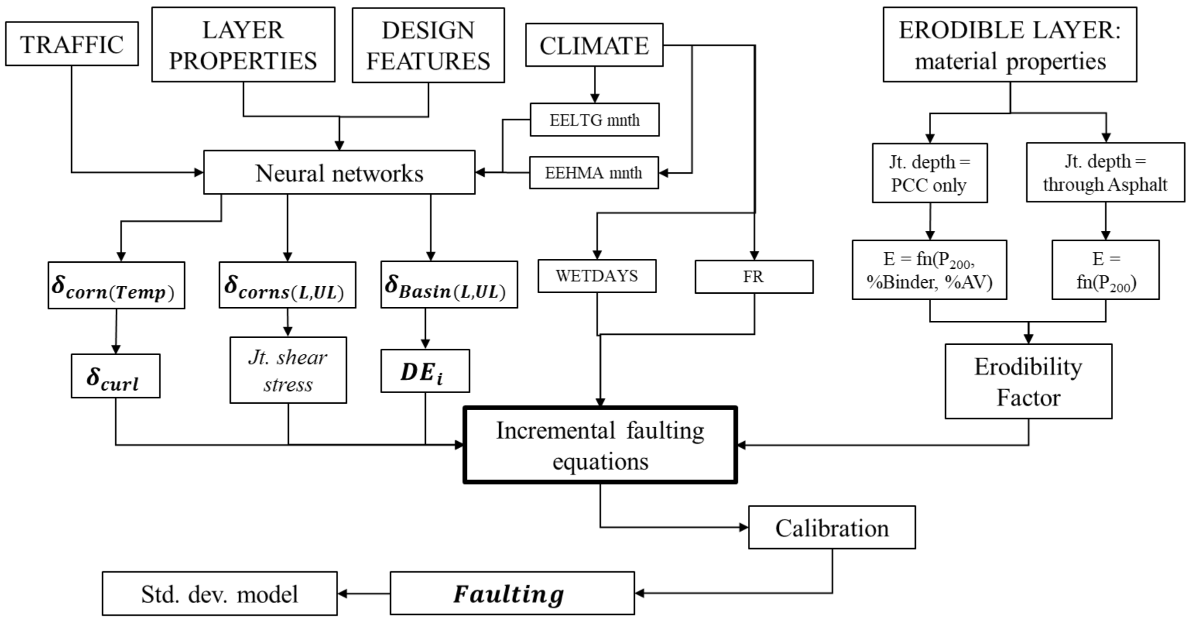

Figure 5-2 Predictive faulting model flowchart.

5.2.1 Climate

This section describes how the temperature throughout the depth of the BCOA is accounted for in the development of the faulting model. Within the current framework, a separate analysis for each structure must be carried out within the Enhanced Integrated Climatic Model (EICM) (Larson and Dempsey 2003). EICM performs an hourly incremental analysis that determines the temperature profile throughout the depth of the pavement structure at specified nodes. This is then used to help establish gradients for use in the design process. Therefore, for each calibration section, an EICM file is created. Within EICM, the structure must be defined including layer thicknesses, the number of nodes for each layer, thermal properties, and permeability, porosity, and water content to model moisture movement in granular layers. An example file containing the inputs for one of the calibration sections is included in Appendix A.

Within the overlay, nodes are placed at 1-in increments. Additionally, using the North American Regional Reanalysis (NARR) climatic database, the nearest weather station to each calibration site is chosen to give hourly values of air temperature, precipitation, wind speed, and percent sunshine for several years that can be output as an .icm profile. To ensure the weather was representative of the given calibration section locations, multiple weather stations were used with triangulation. The analysis is then performed so the hourly nodal temperature depths throughout the structure can be determined. EICM generates a .tem file that contains these nodal temperatures. This information is then used to determine the PCC overlay mean monthly nighttime mid-depth temperature ($T_{mid-depth}$), establish hourly ELTG based on equivalent strain, and to determine the freezing ratio (FR), which is the percentage of time that the top of the asphalt layer is less than 32^{o}F. The .icm file for each EICM analysis is used to establish mean monthly air temperature and the number of rain days (days with precipitation > 0.1 in) in the year (WETDAYS).

Temperature gradients can cause the PCC slab to curl, which influences the magnitude of the corner deflections. A positive temperature gradient is present when the temperature at the top of the PCC slab is warmer than the bottom of the slab. This causes the slab to curl downward, leaving the mid-slab partially supported and the edges fully supported. A negative temperature gradient is present when the temperature at the top of the PCC slab is cooler than the bottom of the slab. This causes the slab to curl upward, leaving the edges and corners of the slab partially supported, while the mid-slab is fully supported. When a slab is curled up, the deflections are expected to be larger than when a slab is curled down due to the support conditions. The larger deflections imply an increase in the potential for the development of faulting. Due to the magnitude of deflections and the support conditions, this analysis only considers when a negative temperature gradient is present. To simplify this, only traffic between 8 pm and 8 am is considered.

It is important to be able to account for the environmental loading effects in addition to the effects due to traffic loading.

The ELTGs are calculated using the temperature-moment concept (Janssen and Snyder 2000) that converts the non-linear temperature profile for a specific hour generated by the EICM into an ELTG based on Equation (5-1) through (5-3). This conversion was proposed by Janssen and Snyder (2000) to ensure that the resultant strains in the overlay resulting from the ELTG and the non-linear temperature gradient are the same. This results in the same deflection profile of the slab for the two conditions.

$$T_{ave} = \sum_{i=1}^{n} \left[\frac{0.5(t_i + t_{i+1})(d_i - d_{i+1})}{(d_1 - d_n)} \right] \tag{5-1}$$

$$TM_0 = -0.25 \sum_{i=1}^{n} [(t_i + t_{i+1})(d_i^2 - d_{i+1}^2) - 2(d_1^2 - d_n^2)T_{ave}] \tag{5-2}$$

$$ELTG = -\frac{12 \cdot TM_0}{h^3} \tag{5-3}$$

Where:

ELTG is the equivalent linear temperature gradient (°F/in),

T_{ave} is the average temperature (°F),

TM_0 is the temperature moment (°F·in^2),

d_i is the depth of the i^{th} node (in), and

t_i is the temperature at depth d_i (°F).

An effective equivalent linear temperature gradient (EELTG) was established for each calibration section to simplify the calibration process by eliminating the need for an hourly incremental analysis. The EELTG is the equivalent linear temperature gradient that when applied throughout the design life results in the same damage (cumulative differential energy) as if the hourly linear temperature gradients were used. To establish the EELTG, first the non-linear temperature gradient for each project is determined on an hourly basis using the EICM (Larson and Dempsey, 2003). Next, the hourly non-linear temperature gradients are converted to hourly ELTGs based on strain equivalency, as described above. Finally, the EELTG is determined as the equivalent linear temperature gradient that can be applied throughout the design life while still providing the same cumulative differential energy as if the hourly linear temperature gradients were used. When calculating the differential energies, 1 million ESALs are applied over the course of the year, with the same number of vehicles applied each day. Hourly traffic distributions were assigned using the percentages incorporated in Pavement ME and summarized in Table 5-1 (ARA 2004). Mean monthly mid-depth temperatures of the slab are used to estimate monthly joint widths so the joint stiffness can be determined and hourly temperatures at mid-depth of the asphalt are used to estimate the dynamic modulus of the asphalt layer.

Table 5-1 Hourly truck traffic distributions from Pavement ME (ARA 2004).

Time period	Distribution (percent)	Time period	Distribution (percent)
12:00 a.m. - 1:00 a.m.	2.3	12:00 p.m. - 1:00 p.m.	5.9
1:00 a.m. - 2:00 a.m.	2.3	1:00 p.m. - 2:00 p.m.	5.9
2:00 a.m. - 3:00 a.m.	2.3	2:00 p.m. - 3:00 p.m.	5.9
3:00 a.m. - 4:00 a.m.	2.3	3:00 p.m. - 4:00 p.m.	5.9
4:00 a.m. - 5:00 a.m.	2.3	4:00 p.m. - 5:00 p.m.	4.6
5:00 a.m. - 6:00 a.m.	2.3	5:00 p.m. - 6:00 p.m.	4.6
6:00 a.m. - 7:00 a.m.	5.0	6:00 p.m. - 7:00 p.m.	4.6
7:00 a.m. - 8:00 a.m.	5.0	7:00 p.m. - 8:00 p.m.	4.6
8:00 a.m. - 9:00 a.m.	5.0	8:00 p.m. - 9:00 p.m.	3.1
9:00 a.m. - 10:00 a.m.	5.0	9:00 p.m. - 10:00 p.m.	3.1
10:00 a.m. – 11:00 a.m.	5.9	10:00 p.m. – 11:00 p.m.	3.1
11:00 a.m. – 12:00 p.m.	5.9	11:00 p.m. – 12:00 a.m.	3.1

It is important to account for the effects of temperature on changes in the stiffness of the asphalt layer due to the affects it has on differential energy. Asphalt is a viscoelastic material that is temperature dependent, which will cause changes in stiffness due to hourly and seasonal temperature changes. When the asphalt layer is very stiff, lower deflections are likely to occur in comparison to when the asphalt layer is at a minimum stiffness. A higher stiffness results in lower deflections and a lower differential energy, whereas a lower stiffness results in higher deflections and a larger differential energy. Therefore, it is important to capture the effect of asphalt stiffness within the prediction process. An equivalent monthly asphalt stiffness was used for each month in the analysis period for the calibration sections, as described below.

The framework used to establish the equivalent monthly asphalt stiffness is similar to the procedure established in the BCOA-ME (Vandenbossche et al. 2016). First, a mastercurve is established for the asphalt modulus using a uniform aggregate gradation. SHRP LTPPBIND version 3.1, which is a Superpave binder selection program developed for the Federal Highway

Administration (FHWA), is used to select the asphalt binder grade according to the location of the project (Pavement System LLC 2005).

For each month, the differential energy is summed for the pavement section based on the loading conditions used when establishing the EELTG. The dynamic modulus of the asphalt (E_{HMA}) is established based on hourly climatic data to determine the monthly differential energy. Then, fminsearch in MATLAB is used to find an equivalent asphalt dynamic modulus, that would result in the same differential energy each month. The EELTG and the 12 monthly equivalent dynamic moduli for each calibration section can be found in Appendix A.

5.2.2 Traffic

5.2.2.1 Axle Load Spectra

The traffic analysis within this procedure uses axle load spectra. The analysis follows a similar procedure to the BCOA-ME (Zi et. al 2016). Direct inputs for predicting joint faulting includes the one-way average daily traffic (ADT), percent of trucks (as a decimal), the number of lanes in each direction, the growth type, and the growth rate. The growth type can either be compound or linear growth and is computed as follows.

Table 5-2 Function used in computing/forecasting truck traffic over time.

Growth type	Model
Non-linear	$G_f = \frac{\left[\left(1 + G_{r,ADTT}\right)^n - 1\right]}{G_{r,ADTT}}$
Linear growth	$G_f = n \times \left(1 + G_{r,ADTT} \times \frac{(n-1)}{2}\right)$

Where:

$G_{r,ADTT}$ is the user-defined growth rate of average daily truck traffic (ADTT), and

n is the design life, years.

The number of lanes is used to determine the lane distribution factor (LDF) as a function of the defined one-way ADT. The LDFs are established based on FHWA recommendations as a function of the number of lanes and the one-way ADT. The LDFs can be seen in Table 5-3.

Table 5-3 Lane distribution factors for multiple-lane highways (ARA 2004).

One-way ADT	2 lanes (one direction): % outer lane	3+ lanes (one direction): % outer lane
2,000	94	82
4,000	88	76
6,000	85	72
8,000	82	70
10,000	81	68
15,000	77	65
20,000	75	63
25,000	73	61
30,000	72	59
35,000	70	58
40,000	69	57
50,000	67	55
60,000	66	53
70,000	-	52

The axle load distributions for single and tandem axles can be seen in Table 5-4. The axle load distributions are adopted from the axle load distributions provided in the ACPA guidelines for "Design of Concrete Pavement for City Streets" (2002). These load distributions are a function of road category, the axle type, and the axle load. These distributions are also used in the BCOA-ME design procedure (Zi et. al 2014).

Table 5-4 Axles per 1000 trucks for different road categories. Source: "Design of Concrete Pavement for City Streets" (2002).

Axle load (kips)	Axles per 1000 trucks			
	Category LR	Category 1	Category 2	Category 3
Single axles				
4	846.15	1693.31	0.00	0.00
6	369.97	732.28	0.00	0.00
8	283.13	483.10	233.60	0.00
10	257.60	204.96	142.70	0.00
12	103.40	124.00	116.76	182.02
14	39.07	56.11	47.76	47.73
16	20.87	38.02	23.88	31.82
18	11.57	15.81	16.61	25.15
20	0.00	4.23	6.63	16.33
22	0.00	0.96	2.60	7.85
24	0.00	0.00	1.60	5.21
26	0.00	0.00	0.07	1.78
28	0.00	0.00	0.00	0.85
30	0.00	0.00	0.00	0.45
Tandem axles				
4	15.12	31.90	0.00	0.00
8	39.21	85.59	47.01	0.00
12	48.34	139.30	91.15	0.00
16	72.69	75.02	59.25	99.34
20	64.33	57.10	45.00	85.94
24	42.24	39.18	30.74	72.54
28	38.55	68.48	44.43	121.22
32	27.82	69.59	54.76	103.63
36	14.22	4.19	38.79	56.25
40	0.00	0.00	7.76	21.31
44	0.00	0.00	1.16	8.01
48	0.00	0.00	0.00	2.91
52	0.00	0.00	0.00	1.19

*Tridem axles are not considered in this design procedure. *LR = Light residential*.

In order to determine the load spectra for each month of the design period, the following steps are taken. First, the monthly AADTT is calculated based on the ADT, growth type, growth rate, and LDF. Next, the number of single and tandem axles per 1000 trucks are determined based on the corresponding road classification for each day using the information provided in Table 5-4.

The number of single and tandem axles per day are determined using the AADTT and the number of single and tandem axles per 1000 truck (Table 5-4). The last step is to ensure the number of single and tandem axles per load level per day are converted into the number of single and tandem axles per load level per month.

Another portion of the framework dealing with traffic considerations is wheel wander. The mean wheel location is assumed to be 18 in from the outer edge of the wheel to the edge of the lane. Also, a standard deviation of 10 in is assumed. Both values are based on the national averages used in Pavement ME as Level 3 default values (ARA 2004). Five-wheel locations are used in this analysis and include distances of 0, 8, 18, 28, and 36 in from the outer edge of the wheel to the edge of the lane. The probability of each wheel wander location based on the assumed standard deviation is 6.7, 24.2, 38.3, 24.2, and 6.7 %, respectively.

5.2.2.2 ESAL Prediction

Although this procedure uses axle load spectra to determine differential energy, ESALs are also determined based on the load spectra previously presented. In order to determine ESALs, the following steps are taken. The equation used for calculating design ESALs is given as:

$$ESAL_{design} = DD \times LDF \times G_f \times ESAL_{daily} \times 365 \quad \textbf{(5-4)}$$

Where:

DD is the directional distribution factor and indicates the fraction of total traffic in the design direction. For one-way traffic, which is required for this procedure, the default value is 1.0.

LDF is the lane distribution factor previously presented.

G_f is the traffic growth factor determined based on the type of growth rate.

$ESALs_{daily}$ is the sum of daily equivalent single axle loads determined for each type of axle load, presented below.

$$ESALs_{daily} = N_R \times LEF \tag{5-5}$$

Where:

N_R is the number of repetitions for a specific axle load per day, and

LEF are the load equivalency factors for each load level to convert into ESALs.

$$N_R = \frac{ADTT}{1000} \times Axles\ per\ 1000\ trucks \tag{5-6}$$

Where:

$Axles\ per\ 1000\ trucks$ is obtained from the axle load distributions provided in Table 5-4.

$ADTT$ is the average daily truck traffic given as:

$$ADTT = ADT \times Truck\ percent \tag{5-7}$$

Where:

$ADT_{One-way}$ is the user-inputted one-way average daily traffic. If unavailable, ADTT can be estimated based on the typical values of ADTT for different road categories given in Table 5-5.

$Truck\ percent$ is the percentage of total traffic comprised of trucks.

Table 5-5 ADTT given for different road categories and classifications (Li et al. 2014).

Classification	ADTT	Road category
Light residential	3	LR
Residential	10 to 50	1
Collector	50 to 500	2
Business	400 to 700	
Minor arterial	300 to 600	
Industrial	300 to 800	3
Major arterial	700 to 1500	

The LEFs can be calculated as follows,

$$LEF = \left(\frac{W_x}{W_{18}}\right)^{-1} \quad \text{(5-8)}$$

Where:

W_x is the number of 18-kip ESALs for any loading x, and $W_x = W_{18}$ for x = 18 kips. W_x is calculated using the following equation:

$$Log\left(\frac{W_x}{W_{18}}\right) = 5.908 - 4.62\,log(L_x + L_2) + 3.28\,log(L_2) + \frac{G_t}{\beta_x} - \frac{G_t}{\beta_{18}} \quad \text{(5-9)}$$

Where:

L_x is the axle loading, (kips),

L_2 is the weight of the axle, (kips) (1 for single axle and 2 for tandem axle),

β_x is a constant to reflect the current loading in (kips), x. $\beta_x = \beta_{18}$ for x = 18 kips, and

G_t is the growth rate.

$$\beta_x = 1 + \frac{3.63(L_x + L_2)^{5.2}}{(h_{PCC} + 1)^{8.46}{L_2}^{3.52}} \quad \text{(5-10)}$$

$$\beta_{18} = 1 + \frac{1.62\,x10^7}{(h_{PCC} + 1)^{8.46}} \quad \text{(5-11)}$$

Where:

h_{PCC} is the PCC thickness, (in).

$$G_t = log\left(\frac{4.5 - P_t}{4.5 - 1.5}\right) \tag{5-12}$$

Where:

P_t is the pavement terminal serviceability.

5.2.3 Model Inputs

With the ELTGs defined for each calibration section, the iterative faulting calculations can be performed. The incremental analysis process can be seen in Figure 5-3.

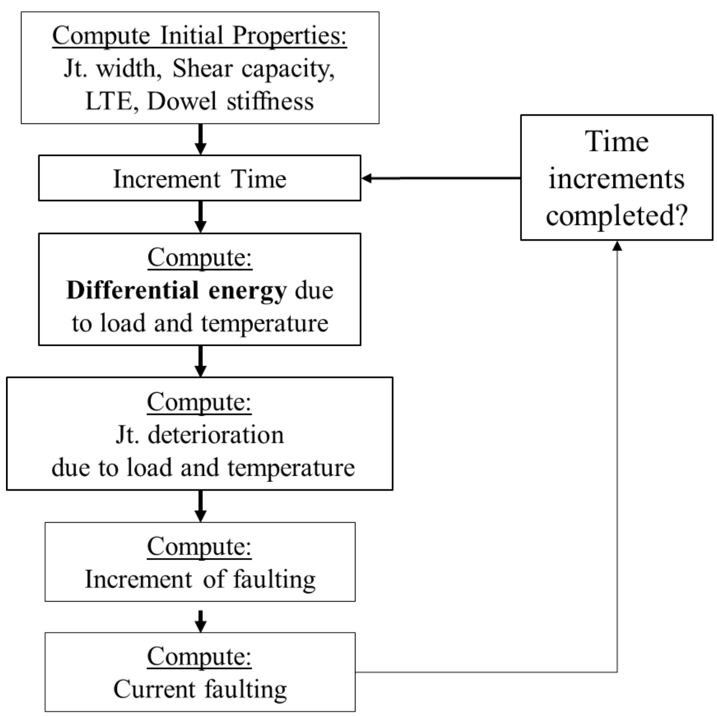

Figure 5-3 Predictive faulting incremental analysis.

The primary calculation for each month is to determine the differential energy using Equations (5-13) and (5-14).

$$\sum \delta_{B,m} = NN_{\Sigma B,A,JD}(JTSpace, l_{eff}, q_i^*, k, \frac{AGG}{k*l_{eff}}, LTE_{shoulder}, s, \Phi) \quad \textbf{(5-13)}$$

$$DE_m = \sum_1^A \sum_1^j \sum_1^i (\frac{1}{2} k \left(\sum \delta_{B,m}\right) * WWpr_i * load_{A,j}) \quad \textbf{(5-14)}$$

Where the variables in Equation (5-13) are defined previously, and

DE_m is the differential energy density deformation accumulated for month m (lb-in),

$WWpr_i$ is wheel wander distribution over the number of bins i,

$load_{A,j}$ is the number of axles of axle type A at each load level j, where A is either single or tandem axle (lbs), and

$\Sigma\delta_{B,m}$ is the difference between the loaded and unloaded slab deflection basins for month m (in^4).

For each calibration section, four files are needed to perform the faulting calculation including input, equivalent monthly asphalt stiffness, .tem, and .icm files. The .tem and .icm EICM files have been previously discussed along with the climatic considerations. Example input and asphalt stiffness text files are shown in Table 5-6. Twenty-two different inputs are specified for each section, as can be seen in Table 5-6a.

Table 5-6 Examples of (a) an input text file and (b) an asphalt stiffness text file.

5	Overlay thickness (in)
4000000	Elastic modulus of overlay (psi)
4000	Compressive strength of overlay (psi)
650	Flexural strength of overlay (psi)
7	Asphalt thickness (in)
0	Blank
250	k-value (psi/in)
144	Joint spacing (in)
0	Joint depth (0=pcc only, 1=pcc and asphalt)
0	Dowel (0 if no, 1 if yes)
0	Dowel diameter (in)
0	LTE of shoulder
5.5	Coefficient of thermal expansion of overlay (*10^-6 in/F/in)
240	Analysis period/ Design life
-1.0062	ELTG
9	Month of construction (September)
550	Cement Content (pcy)
2	Number of lanes in each direction
9383	Average Daily Traffic (ADT)
0.2	Percent trucks in design lane (as decimal)
0	Growth type (0=no growth, 1=linear, 2=compound)
0	Growth rate (%)

a) Input file

September	654,864
October	885,429
November	1,872,463
December	2,967,838
January	2,963,955
February	3,067,968
March	2,435,752
April	1,279,306
May	619,809
June	425,248
July	287,206
August	303,234

b) Asphalt stiffness file

In order to determine the inputs needed for predicting the response of the BCOA using the ANNs, the joint spacing and l_{eff} can be easily calculated from the input file. Note that a default value of 0.18 is assumed for the Poisson's ratio of concrete. The normalized load-pavement weight ratio is $q_m^* = \frac{P_i}{A * \gamma_{eff} * h_{eff}}$. P_i is each load level i (lbs.), and γ_{eff} is 150 lbs/ft^3 for all calibration sections. The modulus of subgrade reaction, k-value is taken directly from the input file. $\frac{AGG}{k * l_{eff}}$ can be calculated based on the LTE of the joint, modulus of subgrade reaction, and the effective radius of relative stiffness. *AGG* is a function of the LTE of the joint, which is defined based on the presence of dowels, aggregate interlock, and the underlying base layer. The LTE of the joint is determined using Equation (5-15) and converted back to *AGG* based on the work by Crovetti (1994).

$$LTE_{Joint} = 100[1 - \left(1 - \frac{LTE_{dowel}}{100}\right)\left(1 - \frac{LTE_{agg}}{100}\right)\left(1 - \frac{LTE_{base}}{100}\right)] \qquad \textbf{(5-15)}$$

Where:

LTE_{dowel} is the joint LTE if dowels are the only mechanism of load transfer (%),

LTE_{agg} is the joint LTE if aggregate interlock is the only mechanism of load transfer (%), and

LTE_{base} is the joint LTE if the base is the only mechanism of load transfer (%).

LTE_{base} is established using the following table.

Table 5-7 LTE_{base} for different base types (ARA 2004).

Base type	**LTE_{base} (%)**
Aggregate base	20
Asphalt-treated or cement-treated	30
Lean concrete base	40
Frozen base	90

If the pavement system is frozen, the LTE of joints increases (ARA 2004). To account for this, when the mean monthly mid-depth PCC temperature is less than 32°F, LTE_{base} is set equal to 90%. Additionally, $LTE_{shoulder}$ is either 90%, if there is a tied concrete shoulder, or 0% for an asphalt shoulder. The wheel wander, s, is normally distributed with the mean located in the wheelpath and a standard deviation of 10 in. Korenev's non-dimensional temperature gradient, Φ, is in accordance with Equation (4-9) presented in the previous chapter on the development of the ANNs. All variables in this equation have been previously defined with the exception of the temperature difference, ΔT. In this procedure, the temperature difference is calculated as the EELTG established based on the equivalency of the differential energy and the diurnal transient non-linear gradients, as described above, plus the default value of the effective built-in temperature difference from Pavement ME of -10 ^{o}F (ARA 2004).

In order to examine the effects of aggregate interlock on joint stiffness, the joint width must be estimated. The joint width for each month is calculated with Equation (5-16). The two variables that still need to be determined to calculate the joint width are the temperature of the PCC overlay at the time the concrete sets and the long-term drying shrinkage in the PCC overlay. The concrete set temperature is estimated using Table 5-8, which requires the mean monthly temperature for the month of paving as well as the cement content. The drying shrinkage strain in the PCC overlay is established based on the tensile strength (correlated from compressive strength) using the recommendations in AASHTO 93. This recommendation is shown in Table 5-9.

$$JW(m) = max\left(12000 * c * JTSpace * \left(CTE * \left(T_c - T(m)\right) + \varepsilon_{sh}\right), 0\right) \quad \textbf{(5-16)}$$

Where:

$JW(m)$ is the joint width for month m (mils),

c is the friction factor (0.85 for asphalt layers when the joint only activates through the PCC layer and 0.65 for non-stabilized base layers when the joint activates through both the PCC and asphalt layers),

$JTSpace$ is the joint spacing in the overlay (ft),

CTE is the overlay PCC coefficient of thermal expansion (in/in/^{o}F),

T_c is the concrete set temperature (^{o}F),

$T(m)$ is the mean mid-depth PCC overlay temperature for month m (^{o}F), and

ε_{sh} is the PCC overlay drying shrinkage strain (in/in).

Table 5-8 PCC set temperature for cement content and mean temperature during month of paving (^{o}F).

Mean monthly air temp. (^{o}F)	Cement content (lbs.)			
	400	500	600	700
40	52	56	59	62
50	66	70	74	78
60	79	84	88	93
70	91	97	102	107
80	103	109	115	121
90	115	121	127	134
100	126	132	139	145

Table 5-9 PCC overlay drying shrinkage strain relationship (ARA 2004).

Tensile strength (psi)	Shrinkage strain (in/in)
400	0.0008
500	0.0006
600	0.00045
700	0.0003
800	0.0002

The non-dimensional aggregate joint stiffness can then be calculated for each month using Equation (5-17) and (5-18) adopted from Zollinger et al. (1998). Note that ΔS_{tot} is equal to zero for the first month of the analysis and the individual monthly increments of loss in shear capacity can be calculated using Equation (5-19).

$$S = 0.5 * h_{PCC} * exp^{-0.032*JW} - \Delta S_{tot} \tag{5-17}$$

$$\log(J_{AGG}) = -3.19626 + 16.09737 * exp^{-exp^{-\left(\frac{S-e}{f}\right)}} \tag{5-18}$$

Where:

S is the aggregate joint shear capacity,

h_{PCC} is the PCC overlay thickness (in),

JW is the joint opening (mils),

$\Delta S_{tot} = \sum_{i=1}^{m} \Delta S_i$ is the cumulative loss of shear capacity at the beginning of the current month,

J_{AGG} is the non-dimensional aggregate joint stiffness for the current monthly increment,

e = 0.35, and

f = 0.38.

$$\Delta S_i = \left\{ \begin{array}{ll} 0 & if\ JW < 0.001 h_{PCC} \\ n_{i,A} * \dfrac{0.005 * 10^{-6}}{1.0 + \left(\dfrac{JW}{h_{PCC}}\right)^{-5.7}} \left(\dfrac{\tau_i}{\tau_{ref}}\right) & if\ 0.001 < JW < 3.8 h_{PCC} \\ n_{i,A} * \dfrac{0.068 * 10^{-6}}{1.0 + 6.0 * \left(\dfrac{JW}{h_{PCC}} - 3\right)^{-1.98}} \left(\dfrac{\tau_i}{\tau_{ref}}\right) & if\ JW > 3.8 h_{PCC} \end{array} \right\} \tag{5-19}$$

Where:

ΔS_i is the loss of shear capacity from all traffic for current month i,

$n_{i,A}$ is the number of axle A load applications for load level i,

h_{PCC} is the overlay slab thickness (in),

JW is the joint opening (mils),

$\tau_i = J_{AGG} * (\Sigma\delta_{L,m} - \Sigma\delta_{UL,m})$ is the shear stress on the transverse joint surface from the response model using corner deflections, and

$\tau_{ref} = 111.1 * \exp(-\exp(0.9988 * \exp(-0.1089 * \log(J_{AGG}))))$ is the reference shear stress derived from the PCA test results.

For a doweled pavement, the model adopted for the non-dimensional dowel stiffness is that from ARA (2004). The initial non-dimensional dowel joint stiffness is calculated using Equation (5-20) and the critical non-dimensional dowel joint stiffness is calculated with Equation (5-21). The non-dimensional dowel stiffness is then calculated using Equation (5-22) and the dowel damage parameter is presented in Equation (5-23).

$$J_0 = \frac{152.8 * A_d}{h_{pcc}} \tag{5-20}$$

$$J_d^* = \begin{cases} 118, & if \dfrac{A_d}{h_{pcc}} > 0.656 \\ 210.0845 \dfrac{A_d}{h_{pcc}} - 19.8, & if\ 0.009615 \leq \dfrac{A_d}{h_{pcc}} \leq 0.656 \\ 0.4, & if \dfrac{A_d}{h_{pcc}} < 0.009615 \end{cases} \tag{5-21}$$

$$J_d = J_d^* + (J_0 - J_d^*) exp\,(-\,DOWDAM) \tag{5-22}$$

$$\Delta DOWDAM = \frac{J_d * \left(\Sigma\delta_{C,A,m}\right) * DowelSpace * n_{i,A}}{d * f_c'} \tag{5-23}$$

Where:

A_d is the area of the dowel bar (in^2),

h_{pcc} is the overlay PCC thickness (in),

J_0 is the initial non-dimensional dowel stiffness,

J_d^* is the critical non-dimensional dowel stiffness,

J_d is the non-dimensional dowel stiffness for current month,

$DOWDAM$ is the cumulative dowel damage for the current month,

$DowelSpace$ is the dowel bar spacing (in),

$n_{i,A}$ is the number of axle A load applications for load level i,

d is the dowel bar diameter (in), and

f_c' is the PCC compressive stress estimated from the modulus of rupture (psi).

Two sets of incremental equations are used to determine faulting. The first set is for when the joint activates only through the PCC layer and the second set is for when the joint activates through both the PCC and asphalt layers. The difference between the two sets of equations is the treatment of the erodibility of the layer/material to undergo pumping. The differential energy is calculated using the corresponding ANNs for the different joint activation depths. The erodibility factor of the layer being eroded away is also dependent on the depth of joint activation. If the joint is likely to only activate through the PCC layer, previously an erodibility value of one is assigned based on the erosion assessment established in the Pavement ME (ARA 2004). However, a new approach was developed to account for the different material properties of the asphalt layer and is presented below.

$$E = fn(\%\ eff.\ binder\ content,\ \%\ air\ voids, P_{200}) \tag{5-24}$$

Where:

% eff. binder content is the percent effective binder content in the asphalt mixture (%),

% air voids is the percent air voids in the asphalt mixture (%), and

P_{200} is the percent fines passing the number 200 sieve (%).

The erodibility classification established in the Pavement ME is used when a joint activates through both the PCC and asphalt layer. An erodibility factor of four is assigned based on the likelihood of the different underlying layers beneath an asphalt layer. In addition to this erodibility classification, the percent of aggregate passing the No. 200 sieve of the layer beneath the asphalt is an input. The different erodibility classes can be seen in Table 5-10.

Table 5-10 Erodibility classification (adopted from ARA 2004).

Erodibility class	Material description and testing
1	Hot mixed asphalt concrete with 6 percent asphalt cement that passes appropriate stripping tests and aggregate tests and a granular subbase layer or a stabilized soil layer (otherwise Class 2).
2	Asphalt treated granular material with 4 percent asphalt cement that passes appropriate stripping test and a granular subbase layer or a treated soil layer or a geotextile fabric is placed between the treated base and subgrade; otherwise Class 3.
3	Asphalt treated granular material with 3 percent asphalt cement that passes appropriate stripping test.
4	Unbound crushed granular material having dense gradation and high-quality aggregates.
5	Untreated soils (PCC slab placed on prepared/compacted subgrade)

When the joint activates only through the PCC, faulting can be predicted using Equations (5-25) through (5-28).

$$F_0 = (C_1 + C_2 * FR^{0.25}) * \delta_{curl} * [C_5 * E]^{C_6} * log(WETDAYS * A\_P_{200}) \quad \textbf{(5-25)}$$

$$F_i = F_{i-1} + C_7 * C_8 * DE_i * [C_5 * E]^{C_6} \quad \textbf{(5-26)}$$

$$\Delta Fault_i = (C_3 + C_4 * FR^{0.25}) * (F_{i-1} - Fault_{i-1})^2 * C_8 * DE_i \quad \textbf{(5-27)}$$

$$Fault_i = Fault_{i-1} + \Delta Fault_i \quad \textbf{(5-28)}$$

Where:

F_0 is the initial maximum mean transverse joint faulting (in),

FR is the base freezing index defined as the percentage of the time that the top of the asphalt is below freezing (<32°F),

δ_{curl} is the maximum mean monthly PCC upward slab corner deflection due to temperature curling and moisture warping (in),

E is the erodibility factor of the asphalt layer as a function of the asphalt mixture properties,

WETDAYS is the average number of annual wet days (> 0.1 in of precipitation),

A_P_{200} is the percent of aggregate passing No. 200 sieve in the asphalt layer (%),

F_i is the maximum mean transverse joint faulting for month *i* (in),

F_{i-1} is the maximum mean transverse joint faulting for month *i*-1 (in)(If i =1, $F_{i-1} = F_0$),

DE_i is the differential energy density accumulated during month *i*,

$\Delta Fault_i$ is the incremental monthly change in mean transverse joint faulting during month *i* (in),

C_1 ... C_8 are the calibration coefficients,

$Fault_{i-1}$ is the mean joint faulting at the beginning of month *i* (0 if i = 1), and

$Fault_i$ is the mean joint faulting at the end of month *i* (in).

When the joint activates through the PCC and asphalt layer, faulting can be predicted using Equations (5-29) through (5-32).

$$F_0 = (C_1 + C_2 * FR^{0.25}) * \delta_{curl} * \left[log\ (1 + C_5 * 5^{EROD}) * log(\frac{P_{200} * WETDAYS}{\rho_s})\right]^{C_6} \quad \textbf{(5-29)}$$

$$F_i = F_0 + C_7 \sum_{j=0}^{m} DE_j * log\ (1 + C_5 * 5^{EROD})^{C_6} \quad \textbf{(5-30)}$$

$$\Delta Fault_i = (C_3 + C_4 * FR^{0.25}) * (F_{i-1} - Fault_{i-1})^2 * C_7 * DE_i \quad \textbf{(5-31)}$$

$$Fault_i = Fault_{i-1} + \Delta Fault_i \quad \textbf{(5-32)}$$

Where:

F_0 is the initial maximum mean transverse joint faulting (in),

FR is the base freezing index defined at the percentage of the time that the top of the base is below freezing (<32°F),

δ_{curl} is the maximum mean monthly PCC upward slab corner deflection due to temperature curling and moisture warping (in),

EROD is the erodibility of the layer beneath the asphalt, as defined in Table 5-10 above,

P_{200} is the percent of aggregate passing No. 200 sieve of the layer beneath the asphalt (%),

WETDAYS is the average number of annual wet days (> 0.1 in of rainfall),

ρ_s is the overburden on the layer beneath the asphalt (lbs),

F_i is the maximum mean transverse joint faulting for month *i* (in),

F_{i-1} is the maximum mean transverse joint faulting for month *i*-1 (in)(If i =1, $F_{i-1} = F_0$),

DE_i is the differential energy density accumulated during month *i*,

$\Delta Fault_i$ is the incremental monthly change in mean transverse joint faulting during month i (in),

$C_1 \ldots C_7$ are the calibration coefficients,

$Fault_{i-1}$ is the mean joint faulting at the beginning of month i (0 if i = 1) (in), and

$Fault_i$ is the mean joint faulting at the end of month i (in).

When there is a section that is likely to have both depths of joint activation based on the FSR, the individual models need to be coupled together. In order to determine the likelihood of the different depths of joint activation within a given section, an extensive study was performed and the results are presented in Chapters 2 and 3 (DeSantis et al. 2016, DeSantis et al. 2018, DeSantis et al. 2019). It was determined that approximately every sixth joint will activate full-depth. This may vary for different structures but is believed to be a suitable approximation. Therefore, the following equation is used to calculate average joint faulting for sections that have joints that activate to different depths.

$$Fault_m = \sum_{i=1}^{m}((\frac{5}{6})\Delta Fault_{PCC,i} + (\frac{1}{6})\Delta Fault_{Full,i}) \quad \textbf{(5-33)}$$

Where:

$Fault_m$ is the mean joint faulting at the end of month m (in),

$\Delta Fault_{PCC,i}$ is the incremental monthly change in mean transverse joint faulting during month i when the joint is only through the PCC layer (in), and

$\Delta Fault_{Full,i}$ is the incremental monthly change in mean transverse joint faulting during month i when the joint is through the PCC layer and the asphalt layer (in).

5.3 Calibration Sections

The calibration database used to calibrate the BCOA faulting model consists of 34 sections from five different states within the United States, Colorado, Illinois, Louisiana, Minnesota, and Missouri. The calibration sections are comprised of 18 sections at MnROAD, eight are sections across the state of Minnesota, five are sections throughout Colorado, and one section for each Illinois, Louisiana, and Missouri. Initially, the calibration was limited to only sections within the state of Minnesota due to limited performance data. However, an ongoing National Cooperative Highway Research Program (NCHRP) study 1-61, "Evaluation of Bonded Concrete Overlays on Asphalt Pavements," aided in supplementing the calibration database. Although these sections only included one measurement of faulting, it was important to be able to include sections within the calibration outside of Minnesota.

The calibration sections were divided into two sets. In one set, the depth of joint activation was through the PCC and in the other set the joint activated through both the PCC and asphalt layer. The depth of joint activation was established using an extensive amount of FWD data and the details can be found in DeSantis et al. 2016. For sections that developed both depths of joint activation, the joints that activated full-depth were separated from the joints that activated only through the PCC. This created two sections, one with joints activating only through the PCC and the other with joints activating full-depth. Two separate calibrations needed to be conducted in order to account for the different trends in faulting due to the different depths of joint activation. Table 5-11 presents a range of values in the calibration data set for the more sensitive parameters. Of the sections, 29 are undoweled while the rest are doweled. The dowel diameter for the doweled sections were all 1 in. If the pavement section has a random joint spacing, the mean joint spacing was used in the analysis. Considering the number of time series observations available, a total of 269 data points are available for calibration of the model.

The age of the sections ranged from approximately 3 to 22 years with an average of 8.2 years of age. In terms of ESALs, the traffic ranged from approximately 0.01 million to 20 million with an average of around 4.5 million ESALs. Detailed information for each calibration section can be found in Appendix A. Some available sections were removed from the calibration database due to performance related distress that influenced the magnitude of faulting. Cell 96 with full-depth joints was eliminated due to severe joint deterioration at these joints. In addition, if diamond grinding was performed on a given calibration section, the survey date and data prior to diamond grinding was used for calibration. Once diamond grinding was performed on a section, the remaining life and faulting data measurements were discarded from calibration.

Table 5-11 Range of parameters for calibration sections.

Parameter	Minimum	Maximum	Average
Age, yrs.	3.0	27.0	10.4
Estimated ESALs	9.06E+04	1.91E+07	5.10E+06
Average joint spacing, ft	4	15	6
Overlay thickness, in	3	8	5
Overlay EMOD[1], psi	3.60E+06	5.02E+06	4.40E+06
Overlay MOR[2], psi	507	902	685
Overlay cement content, lbs.	400	650	500
Existing asphalt thickness, in	3	16	8

[1]EMOD is the elastic modulus of the PCC
[2]MOR is the modulus of rupture of the PCC

5.4 Results of Model Calibration

Calibration of the faulting model requires adjusting the calibration coefficients from Equation (5-25) through (5-32) to minimize the error function defined by Equation (5-34). A macro driven excel spreadsheet was developed to calibrate the two different models (joint activation through the PCC and joint activation through both the PCC and asphalt layers). Additionally, the shape of the erosion function had to be fit based upon the asphalt characteristics identified as being influential in the development of pumping, as depicted in Equation (5-35). The fitted erosion model can be seen in Equations (5-35) and (5-36). The following steps were taken to minimize the error. Several calibration parameters were fixed at a constant value, while the remaining coefficients were varied to find the lowest values of the error function. Once the error is minimized for the varied coefficients, these values are kept constant while the coefficients that were previously held constant are allowed to vary until the lowest possible value of the error function is achieved. These two different sets of coefficients are varied in this manner until the error can be minimized no further. These steps do not guarantee a global minimum error but should provide a reasonable result. Minimization of the bias in the model with the calibration parameters must also be performed in addition to error minimization when selecting the final set of calibration coefficients. Predicted versus measured transverse joint faulting is presented in Figure 5-4. Table 5-12 summarizes all of the calibration coefficients that were established. Table 5-12 also includes the national calibrations for the Pavement ME faulting prediction model. Some of the coefficients within the BCOA framework are used differently than Pavement ME, resulting in different magnitudes. The calibration sections with the measured and predicted faulting can be seen in Figure 5-6 and Figure 5-7.

$$\mathrm{ERROR}(\mathrm{C_1}, \mathrm{C_2}, \mathrm{C_3}, \mathrm{C_4}, \mathrm{C_5}, \mathrm{C_6}, \mathrm{C_7}) = \sum_{\mathrm{i}=1}^{\mathrm{N}} (\mathrm{FaultPredicted_i} - \mathrm{FaultMeasured_i})^2 \tag{5-34}$$

Where:

ERROR is the error function,

$C_1, C_2, \ldots, C_7$ are the calibration coefficients,

$FaultPredicted_i$ is the predicted faulting for ith observation in dataset (in),

$FaultMeasured_i$ is the measured faulting for ith observation in dataset (in), and

N is the number of observations in the dataset.

$$\alpha = \log\left(1 + a * P_{200} + b * \%AV - c * \%Binder\right) \tag{5-35}$$

$$E = \begin{cases} (1.272 * \alpha^2 - 1.916 * \alpha + 0.6718) & Undoweled\ Pavements \\ (1.081 * \alpha^2 - 1.629 * \alpha + 0.5710) & Doweled\ Pavements \end{cases} \quad \alpha > 1.16$$

$$E = \begin{cases} (0.163 * \alpha) & Undoweled\ Pavements \\ (0.139 * \alpha) & Doweled\ Pavements \end{cases} \quad \alpha < 1.16 \tag{5-36}$$

Where:

α is the erodibility index,

a, b, c are the calibration coefficients (8.7346, 1.6989, and 1.8323, respectively),

P_{200} is the percent aggregate passing No. 200 sieve for the asphalt (%),

$\%AV$ is the air voids percentage in the asphalt (%),

$\%Binder$ is the effective binder content of the asphalt (%), and

E is the erodibility to be used in Equations (5-25) through (5-28).

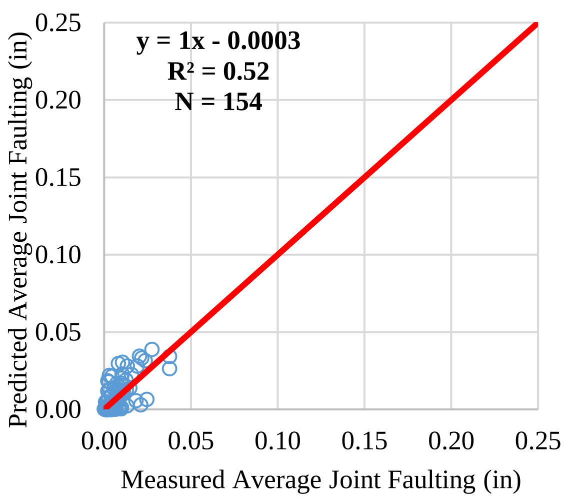

a) Joint activates through PCC

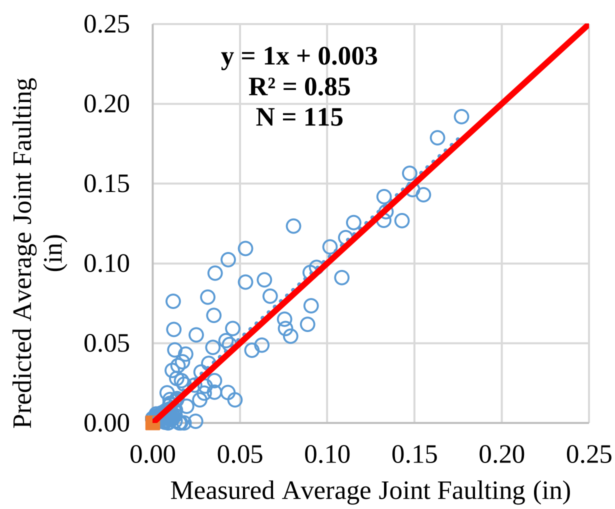

b) Joint activates full-depth through PCC and Asphalt

Figure 5-4 Measured vs. predicted joint faulting.

Table 5-12 Joint faulting calibration coefficients.

Calibration coefficient	Joint activates through PCC	Joint activates full-depth	Pavement ME initial[1]	Pavement ME current[2]
C_1	1.29	1.29	1.29	0.595
C_2	1.1	1.1	1.1	1.636
C_3	0.001725	1.0E-06	0.001725	0.00217
C_4	0.0008	1.0E-05	0.0008	0.00444
C_5	0.05	6.0E-04	250	250
C_6	2.4	4.215	0.4	0.47
C_7	3.562	1.21	1.2	7.3
C_8	1/5E-05	1/5E-05	400[3]	400[3]
Doweled: C_7	(0.75/dowel diameter)* C_7	(7.0*dowel diameter)* C_7		

[1]ARA 2004, Khazanovich et al. 2004
[2]Sachs et al. 2015
[3]Previous model used C_8 as dowel damage coefficient (not used for calibration)

The presented models are an adaptation of the current model within Pavement ME. When the joint only activates through the PCC layer, the major difference between it and the Pavement ME model is the treatment of the erodibility of the asphalt layer. The developed model is able to account for different parameters within the asphalt mixture that are most influential on the likelihood of erosion and pumping to occur. Whereas, the Pavement ME model assigns an erodibility factor equal to 1 for all hot mixed asphalt concrete (see full description in Table 5-10).

When the joint activates through the PCC and asphalt layer, the framework for the model is the same as Pavement ME. However, the developed model is able to account for structural designs more common for BCOAs than JPCPs (i.e. joint spacings less than 10 ft). The model also predicts the response of BCOAs significantly better than the Pavement ME model because it was calibrated with BCOA sections, unlike the Pavement ME model.

These prediction models use a deflection basin to characterize the critical response of a BCOA due to environmental and traffic loading. Whereas, the Pavement ME model uses corner deflections. Details on why this approach was taken is presented in Chapter 4. The total deflection for a deflection basin is much larger than corner deflections, and thus result in larger differential energies. Therefore, an additional calibration coefficient (C_8) was introduced to account for the magnitude in differential energies produced from deflection basins.

5.4.1 Joint Faulting Model Adequacy Checks

A series of model adequacy checks were performed to ensure the model coefficients provide reasonable results in terms of predictability and reasonableness. The tests outlined by Mallela et al. (2009) have been performed and are summarized below. An overall SEE of 0.006 in of faulting and a coefficient of determination, R^2, of 0.52 was achieved for the model that predicts faulting at joints that activate only through the PCC. An overall SEE of 0.023 in of faulting and a coefficient of determination, R^2, of 0.78 was achieved for the model that predicts faulting at joints that activate full-depth. The model bias was checked using the three hypothesis tests outlined in Table 5-13. The null and alternative hypothesis outlined in Table 5-13 were tested and the results summarized in Table 5-14. A significance level of 0.05 was assumed for hypothesis testing. From Table 5-14, none of the three null hypotheses are rejected, indicating that model bias has been removed through the calibration.

Table 5-13 Null and alternative hypothesis tested for faulting models.

Hypothesis 1	Null hypothesis H_o: Linear regression model intercept = 0
	Alternative hypothesis H_a: Linear regression model intercept ≠ 0
Hypothesis 2	Null hypothesis H_o: Linear regression model slope = 1.0
	Alternative hypothesis H_a: Linear regression model slope ≠ 1.0
Hypothesis 3	Null hypothesis H_o: Mean ME Design faulting = Mean measured faulting
	Alternative hypothesis H_a: Mean ME Design faulting ≠ Mean measured faulting

Table 5-14 Results from transverse joint faulting model hypothesis testing.

Hypothesis testing and t-Test				
Model	Test type	Value	95% CI	P-value
Joint activates through PCC	Hypothesis 1: Intercept = 0	0.45	-0.0016 to 0.00103	0.328
	Hypothesis 2: Slope = 1	0.001	0.8459 to 1.1543	0.5
	Paired t-test		-	0.49
Joint activates full-depth	Hypothesis 1: Intercept = 0	0.002	-0.003 to 0.0074	0.204
	Hypothesis 2: Slope = 1	1.0	0.914 to 1.086	0.50
	Paired t-test	-	-	0.275

5.5 Joint Faulting Model Reliability

The BCOA transverse joint faulting model reliability (standard deviation) was determined in a similar manner as was conducted for Pavement ME (ARA 2004). A standard deviation model was developed for each of the different calibrations. The resulting standard deviation models developed for BCOA faulting for a design at a specified level of reliability is presented below in Equation (5-37) and (5-38). The results for both models can be seen in Figure 5-5. The models were established using the data from Table 5-15 and Table 5-16, which was determined from the predicted faulting data.

$$Stdev(FAULT\_PCC) = 0.0781 * (FAULT\_PCC^{0.4777}) \tag{5-37}$$

Where:

Stdev(FAULT_PCC) is the transverse joint faulting standard deviation when the joint only activates through the PCC (in), and

FAULT_PCC is the predicted transverse joint faulting when the joint only activates through the PCC (in).

$$Stdev(FAULT\_FULL) = 0.0638 * (FAULT\_FULL^{0.3003}) \tag{5-38}$$

Where:

Stdev(FAULT_FULL) is the transverse joint faulting standard deviation when the joint activates through the PCC and asphalt layers (in), and

FAULT_FULL is the predicted transverse joint faulting when the joint activates through the PCC and asphalt layers (in).

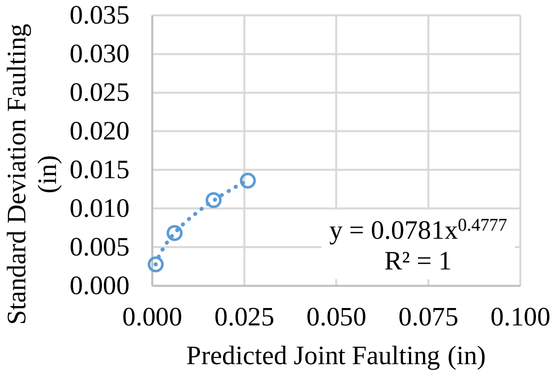

a) Standard deviation for joint activation through PCC

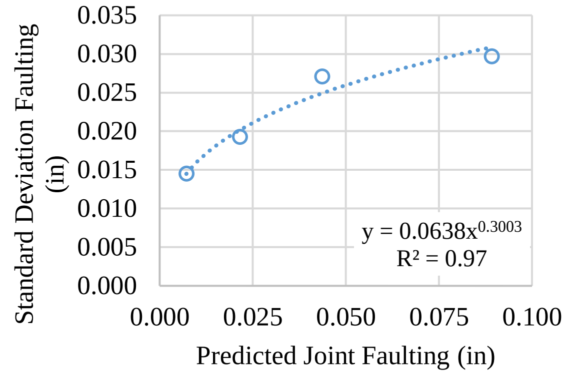

b) Standard deviation for full-depth joint activation

Figure 5-5 Predicted faulting vs. faulting standard deviation.

Table 5-15 Predicted faulting data used to develop faulting standard deviation model for joint activation through the PCC.

Group	Mean predicted joint faulting, in	Std. dev. of predicted joint faulting, in
1	0.0009	0.0028
2	0.0061	0.0068
3	0.0167	0.0111
4	0.0260	0.0136

Table 5-16 Predicted faulting data used to develop faulting standard deviation model for full-depth joint activation.

Group	Mean predicted joint faulting, in	Std. dev. of predicted joint faulting, in
1	0.007	0.015
2	0.022	0.019
3	0.044	0.027
4	0.089	0.030

In order to adjust the mean faulting for the desired reliability level, the following relationship is used.

$$FAULT_R = FAULT - STD(FAULT) * Z_R \qquad \textbf{(5-39)}$$

Where:

$FAULT_R$ is the magnitude of faulting at the desired level of reliability R (in),

FAULT is the predicted faulting determined corresponding to 50 percent reliability (in),

STD(FAULT) is the standard deviation of the predicted faulting using the corresponding established reliability model (in), and

Z_R is the standardized normal deviate corresponding to a reliability level R, presented in Table 5-17.

Table 5-17 Reliability and corresponding standard normal deviate.

Reliability, R (%)	Std. normal deviate, Z_R
50	0
75	-0.674
85	-1.037
90	-1.282
95	-1.645

5.6 Joint Faulting Model Validation

The calibrated models are validated with plots that show the predicted and observed faulting versus traffic for the calibration sections. Figure 5-6 presents the predicted and observed faulting data for each of the calibration sections when joints activated only through the PCC. Figure 5-7 presents the predicted and observed faulting data for each of the calibration sections with joints that activated through the PCC and asphalt layer. Each section has a different x-axis dictated by the level of traffic (ESALs). To better assess the calibration, Table 5-18 and Table 5-19 provides basic design information for each of the calibration sections, joints that activated only through the PCC and joints that activated full-depth, respectively. The basic design information includes the PCC overlay thickness, the remaining asphalt thickness after milling, the panel sizes, and the traffic at the last observed data point. Full design information for all of the calibration sections can be found in Appendix A.

Table 5-18 Calibration sections: PCC depth only.

Section ID	State	Overlay thickness, in	Asphalt thickness, in	Panel size, ft x ft	Dowel diameter, in	Estimated ESALs
Cell 60_PCC	MN	5	7	5x6	None	8.45E+06
Cell 60_PL_PCC	MN	5	7	5x6	None	1.70E+06
Cell 96_PCC	MN	6	7	5x6	None	1.25E+07
Cell 96_PL_PCC	MN	6	7	5x6	None	3.50E+06
Cell 61_PCC	MN	5	7	5x6	None	8.45E+06
Cell 61_PL_PCC	MN	5	7	5x6	None	1.70E+06
Cell 62_PCC	MN	4	8	5x6	None	8.45E+06
Cell 62_PL_PCC	MN	4	8	5x6	None	1.70E+06
Cell 63_PCC	MN	4	8	5x6	None	8.45E+06
Cell 63_PL_PCC	MN	4	8	5x6	None	1.70E+06
06-83A	CO	8	16	6x6	None	5.91E+06
06-83B	CO	6	13	6x6	None	1.02E+07
06-121A	CO	6	13	6x6	None	3.13E+06
06-121B	CO	7	12	6x6	None	4.39E+06
17-27	IL	5	8	5.5x5.5	None	1.00E+07
22-167	LA	5	9	4x4	None	5.57E+06
29-60	MO	4.5	5	4x4	None	1.91E+07

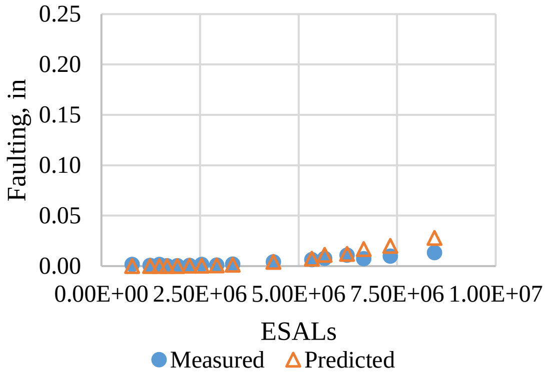

a) Cell 60 driving lane

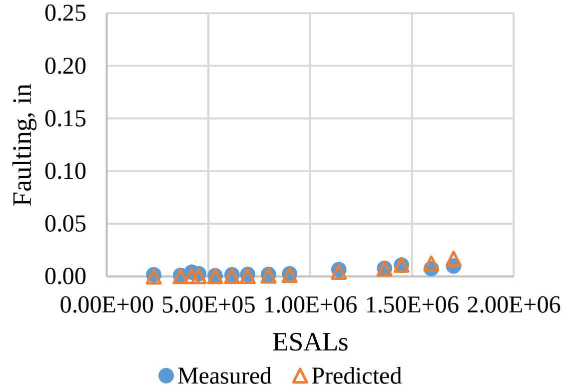

b) Cell 60 passing lane

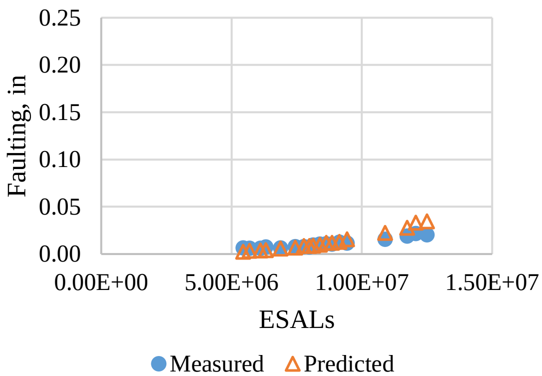

c) Cell 96 driving lane

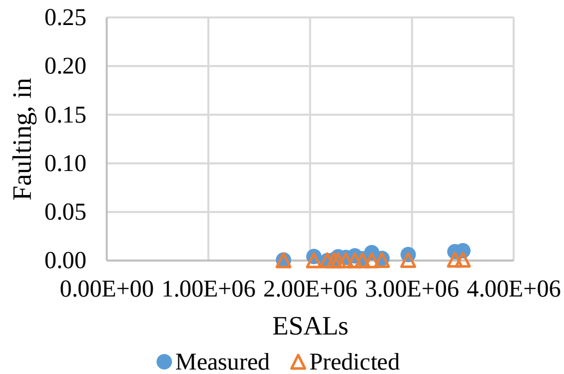

d) Cell 96 passing lane

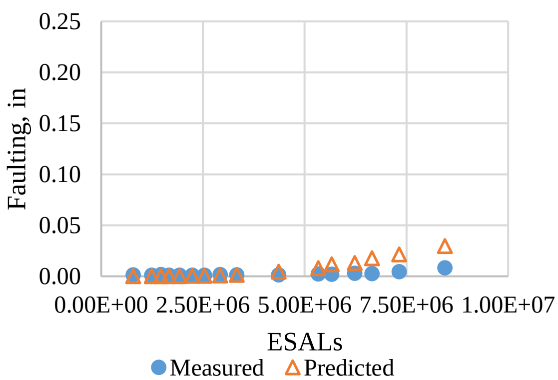

e) Cell 61 driving lane

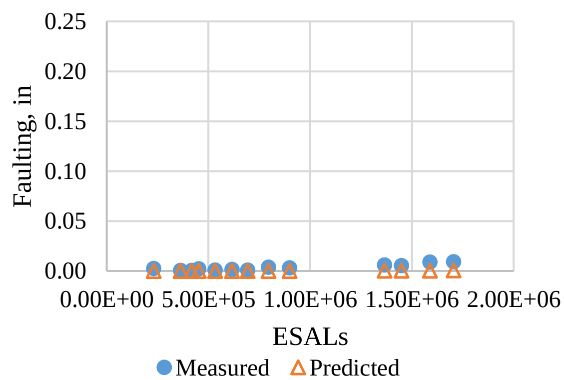

f) Cell 61 passing lane

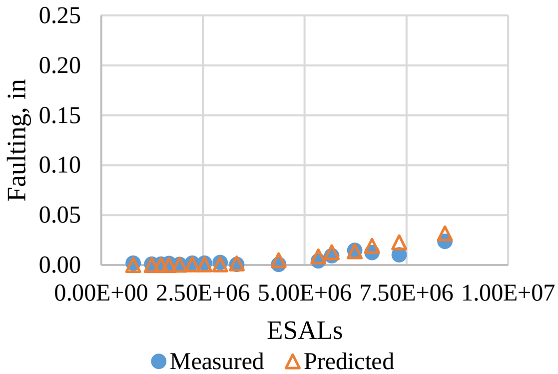

g) Cell 62 driving lane

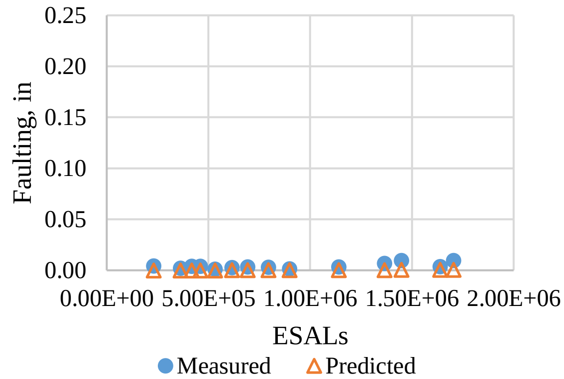

h) Cell 62 passing lane

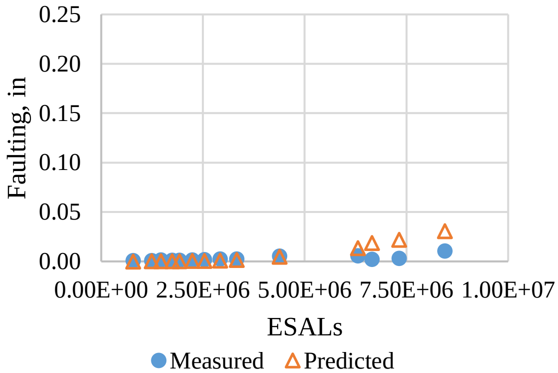

i) Cell 63 driving lane

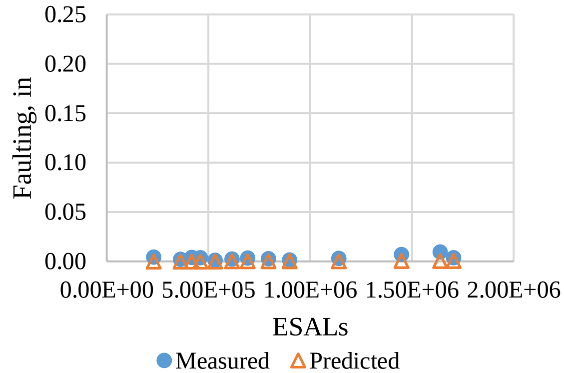

j) Cell 63 passing lane

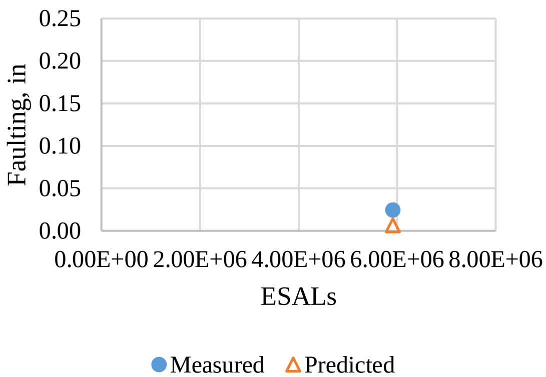

k) 06-83A

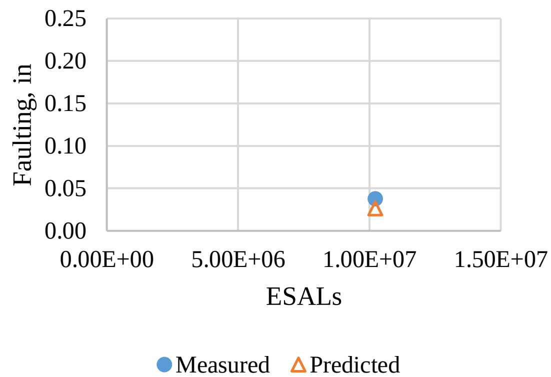

l) 06-83B

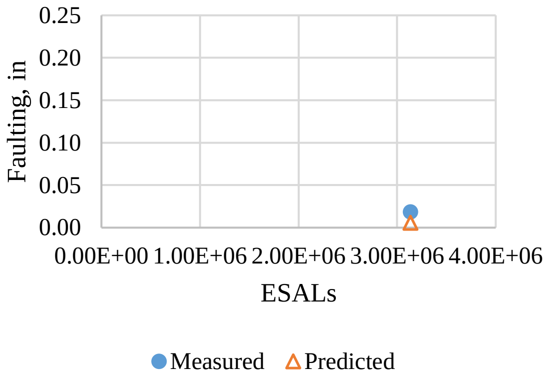

m) 06-121A

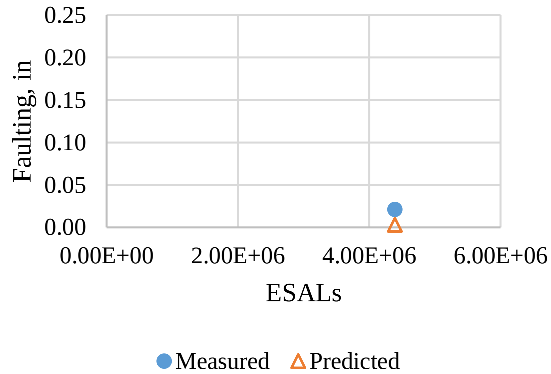

n) 06-121B

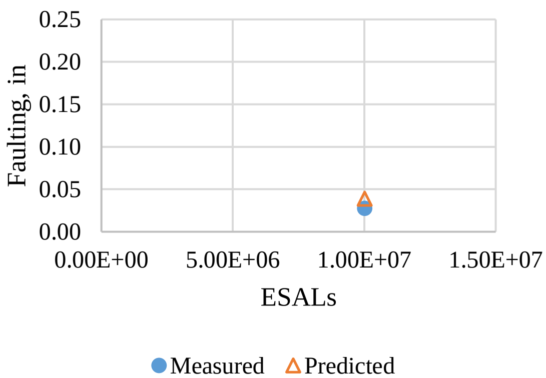

o) 17-27

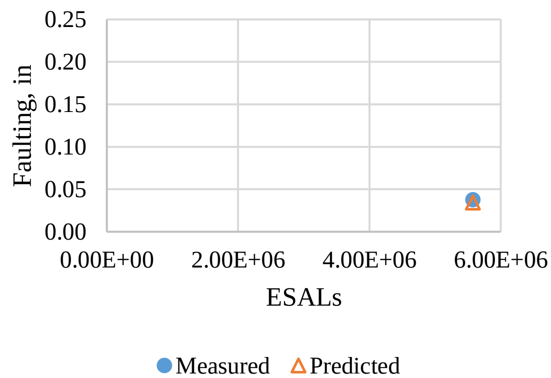

p) 22-167

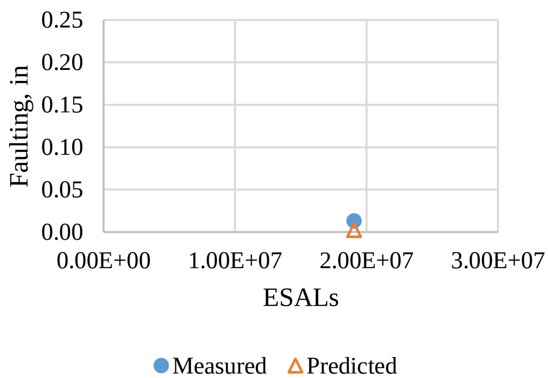

q) 29-60

Figure 5-6 Calibration section plots: measured vs. predicted faulting (PCC depth only).

Table 5-19 Calibration sections: full-depth.

Section ID	State	Overlay thickness, in	Asphalt thickness, in	Panel size, ft x ft	Dowel diameter, in	Estimated ESALs
Cell 92_FULL	MN	6	7	10x12	1	1.16E+07
Cell 92_PL_FULL	MN	6	7	10x12	1	3.19E+06
CSAH 9	MN	7	6	15x12	1	4.35E+05
TH 56_2006-26	MN	6	8.5	15x13.5	1	9.06E+04
06-6	CO	6	9	10x12	1	4.69E+06
Cell 95_FULL	MN	3	10	5x6	None	4.76E+06
Cell 60_FULL	MN	5	7	5x6	None	8.45E+06
Cell 60_PL_FULL	MN	5	7	5x6	None	1.70E+06
Cell 61_FULL	MN	5	7	5x6	None	6.20E+06
Cell 61_PL_FULL	MN	5	7	5x6	None	1.14E+06
Cell 97_FULL	MN	6	7	10x12	None	1.16E+07
CSAH 7_43-607-14	MN	5	6	6x6,6x7	None	3.26E+05
CSAH 22_CP 12-14-22	MN	6	4	6x6	None	1.69E+05
CSAH 22_002-622-033	MN	6	4	6.25x6.25	None	1.28E+05
TH 30_0705-14	MN	6	7.5	12x12	None	3.39E+05
CSAH 22_02-622-31	MN	6	3	6x6,6x7	None	2.26E+05
CSAH 2_43-602-(24-25)	MN	5	5	6x6,6x7	None	2.19E+05

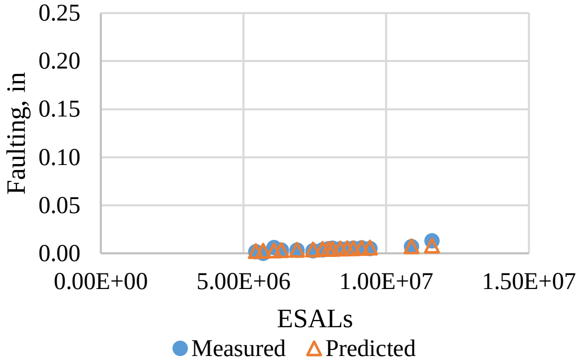

a) Cell 92 driving lane

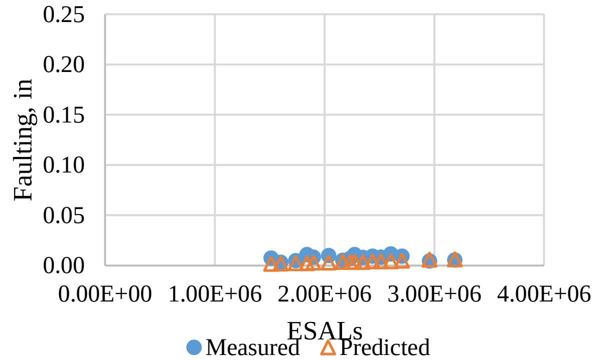

b) Cell 92 passing lane

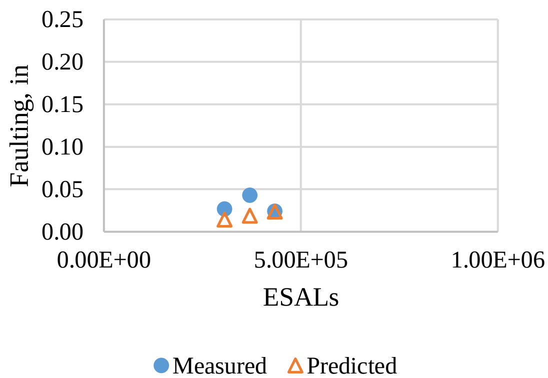

c) CSAH 9

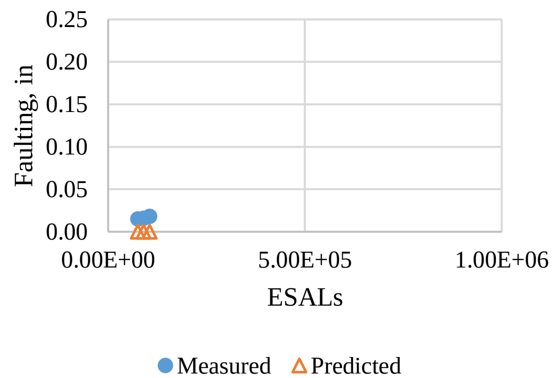

d) TH 56_2006-26

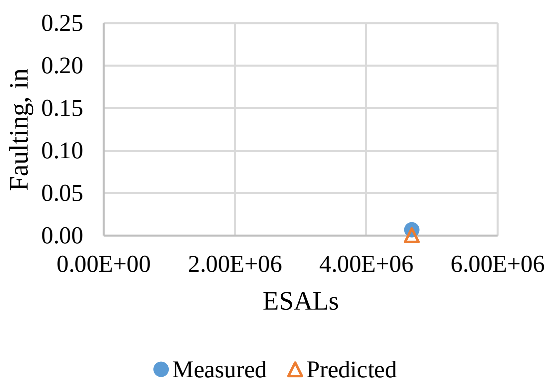

e) 06-06

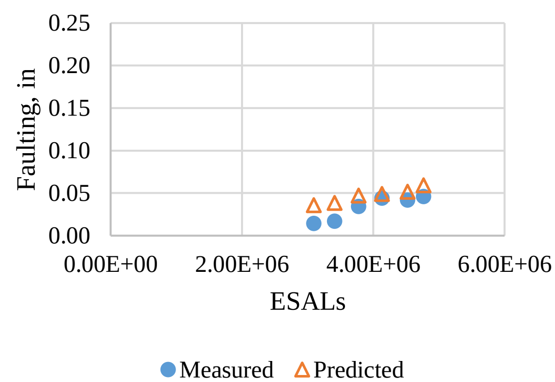

f) Cell 95 driving lane

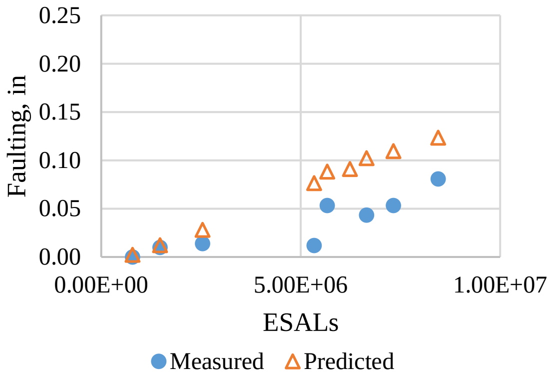

g) Cell 60 driving lane

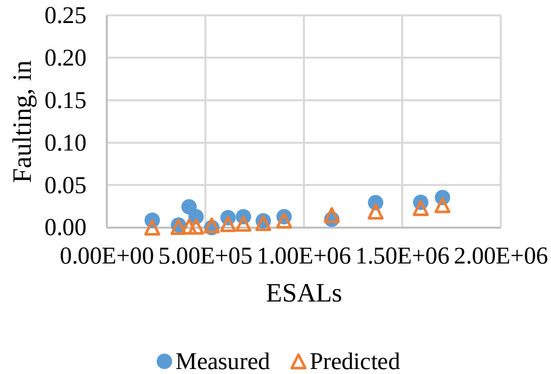

h) Cell 60 passing lane

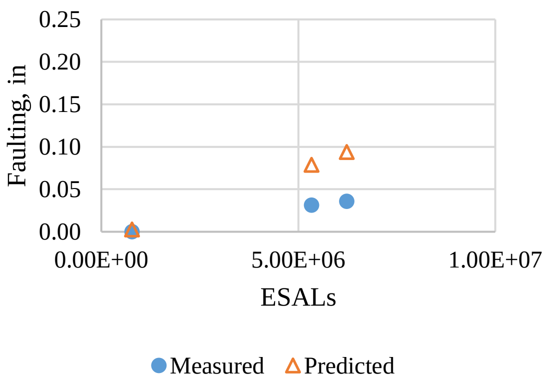

i) Cell 61 driving lane

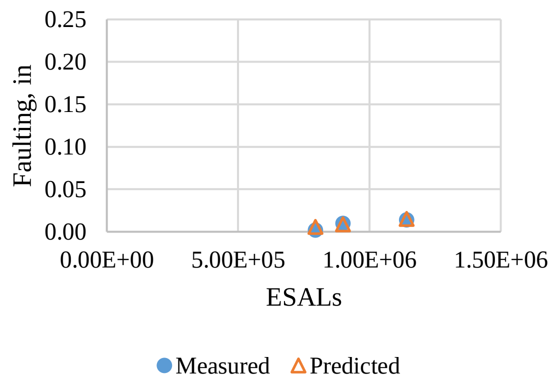

j) Cell 61 passing lane

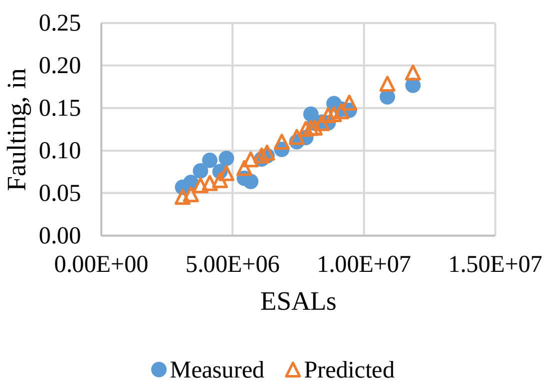

k) Cell 97 driving lane

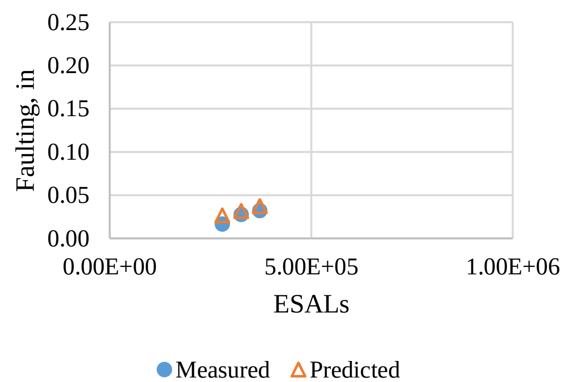

l) CSAH 7_43-607-014

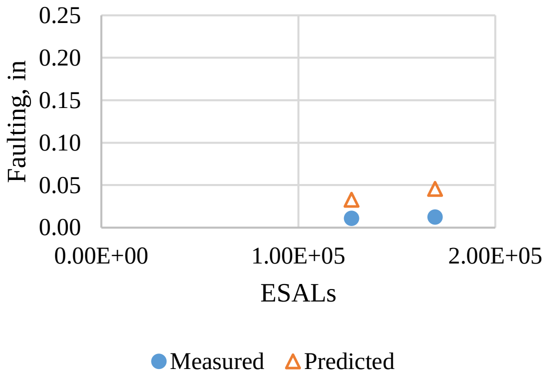

m) CSAH 22_CP 12-14-22

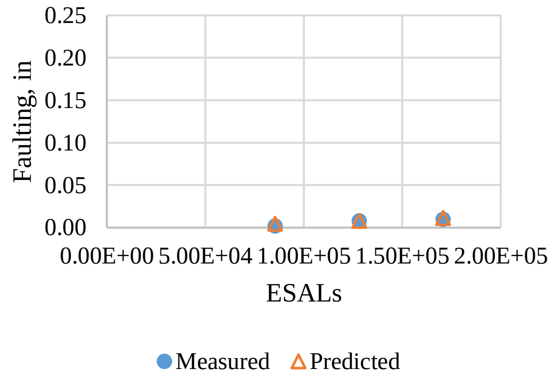

n) CSAH 22_002-622-033

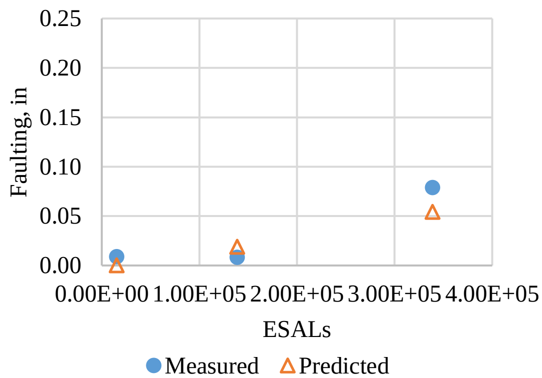

o) TH 30_0705-14

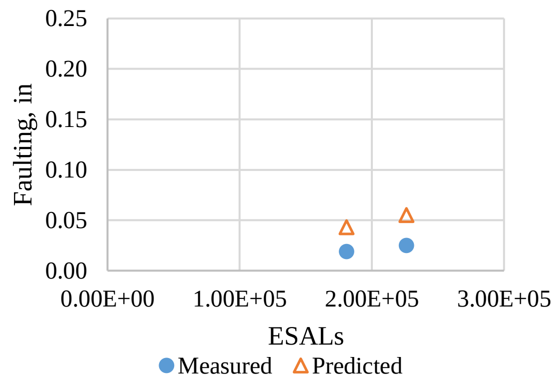

p) CSAH 22_02-622-31

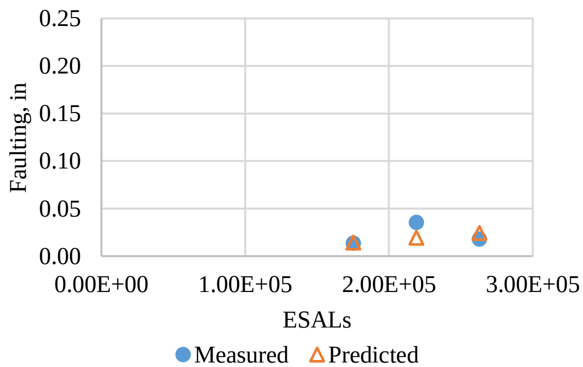

q) CSAH 2_43-602-(24-25)

Figure 5-7 Calibration section plots: measured vs. predicted faulting (full-depth).

By minimizing the ERROR function during calibration, the results are acceptable for the predicted faulting in comparison with the measured performance. A validation of the model was performed to ensure prediction of a BCOA not used within the calibration database. In addition, a comparison of the prediction between the developed model and the prediction model within the Pavement ME is presented.

Model validation was first performed on a section used in calibration, Section 22-167 in Louisiana. The activation depth was only through the PCC layer. This section is a 4 ft by 4 ft, 5-in PCC overlay constructed on an existing asphalt thickness of 9 in. This was to ensure the prediction model was accurately converted from a Microsoft excel framework to a prediction code within MATLAB. Figure 5-8 shows the predictability matches the measured faulting, therefore conversion was successful.

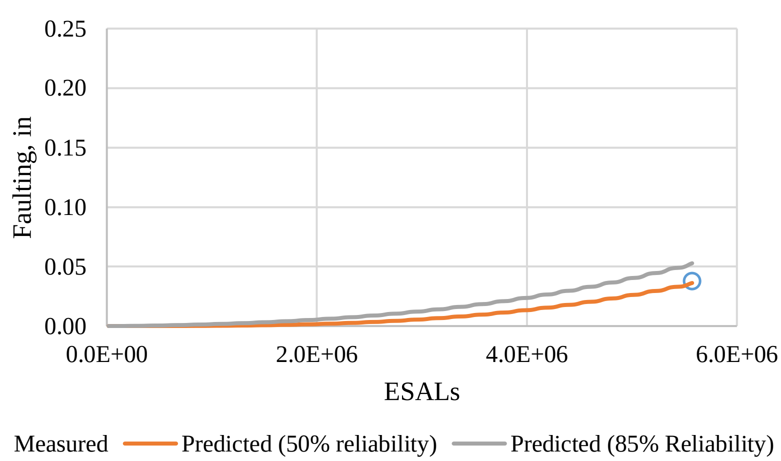

Figure 5-8 Predictive model validation using calibration section 22-167.

Validation was also performed using Cell 96 at MnROAD. This section was not used in the calibration due to the severity of joint deterioration exhibited for joints that activated through the PCC and asphalt layer during its service life. This section is a 5 ft by 6 ft, 6-in PCC overlay constructed on an existing asphalt thickness of 7 in. The prediction for joint activation through the PCC and asphalt appears to underpredict at a 50% reliability level (Figure 5-9b). This can be attributed to the measured data being taken at joints exhibiting deterioration, which likely caused larger faulting to occur.

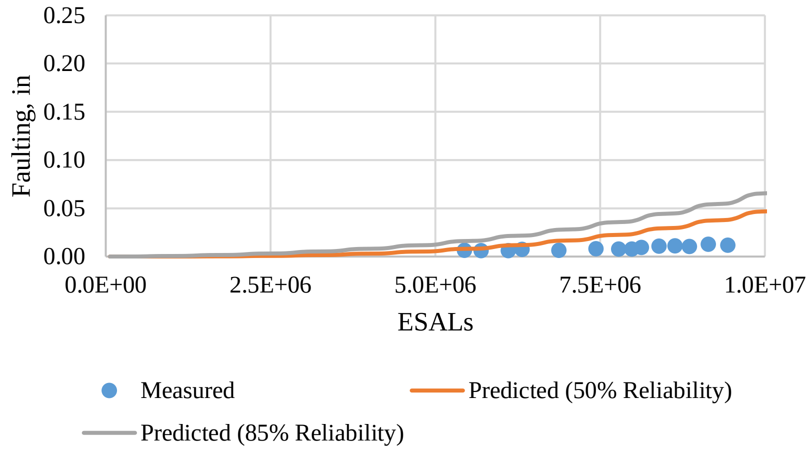

a) Partial depth

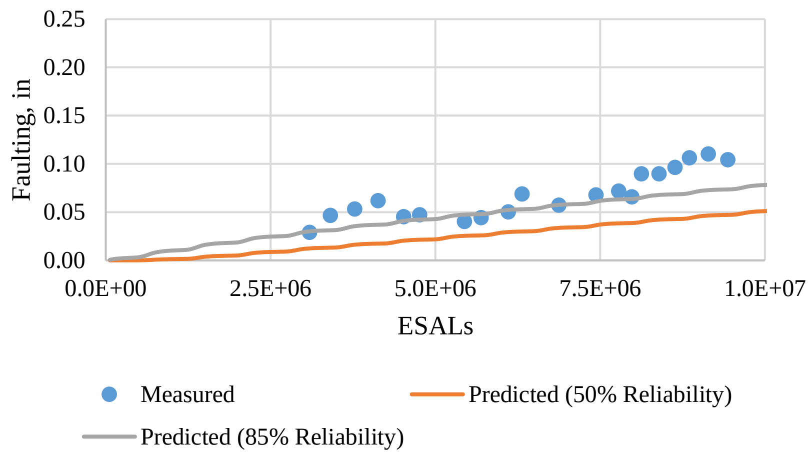

b) Full-depth

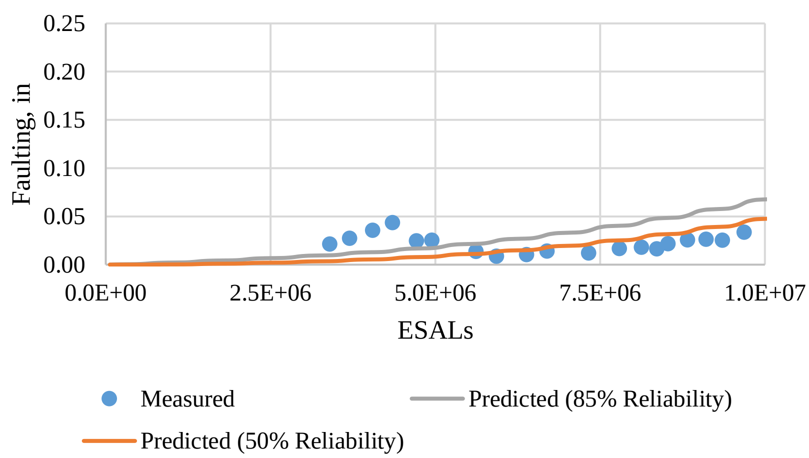

c) Both depths

Figure 5-9 Predictive model validation using MnROAD Cell 96.

Figure 5-10 shows MnROAD Cells 92 and 97, which consist of the same design except for the inclusion of dowels in Cell 92. The design is a 6-in doweled overlay with an asphalt shoulder, 10-ft joint spacing, and 1-in dowels for Cell 92. In Pavement ME, a BCOA is analyzed as a JPCP on an asphalt base, and pumping is assumed to occur at the top of the asphalt layer. The measured and predicted average faulting (both the developed model and Pavement ME) for Cell 92 and 97 can be seen in Figure 5-10. It can be seen that these models predict faulting quite well and show an improvement over Pavement ME.

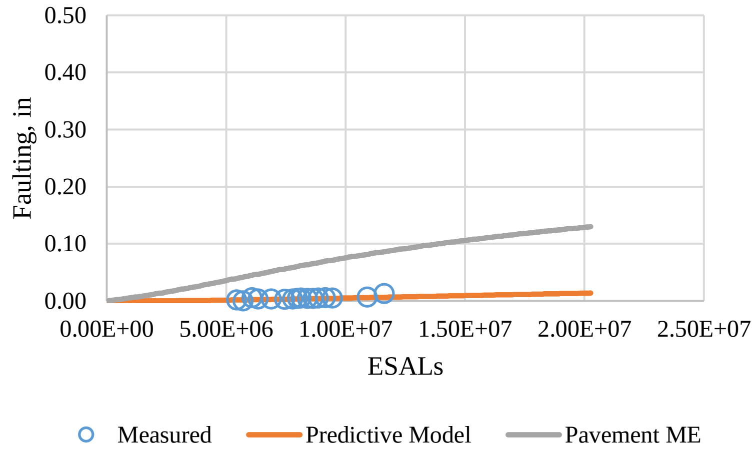

a) Cell 92: 10x12 ft PCC = 6 in, Asphalt = 7 in (1 in Dowels)

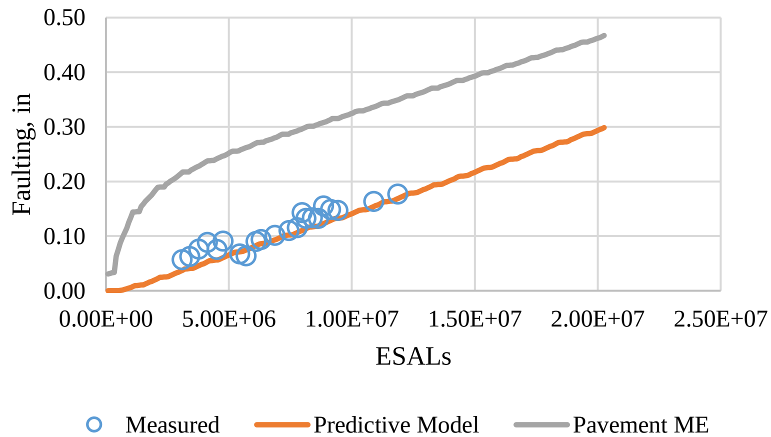

b) Cell 97: 10x12 ft PCC = 6 in, Asphalt = 7 in (No Dowels)

Figure 5-10 Predictive model validation vs. Pavment ME: MnROAD Cells 92 and 97.

5.7 Joint Faulting Model Sensitivity Analysis

A sensitivity analysis of the predicted faulting to various parameters of interest is conducted to further evaluate the different models. In order to check the adequacy of both models, three structural designs were examined. The design parameters for the first structure were as follows: 4-in undoweled PCC overlay (elastic modulus of 4.0E+06 psi, modulus of rupture of 650 psi, CTE of 5.5E-06 in/in/^{o}F, and a cement content of 500 pcy), 6-in dense graded asphalt (binder type of PG 58-16), asphalt shoulder, modulus of subgrade reaction k-value of 250 psi/in, and 10 million ESALs uniformly distributed over 20 years. The design parameters for the second structure were as follows: 6-in undoweled PCC overlay (elastic modulus of 4.0E+06 psi, modulus of rupture of 650 psi, CTE of 5.5E-06 in/in/^{o}F, and a cement content of 500 pcy), 7-in dense graded asphalt (binder type of PG 58-16), asphalt shoulder, modulus of subgrade reaction k-value of 250 psi/in, and 10 million ESALs uniformly distributed over 20 years. The default climate was Pittsburgh, Pennsylvania (Wet-Freeze). The full set of design parameters for each structure can be seen in Table 5-20. A third structure was considered and the sensitivity is presented in Appendix A (Figure A - 1 through Figure A - 13). This structure consisted of: 6-in undoweled PCC overlay (elastic modulus of 4.0E+06 psi, modulus of rupture of 650 psi, CTE of 5.5E-06 in/^{o}F/in, and a cement content of 500 pcy), 4-in dense graded asphalt (binder type of PG 58-16), asphalt shoulder, modulus of subgrade reaction k-value of 250 psi/in, and 10 million ESALs uniformly distributed over 20 years. The reliability level used for design is established as 50% reliability, but the sensitivity of reliability is also examined within this analysis.

Table 5-20 Structures examined in sensistivity analysis.

	Structure 1	Structure 2	Structure 3
PCC thickness (in)	4	6	6
PCC modulus of elasticity (psi)	4.0E+06	4.0E+06	4.0E+06
PCC modulus of rupture (psi)	650	650	650
PCC CTE (in/^{o} F/in)	5.5E-06	5.5E-06	5.5E-06
Cement content (pcy)	500	500	500
EELTG PCC depth (^{o}F/in)	-1.00802	-	-1.00802
EELTG full-depth (^{o}F/in)	-0.85639	-2.60374	-0.85639
Asphalt thickness (in)	6	7	4
Asphalt P200 (%)	7	7	7
Asphalt air voids (%)	6	6	6
Asphalt eff. binder content (%)	5	5	5
k-value (psi/in)	250	250	250
P200 of Subgrade (%)	50	50	50
Design period (months/years)	240/20	240/20	240/20
Joint spacing (ft)	6	12	6
Dowels	None	None	None
Shoulder type	Not Tied	Not Tied	Not Tied
Climate/location	Pittsburgh, PA (Wet-Freeze)	Pittsburgh, PA (Wet-Freeze)	Pittsburgh, PA (Wet-Freeze)
Month of construction	10	10	10
# Lanes in design direction	2	2	2
One-way ADT	20,000	20,000	20,000
Truck % (decimal)	0.07	0.07	0.07

Six different joint spacings were examined: 4 x 4 ft, 6 x 6 ft, 8 x 8 ft, 10 x 12 ft, 12 x 12 ft, and 15 x 12 ft. One parameter was allowed to vary at a time. The effect of the joint spacing on the resulting predicted faulting shows there is a decrease in faulting as the joint spacing decreases. It should be noted that as the joint spacing decreases, the decrease in faulting may not result in the same level of roughness. As there are more joints with a smaller joint spacing, the amount of average faulting does not need to be as large to produce the same ride for a section with more faulting and a larger joint spacing (DeSantis et al. 2016). This was shown in Chapter 2. The different parameters examined include joint spacing, PCC thickness, elastic modulus of the PCC, inclusion of dowels and dowel diameter, shoulder type, asphalt thickness, P200 of the asphalt mixture, percent air voids of the asphalt mixture, percent effective binder of the asphalt mixture, modulus of subgrade reaction, P200 of the subgrade, climate (asphalt stiffness and binder type also varied based on climate), traffic, and reliability. The asphalt binder type was selected using LTPPBIND for the different locations.

5.7.1 Faulting Model Sensitivity Analysis – Structure One

The first structure examined had a thin overlay of 4 in and an asphalt layer of 6 in. The larger panel sizes are not included in the following plots because large panels would fail prematurely due to cracking for such a thin overlay and would therefore never be constructed. For this structure, based on the FSR, the smaller panel sizes are likely to have joints that activate either through the PCC layer and/or through the PCC and asphalt layer within the section. Therefore, all plots for the smaller panel sizes include 3 plots that show faulting that develops for 1. when the joint activates only through the PCC, 2. when the joint activates through both the PCC and asphalt (full-depth), and 3. when both 1 and 2 occur. Figure 5-11 shows an increase in joint spacing increases the magnitude of faulting. This is due to the increase in deflections as the joint spacing increases, causing differential energy to change accordingly.

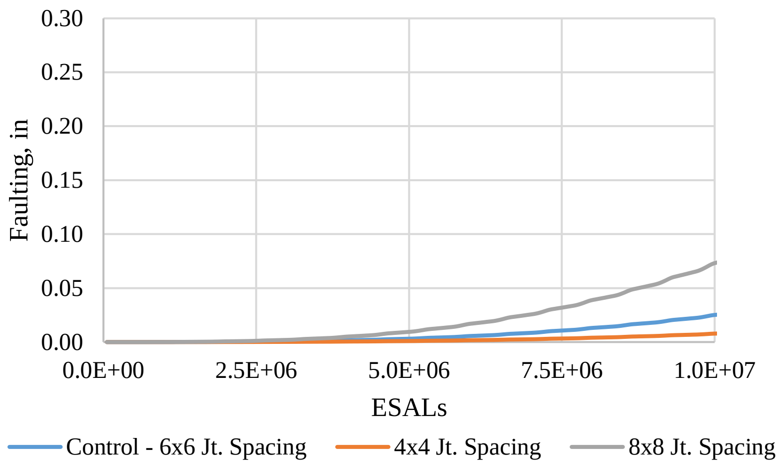

a) Partial depth

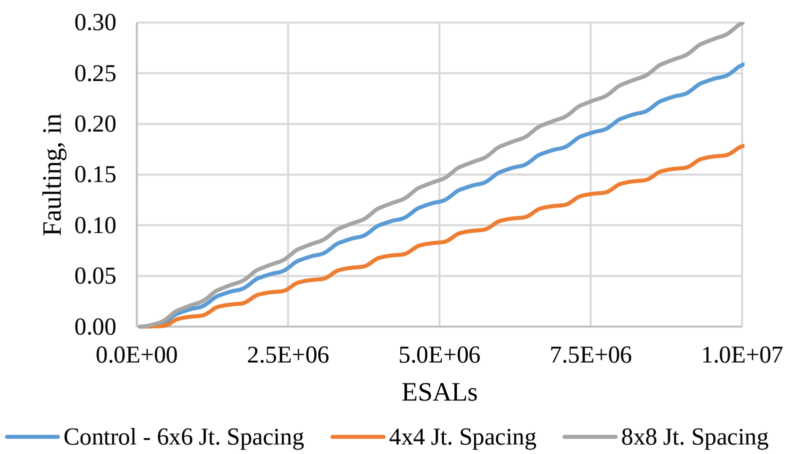

b) Full-depth

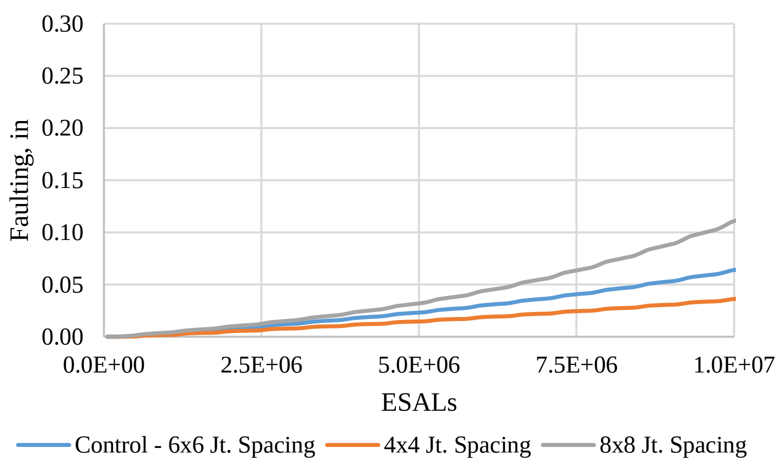

c) Both depths

Figure 5-11 Effect of joint spacing on predicted faulting for Structure 1.

PCC overlay thickness does affect the predicted faulting for the different depths of joint activation. This can be seen in Figure 5-12. An increase in the PCC overlay thickness results in a lower predicted faulting, and vice versa. This can be attributed to the likelihood of a decrease in deflections due to an increase in the thickness of the PCC overlay.

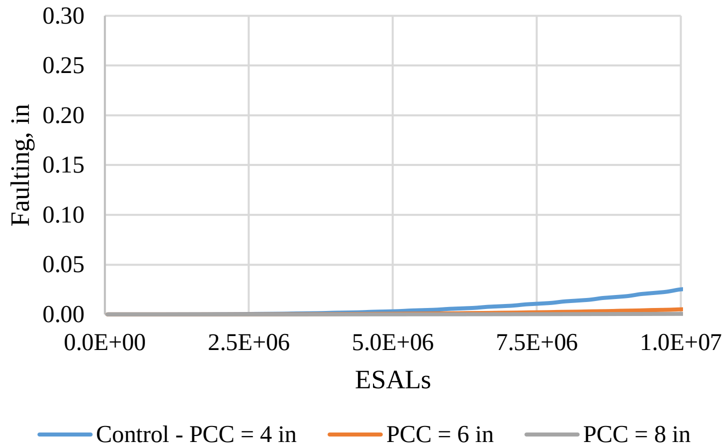

a) Partial depth

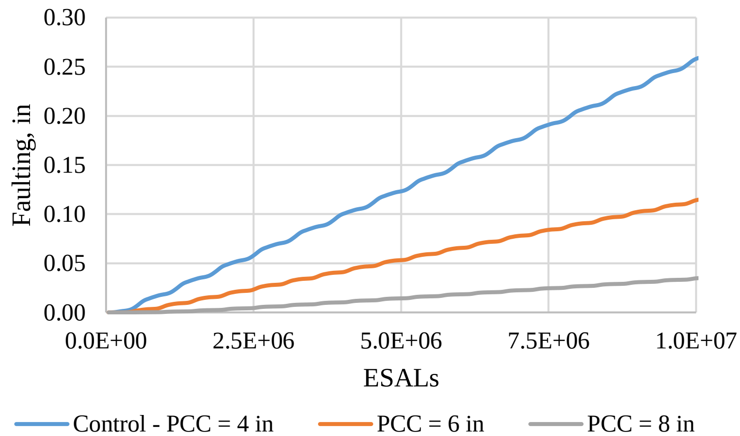

b) Full-depth

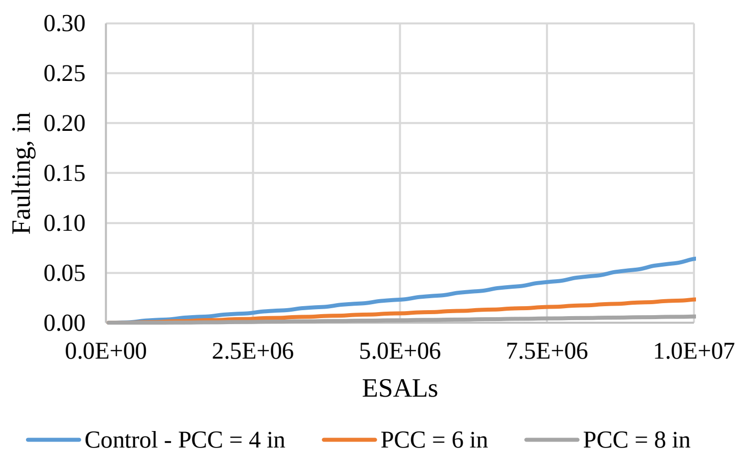

c) Both depths

Figure 5-12 Effect of PCC overlay thickness on predicted faulting for Structure 1.

Shoulder type also has a significant effect on predicted faulting for the different depths of joint activation, as expected. This can be seen in Figure 5-13. A tied PCC shoulder will limit the deflections, overall deflection basin, and will result in a lower differential energy. Therefore, a tied shoulder decreases predicted faulting in comparison with an asphalt shoulder.

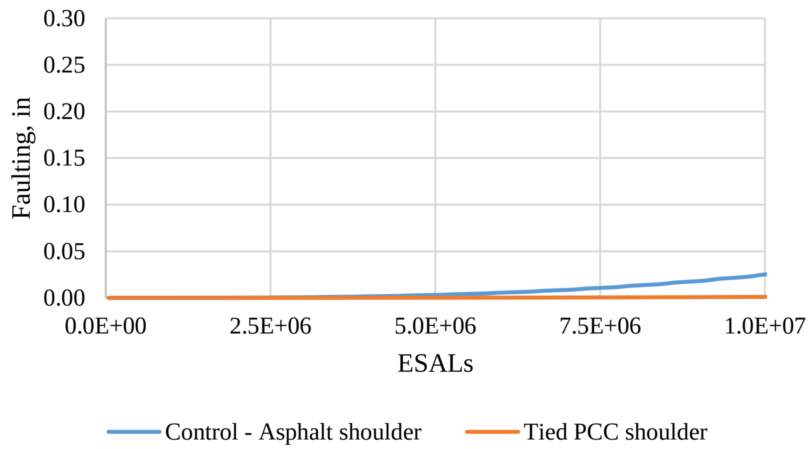

a) Partial depth

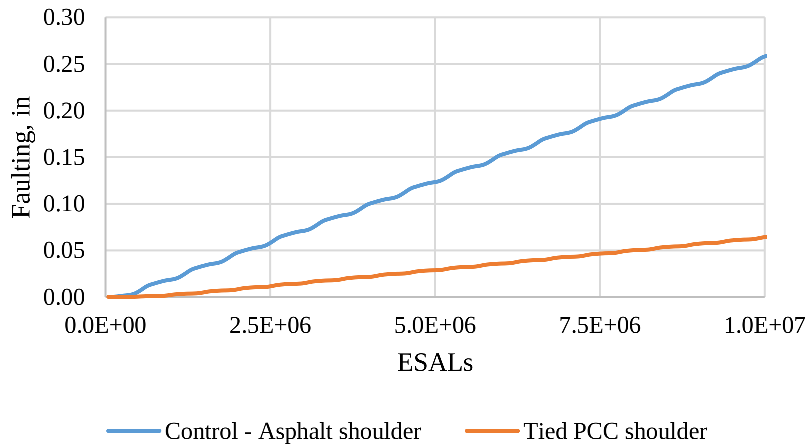

b) Full-depth

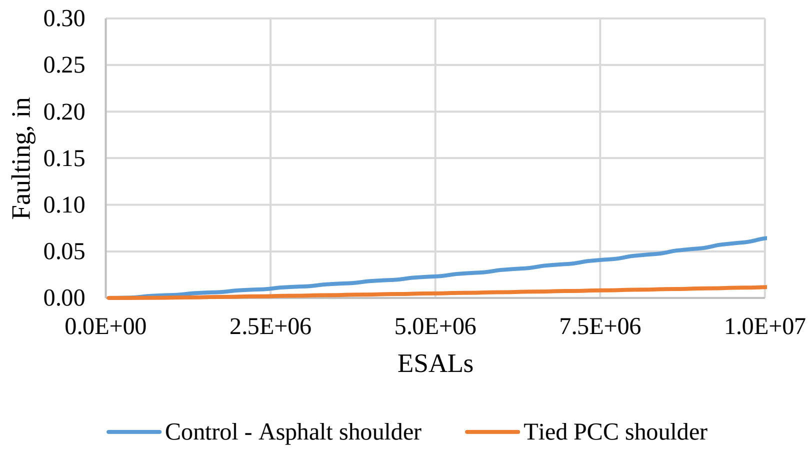

c) Both depths

Figure 5-13 Effect of shoulder type on predicted faulting for Structure 1.

The next variable examined that has a significant effect on predicted faulting is the inclusion of dowel bars. Two different diameters were examined, 1 in and 1.25 in. The PCC overlays are typically going to be between 4 to 6 in and therefore the maximum suggested dowel diameter is 1.25 in and the minimum suggested is 1 in. For this particular structure, it is very unlikely to contain dowel bars due to the thin overlay. The use of dowels greatly reduces the potential for faulting to develop. This can be seen in Figure 5-14. The traffic was extended out to 50×10^6 ESALs to fully show the trends.

In addition, when applying 50 million ESALs over a 20-year analysis period, the magnitude of differential energy is extremely large for Structure 1. The significant amount of differential energy within the first five years results in an infinite amount of predicted faulting when the joint activates through the PCC and asphalt layer. The practicability of this structure with that significant level of traffic over that span of time is unrealistic. This shows the prediction model will not allow users to provide unrealistic inputs, otherwise infinite faulting will be predicted due to the significant magnitude of differential energy.

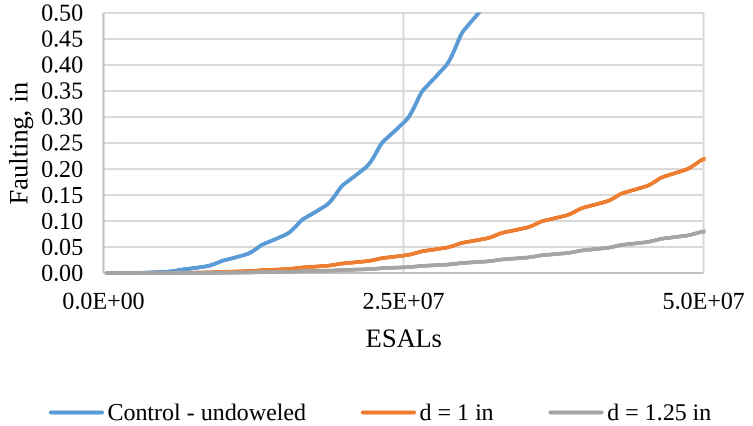

a) Partial depth

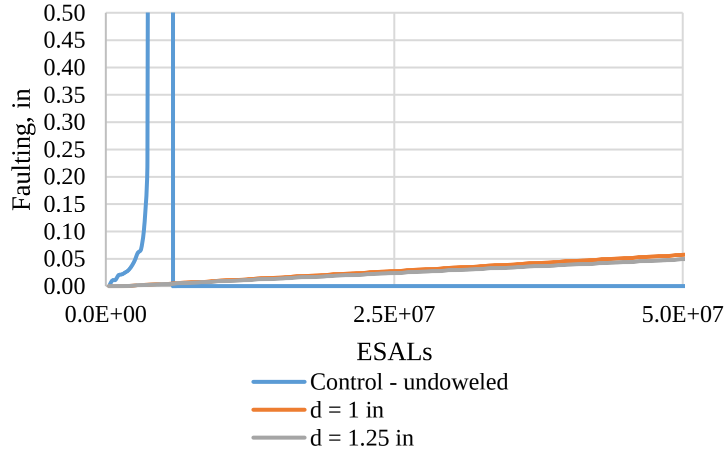

b) Full-depth

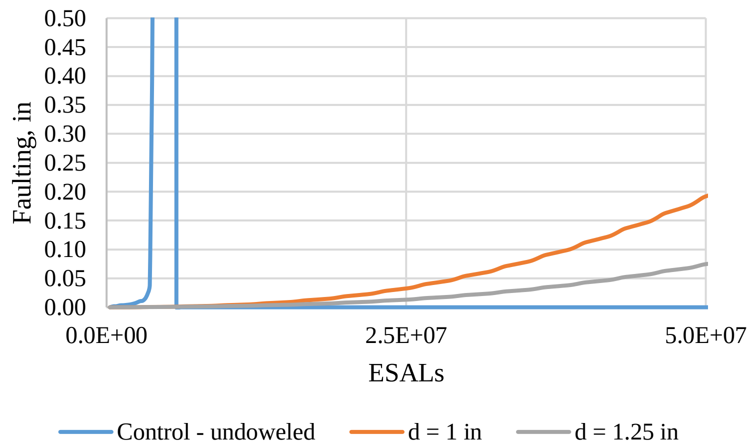

c)Both depths

Figure 5-14 Effect of dowels on predicted faulting for Structure 1.

PCC elastic modulus also has an effect on predicted faulting for the different depths of joint activation. This can be seen in Figure 5-15. However, the effect is insignificant when the joint activates only through the PCC layer. An increase in the PCC elastic modulus, results in a decrease in the predicted faulting. The overall increase in flexural rigidity can reduce the magnitude of deflections, increase the radius of relative stiffness, as well as reduce joint deterioration.

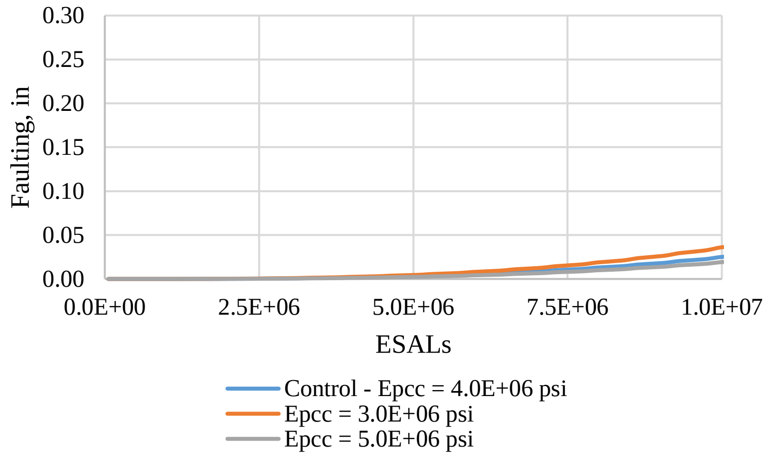

a) Partial depth

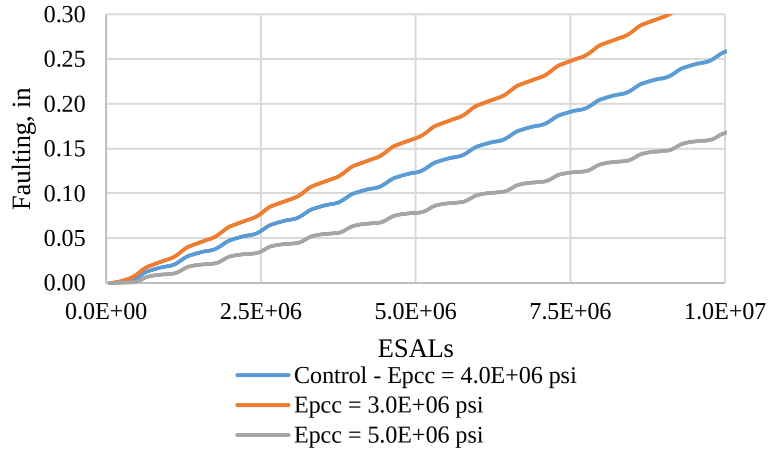

b) Full-depth

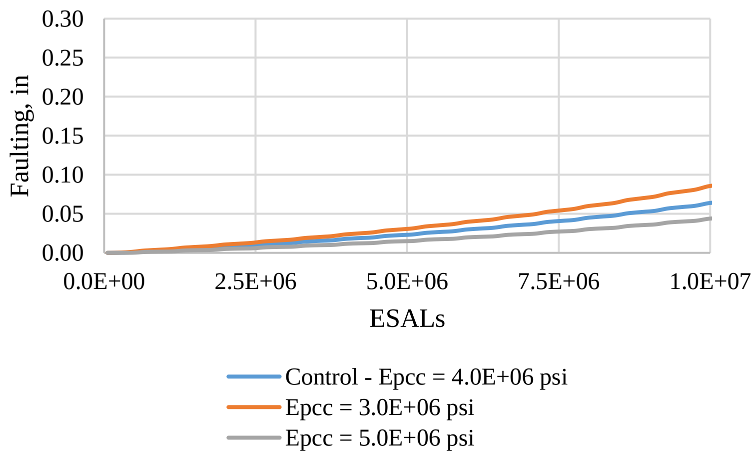

c) Both depths

Figure 5-15 Effect of PCC elastic modulus on predicted faulting for Structure 1.

The next variable examined that also has an effect on predicted faulting is the modulus of subgrade reaction, k-value. Three values were examined, 100 psi/in, 250 psi/in, and 400 psi/in. An increase in the k-value should result in a decrease in deflections, and therefore decrease the predicted faulting. This is the case when the joint activates full-depth, however when the joint only activates through the PCC layer there is a smaller effect due to the continuity of the asphalt layer across the joint at the bottom of the PCC. This can be seen in Figure 5-16.

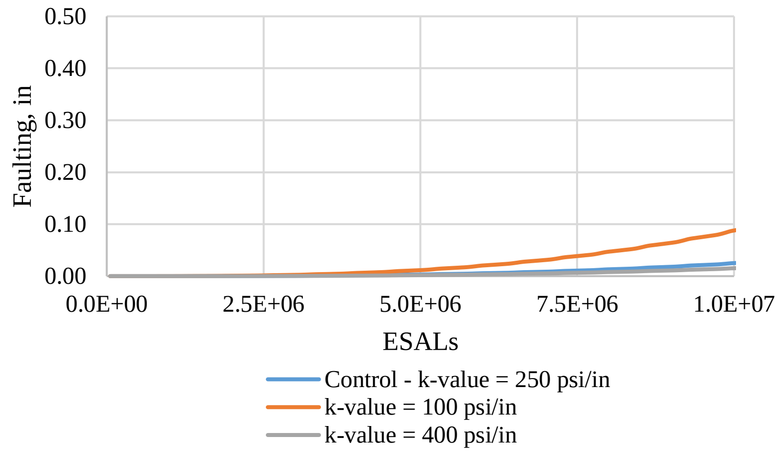

a) Partial depth

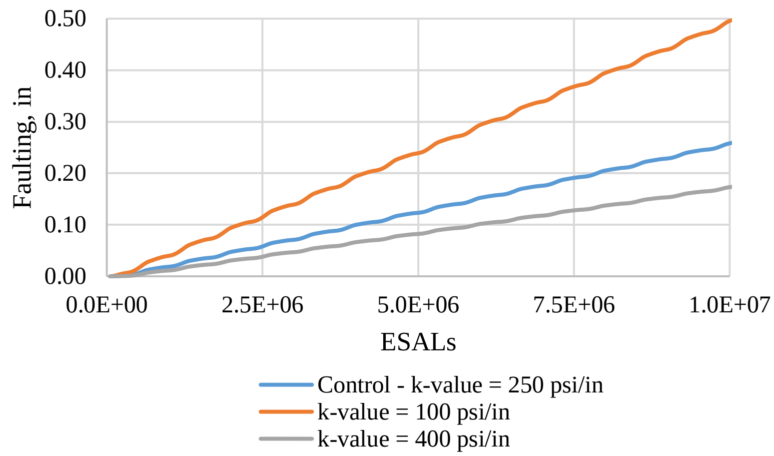

b) Full-depth

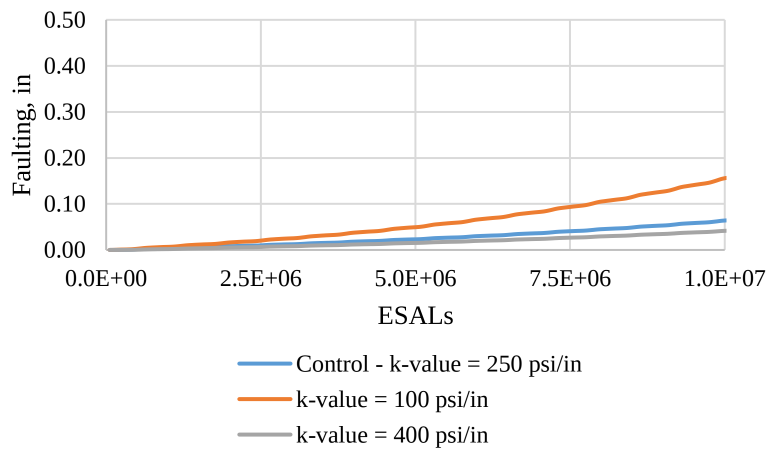

c) Both depths

Figure 5-16 Effect of modulus of subgrade reaction on predicted faulting for Structure 1.

Asphalt thickness has a significant effect on the predicted faulting for the different depths of joint activation. This can be seen in Figure 5-17. An increase in the asphalt layer thickness results in a lower predicted faulting. This can be attributed to the likelihood of a decrease in deflections due to an increase in the stiffness of the asphalt layer.

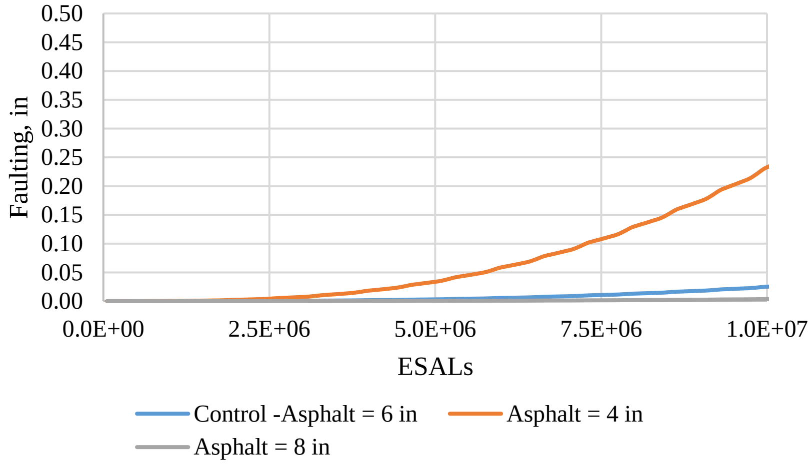

a) Partial depth

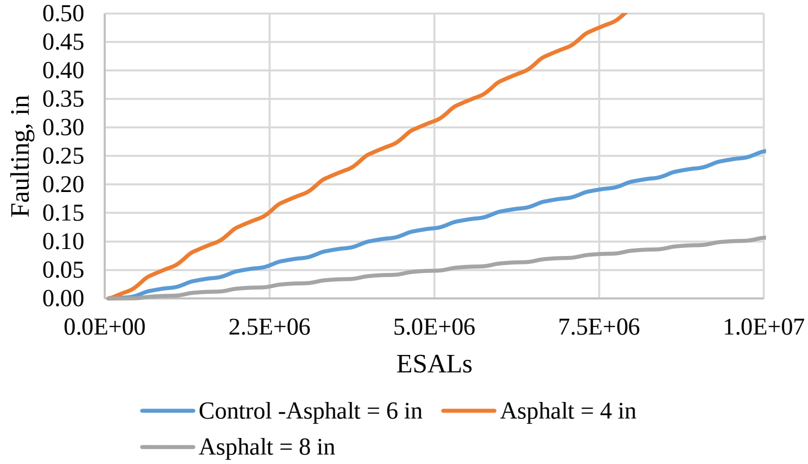

b) Full-depth

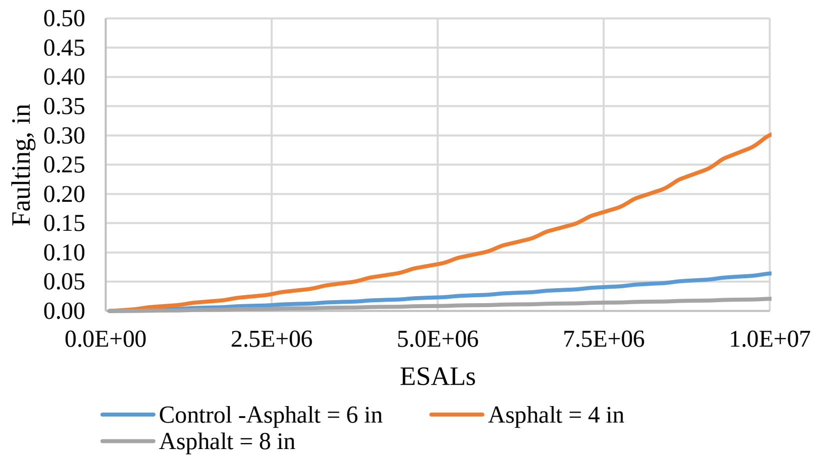

c) Both depths

Figure 5-17 Effect of asphalt thickness on predicted faulting for Structure 1.

Another component of the analysis is to evaluate the sensitivity of the erosion model. There are three components within this model, P200, percent air voids in the wheelpath, and percent of effective binder content within the asphalt mixture. These three variables were determined to predict the resistivity to erosion of a given asphalt mixture. Three levels of each variable are examined, including the control. As expected, due to the structure of the model and the different variables and the range of the variables considered, P200 is the most sensitive. This was followed by percent air voids and then percent effective binder. The sensitivity to each of these parameters can be seen in Figure 5-18 through Figure 5-20, respectively. The erodibility of the asphalt layer will not influence the development of faulting if the joint activates through the asphalt layer since it is the layer beneath the asphalt that will then be eroded. However, these plots are still included to be able to show the average joint faulting, which includes both depths of joint activation.

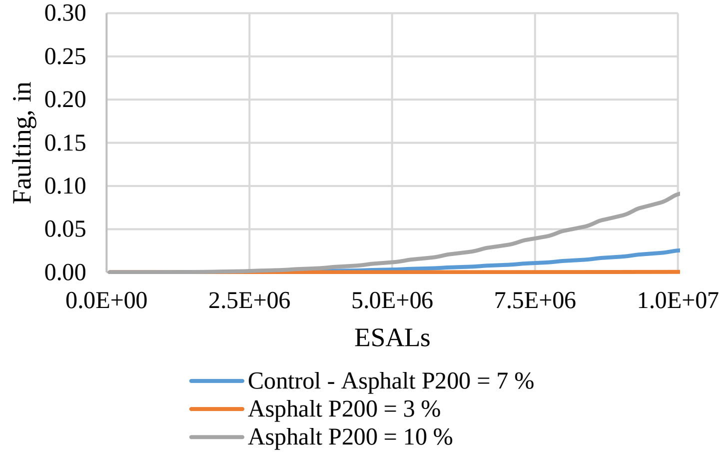

a) Partial depth

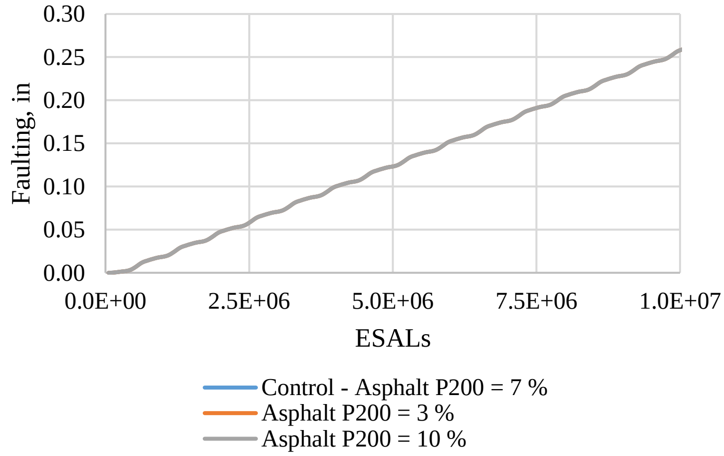

b) Full-depth

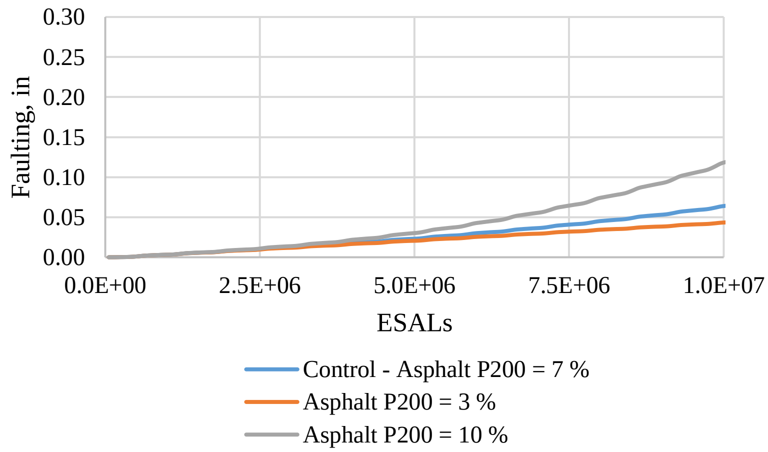

c) Both depths

Figure 5-18 Effect of erodibility (P200) on predicted faulting for Structure 1.

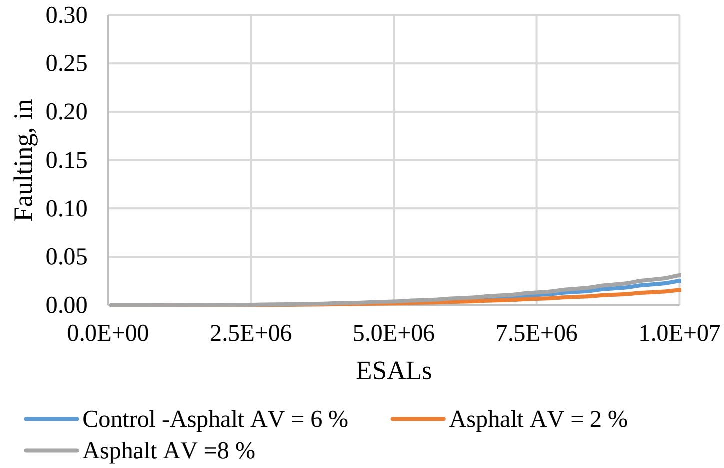

a) Partial depth

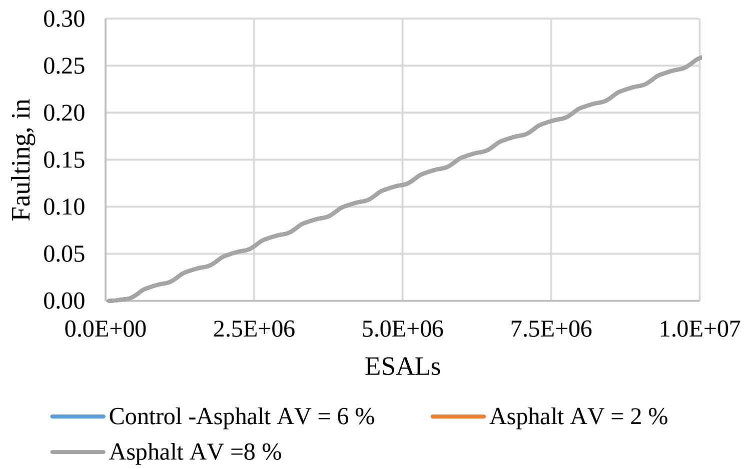

b) Full-depth

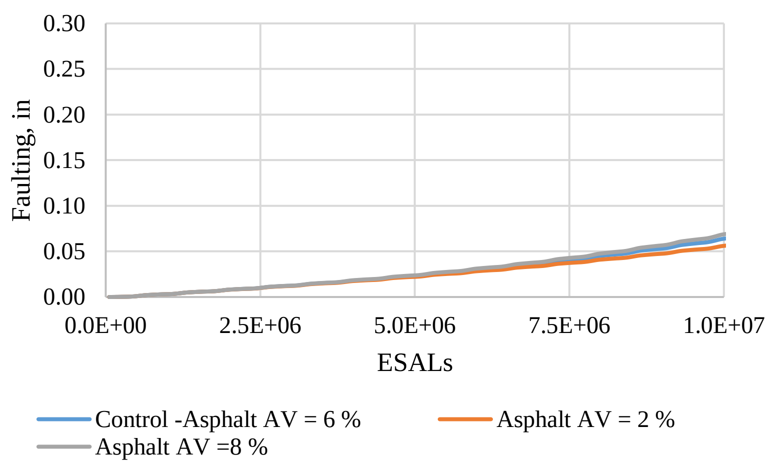

c) Both depths

Figure 5-19 Effect of erodibility (air voids) on predicted faulting for Structure 1.

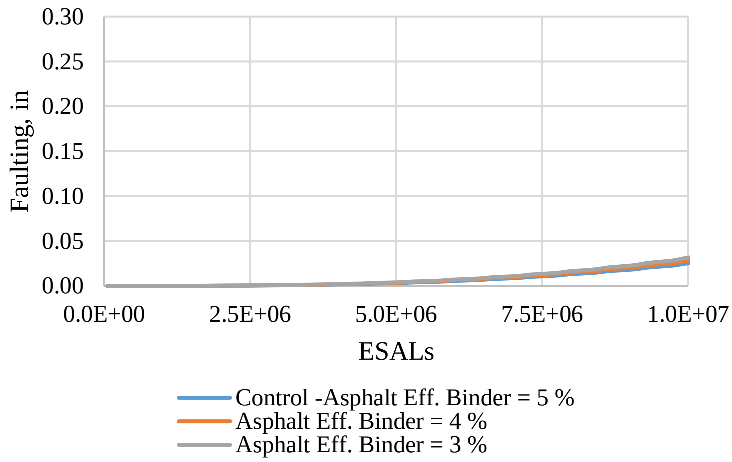

a) Partial depth

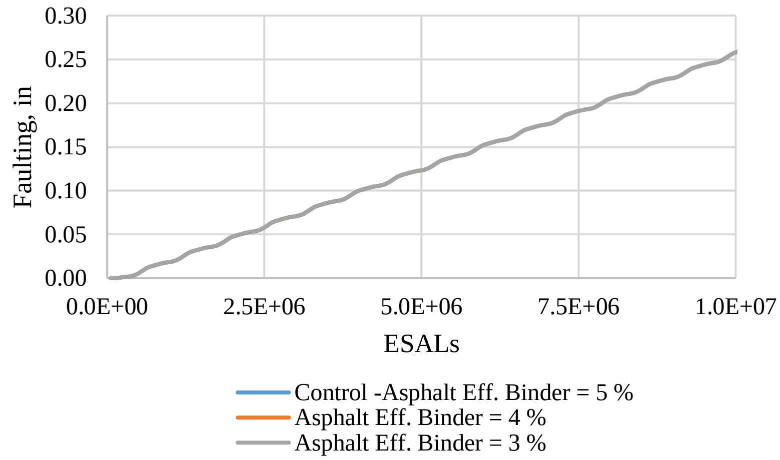

b) Full-depth

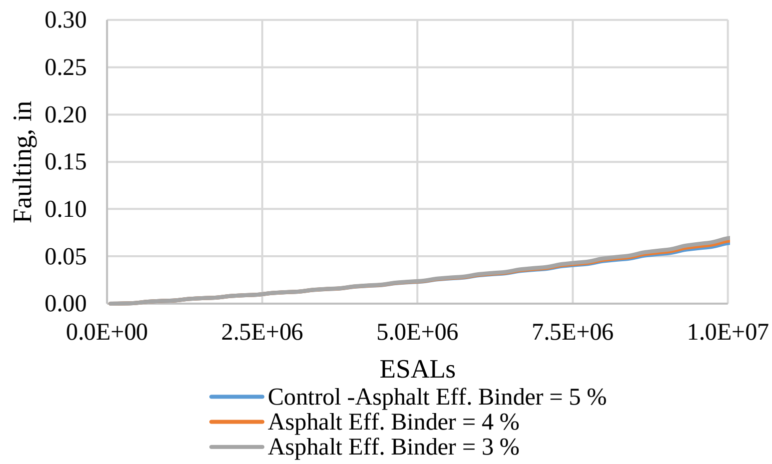

c) Both depths

Figure 5-20 Effect of erodibility (effective binder content) on predicted faulting for Structure 1.

Another variable that was examined within the sensitivity analysis was the effect of traffic volume. Four traffic levels were examined, 5, 10 (control), 20, and 50 million ESALs over a 20-year analysis period. Traffic was distributed uniformly throughout the day as defined in Table 5-1 (ARA 2004). The effects of traffic on predicted faulting for the first structure examined can be seen in Figure 5-21. When the joint only activates through the PCC layer, minimal faulting is observed for lower levels of traffic. This is attributed to the amount of time and traffic for the PCC to become debonded from the asphalt layer. As the interface becomes debonded, an increase in deflections is observed and results in larger differential energy. In conjunction with the increase in deflections, the debonded region is likely to continue to increase in size, which will contribute to additional erosion at the top of the asphalt layer. As this process continues over time and a significant amount of traffic loadings are accumulated, faulting increases exponentially.

In addition, when applying 50 million ESALs over a 20-year analysis period, the magnitude of differential energy is extremely large for Structure 1. The significant amount of differential energy within the first five years results in an infinite amount of predicted faulting when the joint activates through the PCC and asphalt layer. The practicability of this structure with that significant level of traffic over that span of time is unrealistic. This shows the prediction model will not allow users to provide unrealistic inputs, otherwise infinite faulting will be predicted due to the significant magnitude of differential energy.

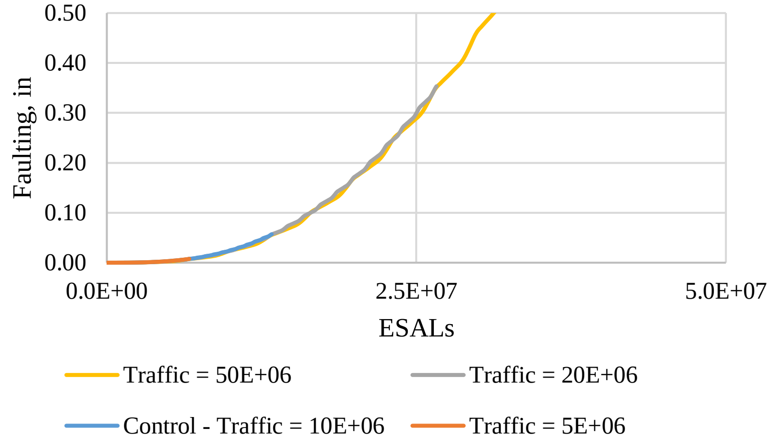

a) Partial depth

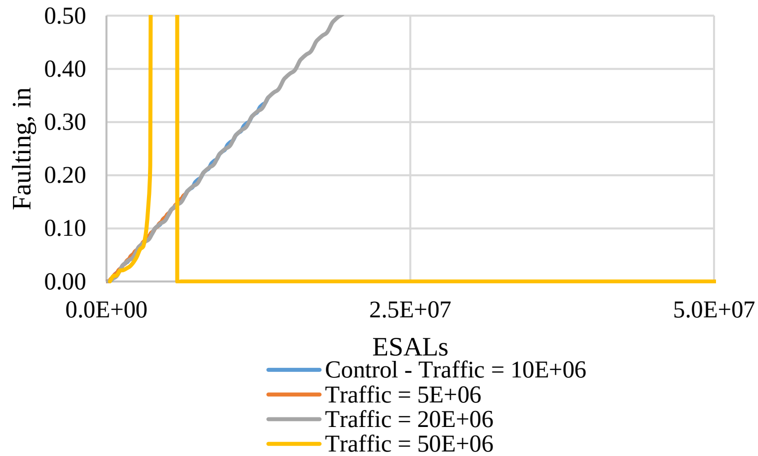

b) Full-depth

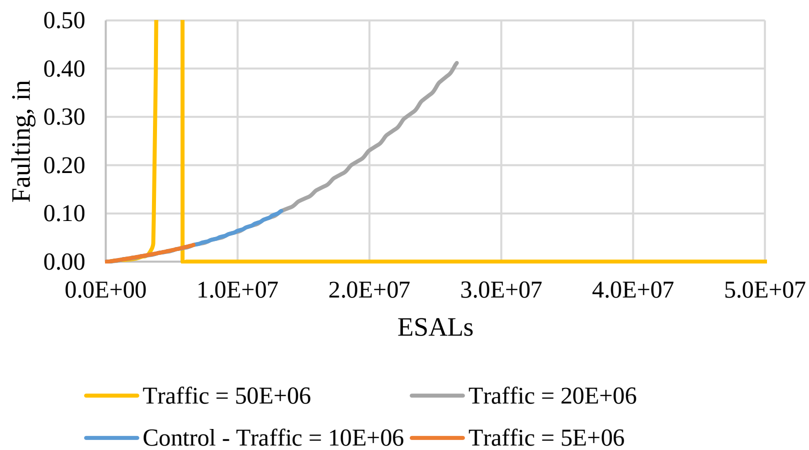

c) Both depths

Figure 5-21 Effect of traffic on predicted faulting for Structure 1.

Four geographical locations were examined to check the sensitivity of climate. The four different locations (including the control section) include, Pittsburgh, PA, Phoenix, AZ, Miami, FL, and Rapid City, SD. These four locations were selected because they represent the four major climate regions, wet/freeze, dry/no-freeze, wet/no-freeze, and dry/freeze, respectively. Along with the different climates, different asphalt elastic moduli were used based on binder selection using LTPPBIND. The following binder grades were used, PG 58-16 (Pittsburgh), PG 70-10 (Phoenix), PG 70-10 (Miami), and PG 58-28 (Rapid City).

The predicted faulting between Phoenix and Miami are very similar when the joint only activates through the PCC, which is attributed to the same asphalt binder grade. The predicted faulting for Pittsburgh and Rapid City are also very similar to Phoenix and Miami. Based on the different climates, appropriate binder grades were selected. The different binder grades account for the site-specific climate, and therefore reduce the significance in fault prediction when the joint only activates through the PCC layer. Additionally, cold climates typically have softer binders to be able to account for winter and summer temperature ranges. With relatively high temperatures in the summer, asphalt in colder temperature regions with a soft binder is less stiff then in the warmer temperature regions where a very stiff binder can be used without developing thermal cracking.

When the joint activates through the PCC and asphalt layer, the prediction between Pittsburgh and Rapid City are almost identical. This can be attributed to similar climates (colder climates than Phoenix or Miami), which can result in a stiff layer beneath the asphalt more often than climates such as Phoenix or Miami. In addition, Pittsburgh and Rapid City both begin to develop faulting prior to Phoenix and Miami. The colder climates result in larger joint widths, which will cause the joints to activate through the PCC and asphalt layer at a faster rate than warmer climates such as Phoenix and Miami. Miami has the largest predicted faulting, which is attributed to a less stiff subgrade (accounted for by the freezing ratio) as well as being in a wet climate (accounted for by WETDAYS). These variables have been previously defined within the Climate section of Chapter 5 (5.2.1 Climate).

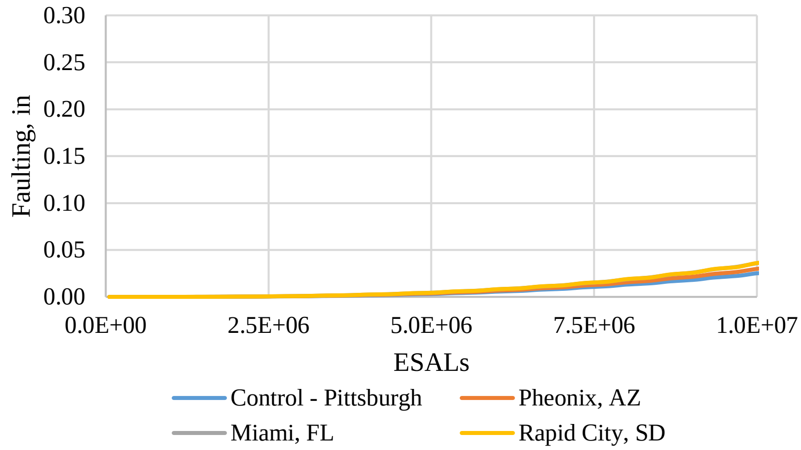

a) Partial depth

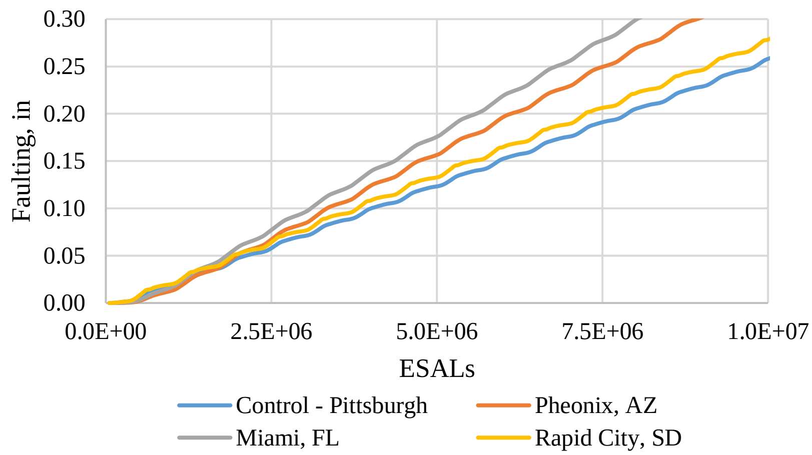

b) Full-depth

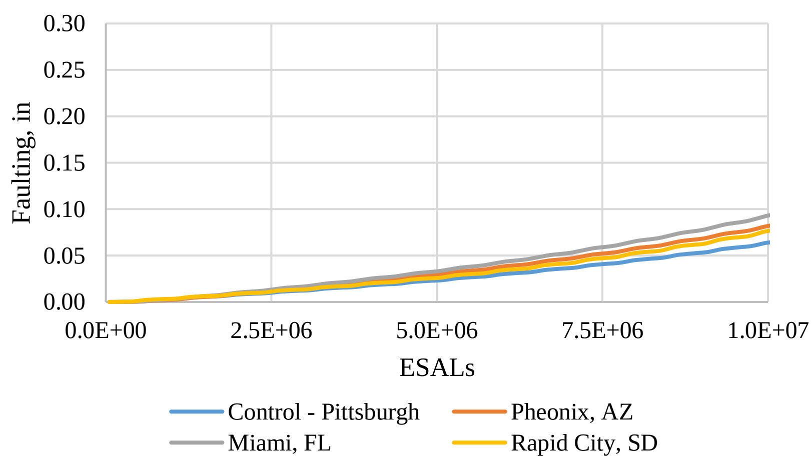

c) Both depths

Figure 5-22 Effect of climate on predicted faulting for Structure 1.

The final variable examined for the first structure is the reliability. Four levels were examined, 50% (control), 75%, 85% (BCOA-ME design guide reliability level), and 95%. As a higher level of reliability is desired, a greater magnitude of faulting will be predicted. This can be seen in Figure 5-23.

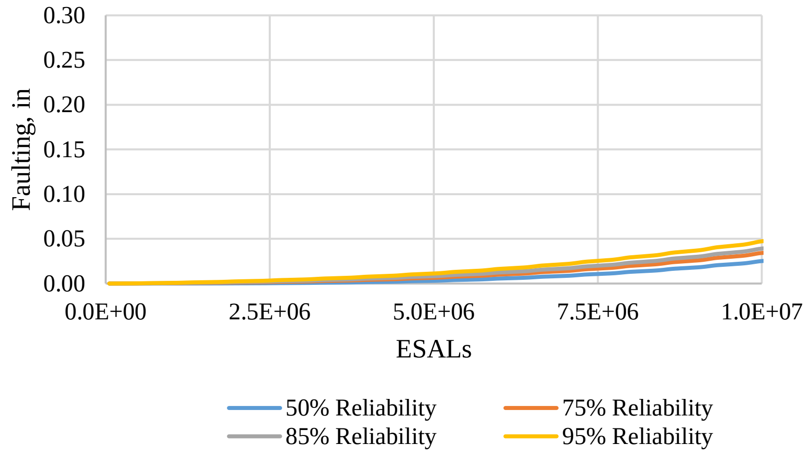

a) Partial depth

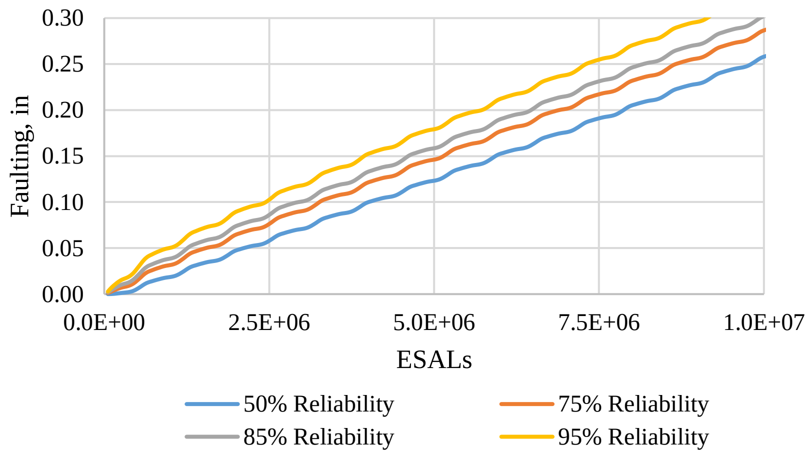

b) Full-depth

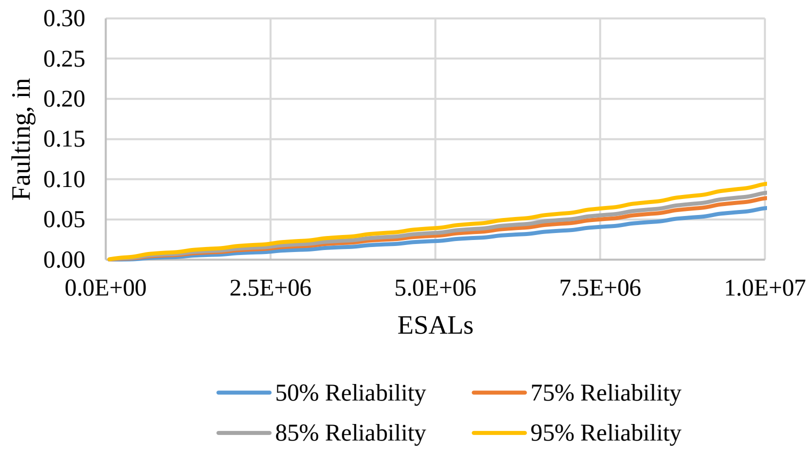

c) Both depths

Figure 5-23 Effect of reliability on predicted faulting for Structure 1.

5.7.2 Faulting Model Sensitivity Analysis – Structure Two

The second structure examined had an overlay of 6 in and a remaining asphalt layer thickness of 7 in. The larger panel sizes are included in the following plots and are the main focus for the sensitivity analysis of the second structure. For this structure, based on the FSR, the smaller panel sizes are likely to develop joints that activate either through the PCC layer and/or through the PCC and asphalt layer within the section. However, plots are only generated for the comparison of full-depth joints. The effects of joint spacing show, as the joint spacing increases, the magnitude of faulting will also increase, as is shown in Figure 5-24. This is due to the increase in deflections as joint spacing increases, causing differential energy to change accordingly.

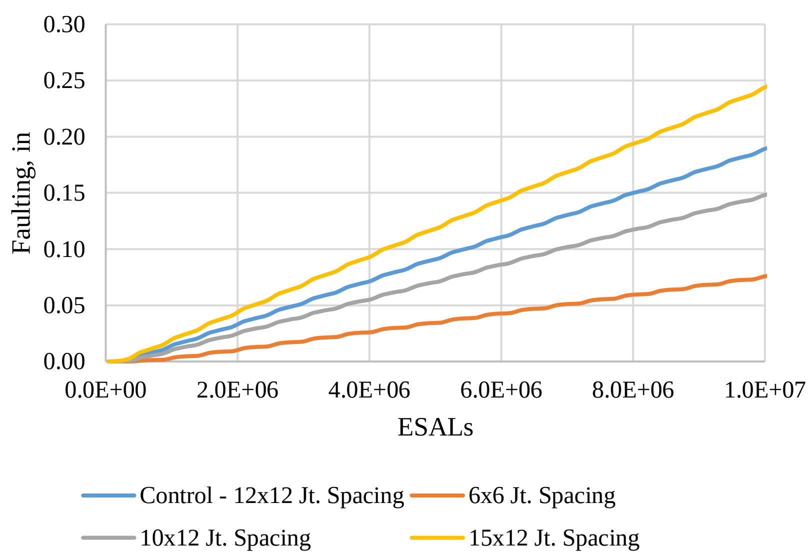

Figure 5-24 Effect of joint spacing on predicted faulting for Structure 2.

PCC overlay thickness does have an effect on predicted faulting for activated joints through the PCC and asphalt layer. This can be seen in Figure 5-25. An increase in the PCC overlay thickness results in a lower predicted faulting, and vice versa. This can be attributed to the likelihood of a decrease in deflections due to an increase in the thickness of the PCC overlay.

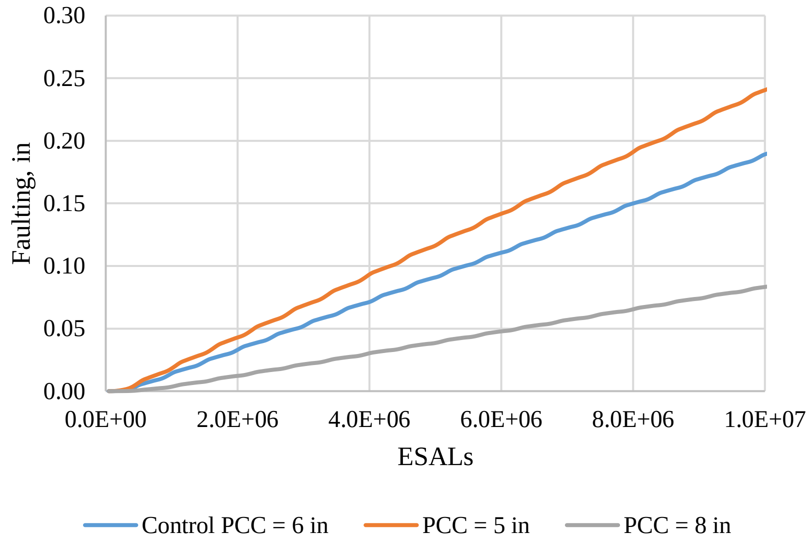

Figure 5-25 Effect of PCC overlay thickness on predicted faulting for Structure 2.

Shoulder type also has a significant effect on predicted faulting for activated joints through the PCC and asphalt layer, as expected. This can be seen in Figure 5-26. A tied PCC shoulder will limit the deflections and overall deflection basin and will result in lower differential energy. Therefore, a tied shoulder decreases predicted faulting in comparison with an asphalt shoulder.

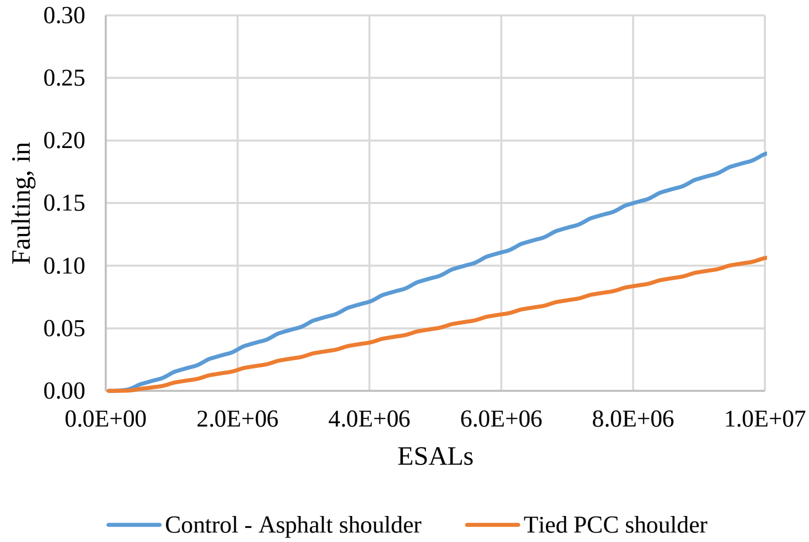

Figure 5-26 Effect of shoulder type on predicted faulting for Structure 2.

The next variable examined that has a significant effect on predicted faulting is the inclusion of dowel bars. Two different diameters were examined, 1 in and 1.25 in. The PCC overlay for Structure 2 is 6 in and therefore the maximum suggested dowel diameter is 1.25 in and the minimum suggested is 1 in. The use of dowels greatly reduces the potential for faulting to develop. This can be seen in Figure 5-27. The traffic was extended out to 50 x 10^6 ESALs to fully show the trends. The y-axis is also extended to 0.5 in due to the increase in predicted faulting.

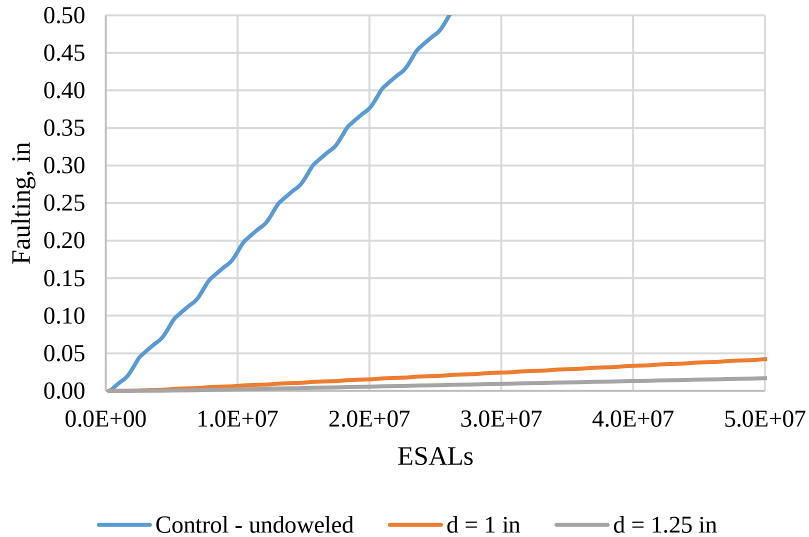

Figure 5-27 Effect of dowels on predicted faulting for Structure 2.

PCC elastic modulus also has an influence on predicted faulting for activated joints through the PCC and asphalt layer. This can be seen in Figure 5-28. An increase in the PCC elastic modulus, results in a decrease in the predicted faulting. The overall increase in flexural rigidity can reduce the magnitude of deflections, increase the radius of relative stiffness, as well as reduce joint deterioration.

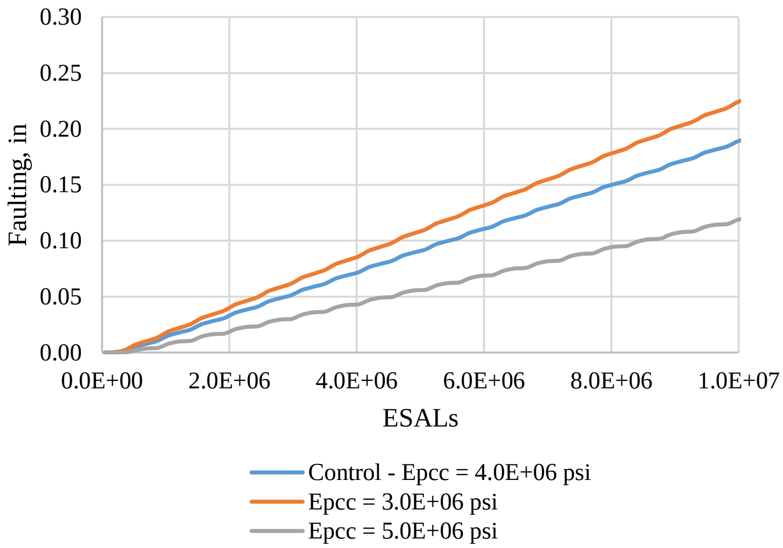

Figure 5-28 Effect of PCC elastic modulus on predicted faulting for Structure 2.

The next variable examined that also has an effect on predicted faulting is the modulus of subgrade reaction, k-value. Three values were examined, 100 psi/in, 250 psi/in, and 400 psi/in. An increase in the k-value should result in a decrease in deflections, and therefore a decrease in the predicted faulting. This can be seen in Figure 5-29.

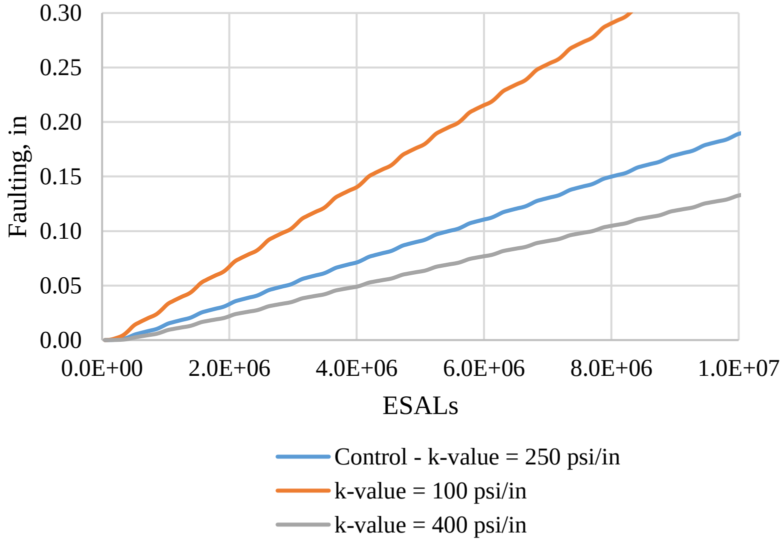

Figure 5-29 Effect of modulus of subgrade reaction on predicted faulting for Structure 2.

Asphalt thickness has a significant effect on the predicted faulting for activated joints through the PCC and asphalt layer. This can be seen in Figure 5-30. An increase in the asphalt layer thickness results in a lower predicted faulting. This can be attributed to the decrease in deflections due to an increase in the stiffness of the asphalt layer.

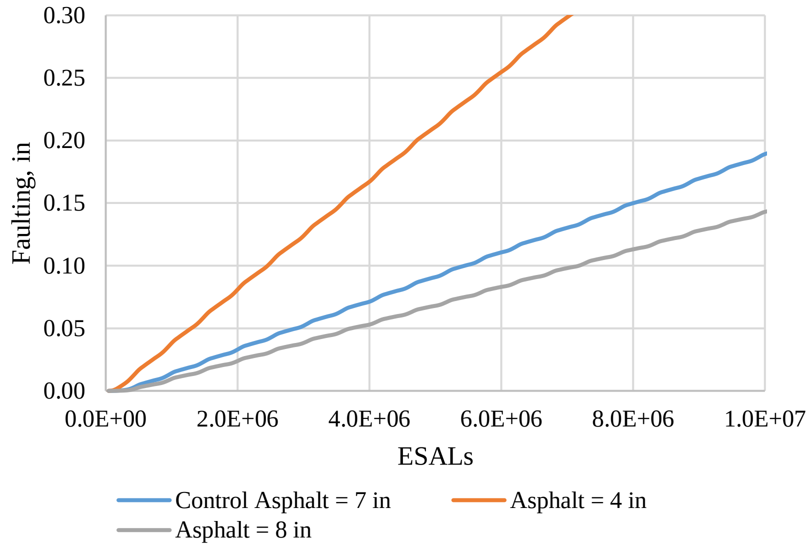

Figure 5-30 Effect of asphalt thickness on predicted faulting for Structure 2.

The next variable examined that does not appear to have an effect on predicted faulting is the percent fines within the subgrade. The control consisted of 50% fines, and an upper (70%) and lower (10%) bound were compared. The effect of this variable is insignificant and can be seen in Figure 5-31. The insignificance of this variable can be attributed to the scaling of this variable dictated by the overburden on the subgrade.

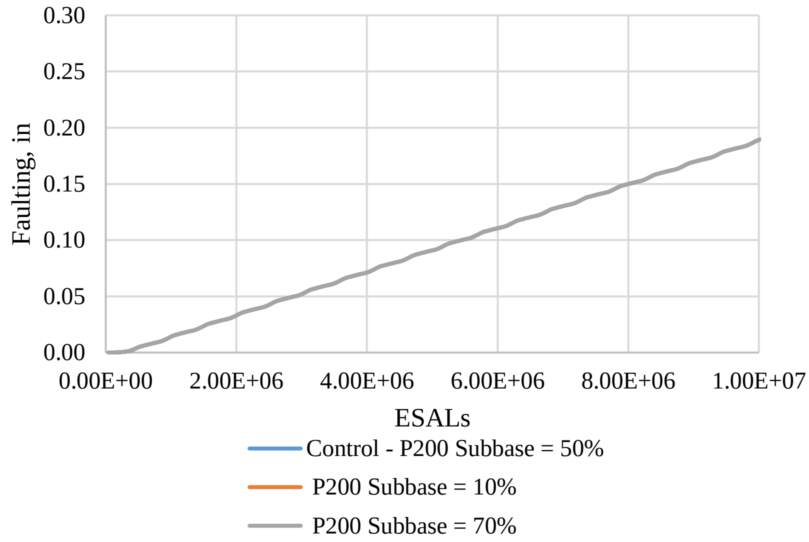

Figure 5-31 Effect of P200 in the subgrade on predicted faulting for Structure 2.

Another variable that was examined within the sensitivity analysis was the effect of traffic volume. Four traffic levels were examined, 5, 10 (control), 20, and 50 million ESALs over a 20-year analysis period. Traffic was distributed uniformly throughout the day as defined in Table 5-1 (ARA 2004). The effects of traffic on predicted faulting for the first structure examined can be seen in Figure 5-32. The y-axis is extended to 0.5 in due to the increased prediction of faulting.

As previously described, when applying 50 million ESALs over a 20-year analysis period, the magnitude of differential energy is extremely large. However, Structure 2 is a stiffer structure than structure 1 due to increased layer thicknesses. The practicability of Structure 2 with that significant level of traffic over that span of time is more realistic than Structure 1.

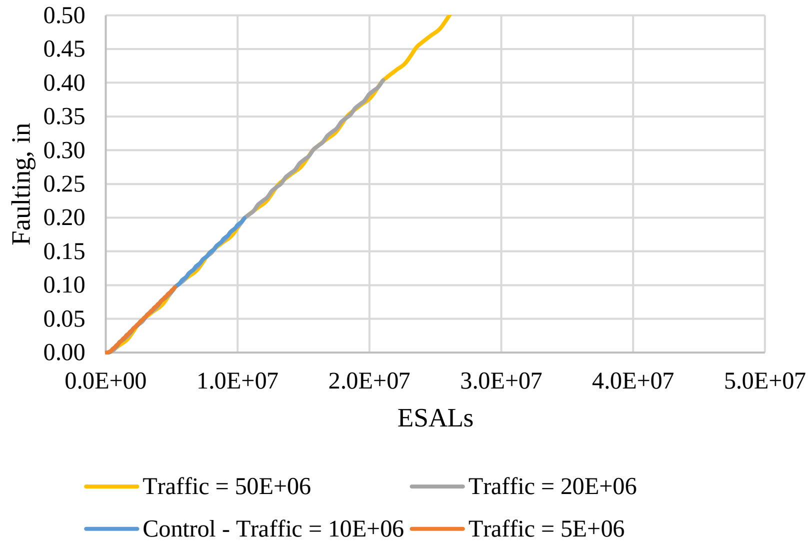

Figure 5-32 Effect of traffic on predicted faulting for Structure 2.

Four geographical locations were examined to check the sensitivity of climate. The four different locations (including the control section) include, Pittsburgh, PA, Phoenix, AZ, Miami, FL, and Rapid City, SD. These four locations were selected to represent each of the four major climate regions, wet/freeze, dry/no-freeze, wet/no-freeze, and dry/freeze, respectively. Along with the different climates, different asphalt elastic moduli were used based on binder selection using LTPPBIND. The following binder grades were used, PG 58-16 (Pittsburgh), PG 70-10 (Phoenix), PG 70-10 (Miami), and PG 58-28 (Rapid City).

When the joint activates through the PCC and asphalt layer, the prediction between Pittsburgh and Rapid City are almost identical. This can be attributed to similar climates (colder climates than Phoenix or Miami), which can result in a stiff layer beneath the asphalt more often than climates such as Phoenix or Miami. Additionally, cold climates typically have softer binders to be able to account for winter and summer temperature ranges. With relatively high temperatures in the summer, asphalt in colder temperature regions with a soft binder is less stiff then in the warmer temperature regions where a very stiff binder can be used without developing thermal cracking.

In addition, Pittsburgh and Rapid City both begin to develop faulting prior to Phoenix and Miami. The colder climates result in larger joint widths, which will cause the joints to activate through the PCC and asphalt layer at a faster rate than warmer climates such as Phoenix and Miami. Miami has the largest predicted faulting, which is attributed to a less stiff subgrade (accounted for by the freezing ratio) as well as being in a wet climate (accounted for by WETDAYS). These variables have been previously defined within the Climate section of Chapter 5 (5.2.1 Climate).

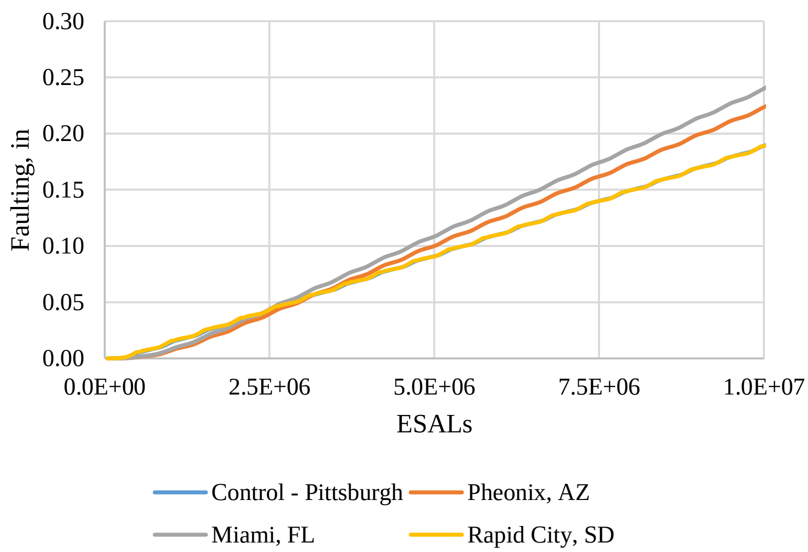

Figure 5-33 Effect of climate on predicted faulting for Structure 2.

The final variable examined for the second structure is the reliability. Four levels were examined, 50% (control), 75%, 85% (BCOA-ME design guide reliability level), and 95%. As a higher level of reliability is desired, a greater magnitude of faulting will be predicted. This can be seen in Figure 5-34.

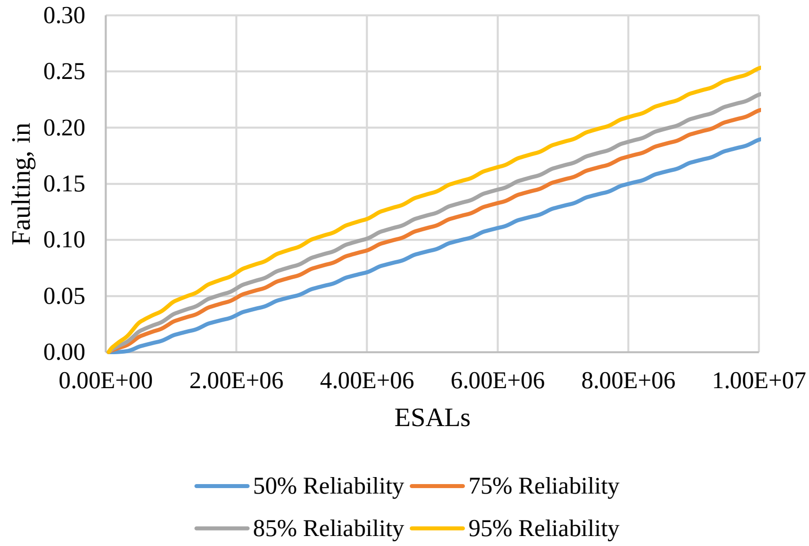

Figure 5-34 Effect of reliability on predicted faulting for Structure 2.

The same analysis performed on Structure 1 and 2 was conducted for the third structure presented in Table 5-20. The overall trends were as expected for each variable and very similar to the results presented for Structure 1. The additional 2 in of PCC, reduced the predicted faulting in comparison to Structure 1. However, the difference was only 0.01 in due to the asphalt thickness reduction of 2 in. The sensitivity analysis performed on Structure 3 can be seen in Appendix A.

5.8 Conclusions

The framework for the model to predict faulting for BCOA was presented. This includes how climatic factors were accounted for within the calibration process. Then a discussion of how differential energy is calculated along with all of the steps to establish the inputs needed for predicting the deflection basins using the ANNs. Finally, the incremental faulting equations are presented.

Two sets of calibrations were performed to account for the different depths of joint activation. When the joint only activates through the PCC, an erosion model was developed to be able to account for the different characteristics of the asphalt mixture that will influence pumping. When the joint activates through the PCC and the asphalt, the erodibility factor is determined based upon the characteristics of the unstabilized layer beneath the asphalt, as is currently done in Pavement ME for conventional pavement design.

With the framework presented, a discussion of the data available to calibrate the faulting model is made that includes the location of pavement sections and relevant design features. The model calibration coefficients were then presented. Model adequacy checks were performed on each of the calibrations to determine statistical adequacy of the models. Simple reliability models (standard deviation) were also developed to account for different levels of reliability. Finally, a sensitivity analysis of the predicted faulting to various parameters of interest is conducted to further evaluate the models.

6.0 Climatic Considerations

6.1 Introduction

This chapter details the development of regression models for climatic related parameters, needed for predicting faulting. Within the current framework, a separate analysis for each structure must be carried out within the EICM (Larson and Dempsey 2003). The EICM is used to perform an hourly incremental analysis that determines the temperature profile in the pavement structure at specified depths. This information is then used in quantifying the effects of climate on the development of faulting.

The overall goal of this chapter is to develop regressions for climatic dependent variables to eliminate the need for conducting a separate analysis for every structure using the EICM when predicting faulting. This approach eliminates computational demand and potential errors by simplifying the climatic inputs. A similar procedure was previously used for the prediction of fatigue cracking for BCOAs and incorporated into the BCOA-ME (Mu and Vandenbossche 2012, Li et al. 2016, Sachs et al. 2016). In order to develop the prediction equations, a factorial design was executed to populate a database with climatic information for a large number of geographical locations within the continental U.S. and pavement structures. Using this database, optimization techniques were performed to establish monthly or annual parameters that represent the effects of hourly environmental changes. The regression analysis and final regressions models are presented for yearly effective equivalent linear temperature gradients, monthly effective asphalt stiffness, mean annual number of days greater than 0.1 in of precipitation (WETDAYS), the percentage of time that the top of the asphalt layer is less than 32^{o}F (freezing ratio), and the PCC overlay mean monthly nighttime mid-depth temperature.

6.2 Effective Equivalent Linear Temperature Gradients

Currently within the BCOA-ME, EELTGs are used to quantify a yearly temperature gradient that is representative of the entire year based on equivalent damage. However, the EELTGs established were developed using equivalent fatigue damage and are used for the prediction of fatigue cracking in the PCC overlay. Whereas, new EELTGs need to be developed based on equivalent differential energy. The differential energy is used to quantify damage when predicting faulting, as described in great detail in Chapters 4 and 5. Therefore, EELTG predictive equations are established using differential energy to equate damage.

6.2.1 Effective Equivalent Linear Temperature Gradient Framework

The EELTG is used as a predictor of differential energy in the ANNs presented in Chapter 4 and 5 when predicting faulting. In order to develop prediction equations for estimating the EELTGs, the methodology adopted in the BCOA-ME was followed (Li et al. 2013 and Roesler et al. 2008). The methodology is shown in Figure 6-1.

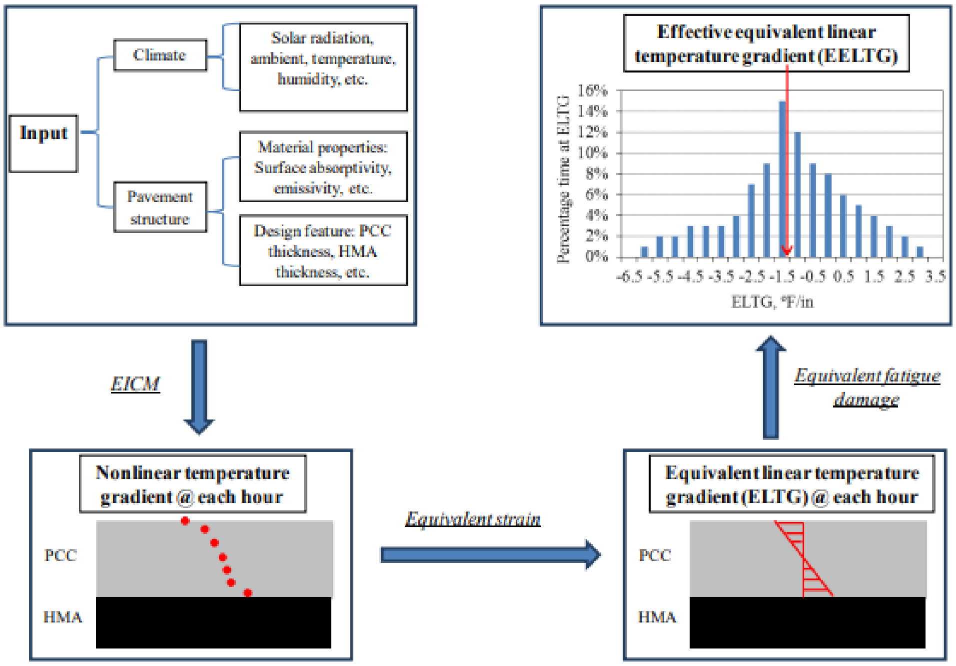

Figure 6-1 Flowchart to generate the EELTG (Li et al. 2016).

As seen in Figure 6-1, the first step in establishing the EELTGs to be used in the design process is to populate a database with the temperature distributions throughout the pavement structure. This database must represent a wide range of climatic conditions and pavement structures. The EICM (Larson and Dempsey 2003) is used to estimate the hourly temperature distributions through the pavement structure for different climatic regions and pavement designs. A total of 173 weather stations were strategically selected to ensure good representation of all of the climatic conditions in the United States was achieved. A map of the United States with all 173 weather stations can be seen in Figure 6-2.

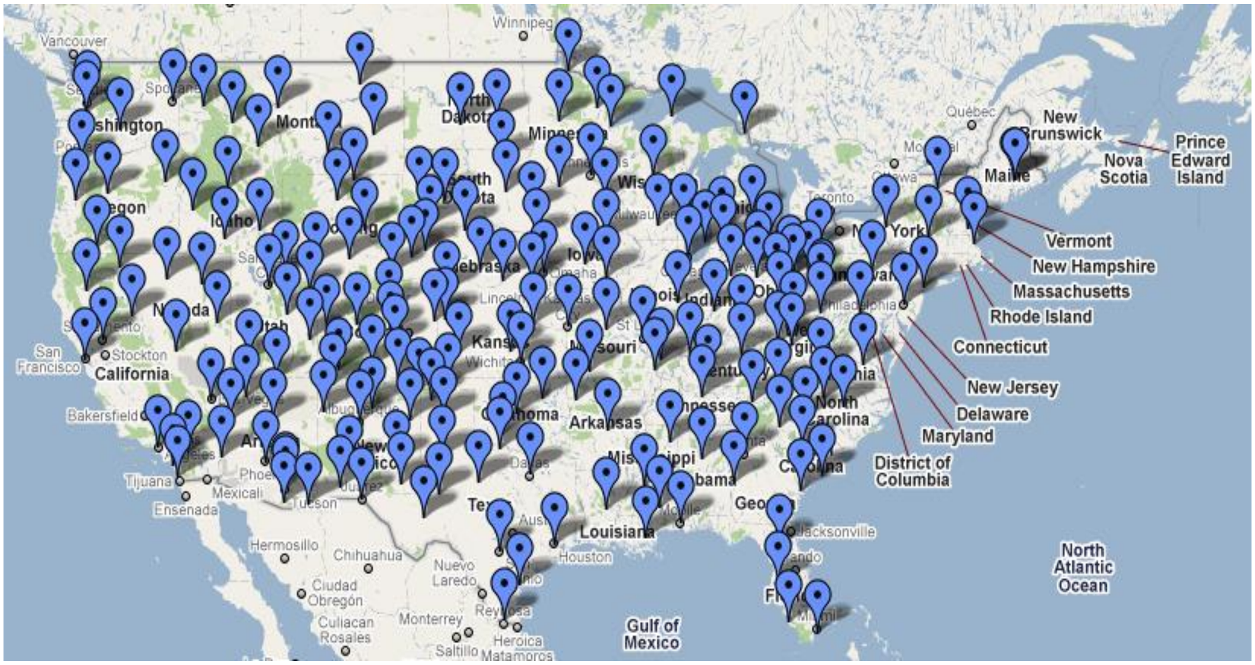

Figure 6-2 Continental United States with weather stations used in cliamtic considerations (background map is the Google Map of the US as of November, 2019).

In order to ensure the database sufficiently represents all climatic regions, the United States was divided into regions based on the annual mean percentage of sunshine and the annual mean daily average temperature (AMDAT). The location of these zones can be seen in Figure 6-3. It was then checked to ensure the 173 weather stations selected provided sufficient representation for each zone. The weather stations selected for inclusion in this analysis are the same as those used for establishing the EELTGs to facilitate predicting the development of cracking in the BCOA-ME.

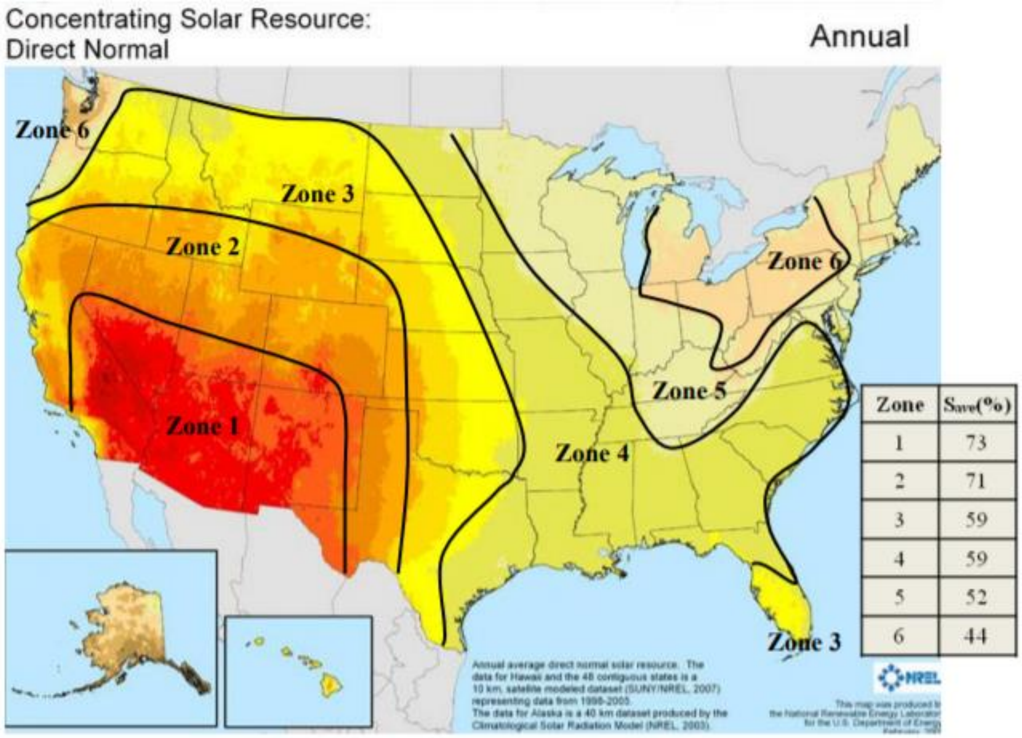

a) Annual mean percentage of sunshine zones (based on the annual concentrating solar resource map of the US in 2009, http://www.nrel.gov/gis/solar.html)

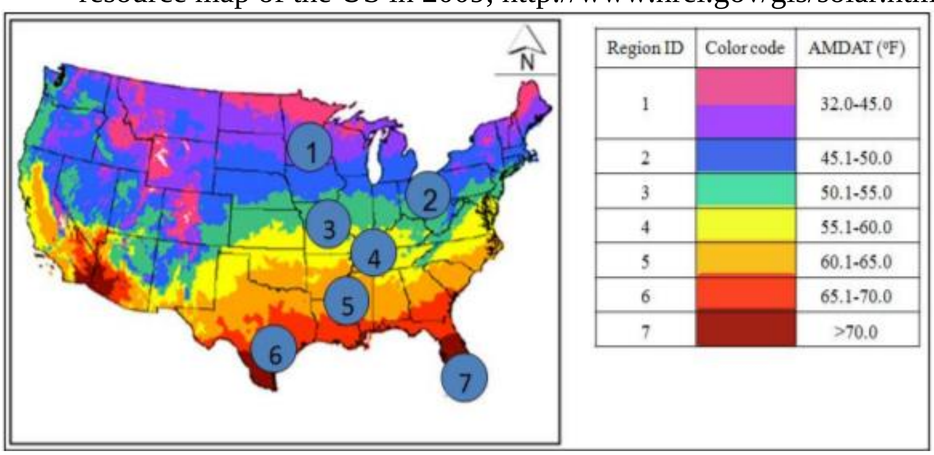

b) Annual mean daily average temperature zones (AMDAT) (http://cdo.ncdc.noaa.gov/climaps/temp0313)

Figure 6-3 Zonal division of the US in terms of annual mean percent sunshine and annual mean daily temperature.

For each weather station, an EICM file was created for each combination of layer thicknesses presented in Table 6-1. The variables considered in the factorial analysis to populate the database for these virtual pavement structures includes weather station (latitude, longitude, and elevation), overlay thickness, asphalt layer thickness, overlay modulus of rupture (stiffness), PCC CTE, dowel diameter, depth of joint activation, and overlay joint spacing.

Table 6-1 Design features for generating EICM database.

	Joint spacing (ft)	
	< 10	≥ 10
PCC layer thickness (in)	3, 4, and 6	5 and 6
Asphalt layer thickness (in)	4 and 8	4, 6, and 8
Joint spacing (ft)	6 x 6 8 x 8	10 x 12 12 x 12
Joint activation depth	PCC only Full-depth	Full-depth
PCC MOR (psi)	550, 650, and 750	
PCC modulus (10^6 psi)	3.5, 4.0, and 4.5	
Dowel diameter (in)	0 and 1.25	
PCC CTE (10^{-6}/°F)	5.0	
k-value (psi/in)	200	
Poisson's ratio of PCC	0.18	
Poisson's ratio of asphalt	0.35	

Within EICM, the structure must have defined properties including layer thicknesses, the number of nodes for each layer, thermal properties, permeability, porosity, and water content. The water content is necessary to model moisture movement in granular layers. The values used for these parameters are the same as those used in Chapter 5 for the calibration sections. The example input file is provided in Appendix A. Within the overlay and asphalt layer, nodes were placed at 1-in increments. Additionally, using the North American Regional Reanalysis (NARR) climatic database, the nearest weather station to each calibration site is chosen to give hourly values of air temperature, precipitation, wind speed, and percent sunshine for several years that can be output as an .icm profile. Weather stations were selected to include a minimum of 5 years of recorded data. The EICM analysis is then performed so the hourly nodal temperatures throughout the depth of the structure can be determined. EICM generates a .tem file that contains these nodal temperatures. The non-linear temperature profiles are then used to establish hourly ELTGs based on equivalent strain. The hourly ELTGs are calculated using the temperature-moment concept presented in Chapter 5 using Equations (5-1) through (5-3) (Janssen and Snyder 2000). The hourly mid-depth asphalt temperature, freezing ratio, which is the percentage of time that the top of the asphalt layer is less than 32^{o}F, and the mean monthly mid-depth overlay temperature is determined as well.

6.2.2 Effective Equivalent Linear Temperature Gradient Regression Equations

The hourly ELTGs are then used to establish the EELTG. As previously described, the EELTG is the ELTG that, when applied throughout the design life, results in the same damage (cumulative differential energy) as if the hourly linear temperature gradients were used.

For determining the differential energies in this analysis, 1 million ESALs (18-kip single axle loads) are applied over the course of the year, hourly distributed according to the percentages presented in the previous chapter (Table 5-1), which results in the same number of vehicles applied each day (ARA, 2004). Mean monthly mid-depth temperatures of the slab are used to estimate monthly joint widths so the joint stiffness can be determined and hourly temperatures at mid-depth of the asphalt are used to estimate the dynamic modulus of the asphalt layer. This procedure is represented in Figure 6-4. The EELTG was established for each pavement structure using climatic data for each weather station. This resulted in 144 different EELTGs for each weather station. A total of 74,736 analyses were performed. This includes 24,912 analyses performed for each of the following: 1. joint spacing less than 10 ft (joint activation only through the PCC), 2. joint spacing less than 10 ft (joint activation through the PCC and asphalt), and 3. joint spacing greater than or equal to 10 ft (joint activation through the PCC and asphalt).

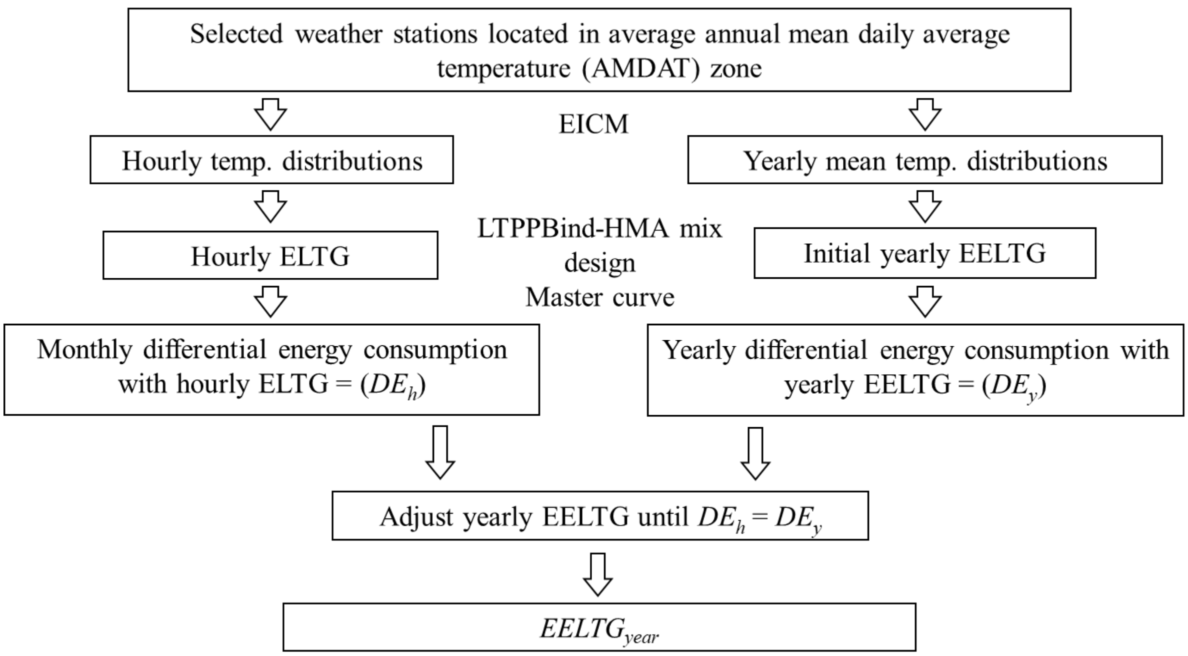

Figure 6-4 EELTG established framework.

A stepwise regression was then performed to establish a linear relationship between the EELTG and site-specific characteristics of the pavement structure. It is important to use the fewest number of variables without sacrificing the accuracy of the prediction to minimize the time and resources necessary that must be allocated in defining these inputs during the design process. The resulting regression models can be seen in the following equations and the statistics summary can be seen in Table 6-2. For partial lane width panel sizes when the joint only activates through the PCC layer:

$$EELTG = -0.3826 + 0.029396\, h_{PCC} - 0.003826\, h_{HMA} + 0.00289\, SunZone - 0.013363\, AmdatZone + 0.000977\, Latitude - 0.000637\, Longitude - 0.000003\, Elev - 0.005086\, P\_Sunshine \tag{6-1}$$

For partial lane width panel sizes when the joint activates through the PCC and asphalt layers:

$$EELTG = 0.202 - 0.27909\, Jt\_space + 0.008705\, LTEshoulder - 0.000423\, MORol + 0.11043\, h_{PCC} + 0.19817\, h_{HMA} - 0.0455\, SunZone + 0.04904\, AmdatZone - 0.00718\, Latitude + 0.001706\, Longitude - 0.01048\, P\_Sunshine \tag{6-2}$$

For full lane width panel sizes when the joint activates through the PCC and asphalt layers:

$$EELTG = -3.852 + 0.008083\, LTEshoulder + 0.000457\, MORol + 0.04662\, h_{PCC} + 0.27047\, h_{HMA} - 0.0451\, SunZone - 0.01384\, AmdatZone - 0.01546\, Latitude + 0.001085\, Longitude - 0.000018\, Elev - 0.00796\, P\_Sunshine \tag{6-3}$$

Where:

EELTG is the effective equivalent linear temperature gradient (^{o}F/in),

h_{PCC} is the PCC overlay thickness (in),

h_{HMA} is the asphalt layer thickness (in),

SunZone is the corresponding sunshine zone, *AmdatZone* is the corresponding annual mean daily average temperature (AMDAT) zone,

Latitude is the corresponding geographical location (degrees),

Longitude is the corresponding geographical location (degrees),

Elev is the corresponding geographical elevation (ft),

P_Sunshine is the percent sunshine for the corresponding geographical location (%),

Jt_space is the transverse joint spacing of the PCC overlay (ft),

LTEshoulder is the lane/shoulder load transfer efficiency (%), and

MORol is the PCC overlay modulus of rupture (psi).

Table 6-2 EELTG regression coefficient of determinations.

Classification	Analysis	R^2
Partial lane width panels - partial depth jt. Equation (6-4)	Stepwise	0.70
Partial lane width panels - full-depth jt. Equation (6-5)	Stepwise	0.61
Full lane width panels - full-depth jt. Equation (6-6)	Stepwise	0.64

Prior to being able to be implemented into the prediction process for faulting in BCOA pavements, the annual mean percentage of sunshine for each zone needs to be decoupled from EICM. In order to do this, the results of percent sunshine from EICM for each weather station in each of the specified sunshine zones were averaged together. The results of the annual mean percentage of sunshine for each sunshine zone can be seen in the following table.

Table 6-3 Annual mean percentage of sunshine for each sunshine zone.

Sunshine zone	Mean (%)	Std. deviation (%)
1	73	17
2	71	10
3	59	12
4	59	12
5	52	9
6	44	11

These developed regressions for EELTG can now be incorporated into the mechanistic empirical design procedure for BCOAs. This adaptation eliminates the need of EICM using Table 6-3, which reduces user time and user error.

6.3 Effective Elastic Asphalt Moduli

Another important component of the mechanistic design of BCOAs is being able to account for the stiffness of the temperature dependent asphalt layer. Due to the temperature changes, the stiffness of the asphalt layer changes accordingly. It is important to account for the change in asphalt stiffness because the magnitude of deflections and therefore differential energy is directly related. Therefore, higher levels of damage or differential energy occur when the asphalt stiffness is at a minimum.

Eliminating the need for predicting hourly temperatures of the asphalt throughout the design period helps in simplifying the design process. To account for the changing asphalt stiffness, the same approach incorporated into the BCOA-ME is adopted here. Monthly asphalt stiffness adjustment factors are established so that an equivalent monthly asphalt stiffness can be used. The equivalent monthly asphalt stiffness equates to the same damage as if hourly changes in asphalt temperature were considered. The framework used to establish the asphalt stiffness adjustment factor (F) for the seven different temperature regions (see Figure 6-3b) is shown in Figure 6-5. For every weather station in each region, monthly asphalt temperature is first estimated using the EICM. The same database of weather stations (see Figure 6-2) used for the EELTG analysis was used for this analysis. Then, using the mastercurve (ARA, 2004) the asphalt modulus was determined for each temperature for all of the regions. Then, the asphalt modulus was determined for each hourly and each monthly mean temperature for each weather station in the region. The differential energy accumulation using the hourly asphalt modulus for a certain month is denoted as DE_h, while the differential energy accumulation using the monthly asphalt modulus for the same month is DE_m. The difference between DE_h and DE_m indicates the effect of hourly asphalt modulus variation and it is a function of design features and material properties. A large number of hypothetical designs are considered for the differential energy (damage) analysis. The design variables considered in the fatigue analysis can be found in Table 6-1. The details of each of these steps is provide below.

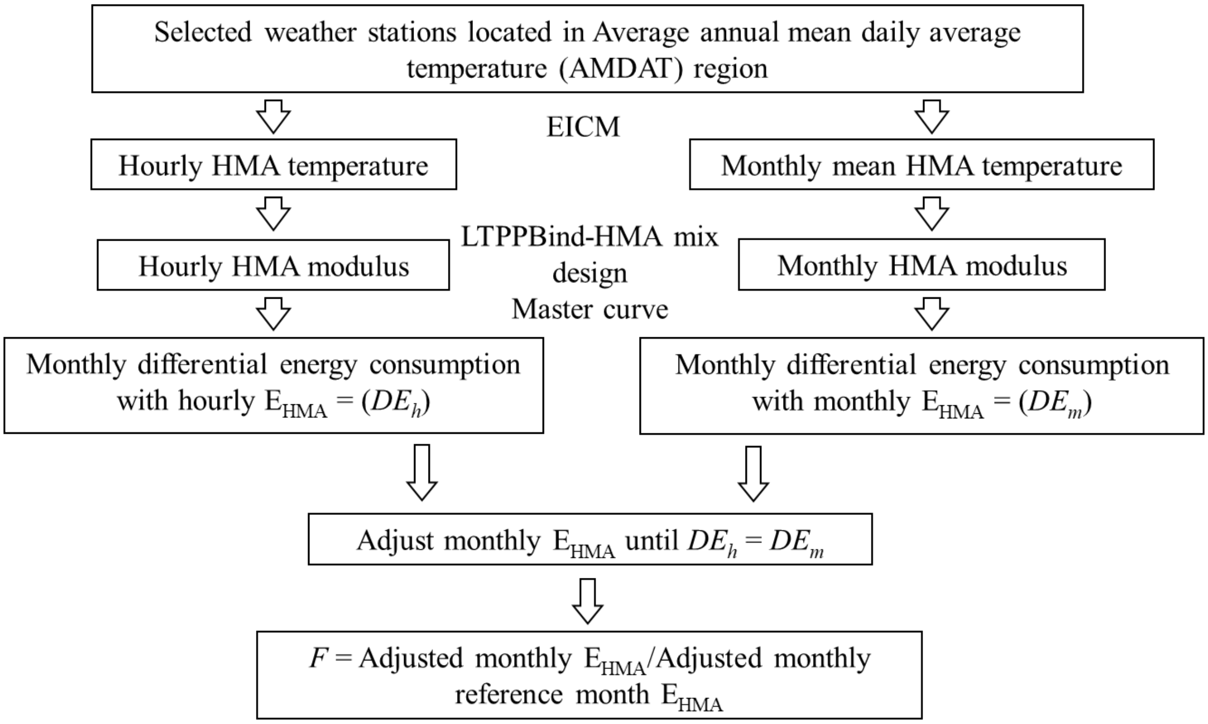

Figure 6-5 Framework for establishing the effective asphalt modulus adjustment factor.

6.3.1 Asphalt modulus characterization

To account for the time-temperature dependent asphalt stiffness, site specific mastercurves are employed to predict the dynamic modulus. A mastercurve is a nonlinear sigmoidal function that has the form given in Equation (6-4) (ARA 2004). This function is dependent on the loading frequency and temperature. The dynamic modulus is also a function of the asphalt mixture and will vary based upon different climatic zones. Components of the asphalt mixture that might vary based upon location includes aggregate gradations and asphalt binders. The different mixture properties are accounted for in Equation (6-5) through (6-12).

$$log|E^*| = \delta + \frac{\alpha}{1 + e^{(\beta+\gamma(\log(t_r))}} \quad \textbf{(6-4)}$$

$$t_r = \frac{t}{a(T)} \quad \textbf{(6-5)}$$

$$\log(t_r) = \log(t) - log[a(T)] \quad \textbf{(6-6)}$$

Where:

*E** is the dynamic modulus (psi),

t_r is the time of loading at the reference temperature (s),

δ, α are the fitting parameters for a given set of data,

δ represents the minimum value of *E**,

δ + *α* represents the maximum value of *E**,

β and *γ* are the parameters describing the shape of the sigmoidal function,

t is the time of loading at a given temperature of interest (s),

a(T) is the shift factor as a function of temperature, and

T is the temperature of interest (Rankine).

In this study, all of the dynamic moduli were determined using a loading time of 0.1 s. It is suggested the loading time should be calculated based on the effective length of the load pulse, which varies with depth and the operational speed of vehicles (ARA 2004). A previous study determined that at an effective length of a load pulse of 60 in, the loading duration is calculated to be 0.05 s and 0.1 s for an operation speed of 65 mph and 35 mph, respectively (Barman et al. 2011). The loading duration of 0.1 s was selected for this analysis because it is more likely to have operational speeds of 35 mph than 65 mph for BCOA applications.

To account for the different asphalt mixture properties, such as aggregate gradation, binder content, and air void content, the fitting parameters *δ* and *α* were determined. *Β* and *γ* depend on the characteristics of the asphalt binder and the magnitude of *δ* and *α*.

$$\delta = 3.750063 + 0.029232\rho_{200} - 0.001767\rho_{200}^2 - 0.002841\rho_4 - 0.058097V_a - 0.82208\left[\frac{Vb_{eff}}{Vb_{eff} + V_a}\right] \quad \textbf{(6-7)}$$

$$\propto = 3.871977 - 0.0021\rho_4 + 0.003958\rho_{38} - 0.000017\rho_{38}^2 + 0.005470\rho_{34} \quad \textbf{(6-8)}$$

$$\beta = 0.603313 - 0.313532log(\eta_{T_r}) \quad \textbf{(6-9)}$$

$$\log(t_r) = \log(t) - c(log(\eta) - log(\eta_{T_r})\,) \quad \textbf{(6-10)}$$

$$\gamma = 0.313351; c = 1.255882 \quad \textbf{(6-11)}$$

Where:

ρ_{34} is the cumulative percent retained on the ¾ in sieve (%),

ρ_{38} is the cumulative percent retained on the 3/8 in sieve (%),

ρ_4 is the cumulative percent retained on the No. 4 sieve (%),

ρ_{200} is the percent passing the No. 200 sieve (%),

V_a is the air void content (%),

V_{beff} is the effective bitumen content (% by volume),

η is the binder viscosity (10^6 poise),

η_{T_r} is the binder viscosity at reference temperature T_r (10^6 poise), and

c is a regression coefficient.

The η is a function of the binder type selected for a given location. The binder type was selected based on temperature the binder is likely to be exposed to, and recommendations were followed using ASTM D 2493 (asphalt viscosity to temperature relationship) (ASTM D 2493).

$$\text{Log}\log\eta = A + VTS\log T_R \quad \textbf{(6-12)}$$

Where:

η is the viscosity of binder (centi poise),

T_R is the temperature (Rankine),

A is the regression intercept, and

VTS is the regression slope of viscosity temperature susceptibility.

The regression values of *A* and *VTS* are also a function of the binder type and grade. The following two tables provide the corresponding regression values based on a given asphalt binder grade (ARA 2004).

Table 6-4 Regression slope of viscosity temperature susceptibility (VTS).

	VTS						
High temp. grade	Low temp. grade						
	-10	-16	-22	-28	-34	-40	-46
46					-3.901	-3.393	-2.905
52	-4.57	-4.541	-4.342	-4.012	-3.602	-3.164	-2.736
58	-4.172	-4.147	-3.981	-3.701	-3.35	-2.968	
64	-3.842	-3.822	-3.68	-3.44	-3.134	-2.798	
70	-3.566	-3.548	-3.426	-3.217	-2.948	-2.648	
76	-3.331	-3.315	-3.208	-3.024	-2.785		
82	-3.128	-3.114	-3.019	-2.856	-2.642		

Table 6-5 Regression intercept (A).

A							
High temp. grade	Low temp. grade						
	-10	-16	-22	-28	-34	-40	-46
46					11.504	10.101	8.755
52	13.386	13.305	12.755	11.84	10.707	9.496	8.31
58	12.316	12.248	11.787	11.01	10.035	8.976	
64	11.432	11.375	10.98	10.312	9.461	8.524	
70	10.69	10.641	10.299	9.715	8.965	8.129	
76	10.059	10.015	9.715	9.2	8.532		
82	9.514	9.475	9.209	8.75	8.151		

In order to determine the variables A and VTS, the binder grade needs to be specified. Therefore, to be able to determine site specific binder grades, SHRP LTPPBIND version 3.1 was utilized (Pavement System LLC, 2005). This software is a Superpave binder selection program developed for the FHWA. LTPPBIND considers the geographical information (longitude, latitude, and elevation), the depth to the surface of the asphalt layer, traffic characteristics, and the reliability. This study examined the variation of geographical information, whereas the other variables remained similar between the different climate regions. For the established weather stations used to develop the EELTG regressions, the same weather stations were used for determining the effective elastic moduli of asphalt (EEHMA) regressions. For each weather station a corresponding binder grade was selected using the LTPPBIND software program and can be seen in Appendix B.

Another component in determining the monthly EEHMA is the aggregate gradation. The default aggregate gradation used in determining the EEHMAs is presented in Table 6-6. Along with the aggregate gradation, the design features and the material properties considered in determining the EEHMAs are presented in Table 6-1.

Table 6-6 Aggregate gradation of the default asphalt mixture.

Sieve size	Percentage finer by weight
1 in	100
3/4 in	97
3/8 in	70
No. 4	55
No. 200	10
Binder content, %	12.5
Air voids, %	5.8
Ref. temp. ^{o}F	70

6.3.2 Equivalent asphalt modulus

To be able to determine the EEHMAs, the procedure developed for the BCOA-ME by the University of Pittsburgh was followed. The framework established in the BCOA-ME determines EEHMA using a fatigue analysis. However, the work that is presented utilized the differential energy concept presented in Chapter 4. The adjusted framework can be seen in Figure 6-5.

The effective asphalt modulus for a given month is the asphalt modulus that, when applied throughout the design life, results in the same damage (cumulative differential energy) as if the hourly asphalt moduli were used. To establish the effective asphalt moduli, first hourly asphalt moduli are determined using the hourly temperatures at mid-depth of the asphalt using the EICM. Next, the hourly differential energy was summed based on the hourly asphalt elastic moduli (EHMAs) for each simulated section for each month. Then, the fminsearch function in MATLAB is used to find a single monthly stiffness (based on an average monthly mid-depth asphalt temperature), which yielded the same amount of differential energy as calculated using the summation of hourly differential energy based on the hourly asphalt moduli (MATLAB 2013). This resulted in 12 monthly effective asphalt moduli that take into consideration the change in temperature in a year. For this analysis, 1 million ESALs (18-kip single axle loads) were applied over the course of the year and distributed hourly according to the percentages presented in the previous chapter (Table 5-1) (ARA 2004). Mean monthly mid-depth temperatures of the slab are used to estimate monthly joint widths so the joint stiffness can be determined.

6.3.2.1 Equivalent asphalt modulus adjustment factors

Instead of developing regressions for 12 effective monthly asphalt moduli, the stiffnesses were normalized to a reference month to obtain 12 adjustment factors (F). In this analysis, January was defined as the reference month. Therefore, the adjustment factor, F, for January is 1.0.

The adjustment factors for the asphalt modulus are a function of the structural features of the pavement structure, the month of the year, as well as the AMDAT zone. To eliminate the number of regressions to be developed for the monthly adjustment factors, linear regression models were developed for F with respect to the design features for each AMDAT zone and damage model (dictated by joint activation depth). The analysis resulted in a total of 21 regressions using the seven AMDAT zones and the three different damage models: 1. partial lane width panels with joints activating only through the PCC, 2. partial lane width panels with joints activating through the PCC and asphalt layer, and 3. full lane width panels with joints activating through the PCC and asphalt layer.

A stepwise regression was performed to examine the statistical significance of each possible variable on the magnitude of F. The monthly average mid-depth asphalt temperatures established using the EICM were used and normalized to the reference month. This was performed by dividing each monthly average by the average mid-depth asphalt temperature of the reference month, January. The developed regression model was selected for all three damage models and all seven AMDAT zones.

$$F = C_1 + C_2 * h_{PCC} + C_3 * h_{HMA} + C_4 * T_{norm} \quad \textbf{(6-13)}$$

Where:

F is the asphalt modulus adjustment factor,

h_{PCC} is the PCC overlay thickness (in),

h_{HMA} is the asphalt layer thickness (in), and

T_{norm} is the normalized mid-depth asphalt temperature for each month obtained from EICM (^oF).

The corresponding regression coefficients for each model and AMDAT zone can be seen in Table 6-7. The model prediction results are also presented.

Table 6-7 Regression coefficients for asphalt modulus adjustment factors.

Model	Zone	C_1	C_2	C_3	C_4	R^2	Adj. R^2
Partial lane width panels: partial depth jt.	1	0.8065	0.0731	0.0194	- 0.3921	0.794	0.793
	2	1.0210	0.0579	0.0124	- 0.4662	0.785	0.784
	3	1.0466	0.0728	0.0232	- 0.6576	0.697	0.697
	4	1.0870	0.0599	0.0083	- 0.5502	0.735	0.734
	5	2.2885	0.0033	- 0.0699	- 0.8471	0.825	0.824
	6	2.7634	- 0.0187	- 0.1327	- 0.7474	0.789	0.787
	7	2.1198	- 0.0096	- 0.0469	- 0.8347	0.739	0.737
Partial lane width panels: full depth jt.	1	1.3310	- 0.0267	0.0299	- 0.4391	0.815	0.814
	2	1.3683	- 0.0269	0.0294	- 0.4961	0.840	0.839
	3	1.6251	- 0.0371	0.0346	- 0.7286	0.740	0.740
	4	1.4501	- 0.0332	0.0354	- 0.6040	0.802	0.802
	5	1.5291	0.0011	0.0220	- 0.8092	0.868	0.868
	6	1.3603	0.0165	0.0183	- 0.7021	0.860	0.859
	7	1.5989	0.0108	0.0031	- 0.7935	0.808	0.807
Full lane width panels: full depth jt.	1	1.4056	- 0.0007	0.0014	- 0.4222	0.895	0.895
	2	1.4109	0.0065	- 0.0022	- 0.4691	0.905	0.904
	3	1.6885	0.0083	- 0.0070	- 0.7068	0.863	0.863
	4	1.6319	0.0086	- 0.0143	- 0.5973	0.883	0.882
	5	1.7399	0.0011	- 0.0043	- 0.8022	0.922	0.922
	6	1.7014	- 0.0090	- 0.0052	- 0.7101	0.911	0.910
	7	1.7463	-0.0057	- 0.0033	- 0.7989	0.860	0.859

6.3.2.2 Asphalt modulus for the reference month

In order to apply the regressions developed for the asphalt modulus adjustment factors, the asphalt modulus for the reference month needs to be determined. Once this stiffness is determined, the other monthly stiffnesses can be determined using the appropriate adjustment factors. The presented regression model was selected for all three damage models and all seven AMDAT zones.

A stepwise regression was performed to examine the statistical significance of each potential variable on the magnitude of asphalt stiffness for the reference month (January). The average mid-depth asphalt temperature for the reference month was established using the EICM. The results of the stepwise regression along with the coefficients can be seen in Table 6-8.

$$E_{HMA(Ref)} = C_1 + C_2 * h_{HMA} + C_3 * Latitude + C_4 * Longitude + C_5 * Elevation + C_6 * T_{mid-depth(Ref)} \quad \textbf{(6-14)}$$

Where:

$E_{HMA(Ref)}$ is the asphalt stiffness for the reference month, January (psi),

h_{HMA} is the asphalt layer thickness (in),

Latitude is the geographical latitude of the project location (degrees),

Longitude is the geographical latitude of the project location (degrees),

Elevation is the distance of the project location above sea level (ft), and

$T_{mid-depth(Ref)}$ is the mid-depth asphalt temperature for the reference month (^{o}F).

Table 6-8 Regression coefficients for asphalt modulus for the reference month.

Model	Zone	C_1	C_2	C_3	C_4	C_5	C_6	R^2	Adj. R^2
Partial lane width panels: partial depth jt.	1	1696361	66781	-10014	-778	10.2	-18332	0.755	0.754
	2	1943962	60563	-16339	2696	-12.7	-20636	0.776	0.775
	3	1813700	52153	-7480	-213	11.3	-19076	0.738	0.738
	4	1747615	51821	-12708	3109	-5.5	-19115	0.773	0.772
	5	1815340	24330	-2402	-148	28.6	-18462	0.807	0.806
	6	1776363	12787	-10205	3327	12.0	-17493	0.820	0.817
	7	1584988	-9210	5241	767	13.1	-15326	0.847	0.845
Partial lane width panels: full depth jt.	1	2563020	-88714	-6382	-823	20.3	-19126	0.676	0.675
	2	2809361	-78663	-18273	3295	-13.3	-20134	0.70	0.699
	3	2713913	-74321	-10782	750	12.0	-20101	0.673	0.672
	4	2307232	-60380	-4350	955	18.0	-19090	0.745	0.744
	5	1914384	-41488	-90	707	23.2	-16770	0.83	0.83
	6	1707282	-30702	-1334	1694	17.8	-15442	0.841	0.839
	7	1273825	-17465	8711	677	13.0	-13095	0.849	0.847
Full lane width panels: full depth jt.	1	1501320	-11598	-6321	491	10.4	-12699	0.895	0.894
	2	1572891	-10152	-10382	2236	-3.43	-12752	0.883	0.882
	3	1515562	-10691	-6336	1301	11.4	-12966	0.867	0.867
	4	1666341	-10323	-10405	1065	9.7	-12332	0.904	0.904
	5	1489808	-11449	-2681	446	16.9	-12633	0.953	0.953
	6	1439950	-11123	-3563	1072	12.9	-12240	0.957	0.957
	7	1212801	-9341	7135	-270	8.9	-11407	0.946	0.945

6.3.3 Equivalent asphalt modulus regression inputs

In order to fully eliminate the necessity of using EICM for these regressions, the inputs T_{norm} and $T_{mid-depth(Ref)}$ were addressed. For the previously developed regression equations, these inputs were taken directly from the temperature distributions from the EICM output file. Therefore, it is necessary to be able to determine these parameters without performing an analysis using the EICM. In order to account for these variables, the procedure conducted by Sachs et al. in the BCOA-ME was followed (2016).

Using the database of EICM outputs for each AMDAT zone, zonal averages were determined for both T_{norm} for each month and $T_{mid-depth(Ref)}$. The values determined for the normalized mid-depth asphalt temperature for each month can be seen in Table 6-9. The values determined for the mid-depth asphalt temperature for the reference month can be seen in Table 6-10. The use of zonal averages eliminates the necessity of using the EICM software to determine the average for each weather station individually.

Table 6-9 Zonal average values and standard deviations of T_{norm} for each AMDAT zone (Sachs et al. 2016).

		T_{norm} for each month											
AMDAT zone		Jan.	Feb.	Mar.	Apr.	May.	June	July	Aug.	Sept.	Oct.	Nov.	Dec.
1	Average	1.0	0.99	1.4	1.91	2.54	2.85	3.11	3.07	2.43	2.1	1.44	0.92
	Std. dev.	0.0	0.13	0.16	0.22	0.41	0.5	0.57	0.54	0.4	0.32	0.23	0.17
2	Average	1.0	1.05	1.35	1.84	2.31	2.57	2.77	2.76	2.24	1.96	1.4	0.97
	Std. dev.	0.0	0.1	0.13	0.23	0.3	0.35	0.39	0.38	0.29	0.27	0.23	0.12
3	Average	1.0	1.12	1.42	1.73	1.96	2.04	2.1	2.12	1.77	1.65	1.27	0.97
	Std. dev.	0.0	0.91	0.69	2.01	4.11	7.31	9.52	9.03	7.63	4.95	3.13	1.67
4	Average	1.0	1.2	1.37	1.78	2.04	2.23	2.36	2.34	1.99	1.79	1.39	1.02
	Std. dev.	0.0	0.12	0.11	0.27	0.32	0.37	0.46	0.43	0.33	0.26	0.17	0.07
5	Average	1.0	1.17	1.29	1.52	1.73	1.86	1.95	1.92	1.68	1.56	1.26	1.04
	Std. dev.	0.0	0.1	0.1	0.19	0.22	0.25	0.28	0.27	0.21	0.16	0.12	0.03
6	Average	1.0	1.15	1.27	1.53	1.77	1.92	2.0	1.99	1.75	1.59	1.29	1.02
	Std. dev.	0.0	0.11	0.03	0.12	0.32	0.39	0.46	0.47	0.32	0.27	0.13	0.1
7	Average	1.0	1.08	1.26	1.38	1.63	1.73	1.82	1.84	1.57	1.44	1.14	1.06
	Std. dev.	0.0	0.05	0.11	0.13	0.22	0.24	0.32	0.34	0.19	0.15	0.05	0.03

Table 6-10 Zonal average values and standard deviations of $T_{mid\text{-}depth}$(Ref) for each AMDAT zone (Sachs et al. 2016).

AMDAT zone		Ref. month (January) mid-depth asphalt temperature (F)
1	Average	27.51
	Std. dev.	7.58
2	Average	29.71
	Std. dev.	5.61
3	Average	33.02
	Std. dev.	7.95
4	Average	37.73
	Std. dev.	6.8
5	Average	46.58
	Std. dev.	6.59
6	Average	46.67
	Std. dev.	8.98
7	Average	51.55
	Std. Dev.	11.1

6.3.4 Determination of Asphalt Modulus

In addition to determining the effective monthly asphalt modulus, it is important to consider the existing conditions of the asphalt layer. The asphalt layer can have fatigue cracking and other distress present, which will influence the asphalt dynamic modulus. To be able to account for the existing asphalt conditions, the following procedure is performed.

The undamaged asphalt dynamic modulus is first estimated for a reference temperature of 70^oF using a mastercurve (ARA 2004). This undamaged modulus is then converted to a damaged modulus to reflect the asphalt layer condition. The relationship between the undamaged and damaged asphalt modulus is as follows (ARA 2004):

$$E_{HMA(dam)} = 10^{\delta} + \frac{E_{HMA} - 10^{\delta}}{1 + e^{-0.3+5*LOG(d_{AC})}} \tag{6-15}$$

Where:

$E_{HMA(dam)}$ is the damaged asphalt modulus (psi),

δ is a regression parameter and is estimated as 2.84 for the default HMA mixture used in the Pavement ME,

E_{HMA} is the undamaged (new) asphalt modulus for a specific reduced time which in this procedure is 0.1 s, and

d_{AC} is the fatigue damage in the asphalt layer.

Using the relationship presented in Equation (6-15), the reduction of the asphalt modulus can be determined. The reduction factor for the asphalt modulus is as follows:

$$\Delta E = \frac{E_{HMA} - E_{HMA(dam)}}{E_{HMA}} \tag{6-16}$$

Where:

ΔE is the reduction factor for the asphalt modulus.

The asphalt damage factor is related to the existing asphalt layer condition based on the percentage of fatigue cracking as can be seen in Figure 6-6. For the application of bonded concrete overlays, Harrington (2008) recommends that fatigue cracking be less than 15% for primary and secondary roadways. In this procedure, the asphalt layer conditions for whitetopping are categorized into 'adequate' and 'marginal' based on their current condition (Zi et al. 2014). 'Adequate' asphalt conditions represent approximately 0-8% fatigue cracking and a damage factor of 0.3; and ‘marginal’ asphalt conditions represent approximately 8-20% fatigue cracking and a damage factor of 0.4. This is converted to an asphalt layer condition reduction percentage of 5 and 12.5 percent, respectively, as presented in Table 6-11. The reduction in asphalt dynamic modulus is then applied to the EEHMAs determined for each month.

Table 6-11 Reduction factor for the asphalt modulus (Zi et. al 2014).

Existing asphalt pavement conditions	Fatigue cracking, %	Damage factor	Asphalt modulus reduction, %
Adequate	0-8	0.3	5
Marginal	8-20	0.4	12.5

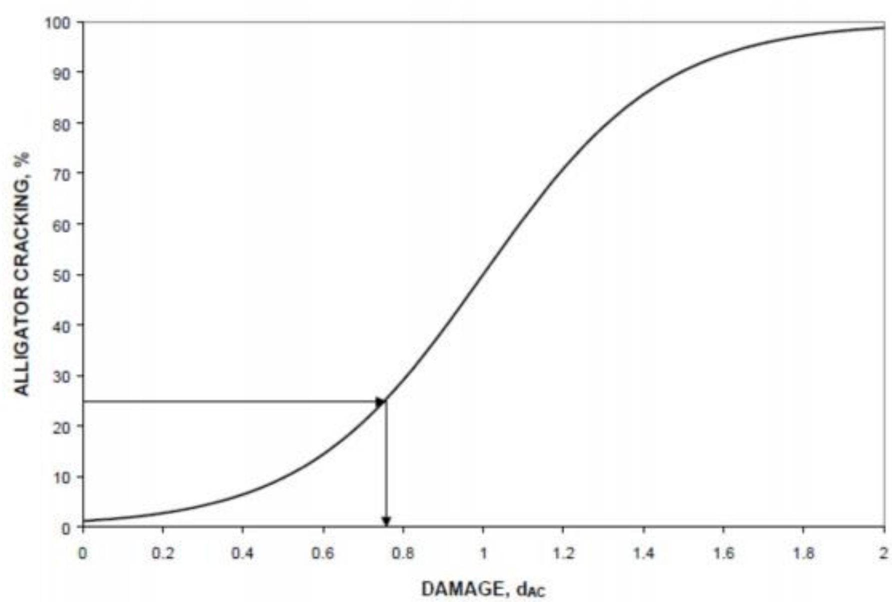

Figure 6-6 Relationship between fatigue (alligator) cracking and damage factor (ARA 2004).

6.4 Other Climatic Considerations

Other climatic related variables also need to be accounted to completely decouple the EICM from the design process when predicting faulting. The first variable to be determined is the number of WETDAYS for a specific project location. Regression models need to be developed to predict the number of days in a year with precipitation greater than 0.1 in. Another parameter that is directly used in the iterative predictive faulting model, which must be addressed is the freezing ratio. Regression models must predict the freezing ratio for specific project locations based on the longitude, latitude, elevation, and other structural features of the BCOA pavement. The third variable is the mean monthly nighttime mid-depth temperature of the PCC overlay. Without these site-specific variables, the prediction of faulting cannot occur independent of the EICM.

6.4.1 WETDAYS

Faulting is caused by the pumping mechanism, as outlined in Chapter 1. One of the main factors to contribute to pumping is free moisture. The free moisture is accounted for in the faulting model as a direct input in the incremental equations. As previously stated, WETDAYS is defined as the average number of days in a year with precipitation greater than 0.1 in.

The database of EICM analyses created to determine the other climatic considerations was utilized to develop a linear regression model for predicting WETDAYS. The database was populated using the 173 weather stations outlined above. Each weather station has an .icm file that provides hourly values of air temperature, precipitation, wind speed, and percent sunshine for several years. For each weather station, the hourly precipitation was analyzed and the total number of days greater than 0.1 in of precipitation was determined.

A stepwise regression was performed to examine the statistical significance of each possible variable on the magnitude of WETDAYS. The results of the stepwise regression along with the coefficients can be seen in Table 6-12 and Figure 6-7.

$$WETDAYS = C_1 + C_2 * SunZone + C_3 * AmdatZone + C_4 * Latitude + C_5 * Longitude + C_6 * P\_Sunshine \quad \textbf{(6-17)}$$

Table 6-12 WETDAYS regression coefficients.

C_1	C_2	C_3	C_4	C_5	C_6	R^2
-102.3	25.81	2.063	-1.216	0.3804	1.429	0.59

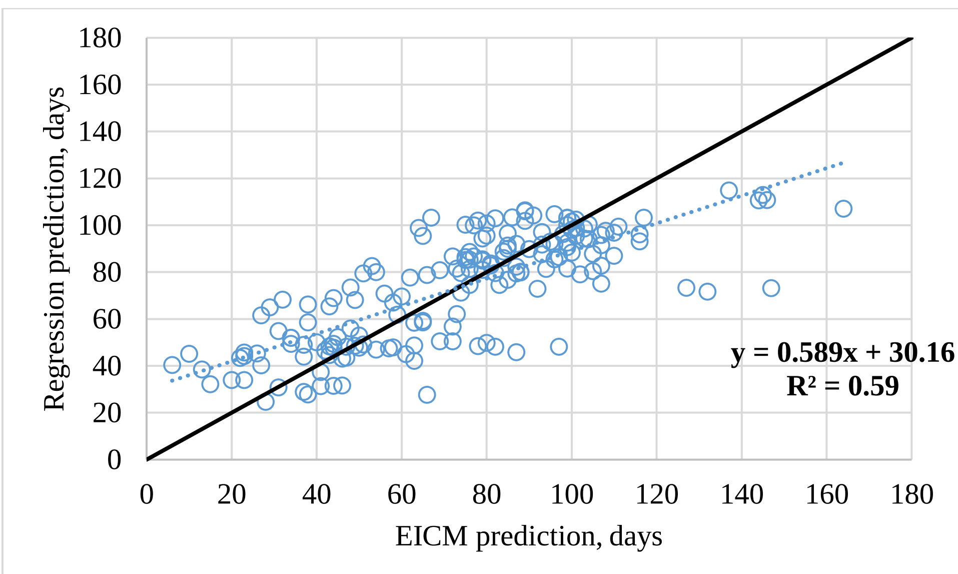

Figure 6-7 Stepwise regression for WETDAYS.

6.4.2 Freezing ratio

The freezing ratio is defined as the percentage of time that the top of the base layer (asphalt layer in this case) is less than 32 ^{o}F (freezing temperature). The significance of this variable is to be able to know how often the base layer is frozen. Deflections decrease significantly when the base layer is frozen, which reduces the differential energy and therefore the development of faulting.

The database of EICM analyses created to determine the other climatic variables was utilized to develop a linear regression for the freezing ratio. Using the hourly incremental temperature analysis, the freezing ratio was calculated for each analysis within the factorial.

A stepwise regression was performed to examine the statistical significance of each possible variable on the magnitude of the freezing ratio. A stepwise regression was performed using all of the data to develop a single equation. In addition, a stepwise regression was performed by breaking the data into the six sunshine zones. The results of the selected stepwise regression along with the coefficients can be seen in Table 6-13.

$$FR = C_1 + C_2 * h_{PCC} + C_3 * h_{HMA} + C_4 * AmdatZone + C_5 * Latitude + C_6 * Longitude + C_7 * Elevation \quad \textbf{(6-18)}$$

Table 6-13 Freezing ratio regression coefficients.

Sun. zone	C_1	C_2	C_3	C_4	C_5	C_6	C_7	R^2	Adj. R^2
1	-87.1	-0.111	-0.140	-2.58	0.711	0.705	4.2E-04	0.703	0.699
2	73.21	-0.094	-0.281	-7.332	0.878	-0.551	-3.5E-03	0.612	0.607
3	80.4	-0.008	-0.136	-5.342	0.096	-0.563	7.4E-04	0.688	0.686
4	-53.71	-0.004	-0.106	-3.141	0.864	0.502	3.1E-03	0.921	0.920
5	-77.15	0.066	-0.218	-1.763	1.998	0.149	1.9E-03	0.923	0.922
6	-15.74	-0.017	-0.255	-2.072	1.821	-0.495	9.4E-04	0.842	0.840

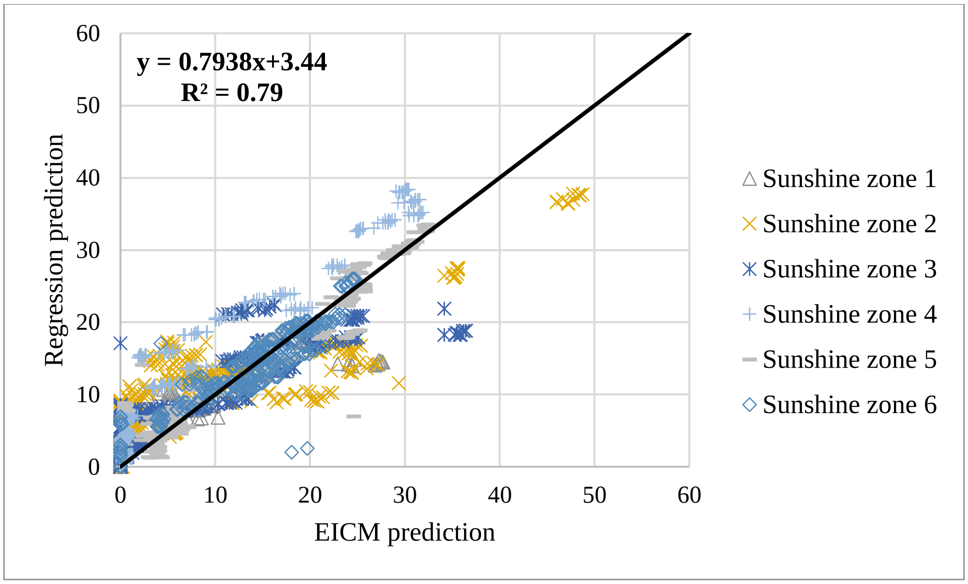

Figure 6-8 Stepwise regression for freezing ratio, FR.

6.4.3 Mean monthly nighttime mid-depth PCC temperature

The last parameter that must be defined to fully eliminate the necessity of incorporating the EICM in the design process is the mean monthly nighttime mid-depth temperature of the PCC overlay. This temperature is necessary to be able to determine monthly changes in magnitude of the joint widths, which affect the magnitude of aggregate interlock between the two adjacent slabs.

To develop the regression models, the mean monthly nighttime mid-depth temperature of the PCC overlay for each month is determined using temperature distributions from the EICM output with data between 8 pm and 8 am. In order to account for this variable without incorporating the EICM software in the design process, the procedure conducted by Sachs et al. to determine T_{norm} for each month and $T_{mid-depth(Ref)}$ in the BCOA-ME was followed (2016). First a regression was developed to determine $T_{mid-depth(Ref)}$ using the temperature distributions from EICM analyses. The stepwise regression resulted in a R^2 equal to 0.81 and can be seen in Equation (6-19). The prediction can be seen in Figure 6-9.

$$T_{mid-depth(Ref)} = 58.72 - 0.123h_{PCC} - 1.455SunZone + 5.817AMDATzone - 0.67Latitude + 0.2429\ Longitude + 0.00104\ Elevation - 0.584\ P\_Sunshine \tag{6-19}$$

Where:

$T_{mid-depth(Ref)}$ is the mean monthly nighttime mid-depth PCC temperature for the reference month (January), (°F).

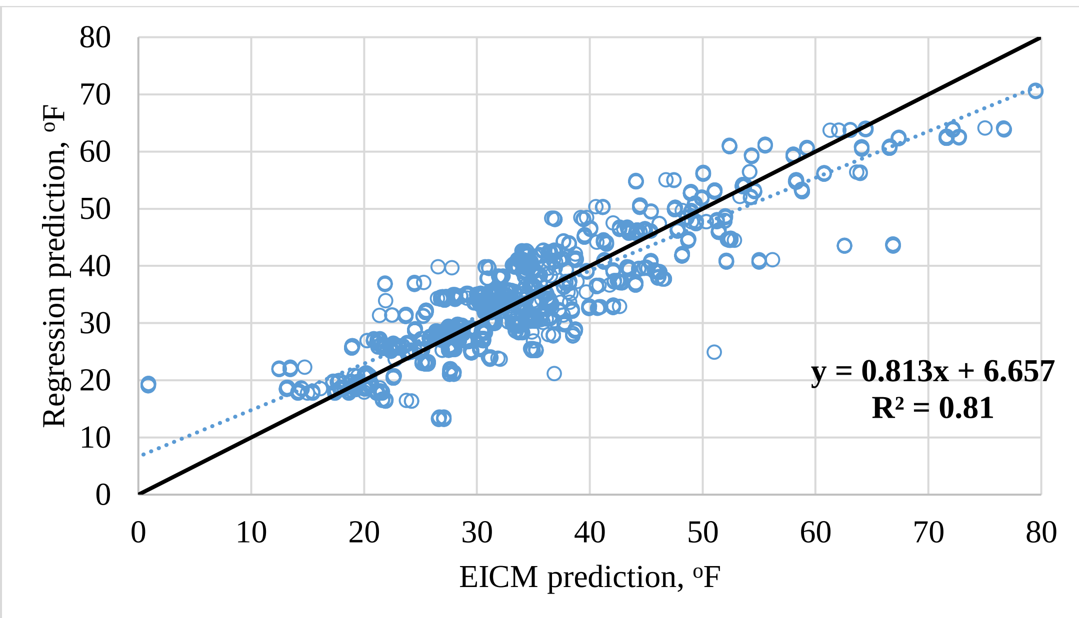

Figure 6-9 Stepwise regression for $T_{mid-depth(Ref)}$, °F.

Using the database of EICM outputs for each AMDAT zone, zonal averages were determined for the T_{norm} for each month. The values determined for the mean monthly nighttime mid-depth temperature of the PCC overlay for each month can be seen in Table 6-14.

Table 6-14 Mean monthly nighttime PCC mid-depth temperature, T_{norm}.

AMDAT zone	**$T_{mid-depth(Ref)}$, °F (Avg./Std. dev.)**	**T_{norm} for each month , °F/ °F**											
		Jan.	Feb.	Mar.	Apr.	May	June	July	Aug.	Sept.	Oct.	Nov.	Dec.
1	21.62	1.0	1.0	1.8	2.7	3.6	4.1	4.6	4.6	3.8	2.8	2.3	1.2
	7.65	0.0	1.2	4.8	7.8	11.1	13.9	16.8	16.4	13.5	8.2	5.9	0.3
2	29.44	1.0	1.1	1.4	2.0	2.5	2.9	3.1	3.1	2.6	2.1	1.8	1.3
	5.05	0.0	0.1	0.1	0.4	0.4	0.5	0.5	0.5	0.4	0.3	0.3	0.3
3	33.53	1.0	1.2	1.4	2.0	2.4	2.6	2.8	2.8	2.4	1.9	1.7	1.3
	5.48	0.0	0.1	0.2	0.3	0.4	0.4	0.5	0.5	0.4	0.3	0.2	0.2
4	39.67	1.0	1.2	1.4	1.8	2.1	2.4	2.5	2.5	2.2	1.8	1.6	1.3
	7.86	0.0	0.1	0.1	0.3	0.3	0.4	0.4	0.4	0.3	0.2	0.2	0.1
5	47.79	1.0	1.2	1.3	1.6	1.9	2.0	2.1	2.1	1.9	1.6	1.4	1.2
	4.97	0.0	0.1	0.1	0.1	0.1	0.2	0.2	0.2	0.2	0.1	0.1	0.1
6	53.62	1.0	1.2	1.3	1.5	1.7	1.8	1.9	1.9	1.7	1.5	1.3	1.1
	4.54	0.0	0.1	0.1	0.1	0.2	0.2	0.2	0.2	0.2	0.1	0.1	0.1
7	67.69	1.0	1.1	1.2	1.3	1.4	1.5	1.5	1.6	1.5	1.3	1.2	1.1
	8.24	0.0	0.0	0.1	0.1	0.2	0.2	0.2	0.2	0.2	0.1	0.1	0.1

An analysis was performed to show the predictability of the developed regression against the zonal averages for the reference month (January). A good trend can be seen in Figure 6-10, indicating it is possible to use the AMDAT zonal averages without significantly losing predictability.

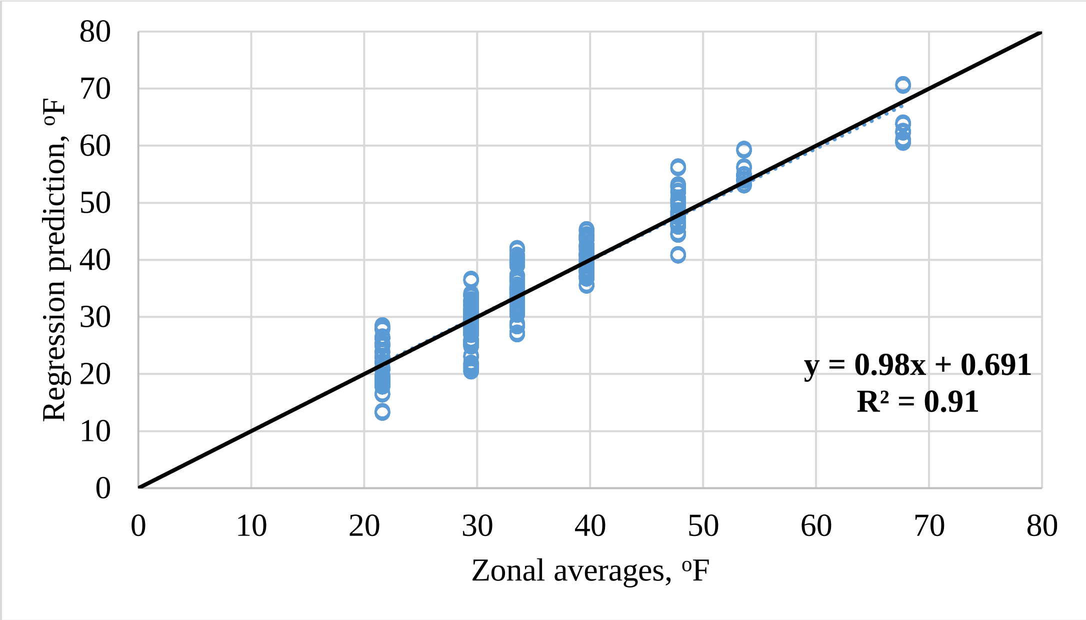

Figure 6-10 $T_{mid-depth(Ref)}$: AMDAT zonal averages vs. stepwise regression.

To determine the mean monthly nighttime mid-depth PCC temperature for each corresponding AMDAT zone and month, i, the following equation is to be used.

$$T_{mid-depth}(i) = T_{mid-depth(Ref)} * T_{norm}(i) \quad \textbf{(6-20)}$$

Where:

$T_{mid-depth}$ is the mean monthly nighttime mid-depth PCC temperature (°F) for month i.

6.5 Conclusions

It is important to be able to implement the developed predictive faulting model into the current design procedure. In order to do so, the faulting model needed to be decoupled from the EICM. Decoupling the EICM from the design process was accomplished through the development of linear regression equations for a number of variables, including the overlay temperature gradient and the temperature dependent asphalt stiffness.

First, a database was populated with numerous EICM analyses that include a large range of climatic conditions and BCOA structures. This database was used for developing all regression equations presented within this chapter. A previously established framework was modified to establish EELTG for BCOA pavements. These were established by running an hourly incremental analysis to determine a single EELTG that resulted in the same amount of differential energy as the hourly changes in ELTGs in the corresponding year. Linear regression equations were then developed for determining the EELTG based on the project location (longitude, latitude, and elevation), other structural features of the BCOA pavement, and the three different differential energy models (partial lane width panels with joints only through the PCC, partial lane width panels with joints through the PCC and asphalt layer, and full lane width panels with joints through the PCC and asphalt layer).

Second, effective monthly asphalt stiffness regression equations were developed to account for the monthly changes in temperature. These were established by performing an hourly incremental analysis to determine an effective monthly asphalt stiffness that resulted in the same amount of differential energy as the hourly changes in stiffness in the corresponding month. Regression equations were developed for asphalt adjustment factors for each month in the year based on normalized mid-depth asphalt temperatures. The effective monthly asphalt stiffness for the reference month (January) was also established as a function of the average mid-depth asphalt temperature for the reference month. This allowed for the calculation of the 12 effective monthly asphalt stiffnesses in a year.

Third, other climatic related variables needed to be accounted for without the use of the temperature distributions generated using the EICM. Regression equations were developed for the number of WETDAYS for a specific project location based on the longitude, latitude, and elevation. Another parameter that was directly used in the iterative predictive faulting model is the freezing ratio. Regression equations were developed for the freezing ratio for a specific project location based on the longitude, latitude, elevation, and other structural features of the BCOA pavement. The last parameter needed is the mean monthly nighttime mid-depth temperature of the PCC overlay. This temperature is necessary to be able to determine monthly changes in magnitude of the joint width, which affects the magnitude of aggregate interlock load transfer between the two adjacent slabs.

Finally, through the development of all of these regression equations, it is believed that the developed predictive faulting model can be implemented into the current design procedure, the BCOA-ME developed by the University of Pittsburgh.

7.0 Concluding Remarks and Future Work

Currently available BCOA design procedures only have the capability of predicting the performance life using fatigue cracking as the failure criteria. Therefore, there is a great need to be able to incorporate faulting as a failure criterion into the design process for BCOAs. In order to be able to develop a faulting model, an in-depth investigation was conducted on the joint performance of BCOAs. It was determined, faulting in BCOA can develop from pumping that can initiate at one of two separate locations; 1. in the asphalt layer or 2. in the granular material beneath the asphalt. The source of the fines being pumped will depend on the depth at which the joint activates. It has been shown that while some joints activate only through the PCC layer, others will activate through both the PCC layer and asphalt layer. An extensive analysis was performed using FWD data to identify the depth of activation for each joint based on the LTE of the joint within a given section for a range of pavement structures. Cores provided validation of this methodology. The structural design features and material properties of these sections, along with their respective joint activation depths, were examined so that trends could be identified. The flexural strength ratio between the overlay and the asphalt and joint spacing were found to be good predictors of the depth of activation. Finally, material properties such as the CTE of the different layers, drying shrinkage of the PCC, creep of the asphalt, and fracture properties of the materials will also influence joint activation depth.

After establishing how these BCOAs develop faulting, it was important to develop a calibration database of representative structures. An investigation was performed to assess if the trends in which faulting develops in conventional concrete pavements and UBOLs is similar to that of BCOA. If this can be proven true, then performance data for these structures could be used to supplement the calibration database for the BCOAs. It was determined faulting data for JPCPs on a stabilized base could not be used to supplement the calibration when joints activate through the PCC and asphalt layer. This is because the level of faulting that develops in a BCOA does not appear to approach an asymptotic value as traffic loads are accumulated, as was exhibited with conventional pavements. It was also determined that faulting data for UBOLs could also not be included in the calibration database for BCOAs with joints that only activate through the PCC layer. There was insufficient performance data to establish if the rate at which faulting developed in UBOLs was similar to that of BCOAs. In addition, the mixtures of the asphalt interlayers used in the UBOLs varied drastically in comparison to the BCOA existing asphalt. These interlayers could be newly placed or an existing surface layer, as well as an open graded or dense graded asphalt. The different mixture designs and material properties could contribute to a different trend in the development of faulting in comparison to faulting trends visible in BCOAs. Although UBOLs were not included for this calibration, as more UBOLs are constructed and additional performance data becomes available for a larger range of asphalt interlayer materials, the inclusion of UBOL faulting data may be beneficial. Therefore, the BCOA calibration database could not be supplement with performance data from conventional JPCPs or UBOLs. Within this analysis, the suitability of applying one faulting model for different concrete pavement structures was also assessed. In conclusion, it was found that the current faulting prediction model used in the Pavement ME design software does not accurately capture the trends in fault development for UBOL. This is also the case for BCOAs when the joint only activates through the PCC.

In order to accurately model the response of a BCOA, a computational model capable of accounting for both depths of joint activation was developed using the 3-D FEM software, ABAQUS. The computational model was validated with FWD data collected for field sections constructed at MnROAD and at the UCPRC testing facility. The critical response obtained from each model is the 2 x 6 ft deflection basin on the approach and leave slabs adjacent to the loaded transverse joint. The deflection basins are to determine the difference in energy density more accurately on both sides of the joint as compared to the traditional approach of using corner deflections. A fractional factorial experiment was designed to minimize the number of computational analyses that needed to be performed using the FEM. A total of 19,440 FEM analyses were performed to populate the database. This database was then used to train ANNs so the critical response of the BCOA to environmental and traffic loading conditions could be rapidly predicted without the need to perform an FEM analysis.

These ANNs were then incorporated into the framework adopted for predicting joint faulting for BCOA. The established framework follows the current design procedure used in the Pavement ME. A discussion of how the differential energy concept is utilized along with each of the steps required to establish the inputs for the ANNs is presented. This includes how climatic factors are treated, primarily the hourly temperature gradient for the overlay and the hourly temperature dependent asphalt stiffness. Finally, the incremental faulting equations are presented. Within the incremental faulting equations, an erosion prediction model was developed to assess the existing asphalt pavement surface and overall contribution to the development of faulting. With the framework presented, a discussion of the data available to calibrate the faulting model is made; including the location of each pavement section and the relevant design features. The model calibration is then presented and an extensive model validation was performed.

In order to implement the field calibrated predictive faulting model into the current design procedure, there are a few parameters related to the climate features that needed to be addressed. These parameters include accounting for PCC temperature gradients, temperature dependent asphalt stiffness, average annual number of days with precipitation greater than 0.1 in, annual percentage of time the base layer is frozen, and the mean monthly nighttime mid-depth PCC temperature. These climatic features can all be determined using the EICM software. However, the objective of this framework is to implement this model into the current design procedure, BCOA-ME, and is important to eliminate the need of any external resource such as the EICM. Therefore, regression equations were developed to be able to estimate these parameters as a function of the structural design of the BOCA pavement and the geographic location of the pavement. The BOCA faulting model is now able to be implemented into the BCOA-ME design procedure.

A limitation of the developed prediction model is the calibration database includes a significant number of sections from one state, Minnesota. There was a limited number of constructed sections with proficient measured field performance data. Also, some sections that were measured only included the number of joints that were in a certain range of faulting. Instead of recording and presenting the faulting for consecutive joints, the total number of joints were recorded if they had a magnitude of faulting within a certain range. A significant amount of effort was made to obtain as much performance data as possible to supplement the calibration sections. A study was performed to examine different JPCP on different base layers, along with UBOL to supplement the calibration database for BCOAs. In addition to the climatic region limitation, the range of structural features and traffic levels were also limited. One of the structural features that will be beneficial to increase the calibration database is the asphalt characteristics (mixture properties). An erosion model was developed based on a few different parameters of the asphalt mixture. However, a limited number of sections resulted in a limited number of different asphalt layers. Therefore, more sections with different asphalt material properties will enhance the erosion prediction model and overall faulting prediction model. It is believed that the results from these models are sufficient until additional data is available to supplement the calibration database and another calibration can be performed. As more performance data becomes available, it will be possible to recalibrate the models with the additional data in the future.

Appendix A Calibration Database

For each calibration section, detailed information is presented in the following tables which is required for the faulting model calculation.

Table A-1 Calibration sections project information.

Source	Section ID	Overlay const. date	Age, yrs.	Estimated ESALs	Long., deg	Lat., deg
MnROAD	Cell60_PCC	Oct-04	8.59	8.45E+06	44.6	-93.8
MnROAD	Cell60_PL_PCC	Oct-04	6.98	1.70E+06	44.6	-93.8
MnROAD	Cell60_FULL	Oct-04	8.59	8.45E+06	44.6	-93.8
MnROAD	Cell60_PL_FULL	Oct-04	6.98	1.70E+06	44.6	-93.8
MnROAD	Cell61_PCC	Oct-04	8.59	8.45E+06	44.6	-93.8
MnROAD	Cell61_PL_PCC	Oct-04	6.98	1.70E+06	44.6	-93.8
MnROAD	Cell61_FULL	Oct-04	6.50	6.20E+06	44.6	-93.8
MnROAD	Cell61_PL_FULL	Oct-04	4.70	1.14E+06	44.6	-93.8
MnROAD	Cell62_PCC	Oct-04	8.59	8.45E+06	44.6	-93.8
MnROAD	Cell62_PL_PCC	Oct-04	6.98	1.70E+06	44.6	-93.8
MnROAD	Cell63_PCC	Oct-04	8.59	8.45E+06	44.6	-93.8
MnROAD	Cell63_PL_PCC	Oct-04	6.98	1.70E+06	44.6	-93.8
MnROAD	Cell92_FULL	Oct-97	12.51	1.16E+07	44.6	-93.8
MnROAD	Cell92_PL_FULL	Oct-97	12.51	3.19E+06	44.6	-93.8
MnROAD	Cell95_PCC	Oct-97	4.95	4.76E+06	44.6	-93.8
MnROAD	Cell95_PL_PCC	Oct-97	4.95	1.33E+06	44.6	-93.8
MnROAD	Cell95_FULL	Oct-97	4.95	4.76E+06	44.6	-93.8
MnROAD	Cell95_PL_FULL	Oct-97	4.95	1.33E+06	44.6	-93.8
MnROAD	Cell96_PCC	Oct-97	13.53	1.25E+07	44.6	-93.8
MnROAD	Cell96_PL_PCC	Oct-97	13.98	3.50E+06	44.6	-93.8
MnROAD	Cell96_FULL	Oct-97	12.66	1.17E+07	44.6	-93.8
MnROAD	Cell97_FULL	Oct-97	12.51	1.16E+07	44.6	-93.8
MnDOT	CSAH 22_002-622-033	2013	3.00	1.28E+05	45.3	-93.2
MnDOT	CSAH 22_CP 12-14-22	2012	4.00	1.69E+05	45.3	-93.2
MnDOT	CSAH 22_02-622-31	2011	5.00	2.26E+05	45.3	-93.2
MnDOT	TH 56_2006-26	2010	6.00	9.06E+04	44.1	-92.9
MnDOT	TH 30_0705-14	1993	22.00	3.39E+05	43.89	-94.2
MnDOT	CSAH 7_43-607-14	2009	7.00	3.26E+05	44.8	-94.3
MnDOT	CSAH 2_43-602-(24-25)	2011	5.00	2.19E+05	44.82	-94.17
NCHRP 1-61	06-6	1997	22.00	4.69E+06	40.63	-102.55
NCHRP 1-61	06-121A	2011	8.00	3.13E+06	39.87	-105.09
NCHRP 1-61	06-121B	2001	18.00	4.39E+06	39.58	-105.09
NCHRP 1-61	06-83A	2005	14.00	5.91E+06	39.61	-104.81
NCHRP 1-61	06-83B	1999	20.00	1.02E+07	39.62	-104.82
NCHRP 1-61	17-27	2003	16.00	1.00E+07	39.82	-89.10
NCHRP 1-61	22-167	1992	27.00	5.57E+06	31.93	-92.64
NCHRP 1-61	29-60	1999	20.00	1.91E+07	36.84	-94.41

Table A-2 Calibration sections design features.

Section ID	Avg. joint spacing	Lane width	Tied PCC shoulder	Dowel diameter, in
Cell60_PCC	5	6	No, AC	None
Cell60_PL_PCC	5	6	No, AC	None
Cell60_FULL	5	6	No, AC	None
Cell60_PL_FULL	5	6	No, AC	None
Cell61_PCC	5	6	No, AC	None
Cell61_PL_PCC	5	6	No, AC	None
Cell61_FULL	5	6	No, AC	None
Cell61_PL_FULL	5	6	No, AC	None
Cell62_PCC	5	6	No, AC	None
Cell62_PL_PCC	5	6	No, AC	None
Cell63_PCC	5	6	No, AC	None
Cell63_PL_PCC	5	6	No, AC	None
Cell92_FULL	10	12	No, AC	1
Cell92_PL_FULL	10	12	No, AC	1
Cell95_PCC	5	6	No, AC	None
Cell95_PL_PCC	5	6	No, AC	None
Cell95_FULL	5	6	No, AC	None
Cell95_PL_FULL	5	6	No, AC	None
Cell96_PCC	5	6	No, AC	None
Cell96_PL_PCC	5	6	No, AC	None
Cell96_FULL	5	6	No, AC	None
Cell97_FULL	10	12	No, AC	None
CSAH 22_002-622-033	6.25	6.25	No, AC	None
CSAH 22_CP 12-14-22	6	6	No, AC	None
CSAH 22_02-622-31	6	6, 7	No, AC	None
TH 56_2006-26	15	13.5	No, AC	1
TH 30_0705-14	12	12	No, AC	None
CSAH 7_43-607-14	6	6, 7	No, Agg.	None
CSAH 2_43-602-(24-25)	6	6, 7	No, Agg.	None
06-6	10	12	Yes	1
06-121A	6	6	Yes	None
06-121B	6	6	Yes	None
06-83A	6	6	Yes	None
06-83B	6	6	Yes	None
17-27	5.5	5.5	No, Agg.	None
22-167	4	4	Yes	None
29-60	4	4	No, AC	None

Table A-3 Calibration sections structural details.

Section ID	Overlay thickness, in	Overlay EMOD, psi	Overlay MOR, psi	Overlay CTE, $x10^{-6}$ in/in/ºF	Overlay cement content, lbs.	Asphalt thickness, in
Cell60_PCC	5.0	4.58E+06	595	4.11	400	7.0
Cell60_PL_PCC	5.0	4.58E+06	595	4.11	400	7.0
Cell60_FULL	5.0	4.58E+06	595	4.11	400	7.0
Cell60_PL_FULL	5.0	4.58E+06	595	4.11	400	7.0
Cell61_PCC	5.0	4.42E+06	545	4.39	400	7.0
Cell61_PL_PCC	5.0	4.42E+06	545	4.39	400	7.0
Cell61_FULL	5.0	4.42E+06	545	4.39	400	7.0
Cell61_PL_FULL	5.0	4.42E+06	545	4.39	400	7.0
Cell62_PCC	4.0	4.89E+06	575	3.89	400	8.0
Cell62_PL_PCC	4.0	4.89E+06	575	3.89	400	8.0
Cell63_PCC	4.0	5.02E+06	560	4.11	400	8.0
Cell63_PL_PCC	4.0	5.02E+06	560	4.11	400	8.0
Cell92_FULL	6.0	4.80E+06	860	5.5	650	7.0
Cell92_PL_FULL	6.0	4.80E+06	860	5.5	650	7.0
Cell95_PCC	3.0	4.70E+06	840	5.5	650	10.0
Cell95_PL_PCC	3.0	4.70E+06	840	5.5	650	10.0
Cell95_FULL	3.0	4.70E+06	840	5.5	650	10.0
Cell95_PL_FULL	3.0	4.70E+06	840	5.5	650	10.0
Cell96_PCC	6.0	4.70E+06	890	5.5	650	7.0
Cell96_PL_PCC	6.0	4.70E+06	890	5.5	650	7.0
Cell96_FULL	6.0	4.70E+06	890	5.5	650	7.0
Cell97_FULL	6.0	4.70E+06	830	5.5	650	7.0
CSAH 22_002-622-033	6.0	4.00E+06	650	6.0	420	4.0
CSAH 22_CP 12-14-22	6.0	4.00E+06	650	6.0	405	4.0
CSAH 22_02-622-31	6.0	4.00E+06	650	6.0	400	3.0
TH 56_2006-26	6.0	4.00E+06	738	3.8	413	8.5
TH 30_0705-14	6.0	4.00E+06	507	6.6	420	7.5
CSAH 7_43-607-14	5.0	4.00E+06	679	5.3	420	6.0
CSAH 2_43-602-(24-25)	5.0	4.00E+06	650	5.3	420	5.0
06-6	6.0	4.00E+06	650	4.8	520	9.0
06-121A	6.0	4.00E+06	650	4.8	520	13.0
06-121B	7.0	4.00E+06	650	4.8	520	12.0
06-83A	8.0	4.00E+06	650	4.8	520	16.0
06-83B	6.0	4.00E+06	650	4.8	520	13.0
17-27	5.0	3.60E+06	900	3.8	534	8.0
22-167	5.0	4.00E+06	600	6.0	564	9.0
29-60	4.5	4.00E+06	650	4.5	592	5.0

Table A-4 Calibration section EELTG and EHMA.

Section ID	EELTG (in/in/ºF)	E_{HMA} ($x10^6$ psi)											
		Jan.	Feb.	Mar.	Apr.	May	June	July	Aug.	Sept.	Oct.	Nov.	Dec.
Cell60_PCC	-2.582	2.96	3.07	2.44	1.28	0.62	0.43	0.29	0.3	0.65	0.89	1.87	2.97
Cell60_PL_PCC	-2.582	2.96	3.07	2.44	1.28	0.62	0.43	0.29	0.3	0.65	0.89	1.87	2.97
Cell60_FULL	-1.278	2.96	3.07	2.44	1.28	0.62	0.43	0.29	0.3	0.65	0.89	1.87	2.97
Cell60_PL_FULL	-1.278	2.96	3.07	2.44	1.28	0.62	0.43	0.29	0.3	0.65	0.89	1.87	2.97
Cell61_PCC	-2.582	2.96	3.07	2.44	1.28	0.62	0.43	0.29	0.3	0.65	0.89	1.87	2.97
Cell61_PL_PCC	-2.582	2.96	3.07	2.44	1.28	0.62	0.43	0.29	0.3	0.65	0.89	1.87	2.97
Cell61_FULL	-1.278	2.96	3.07	2.44	1.28	0.62	0.43	0.29	0.3	0.65	0.89	1.87	2.97
Cell61_PL_FULL	-1.278	2.96	3.07	2.44	1.28	0.62	0.43	0.29	0.3	0.65	0.89	1.87	2.97
Cell62_PCC	-3.207	2.95	3.06	2.4	1.24	0.62	0.42	0.29	0.31	0.65	0.89	1.91	2.98
Cell62_PL_PCC	-3.207	2.95	3.06	2.4	1.24	0.62	0.42	0.29	0.31	0.65	0.89	1.91	2.98
Cell63_PCC	-3.207	2.95	3.06	2.4	1.24	0.62	0.42	0.29	0.31	0.65	0.89	1.91	2.98
Cell63_PL_PCC	-3.207	2.95	3.06	2.4	1.24	0.62	0.42	0.29	0.31	0.65	0.89	1.91	2.98
Cell92_FULL	-1.855	2.96	3.07	2.44	1.28	0.62	0.43	0.29	0.3	0.65	0.89	1.87	2.97
Cell92_PL_FULL	-1.855	2.96	3.07	2.44	1.28	0.62	0.43	0.29	0.3	0.65	0.89	1.87	2.97
Cell95_FULL	-3.012	2.95	3.05	2.4	1.26	0.62	0.42	0.29	0.31	0.65	0.89	1.89	2.98
Cell95_PL_FULL	-3.012	2.95	3.05	2.4	1.26	0.62	0.42	0.29	0.31	0.65	0.89	1.89	2.98
Cell96_PCC	-1.857	2.96	3.07	2.44	1.28	0.62	0.43	0.29	0.3	0.65	0.89	1.87	2.97
Cell96_PL_PCC	-1.857	2.96	3.07	2.44	1.28	0.62	0.43	0.29	0.3	0.65	0.89	1.87	2.97
Cell97_FULL	-1.857	2.96	3.07	2.44	1.28	0.62	0.43	0.29	0.3	0.65	0.89	1.87	2.97
CSAH 22_002-622-033	-0.748	2.94	3.06	2.43	1.21	0.61	0.41	0.28	0.3	0.64	0.89	1.93	2.98
CSAH 22_CP 12-14-22	-0.748	2.94	3.06	2.43	1.21	0.61	0.41	0.28	0.3	0.64	0.89	1.93	2.98
CSAH 22_02-622-31	-3.389	2.93	3.05	2.41	1.19	0.61	0.41	0.28	0.3	0.64	0.89	1.95	2.99
TH 56_2006-26	-2.016	2.89	3.01	2.35	1.21	0.66	0.44	0.3	0.33	0.67	0.87	1.9	2.96
TH 30_0705-14	-2.124	2.91	3.01	2.38	1.11	0.61	0.41	0.27	0.3	0.58	0.83	1.87	2.97
CSAH 7_43-607-14	-2.74	2.88	3.04	2.43	1.17	0.6	0.41	0.28	0.3	0.59	0.83	1.97	3
CSAH 2_43-602-(24-25)	-1.227	2.98	3.07	2.43	1.31	0.64	0.44	0.31	0.31	0.68	0.93	1.91	2.99
06-6	-2.224	1.46	1.55	1.19	0.91	0.61	0.46	0.31	0.35	0.54	0.91	1.22	1.55
06-121A	-2.351	1.03	1.03	1.03	0.91	0.86	0.62	0.4	0.46	0.72	0.86	1.0	1.03
06-121B	-2.159	2.36	2.42	1.29	0.88	0.67	0.41	0.29	0.34	0.46	0.83	1.3	2.01
06-83A	-2.052	2.36	2.42	1.29	0.88	0.67	0.41	0.29	0.34	0.46	0.83	1.3	2.01
06-83B	-2.351	1.03	1.03	1.03	0.91	0.86	0.62	0.4	0.46	0.72	0.86	1.0	1.03
17-27	-2.989	1.3	1.34	1.61	0.74	0.44	0.36	0.22	0.26	0.43	0.95	1.26	1.61
22-167	-2.945	1.28	1.15	0.97	0.49	0.31	0.26	0.18	0.2	0.3	0.51	0.67	1.13
29-60	-2.909	1.05	0.9	0.82	0.52	0.48	0.4	0.32	0.33	0.47	0.63	0.75	0.82

Table A-5 EICM example inputs: calibration section 06-6.

Model characteristics	Parameters within analysis	User inputs
Integrated model initialization	Section ID	06-6
	First month in analysis period	January
	Length of analysis (days/yrs)	1825/5
	Time increment output (hrs)	1
	Latitude (degrees)	40.625
	Longitude (degrees)	-102.548
	Elevation (ft)	2510
Climatic/boundary conditions	Import climate file .icm (temp., rainfall, wind speed, % sunshine, and water table depth)	
Thermal properties	Surface short-wave absorptivity	0.8
	Time of day when min. air temp. occurs	4
	Time of day when max. air temp. occurs	15
	Upper temperature limit of freezing range (F)	32
	Lower temperature limit of freezing range (F)	30.2
TTI infiltration and drainage model inputs	Linear length cracks/joints one side pavement (ft)	100
	Total length surveyed for cracks and joints (ft)	100
	Type of fines added to base course	Inert filler
	% of fines added to base course (%)	2.5
	% of gravel in base course (%)	70
	% of sand in base course (%)	27.5
	One side width of base (ft)	25
	Slope ratio/base tangent value (%)	1.5
PCC material properties	Thickness of layer (in)	6
	Number of elements this layer	6
	Thermal conductivity (BTU/hr-ft-F)	1
	Heat capacity (BTU/lb-F)	0.2
	Total unit weight of PCC (pcf)	150
Asphalt cement material properties	Thickness of layer (in)	9
	Number of elements this layer	9
	Thermal conductivity (BTU/hr-ft-F)	0.67
	Heat capacity (BTU/lb-F)	0.22
	Total unit weight of PCC (pcf)	150

Table A-5 (contd.).

Model characteristics	Parameters within analysis	User inputs
Base layer material properties	Thickness of layer (in)	12
	Number of elements this layer	2
	Porosity	0.172
	Saturated permeability (ft/hr)	999
	Dry unit weight (pcf)	137
	Dry thermal conductivity (BTU/hr-ft-F)	0.3
	Dry heat capacity ((BTU/ft^3-F)	0.18
	Initial volumetric water content (%)	0.061
	Soil water charateristic curve parameters:	
	af (Fredlund-Xing)	1.5
	bf (Fredlund-Xing)	7.5
	cf (Fredlund-Xing)	1.2
	hr (Fredlund-Xing)	0.12
	PI:	0
	D60 (in)	0.47
	% Passing No.4 (%)	37
	% Passing No.200 (%)	10
Subbase layer material properties	Thickness of layer (in)	220
	Number of elements this layer	22
	Porosity	0.42
	Saturated permeability (ft/hr)	4.80E-06
	Dry unit weight (pcf)	99
	Dry thermal conductivity (BTU/hr-ft-F)	0.18
	Dry heat capacity ((BTU/ft^3-F)	0.185
	Initial volumetric water content (%)	0.176
	Soil water charateristic curve parameters:	
	af (Fredlund-Xing)	1.5
	bf (Fredlund-Xing)	7.5
	cf (Fredlund-Xing)	1.2
	hr (Fredlund-Xing)	0.12
	PI:	12
	D60 (in)	0.002
	% Passing No.4 (%)	90
	% Passing No.200 (%)	77.5

Table A-6 Sensitivity analysis corresponding variables for Structure 3.

Parameter	Value
Hol (in)	6
Eol (psi)	4000000
f'c (psi)	0
MOR (psi)	650
Hhma (in)	4
P200 HMA (%)	7
%AV HMA (%)	6
%Eff Bind HMA	5
k-value(psi/in)	250
P200 base (%)	50
Jt. spacing (in)	72
Dowel diameter (in)	0
Shoulder type	0
CTE-OL (^{o}F/in/in)	5.5
Design period (months)	240
EELTG PCC depth (^{o}F/in)	-1.00802
EELTG full-depth (^{o}F/in)	-0.85639
Month of construction	10
Cement content (pcy)	500
# Lanes	2
ADT one-way	20000
Truck %	0.07

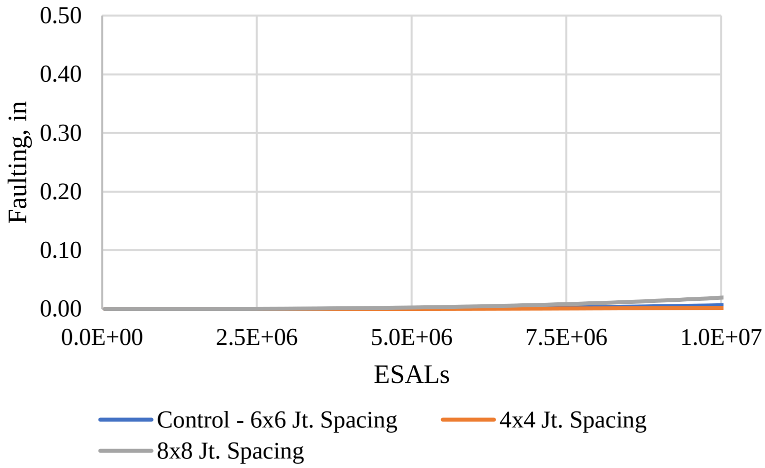

a) Partial depth

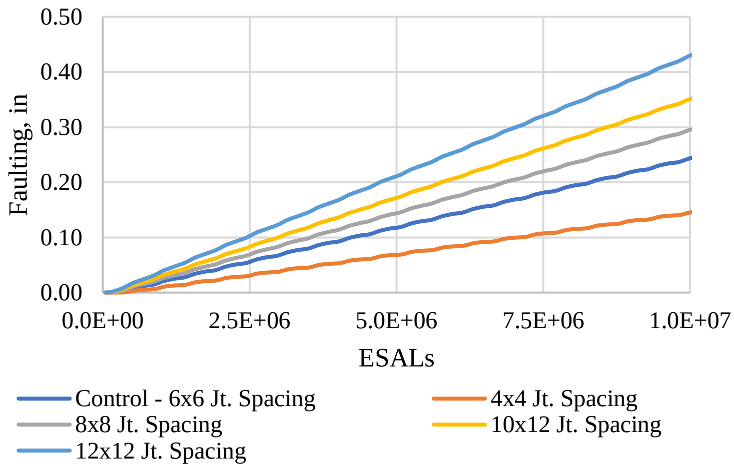

b) Full-depth

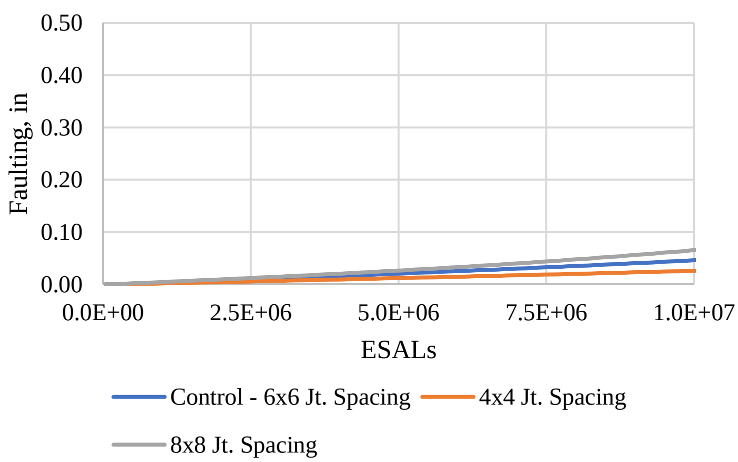

c) Both depths

Figure A-1 Effect of joint spacing on predicted faulting for Structure 3.

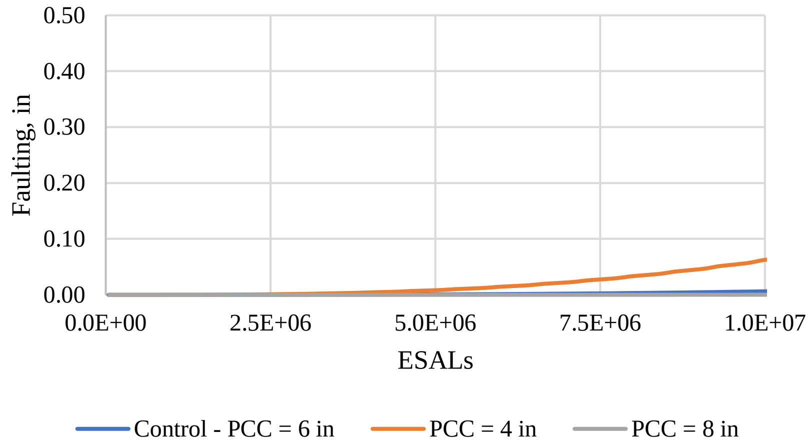

a) Partial Depth

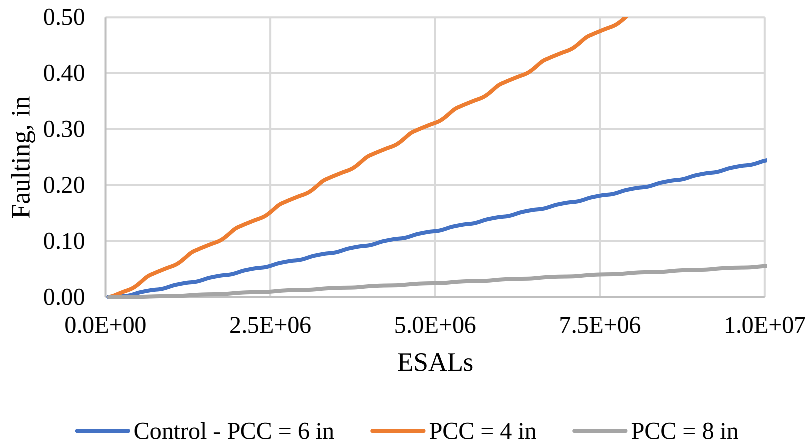

b) Full-depth

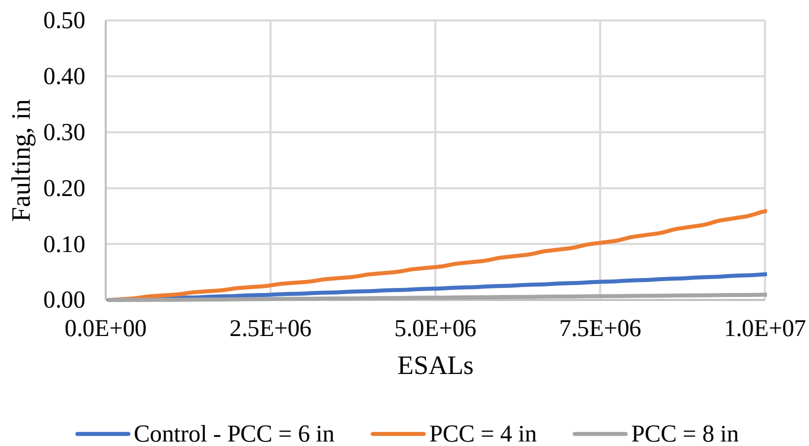

c) Both Depths

Figure A-2 Effect of PCC overlay thickness on predicted faulting for Structure 3.

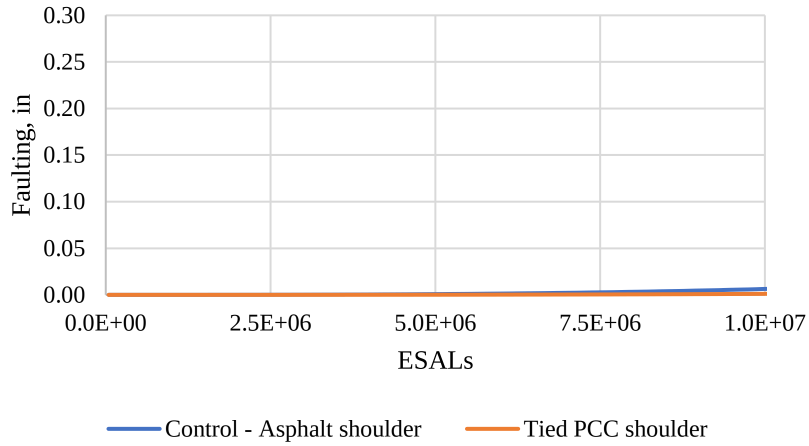

a) Partial depth

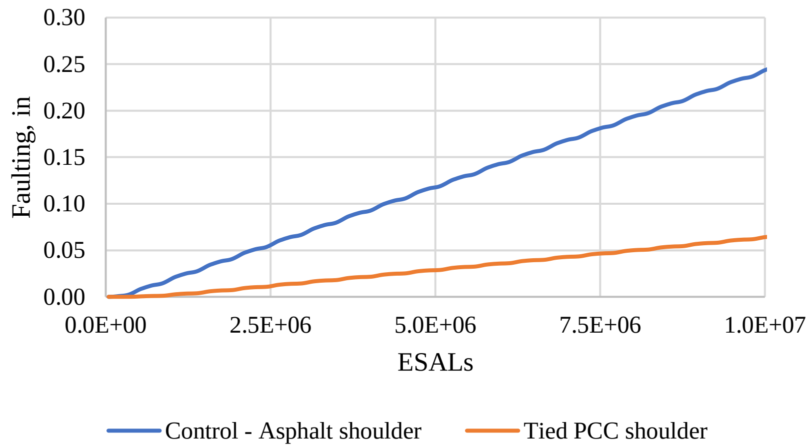

b) Full-depth

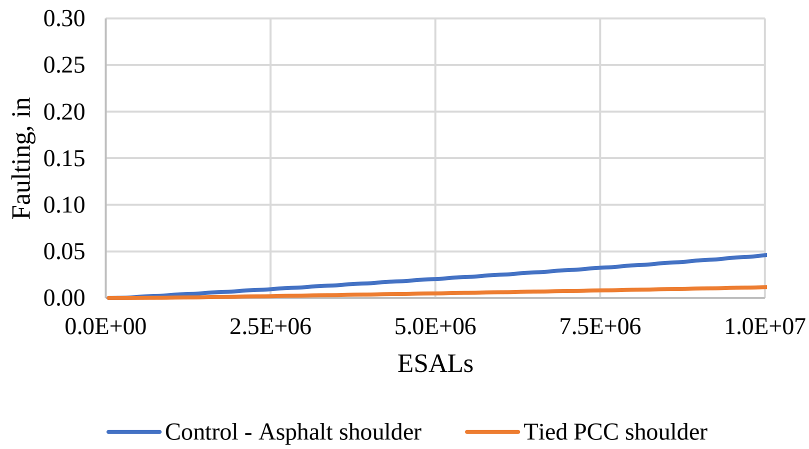

c) Both depths

Figure A-3 Effect of shoulder type on predicted faulting for Structure 3.

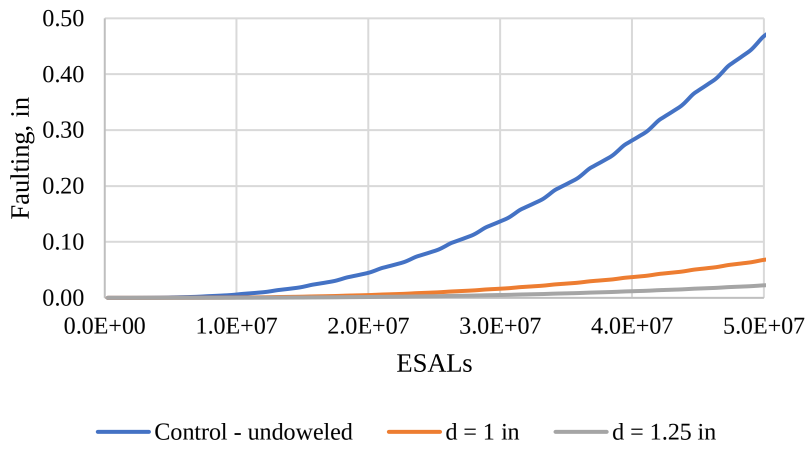

a) Partial depth

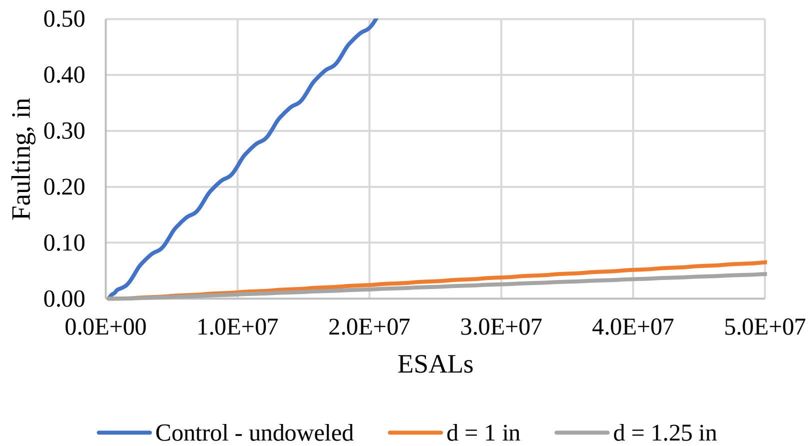

b) Full-depth

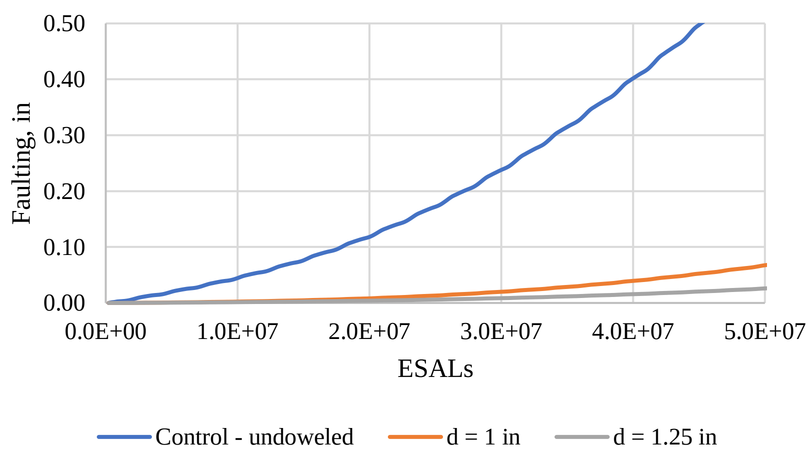

c) Both depths

Figure A-4 Effect of dowels on predicted faulting for Structure 3.

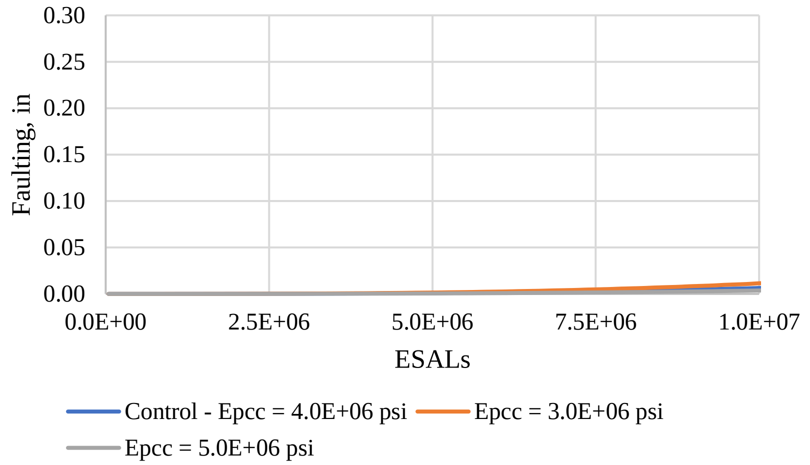

a) Partial depth

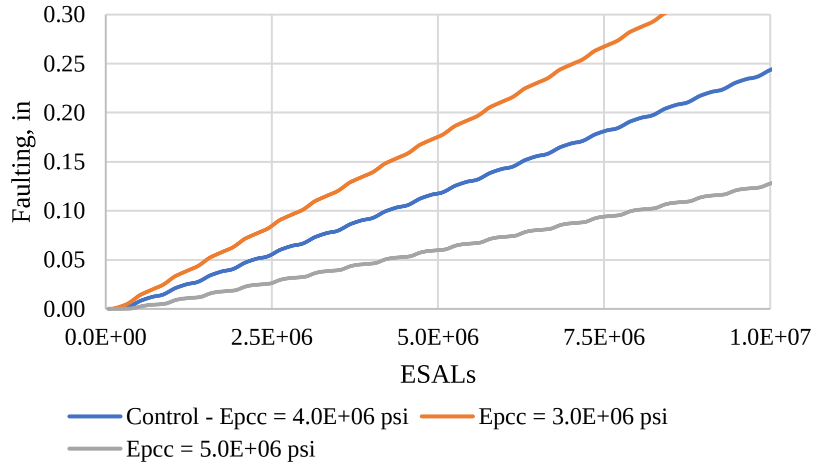

b) Full-depth

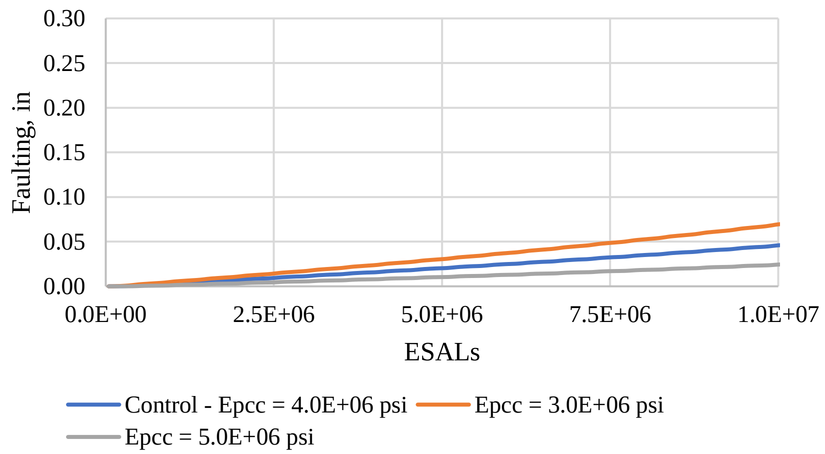

c) Both depths

Figure A-5 Effect of PCC elastic modulus on predicted faulting for Structure 3.

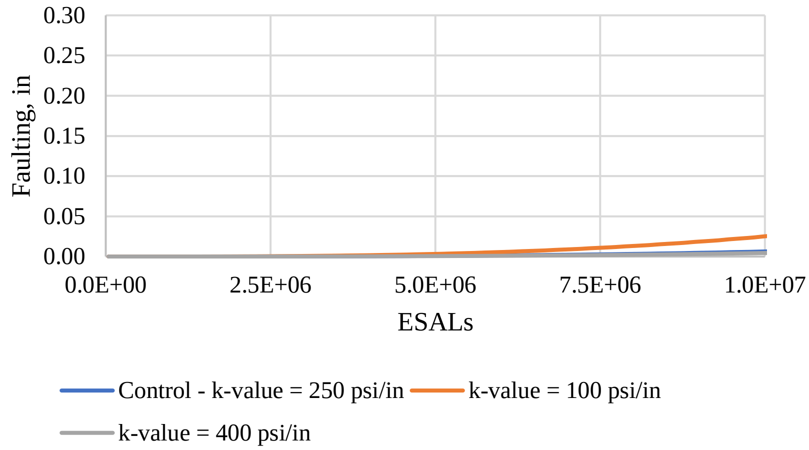

a) Partial depth

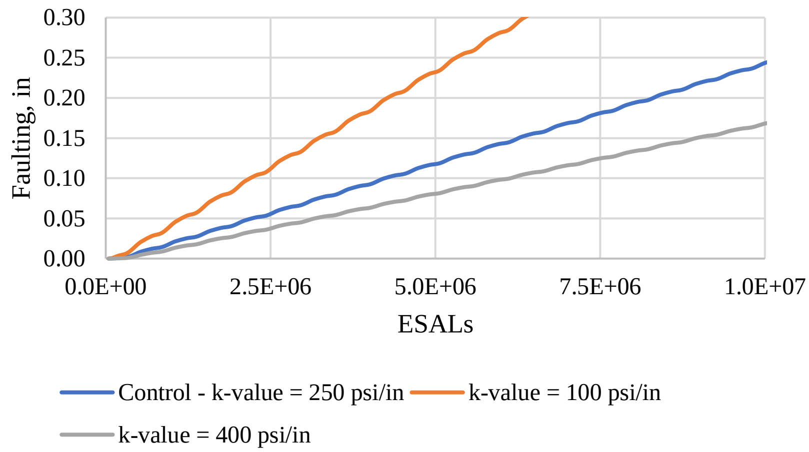

b) Full-depth

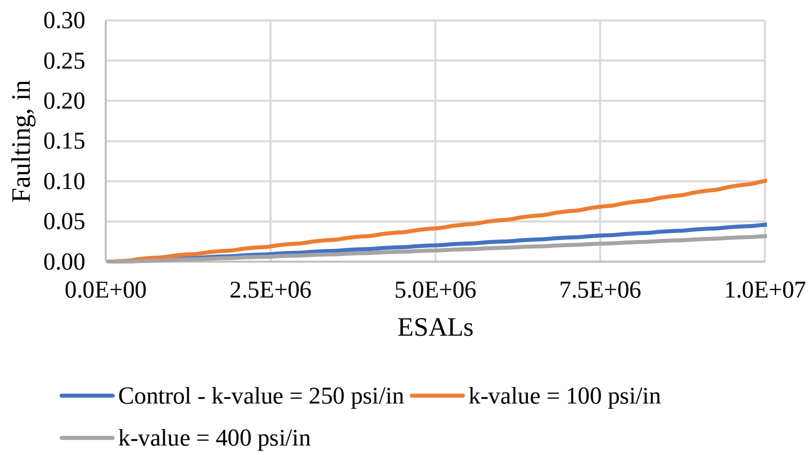

c) Both depths

Figure A-6 Effect of modulus of subgrade reaction on predicted faulting for Structure 3.

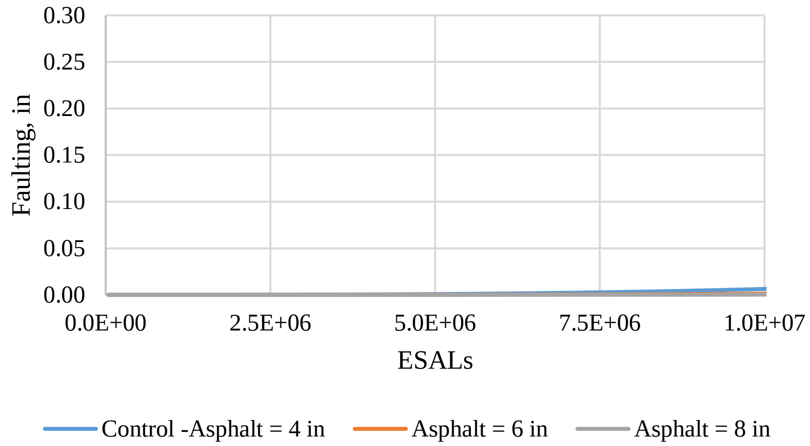

a) Partial depth

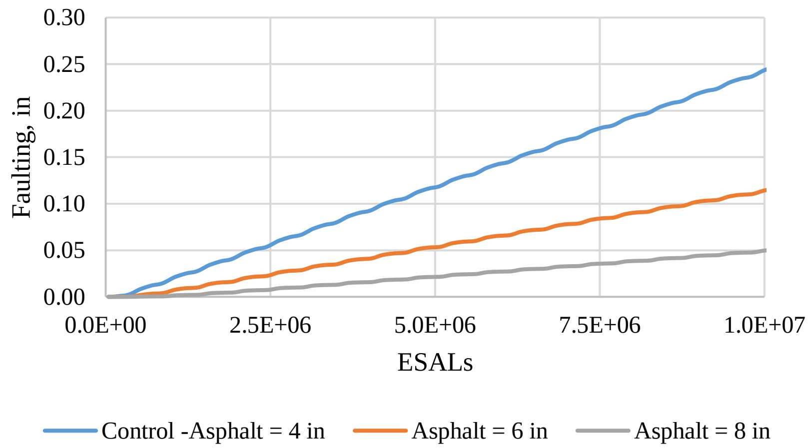

b) Full-depth

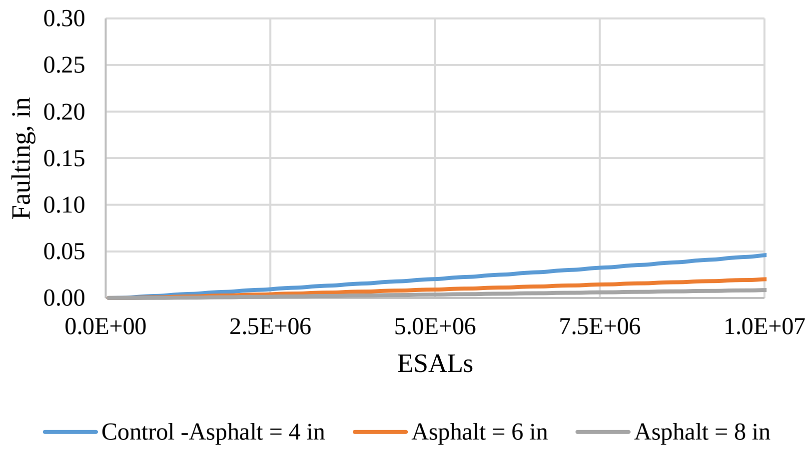

c) Both depths

Figure A-7 Effect of asphalt thickness on predicted faulting for Structure 3.

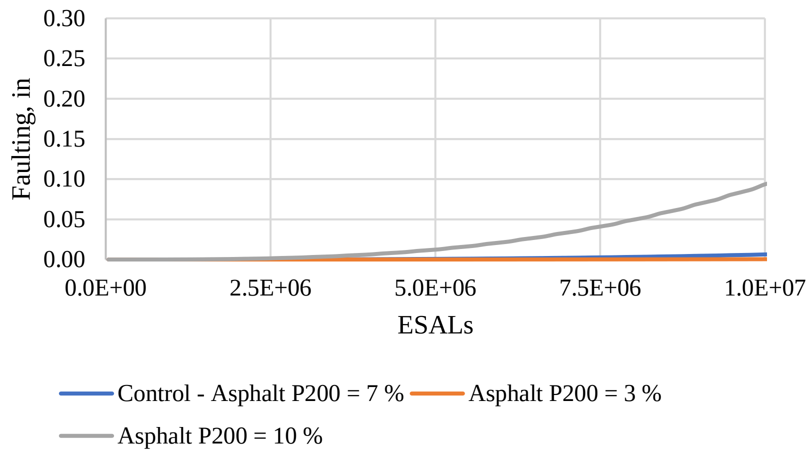

a) Partial depth

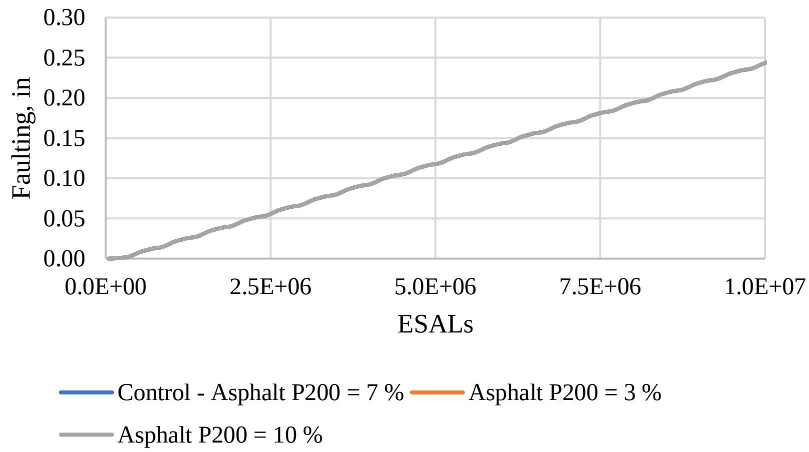

b) Full-depth

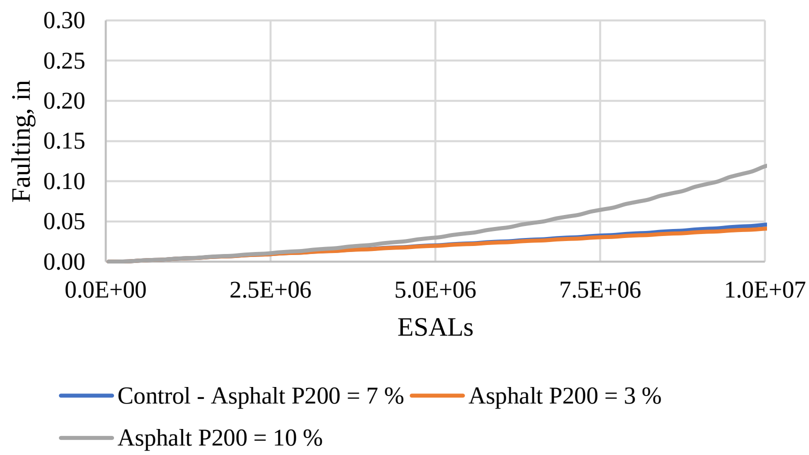

c) Both depths

Figure A-8 Effect of erodibility (P200) on predicted faulting for Structure 3.

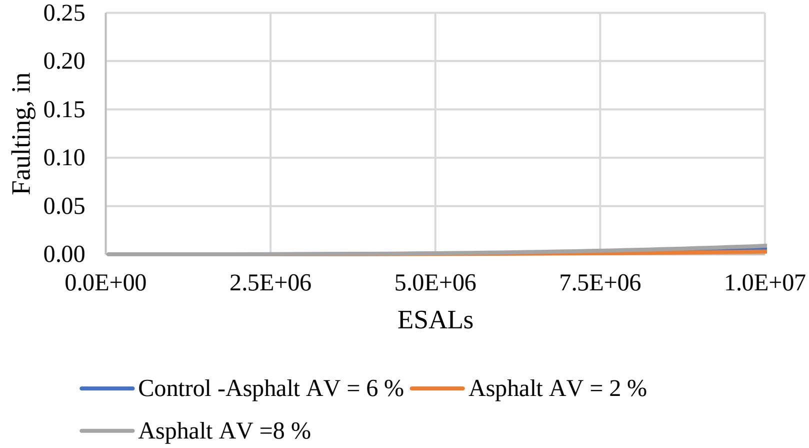

a) Partial depth

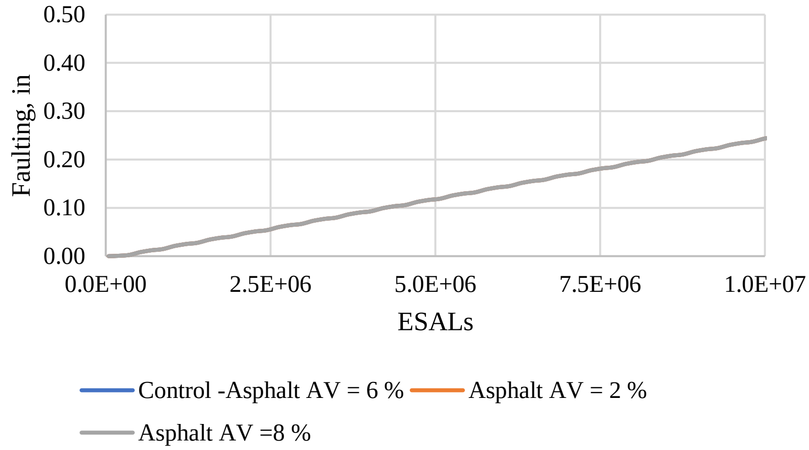

b) Full-depth

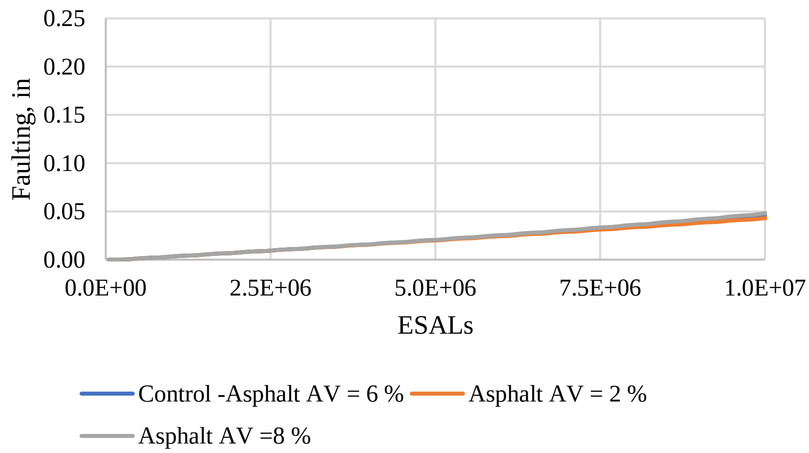

c) Both depths

Figure A-9 Effect of erodibility (air voids) on predicted faulting for Structure 3.

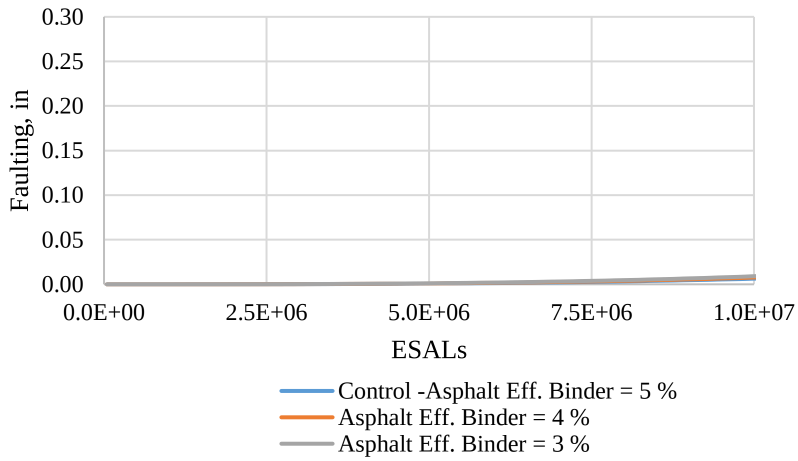

a) Partial depth

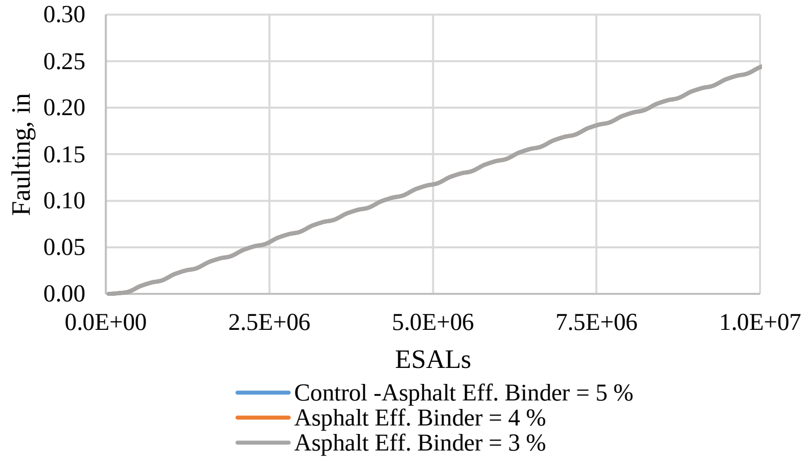

b) Full-depth

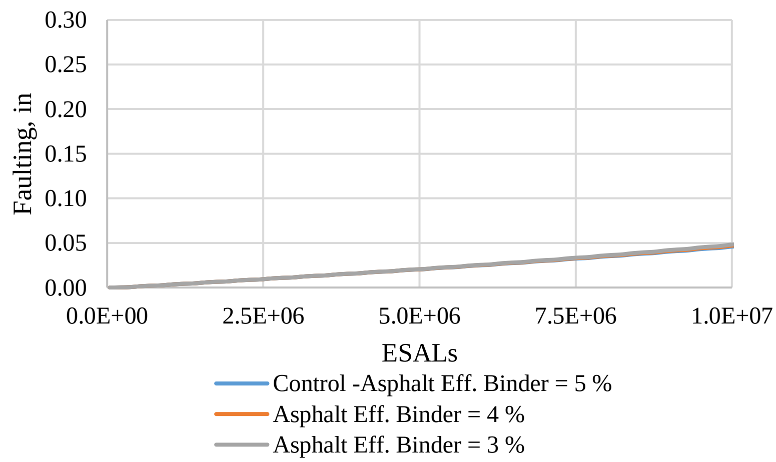

c) Both depths

Figure A-10 Effect of erodibility (effective binder content) on predicted faulting for Structure 3.

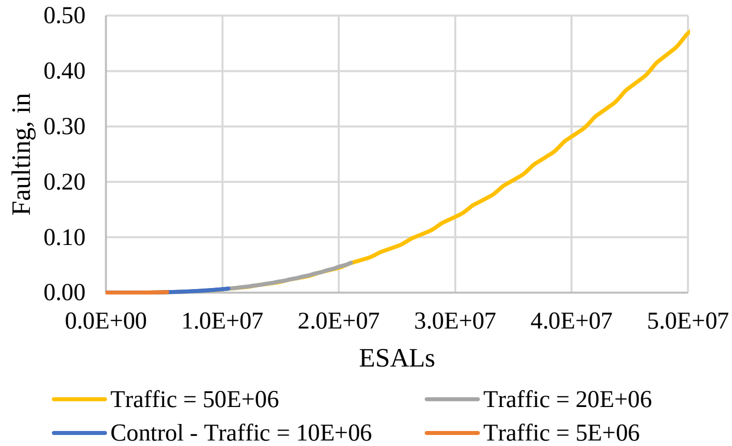

a) Partial depth

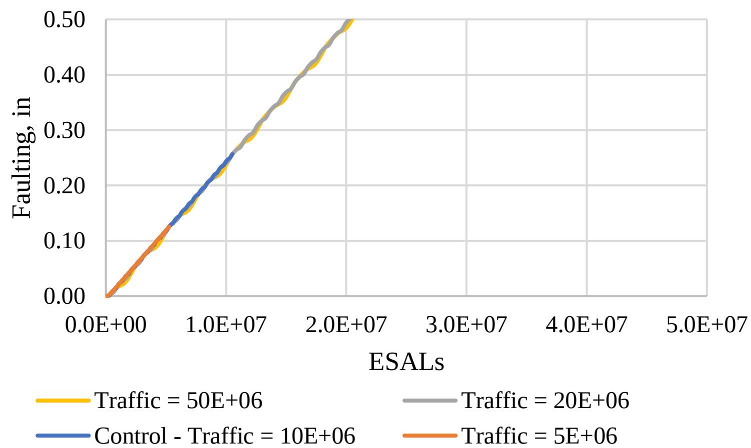

b) Full-depth

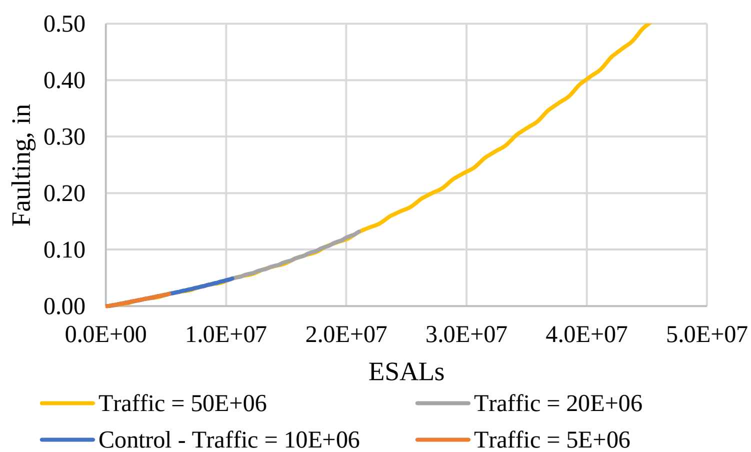

c) Both depths

Figure A-11 Effect of traffic on predicted faulting for Structure 3.

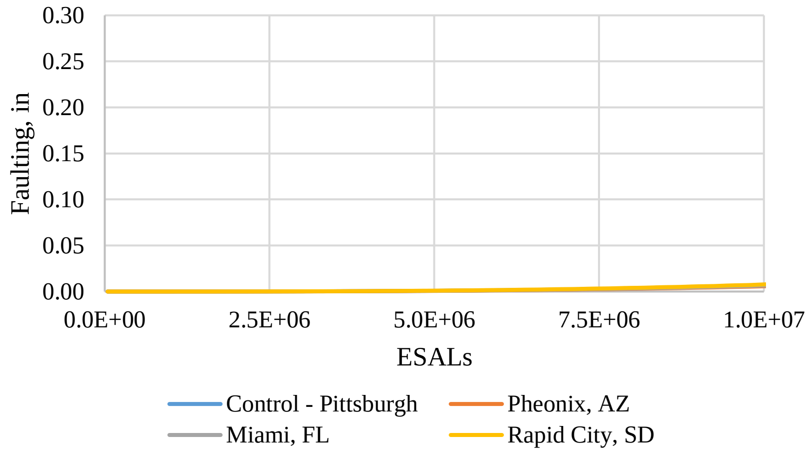

a) Partial depth

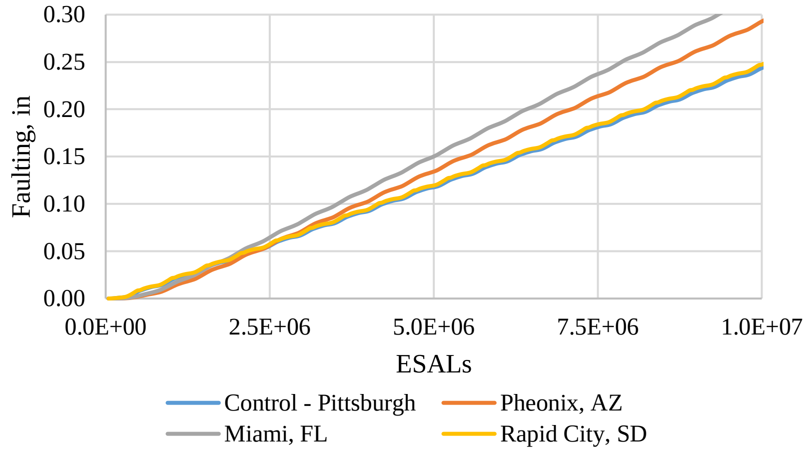

b) Full-depth

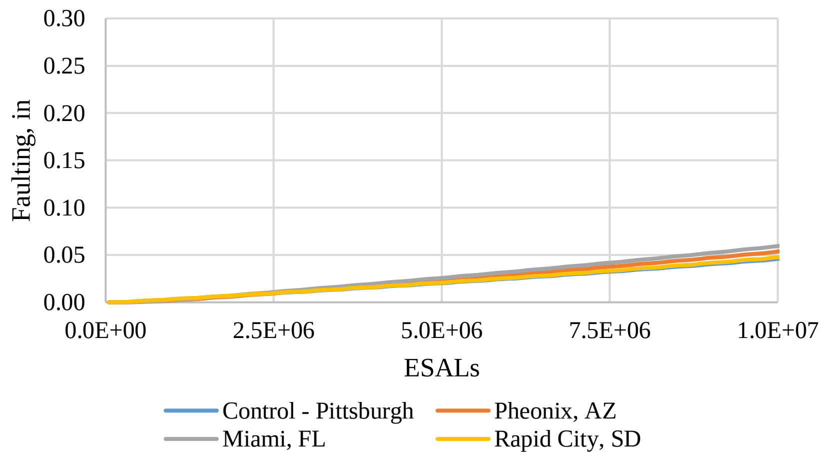

c) Both depths

Figure A-12 Effect of climate on predicted faulting for Structure 3.

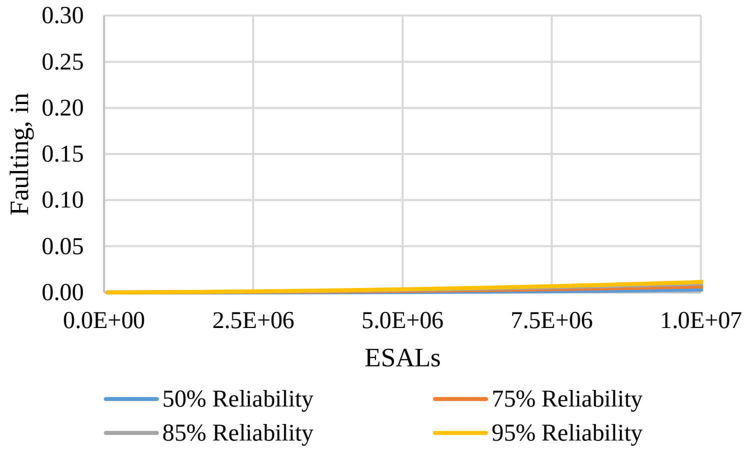

a) Partial depth

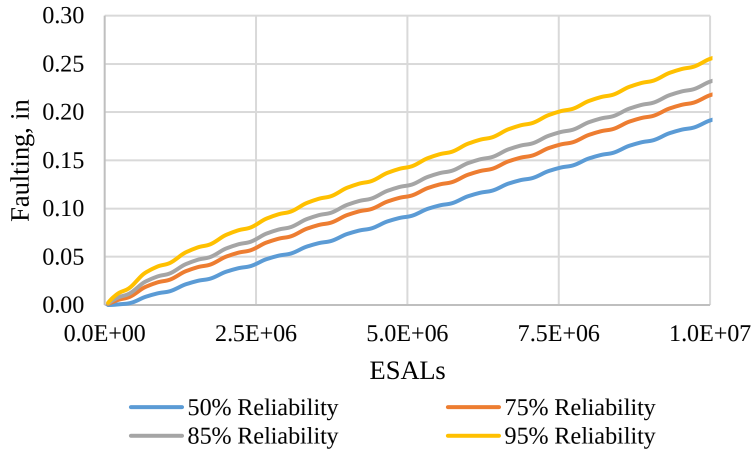

b) Full-depth

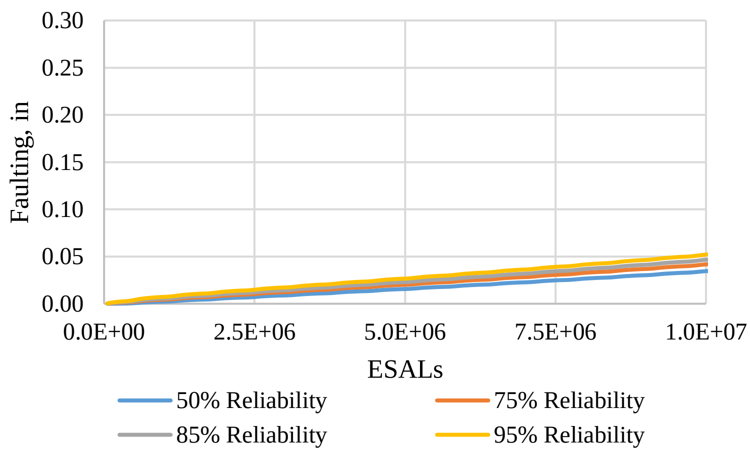

c) Both depths

Figure A-13 Effect of reliability on predicted faulting for Structure 3.

Appendix B Climatic Database

Table B-1 Climatic database.

Weather station ID	Location	Latitude	Longitude	Elevation	Sunshine zone	AMDAT zone
1	NOGALES, AZ	31.25	110.51	3887	1	5
3	ALBUQUERQUE, NM	35.02	106.37	5308	1	4
4	LAS VEGAS, NV	37.39	115.1	2091	1	6
6	FLAGSTAFF, AZ	35.08	111.4	7003	1	2
9	PAGE, AZ	36.56	111.27	4292	1	4
10	PHOENIX, AZ	33.26	111.59	1106	1	7
11	BLYTHE, CA	33.37	114.43	394	1	7
13	FARMINGTON, NM	36.44	108.14	5531	1	3
14	ROSWELL, NM	33.19	104.32	3652	1	5
16	ELY, NV	39.17	114.51	6255	1	2
17	TONOPAH, NV	38.04	117.05	2384	1	3
18	PALM SPRINGS, CA	33.50	116.31	447	1	7
19	OCEANSIDE, CA	33.13	117.21	28	1	4
20	CEDAR CITY, UT	37.42	113.06	5626	1	3
21	MOAB, UT	38.46	109.45	4575	1	3
22	ALAMOSA, CO	37.26	105.52	7536	1	1
23	DURANGO, CO	37.08	107.46	6677	1	2
25	EL PASO, TX	31.49	106.23	3945	1	5
32	SANTA FE, NM	35.37	106.05	6335	1	3
34	MIDLAND, TX	31.56	102.13	2866	2	5
37	BURLINGTON, CO	39.14	102.17	4198	2	3
38	REDDING, CA	40.31	122.19	513	2	5
39	SALT LAKE CITY, UT	42.05	111.58	4224	2	3
40	AMARILLO, TX	35.13	101.43	3589	2	4
42	GOODLAND, KS	39.22	101.41	3657	2	3
43	CHEYENNE, WY	41.10	104.49	6128	2	2
44	EVANSTON, WY	41.16	111.02	7143	2	1
45	TWIN FALLS, ID	42.29	114.29	7143	2	2
46	ELKO, NV	40.50	115.47	7143	2	1
47	KLAMATH FALLS, OR	42.09	121.43	4090	2	2
48	ALTURAS, CA	41.29	120.34	4090	2	2

Table B-1 (contd.)

49	CLAYTON, NM	36.27	103.09	4971	2	3
51	FORT STOCKTON, TX	30.55	102.55	3015	2	6
52	DALHART, TX	36.01	102.33	4304	2	3
53	GARDEN CITY, KS	37.56	100.43	2880	2	3
54	COLORADO SPRINGS, CO	38.49	104.43	6183	2	2
55	DENVER, CO	39.50	104.40	5382	2	2
58	CASPER, WY	42.54	106.28	5351	2	2
59	RAWLINS, WY	41.49	107.12	4090	2	1
60	ROCK SPRINGS, WY	41.35	109.04	821	2	1
61	PRICE, UT	39.33	110.45	5877	2	2
63	POCATELLO, ID	42.55	112.34	4454	2	2
64	BOISE, ID	43.34	116.13	2861	2	3
65	WINNEMUCCA, NV	40.54	117.49	6255	2	3
66	SACRAMENTO, CA	38.31	121.29	41	2	4
67	MIAMI, FL	25.49	80.18	29	3	7
68	DALLAS, TX	32.54	97.02	562	3	5
69	WICHITA, KS	37.39	97.26	1341	3	4
70	GREAT FALLS, MT	47.28	111.23	3673	3	2
71	MC ALLEN, TX	26.11	98.14	4090	3	7
72	SAN ANTONIO, TX	29.32	98.28	821	3	6
73	TULSA, OK	36.12	95.53	821	3	5
74	RAPID CITY, SD	44.03	103.03	3153	3	2
75	SHERIDAN, WY	44.46	106.59	3945	3	1
76	GLASGOW, MT	48.13	106.37	2271	3	1
78	SPOKANE, WA	47.37	117.32	2384	3	2
79	TAMPA, FL	27.58	82.32	2271	3	7
80	NAPLES, FL	26.01	81.47	21	3	7
81	ABILENE, TX	32.25	99.41	1792	3	5
82	WICHITA FALLS, TX	33.59	98.29	6183	3	5
83	LAWTON, OK	34.34	98.25	1110	3	5
84	OKLAHOMA CITY, OK	35.23	97.36	1284	3	4
85	HUTCHINSON, KS	38.04	97.52	1523	3	4
86	MANHATTAN, KS	39.08	96.41	1045	3	4
87	PHILIP, SD	44.03	101.36	2208	3	2
88	PINE RIDGE, SD	43.01	102.31	3276	3	2
90	BILLINGS, MT	45.49	108.32	3582	3	2
91	BUTTE, MT	45.58	112.30	4292	3	1
92	MILES CITY, MT	46.26	105.53	3945	3	1

Table B-1 (contd.)

93	MISSOULA, MT	46.55	114.05	3202	3	1
95	REDMOND, OR	44.15	121.09	3072	3	2
96	YAKIMA, WA	46.34	120.32	3652	3	2
97	HOUSTON, TX	31.56	95.22	121	4	6
99	JACKSON, MS	32.19	90.05	296	4	5
100	COLUMBUS, GA	32.31	84.56	435	4	5
101	ATLANTA, GA	33.38	84.26	974	4	5
102	KANSAS CITY, MO	39.18	94.43	1008	4	3
103	HAGERSTOWN, MD	39.43	77.44	737	4	3
104	ABERDEEN, SD	45.27	98.25	1306	4	1
105	RICHMOND, VA	37.31	77.19	167	4	5
106	RALEIGH/DURHAM, NC	35.52	78.47	430	4	4
107	COLUMBIA, SC	33.56	81.07	365	4	5
108	GAINESVILLE, FL	29.41	82.16	152	4	6
109	MOBILE, AL	30.41	88.15	212	4	6
110	ALEXANDRIA, LA	31.23	92.18	97	4	5
111	LITTLE ROCK, AR	34.45	92.14	292	4	5
112	DES MOINES, IA	41.32	93.40	971	4	3
113	SIOUX FALLS, SD	43.35	96.45	1428	4	1
114	JAMESTOWN, ND	46.56	98.41	1496	4	1
115	BISMARCK, ND	46.46	100.45	1654	4	1
116	HURON, SD	44.23	98.14	1284	4	1
117	SIOUX CITY, IA	42.23	96.23	1139	4	2
118	OTTUMWA, IA	41.07	92.27	844	4	2
120	OMAHA, NE	41.19	95.54	1028	4	3
121	ST LOUIS, MO	38.45	90.22	710	4	4
122	COLUMBIA, MO	38.49	92.13	884	4	3
123	SPRINGFIELD, MO	37.14	93.23	1280	4	4
124	CAPE GIRARDEAU, MO	37.14	89.34	339	4	4
125	FAYETTEVILLE, AR	36.01	94.10	1247	4	4
126	CORPUS CHRISTI, TX	27.46	97.31	48	4	7
127	NEW ORLEANS, LA	29.59	90.15	7	4	6
128	HATTIESBURG, MS	31.16	89.15	147	4	5
129	TUPELO, MS	34.16	88.46	350	4	5
130	BIRMINGHAM, AL	33.34	86.45	639	4	5
131	CHARLESTON, SC	32.54	80.02	48	4	5
132	GREENVILLE, SC	34.51	82.21	1037	4	4
133	GREENSBORO, NC	36.06	79.56	907	4	4

Table B-1 (contd.)

134	CHARLOTTE, NC	35.13	80.56	724	4	4
135	CINCINNATI, OH	39.06	84.25	512	5	3
136	CHAMPAIGN, IL	40.02	88.17	752	5	3
137	NEW YORK, NY	40.4	73.48	32	5	3
138	MINNEAPOLIS, MN	44.53	93.14	874	5	2
139	DULUTH, MN	46.50	92.11	1429	5	1
140	WAUSAU, WI	44.56	89.38	1192	5	2
141	SAULT STE MARIE, MI	46.28	84.22	727	5	1
142	INDIANAPOLIS, IN	39.43	86.16	797	5	3
143	LEXINGTON, KY	38.02	84.37	980	5	3
145	BALTIMORE, MD	39.1	76.41	196	5	3
146	ALBANY, NY	42.45	73.48	281	5	2
147	MANCHESTER, NH	42.56	71.26	269	5	2
148	BANGOR, ME	44.49	68.49	197	5	1
149	BAUDETTE, MN	48.44	94.37	1083	5	1
150	HIBBING, MN	47.23	92.50	1355	5	1
151	PARK RAPIDS, MN	46.54	95.04	1453	5	1
152	REDWOOD FALLS, MN	44.33	95.05	1024	5	1
153	ROCHESTER, MN	43.54	92.29	1326	5	1
154	MILWAUKEE, WI	42.57	87.54	680	5	2
155	MADISON, WI	43.08	89.21	860	5	2
156	HANCOCK, MI	47.10	88.29	1073	5	2
157	WATERLOO, IA	42.33	92.24	863	5	2
158	CHICAGO, IL	41.59	87.55	658	5	3
159	CARBONDALE/ MURPHYBORO, IL	37.47	89.15	430	5	3
160	BURLINGTON, VT	44.28	73.09	348	5	2
161	EVANSVILLE, IN	38.02	87.32	421	5	4
162	BOWLING GREEN, KY	36.59	86.26	539	5	4
164	BRISTOL/JHNSN CTY/KNGSPRT, TN	36.29	82.24	1539	5	3
165	ROANOKE, VA	37.19	79.58	1192	5	4
167	BOSTON, MA	42.22	71.01	180	5	3
168	PHILADELPHIA, PA	39.52	75.14	62	5	4
169	CLEVELAND, OH	41.24	81.51	805	6	3
170	ERIE, PA	42.05	80.11	756	6	2
171	PORTLAND, OR	45.35	122.36	223	6	3
172	SEATTLE, WA	47.28	122.19	450	6	3
173	DETROIT, MI	42.13	83.21	631	6	2
174	FORT WAYNE, IN	41.01	85.13	806	6	2

Table B-1 (contd.)

175	FINDLAY, OH	41.01	83.40	800	6	3
176	NEWARK, OH	40.01	82.28	882	6	3
177	PARKERSBURG, WV	39.21	81.26	866	6	3
178	PITTSBURGH, PA	40.30	80.14	1175	6	3
179	WILLIAMSPORT, PA	41.14	76.55	543	6	2
180	SYRACUSE, NY	43.07	76.06	417	6	2
181	EUGENE, OR	44.08	123.13	363	6	3
182	TACOMA, WA	47.16	122.35	296	6	3
183	GRAND RAPIDS, MI	42.53	85.31	788	6	2
184	KALAMAZOO, MI	42.14	85.33	895	6	2
185	SAGINAW, MI	43.32	84.05	666	6	2
186	TOLEDO, OH	41.34	83.29	623	6	3
187	MANSFIELD, OH	40.49	82.31	1300	6	2
188	AKRON, OH	40.55	81.26	1241	6	3
189	YOUNGSTOWN/ WARREN, OH	41.15	80.40	1193	6	2
190	MORGANTOWN, WV	39.98	79.55	1245	6	3
191	CHARLESTON, WV	38.23	81.35	1026	6	3
192	HUNTINGTON, WV	38.23	82.34	825	6	3
193	WILKES-BARRE/ SCRANTON, PA	41.20	75.44	958	6	2
194	HARRISBURG, PA	40.11	76.46	314	6	3
195	DU BOIS, PA	41.11	78.54	1807	6	2
196	ALTOONA, PA	40.18	78.19	1495	6	2
197	BRADFORD, PA	41.48	78.38	2125	6	1
198	ROCHESTER, NY	43.07	77.41	588	6	2
199	BINGHAMTON, NY	42.13	75.59	1630	6	2
200	PLATTSBURGH, NY	44.41	73.31	352	6	1
201	WATERTOWN, NY	43.59	76.01	332	6	2
202	BELLINGHAM, WA	48.47	122.32	168	6	2

Table B-2 Climatic database corresponding asphalt binders.

Weather station ID	Location	Latitude	Longitude	Elevation	PG temperature		% Avg. sunshine
1	NOGALES, AZ	31.25	110.51	3887	70	-10	73
3	ALBUQUERQUE, NM	35.02	106.37	5308	64	-16	73
4	LAS VEGAS, NV	37.39	115.1	2091	64	-10	73
6	FLAGSTAFF, AZ	35.08	111.4	7003	58	-16	73
9	PAGE, AZ	36.56	111.27	4292	64	-10	73
10	PHOENIX, AZ	33.26	111.59	1106	70	-10	73
11	BLYTHE, CA	33.37	114.43	394	76	-10	73
13	FARMINGTON, NM	36.44	108.14	5531	64	-16	73
14	ROSWELL, NM	33.19	104.32	3652	70	-16	73
16	ELY, NV	39.17	114.51	6255	52	-22	73
17	TONOPAH, NV	38.04	117.05	2384	64	-16	73
18	PALM SPRINGS, CA	33.50	116.31	447	70	-10	73
19	OCEANSIDE, CA	33.13	117.21	28	64	-10	73
20	CEDAR CITY, UT	37.42	113.06	5626	58	-22	73
21	MOAB, UT	38.46	109.45	4575	64	-16	73
22	ALAMOSA, CO	37.26	105.52	7536	58	-22	73
23	DURANGO, CO	37.08	107.46	6677	58	-22	73
25	EL PASO, TX	31.49	106.23	3945	70	-10	73
32	SANTA FE, NM	35.37	106.05	6335	64	-16	73
34	MIDLAND, TX	31.56	102.13	2866	70	-10	71
37	BURLINGTON, CO	39.14	102.17	4198	64	-22	71
38	REDDING, CA	40.31	122.19	513	58	-10	71
39	SALT LAKE CITY, UT	42.05	111.58	4224	52	-22	71
40	AMARILLO, TX	35.13	101.43	3589	64	-16	71
42	GOODLAND, KS	39.22	101.41	3657	64	-22	71
43	CHEYENNE, WY	41.10	104.49	6128	58	-28	71
44	EVANSTON, WY	41.16	111.02	7143	58	-28	71
45	TWIN FALLS, ID	42.29	114.29	7143	58	-16	71
46	ELKO, NV	40.50	115.47	7143	58	-22	71
47	KLAMATH FALLS, OR	42.09	121.43	4090	58	-22	71
48	ALTURAS, CA	41.29	120.34	4090	58	-16	71
49	CLAYTON, NM	36.27	103.09	4971	64	-16	71
51	FORT STOCKTON, TX	30.55	102.55	3015	70	-10	71
52	DALHART, TX	36.01	102.33	4304	64	-16	71
53	GARDEN CITY, KS	37.56	100.43	2880	66	-16	71

Table B-2 (contd.)

54	COLORADO SPRINGS, CO	38.49	104.43	6183	64	-22	71
55	DENVER, CO	39.50	104.40	5382	58	-22	71
58	CASPER, WY	42.54	106.28	5351	58	-28	71
59	RAWLINS, WY	41.49	107.12	4090	58	-28	71
60	ROCK SPRINGS, WY	41.35	109.04	821	58	-28	71
61	PRICE, UT	39.33	110.45	5877	58	-16	71
63	POCATELLO, ID	42.55	112.34	4454	58	-22	71
64	BOISE, ID	43.34	116.13	2861	58	-16	71
65	WINNEMUCCA, NV	40.54	117.49	6255	64	-16	71
66	SACRAMENTO, CA	38.31	121.29	41	64	-10	71
67	MIAMI, FL	25.49	80.18	29	70	-10	59
68	DALLAS, TX	32.54	97.02	562	70	-10	59
69	WICHITA, KS	37.39	97.26	1341	64	-16	59
70	GREAT FALLS, MT	47.28	111.23	3673	52	-28	59
71	MC ALLEN, TX	26.11	98.14	4090	70	-10	59
72	SAN ANTONIO, TX	29.32	98.28	821	70	-10	59
73	TULSA, OK	36.12	95.53	821	64	-16	59
74	RAPID CITY, SD	44.03	103.03	3153	58	-28	59
75	SHERIDAN, WY	44.46	106.59	3945	58	-28	59
76	GLASGOW, MT	48.13	106.37	2271	52	-28	59
78	SPOKANE, WA	47.37	117.32	2384	52	-22	59
79	TAMPA, FL	27.58	82.32	2271	70	-10	59
80	NAPLES, FL	26.01	81.47	21	70	-10	59
81	ABILENE, TX	32.25	99.41	1792	70	-10	59
82	WICHITA FALLS, TX	33.59	98.29	6183	70	-10	59
83	LAWTON, OK	34.34	98.25	1110	64	-16	59
84	OKLAHOMA CITY, OK	35.23	97.36	1284	64	-16	59
85	HUTCHINSON, KS	38.04	97.52	1523	64	-16	59
86	MANHATTAN, KS	39.08	96.41	1045	64	-22	59
87	PHILIP, SD	44.03	101.36	2208	58	-28	59
88	PINE RIDGE, SD	43.01	102.31	3276	58	-28	59
90	BILLINGS, MT	45.49	108.32	3582	58	-28	59
91	BUTTE, MT	45.58	112.30	4292	58	-28	59
92	MILES CITY, MT	46.26	105.53	3945	52	-28	59
93	MISSOULA, MT	46.55	114.05	3202	58	-28	59
95	REDMOND, OR	44.15	121.09	3072	58	-22	59
96	YAKIMA, WA	46.34	120.32	3652	58	-16	59
97	HOUSTON, TX	31.56	95.22	121	70	-10	59

Table B-2 (contd.)

99	JACKSON, MS	32.19	90.05	296	70	-10	59
100	COLUMBUS, GA	32.31	84.56	435	64	-10	59
102	KANSAS CITY, MO	39.18	94.43	1008	58	-16	59
103	HAGERSTOWN, MD	39.43	77.44	737	58	-16	59
104	ABERDEEN, SD	45.27	98.25	1306	58	-28	59
105	RICHMOND, VA	37.31	77.19	167	64	-10	59
106	RALEIGH/ DURHAM, NC	35.52	78.47	430	64	-10	59
107	COLUMBIA, SC	33.56	81.07	365	64	-10	59
108	GAINESVILLE, FL	29.41	82.16	152	70	-10	59
109	MOBILE, AL	30.41	88.15	212	64	-10	59
110	ALEXANDRIA, LA	31.23	92.18	97	64	-10	59
111	LITTLE ROCK, AR	34.45	92.14	292	64	-10	59
112	DES MOINES, IA	41.32	93.40	971	58	-22	59
113	SIOUX FALLS, SD	43.35	96.45	1428	58	-28	59
114	JAMESTOWN, ND	46.56	98.41	1496	52	-28	59
115	BISMARCK, ND	46.46	100.45	1654	52	-28	59
116	HURON, SD	44.23	98.14	1284	58	-28	59
117	SIOUX CITY, IA	42.23	96.23	1139	58	-22	59
118	OTTUMWA, IA	41.07	92.27	844	58	-22	59
120	OMAHA, NE	41.19	95.54	1028	58	-22	59
121	ST LOUIS, MO	38.45	90.22	710	64	-22	59
122	COLUMBIA, MO	38.49	92.13	884	64	-22	59
123	SPRINGFIELD, MO	37.14	93.23	1280	64	-16	59
124	CAPE GIRARDEAU, MO	37.14	89.34	339	64	-22	59
125	FAYETTEVILLE, AR	36.01	94.10	1247	64	-16	59
126	CORPUS CHRISTI, TX	27.46	97.31	48	70	-10	59
127	NEW ORLEANS, LA	29.59	90.15	7	64	-10	59
128	HATTIESBURG, MS	31.16	89.15	147	64	-10	59
129	TUPELO, MS	34.16	88.46	350	64	-10	59
130	BIRMINGHAM, AL	33.34	86.45	639	64	-10	59
131	CHARLESTON, SC	32.54	80.02	48	64	-10	59
132	GREENVILLE, SC	34.51	82.21	1037	64	-10	59
133	GREENSBORO, NC	36.06	79.56	907	64	-16	59
134	CHARLOTTE, NC	35.13	80.56	724	64	-10	59
135	CINCINNATI, OH	39.06	84.25	512	58	-16	52
136	CHAMPAIGN, IL	40.02	88.17	752	58	-22	52
137	NEW YORK, NY	40.4	73.48	32	58	-16	52
138	MINNEAPOLIS, MN	44.53	93.14	874	58	-28	52
139	DULUTH, MN	46.50	92.11	1429	52	-28	52

Table B-2 (contd.)

140	WAUSAU, WI	44.56	89.38	1192	58	-28	52
141	SAULT STE MARIE, MI	46.28	84.22	727	52	-28	52
142	INDIANAPOLIS, IN	39.43	86.16	797	58	-16	52
143	LEXINGTON, KY	38.02	84.37	980	58	-16	52
145	BALTIMORE, MD	39.1	76.41	196	64	-16	52
146	ALBANY, NY	42.45	73.48	281	58	-22	52
147	MANCHESTER, NH	42.56	71.26	269	52	-16	52
148	BANGOR, ME	44.49	68.49	197	52	-22	52
149	BAUDETTE, MN	48.44	94.37	1083	52	-28	52
150	HIBBING, MN	47.23	92.50	1355	52	-28	52
151	PARK RAPIDS, MN	46.54	95.04	1453	52	-28	52
152	REDWOOD FALLS, MN	44.33	95.05	1024	58	-28	52
153	ROCHESTER, MN	43.54	92.29	1326	58	-28	52
154	MILWAUKEE, WI	42.57	87.54	680	58	-22	52
155	MADISON, WI	43.08	89.21	860	58	-28	52
156	HANCOCK, MI	47.10	88.29	1073	52	-28	52
157	WATERLOO, IA	42.33	92.24	863	58	-22	52
158	CHICAGO, IL	41.59	87.55	658	58	-22	52
159	CARBONDALE/ MURPHYBORO, IL	37.47	89.15	430	58	-22	52
160	BURLINGTON, VT	44.28	73.09	348	52	-28	52
161	EVANSVILLE, IN	38.02	87.32	421	58	-16	52
162	BOWLING GREEN, KY	36.59	86.26	539	64	-16	52
164	BRISTOL/JHNSN CTY/ KNGSPRT, TN	36.29	82.24	1539	64	-16	52
165	ROANOKE, VA	37.19	79.58	1192	64	-16	52
167	BOSTON, MA	42.22	71.01	180	58	-16	52
168	PHILADELPHIA, PA	39.52	75.14	62	58	-16	52
169	CLEVELAND, OH	41.24	81.51	805	58	-22	44
170	ERIE, PA	42.05	80.11	756	52	-22	44
171	PORTLAND, OR	45.35	122.36	223	52	-10	44
172	SEATTLE, WA	47.28	122.19	450	52	-10	44
173	DETROIT, MI	42.13	83.21	631	58	-22	44
174	FORT WAYNE, IN	41.01	85.13	806	58	-16	44
175	FINDLAY, OH	41.01	83.40	800	58	-22	44
176	NEWARK, OH	40.01	82.28	882	58	-16	44
177	PARKERSBURG, WV	39.21	81.26	866	58	-16	44
178	PITTSBURGH, PA	40.30	80.14	1175	58	-16	44
179	WILLIAMSPORT, PA	41.14	76.55	543	52	-16	44

Table B-2 (contd.)

180	SYRACUSE, NY	43.07	76.06	417	52	-22	44
181	EUGENE, OR	44.08	123.13	363	52	-10	44
182	TACOMA, WA	47.16	122.35	296	58	-16	44
183	GRAND RAPIDS, MI	42.53	85.31	788	58	-22	44
184	KALAMAZOO, MI	42.14	85.33	895	58	-22	44
185	SAGINAW, MI	43.32	84.05	666	58	-22	44
186	TOLEDO, OH	41.34	83.29	623	58	-16	44
187	MANSFIELD, OH	40.49	82.31	1300	58	-22	44
188	AKRON, OH	40.55	81.26	1241	58	-22	44
189	YOUNGSTOWN/ WARREN, OH	41.15	80.40	1193	58	-22	44
190	MORGANTOWN, WV	39.98	79.55	1245	58	-22	44
191	CHARLESTON, WV	38.23	81.35	1026	58	-16	44
192	HUNTINGTON, WV	38.23	82.34	825	58	-16	44
193	WILKES-BARRE/ SCRANTON, PA	41.20	75.44	958	52	-22	44
194	HARRISBURG, PA	40.11	76.46	314	58	-16	44
195	DU BOIS, PA	41.11	78.54	1807	52	-22	44
196	ALTOONA, PA	40.18	78.19	1495	52	-22	44
197	BRADFORD, PA	41.48	78.38	2125	52	-22	44
198	ROCHESTER, NY	43.07	77.41	588	52	-22	44
199	BINGHAMTON, NY	42.13	75.59	1630	52	-22	44
200	PLATTSBURGH, NY	44.41	73.31	352	52	-28	44
201	WATERTOWN, NY	43.59	76.01	332	52	-22	44
202	BELLINGHAM, WA	48.47	122.32	168	58	-16	44

Bibliography

AASHTO. *AASHTO Guide for the Design of Pavement Structures.* American Association of State Highway and Transportation Officials. Washington, D.C., 1993.

AASHTO. AASHTOWare® DARWin-ME™ v.1.0 Mechanistic-Empirical Pavement Design Software. American Association of State Highway and Transportation Officials, Washington, D.C. 2011.

AASHTO. AASHTOWare Pavement ME Design. American Association of State Highway and Transportation Officials, Washington, D.C. 2012.

ABAQUS Inc. *ABAQUS software version 6.13: Analysis user's manual.* ABAQUS Inc., Providence, RI, 2013.

Alland, K., J.M. Vandenbossche, S. Sachs, and J.W. DeSantis. Failure Modes in Unbonded Concrete Overlays. In: Proceedings of the 11th International Conference on Concrete Pavements (ICCP). San Antonio, TX, 2016, pp. 620-637.

Applied Research Associates (ARA), Inc., ERES Division. *Guide for Mechanistic-Empirical Design of New and Rehabilitated Pavement Structures*. Final Report NCHRP 1-37A. Transportation Research Board of the National Academies, Washington, D.C., 2004.

ASTM D2493 / D2493M-16. Standard Practice for Viscosity-Temperature Chart for Asphalt Binders. ASTM International, West Conshohocken, PA, 2016.

Bakhsh, K. and Zollinger, D. Faulting prediction model for design of concrete pavement structures. Pavement Materials, Structures, and Performance: ASCE Journal of Transportation Engineering, Vol. 239, 2014, pp. 327–342.

Barman, M., F. Mu, and J.M. Vandenbossche. De*velopment of a Rational of Mechanistic-Empirical Based Design Guide for Thin and Ultra-thin Whitetopping: Task 1 Report.* University of Pittsburgh, Pittsburgh, PA, 2011.

Burnham, T.R. "Forensic Investigation Report for Mn/ROAD Ultra-thin Whitetopping Test Cells 93, 94, and 95. Report MN/RC -2005-45. 2005.

Burnham, T.R. *Construction Report for MnROAD Thin Whitetopping Test Cells 60-63*. Report MN/RC – 2006-18. 2006.

Burnham, T.R., B. Izevbekhai, J. Gallagher, and S. Huerta. Development of Performance Curves for Whitetopping in Minnesota. Minnesota Department of Transportation, Report No. MN/RC 2019-16. 2019.

Byrum, C.R., Hansen, W., and Kohn, S.D. The effect of PCC strength and other parameters on the performance of PCC pavements. In: Proceedings of the 6th International Purdue Conference on Concrete Pavement Design and Materials for High Performance. Purdue University, 1997, pp. 373–393.

Crovetti, J.A. Design and Evaluation of Jointed Concrete Pavement Systems Incorporating Open-Graded Permeable Bases. *Ph.D. Dissertation*, University of Illinois at Urbana-Champaign. 1994.

Davids, W., G. Turkiyyah, and J. Mahoney. EverFE: Rigid Pavement Three-Dimensional Finite Element Analysis Tool. *Transportation Research Record: Journal of the Transportation Research Board*, No. 1629, 1998, pp. 41-49.

DeSantis, J.W., J.M. Vandenbossche, K. Alland, S. Sachs, T. Burnham, and A. Montenegro. Joint Performance in Bonded Concrete Overlays of Asphalt. In: Proceedings of the 11th International Conference for Concrete Pavements (ICCP). San Antonio, TX, 2016, pp. 638-660.

DeSantis, J.W., J.M. Vandenbossche, K. Alland, and J. Harvey. Development of Artificial Neural Networks for Predicting the Response of Bonded Concrete Overlays of Asphalt for Use in a Faulting Prediction Model. *Transportation Research Record: Journal of the Transportation Research Board.* No. 2672, 2018. pp. 360-370.

DeSantis, J.W., S. Sachs, and J.M. Vandenbossche. Faulting Development in Concrete Overlays and Pavements. International Journal of Pavement Engineering DOI: 10.1080/10298436.2018.1548706. 2019.

ERES Consultants, Inc. *Evaluation of Unbonded Portland Cement Concrete Overlays*. National Cooperative Highway Research Program Report No. 425, Transportation Research Board, Washington, DC. 1999.

Guo, E., L. Ricalde, and I. Kawa. FAA Finite Element Design Procedure for Rigid Pavements. Report No. DOT/FAA/AR-07/33. Federal Aviation Administration, Washington, D.C., 2007.

Hoerner, T.E. Guide to Developing Performance-Related Specifications for PCC Pavements, Volume IV: Appendix G – Pavespec 2.0 User Guide. FHWA-RD-99-059. Washington, DC: Federal Highway Administration, 1999.

Ioannides A.M., Khazanovich L., and Becque J.L. *Structural Evaluation of Base Layers in Concrete Pavement Systems.* Transportation Research Record 1370, Washington D. C. 1992.

Janssen, D.J. and M. B. Snyder. *The Temperature-Moment Concept for Evaluating Pavement Temperature Data.* Journal of Infrastructure Engineering. Vol.6, No.2, pp. 81-83, 2000.

Jung, Y.S. and Zollinger, D.G. New Laboratory-Based Mechanistic-Empirical Model for Faulting in Jointed Concrete Pavement. *Transportation Research Record: Journal of the Transportation Research Board*, No. 2226, 2011, pp. 60–70.

Khazanovich, L. *Structural Analysis of Multi-Layered Concrete Pavement Systems.* PhD Dissertation. University of Illinois, Urbana, 1994.

Khazanovich, L., Yu, H.T., Rao, S., Galasova, K., Shats, E., and R. Jones. *ISLAB2000 - Finite Element Analysis Program for Rigid and Composite Pavements. User's Guide*. ERES Consultants, Champaign, IL, 2000.

Khazanovich, L., M. Darter, H.T. Yu. Mechanistic-Empirical Model to Predict Transverse Joint Faulting. *Transportation Research Record: Journal of the Transportation Research Board*, No. 1896, 2004, pp. 34-45.

Knott, J.F., *Fundamentals of Fracture Mechanics*, John Wiley – Halsted Press, New York, 1973.

Kuo, C.M. *Three-dimensional Finite Element Analysis of Concrete Pavement.* PhD Dissertation, University of Illinois at Urbana-Champaign, 1994.

Larralde, J. Structural Analysis of Rigid Pavements with Pumping. *Ph.D. Dissertation,* Purdue University, West Lafayette, Ind., 1984.

Larson, G., and B. Dempsey. *Enhanced integrated climatic model*. University of Illinois, Urbana, IL, 2003.

Li, Z., and J.M Vandenbossche. Redefining the Failure Mode for Thin and Ultra-thin Whitetopping with a 1.8-x1.8-m (6-x6-ft) Joint Spacing. *Transportation Research Record: Journal of the Transportation Research Board*, No. 2368, 2013, pp. 133-146.

Li, Z., Dufalla, N., Mu, F., and Vandenbossche, J.M. "Bonded Concrete Overlay of Asphalt Pavements Mechanistic-Empirical Design Guide (BCOA-ME)", Theory Manual, FHWA TFP study 5(165), 2013.

Li, Z., J.M. Vandenbossche, and N. Dufalla. Structural Model for Longitudinal Cracking in Bonded Whitetopping with a 1.83-m x 1.83-m (6-ft x 6-ft) Joint Spacing. American Society of Civil Engineering Journal of Transportation Engineering, Part B: Pavements, Vol. 143, No. 4, 2017.

Mack, J.W., L.W. Cole, and J.P. Mohsen. Analytical Considerations for Thin Concrete Overlays on Asphalt. *Transportation Research Record: Journal of the Transportation Research Board*, No. 1388, 1993, pp. 167–173.

Mack, J.W., L.D. Hawbaker, and L.W. Cole. Ultrathin Whitetopping: State-of-the-Practice for Thin Concrete Overlays of Asphalt. *Transportation Research Record: Journal of the Transportation Research Board*, No. 1610, 1998, pp. 39–43.

Mallela, J., Titus Glover, L., Darter, M.I., Von Quintus, H., Gotlif, A., Stanley, M., and S. Sadasivam. *Guidelines for Implementing NCHRP 1-37A M-E Design Procedures in Ohio: Volume 1— Summary of Findings, Implementation Plan, and Next Steps*. FHWA Report No. FHWA/OJ-2009/9A, 2009, pp. 1-112.

MATLAB and Statistics Toolbox Release 2013a, The MathWorks, Inc., Natick, MA.

Montgomery, *D. Design and Analysis of Experiments 8th Edition*. John Wiley & Sons, Inc., New York, 2013.

Mu F. and J.M. Vandenbossche. *Development of a Rational of Mechanistic-Empirical Based Design Guide for Thin and Ultra-Thin Whitetopping. Task 2 Report: Review and Selection of Structural Response Models.* University of Pittsburgh, Pittsburgh, PA, 2011

Mu F. and J.M. Vandenbossche. Establishing Effective Linear Temperature Gradients for Ultrathin Bonded Concrete Overlays on Asphalt Pavements. *Transportation Research Record: Journal of the Transportation Research Board*, No. 2305, 2012, pp. 24-31.

National Pavement and Concrete Technology Center. Faulting Study on BCOA Pavements in Iowa. In *Concrete Overlay Performance on Iowa's Roadways, 2017*. National Pavement and Concrete Technology Center, Ames, IA.

Owusu-Antwi, E.B., Titus-Glover, L., Khazanovich, L., and J.R. Roesler. *Development and Calibration of Mechanistic-Empirical Distress Models for Cost Allocation*. Final Report, Federal Highway Administration, Washington, DC, March 1997.

Packard, R.G. *Design Considerations for Control of Joint Faulting of Undoweled Pavements.* Proceedings of the International Conference on Concrete Pavement Design. Lafayette, Purdue University, 1977.

Pavement Systems LLC. "A Superpave Binder Selection Program." Federal Highway Administration Asphalt Team, Bethesda, MD. 2005.

Rasmussen, R.O., et al. Identification of Pavement Failure Mechanisms at FHWA Accelerated Loading Facility Ultrathin Whitetopping Project. *Transportation Research Record: Journal of the Transportation Research Board*, No. 1816, Washington, DC. 2002, pp. 148–155.

Rasmussen, R. and Garber, S. Nonwoven Geotextile Interlayers for Separating Cementitious Pavement Layers: German Practice and US Field Trials. Washington, DC: FHWA, U.S. Department of Transportation. 2009.

Ripley, B.D. Pattern Recognition and Neural Networks. Cambridge University Press, 1996.

Roesler, J., et al. Design and Concrete Material Requirements for Ultrathin Whitetopping. FHWA-ICT-08-016. Illinois Center for Transportation, Rantoul, IL, 2008.

Sachs, S.G., Vandenbossche, J.M., and M.B. Snyder. *Calibration of National Rigid Pavement Performance Models for the Pavement Mechanistic-Empirical Design Guide*. Transportation Research Board, Transportation Research Record 2524, 2015, pp. 59-67.

Sachs, S.G., J.M. Vandenbossche, K. Alland, J.W. DeSantis, and L. Khazanovich. Laboratory investigation into the effects of different interlayer systems on reflective cracking in unbonded overlays of existing concrete pavements. *Transportation Research Record: Journal of the Transportation Research Board*, No. 2591, Washington, DC. 2016, pp. 33–41.

Sachs, S.G., J.M. Vandenbossche, Z. Li, and M. Barman. Accounting for Temperature Susceptibility of Asphalt Stiffness when Designing Bonded Concrete Overlays of Asphalt Pavements. ASCE Journal of Transportation Engineering 142 (10): 04016040. 2016.

Sachs, S. *Development of a Joint Faulting Model for Unbonded Concrete Overlays of Existing Concrete Pavements Through a Laboratory and Numeric Analysis*. PhD Dissertation, University of Pittsburgh, 2017.

Simpson, A.L., Rauhut, J.B., Jordahl, P.R., Owusu-Antwi, E.B., Darter, M.I., and R. Ahmad. *Early Analysis of LTPP General Pavement Studies Data, Volume 3: Sensitivity Analyses for Selected Pavement Distresses*. Report SHRP-P-393, Strategic Highway Research Program, Washington, DC, 1994.

Titus-Glover, L., Owusu-Antwi, E.B., and M.I. Darter. *Design and Construction of PCC Pavements, Volume III: Improved PCC Performance.* Report No. FHWA-RD-98-113, Federal Highway Administration, Washington, DC, January 1999.

Totsky, O.N. *Behavior of Multi-Layered Plates and Beams on Winkler Foundation* (in Russian). *Stroitel'naya Mekhanika i Raschet Sooruzhenii,* Vol. 6, 1981, pp. 54-58.

Vandenbossche, J. M. and Rettner, D. L. “The Construction of US-169 and I-94 Experimental Thin and Ultra-Thin Whitetopping Sections in Minnesota.” Report MN/RC -2001-07. 1998.

Vandenbossche, J. M. and A. J. Fagerness. Performance, Analysis, and Repair of Ultrathin and Thin Whitetopping at Minnesota Road Research Facility. *Transportation Research Record: Journal of the Transportation Research Board*, No. 1809, 2002. pp. 191-198.

Vandenbossche, J. M., and Barman, M. “Bonded Whitetopping Overlay Design Considerations for Prevention of Reflection Cracking, Joint Sealing, and the Use of Dowel Bars.” *Transportation Research Record: Journal of the Transportation Research Board*, No.2155, 2010. pp. 3-11.

Vandenbossche, J.M., N. Dufalla, and Z. Li, “Bonded Concrete Overlay of Asphalt Mechanistic-Emperical Design Procedure,” *International Journal for Pavement Engineers,* Vol. 18, No. 11, 2016, pp. 1 -12.

Wu, C.L., Mack, J.W., Okamoto, P.A., and R.G. Packard. *Prediction of Faulting of Joints in Concrete Pavements.* Proceedings, Fifth International Conference on Concrete Pavement Design and Rehabilitation, Vol. 2., Purdue University, West Lafayette, IN, April 1993.

Wu, C.L., S.M. Tarr, T.M. Refai, M.A. Nagi, and M.J. Sheehan. *Development of Ultrathin Whitetopping Design Procedure.* Research and Development Series No. 2124. Portland Cement Association, Skokie, IL, 1998.

Yu, H.T., Darter, M.I., Smith, K.D., Jiang, J., and L. Khazanovich. *Performance of Concrete Pavements Volume III - Improving Concrete Pavement Performance.* Final Report, Contract DTFH61-91-C-00053, Federal Highway Administration, McLean, VA, 1996.